Focused-Ion-Beam Micromachined Unstable Resonator Semiconductor Lasers

Zhuoyu Bao
B.S., Anqing Teacher's College, Anhui, China, 1985
M.S., Wuhan Institute of Physics, The Chinese Academy of Science, 1988

A dissertation submitted to the faculty of the
Oregon Graduate Institute of Science & Technology
in partial fulfillment of the
requirements for the degree
Doctor of Philosophy
in
Applied Physics

January 1995

The dissertation "Focused-Ion-Beam Micromachined Unstable Resonator Semiconductor Lasers" by Zhuoyu Bao has been examined and approved by the following Examination Committee:

Richard K. DeFreez, Thesis Advisor
Associate Professor

Anthony E. Bell
Associate Professor

Reinhart Engelmann
Professor

Joseph Puretz, Ph.D.
FEI Company

Geoffrey A. Wilson, Ph.D.
Coherent Technology, Inc.

This dissertation is dedicated to my late grandmother

Ms. Huizhen Hu Bao

ACKNOWLEDGEMENTS

I want to thank my advisor, Prof. Rick DeFreez, for giving me the opportunity to work on unstable resonator semiconductor lasers, and for consistent guidance of my work during the past four years. I want to thank Prof. Tony Bell, Prof. Reinhart Engelmann, Dr. Joe Puretz, and Dr. Geoff Wilson for their help during my stay at Oregon Graduate Institute and/or during the final stage of completing my dissertation. I would also like to thank Dr. Greg Dente, from whom I benefited immensely.

I want to thank Peter Carleson for teaching me how to perform focused-ion-beam micromachining and master many other lab skills. I enjoyed working with him. I am very grateful to Linda DeHainaut, Marc Felisky, David Gallant, Craig Largent, Chuck Moeller, and Mike Tilton. They gave me enormous help.

I want to thank Profs. Fred Holmes, Rao Gudimetla, Jon Orloff, Jim Parsons, and Raj Solanki for their assistance in my course study and generous support throughout my stay at OGI. I also thank Kathy Feyer, John Hunt, Don Johansen, and Bev Kyler for their kind help.

Many thanks go to Prof. Clancy Hinrichs, Dr. Tianbao Xie, Prof. Bill Mackie, Gary Cabe, Gerald Magera and Mark Hinrichs. I appreciate their help during my stay in Linfield Research Institute.

I enjoyed my interactions with Shafqat Ahmed, Brian Baird, Yijun Cai, Ajay Chaddha, Feng Chen, Chaodan Deng, Genying Gao, Sukryong Hahn, Weiran Kong, Raghu Ranganathan, Badhi Rask, Yunlong Sun, Jin Wu, Cangsang Zhao, and Chunyan Zhou. I appreciate their help and friendship.

I dedicate this work to my late grandmother, Ms. Huizhen Hu Bao, whose love, care, and inspiration were critical to the survival of my early childhood in a then extremely harsh society, and the continuation of my early education. I want to express my deepest appreciation to my parents, brothers and sisters for their consistent love and sacrifice. Finally, I want to give my deepest thanks to my wife Mei for her love, care, and tolerance to my spending late evenings and weekends at OGI on this dissertation. I love them all.

Table of Contents

List of Figures

List of Tables

List of Frequently Used Symbols

Symbol	Description
A	Light emitting area
A_{idle}	Area pumped inefficiently for an URSL with rectangular stripe
a ($a_{1,2}$)	Laser output aperture width
Brightness	Brightness (radiance) of an optical source
b	gain coefficient (dg/dJ)
c	Speed of light in vacuum
E_g	Bandgap voltage
$E(y,z)$	Spatial distribution of electrical field
G	Net gain
g	Optical gain
g_{th}	Threshold gain
$g_{1,2}$	$g_{1,2} = 1 - L/R_{1,2}$
h	Planck constant
$h_{\perp}$	Transverse virtual source size (FWHM)
$h_{\parallel}$	Lateral virtual source size (FWHM)
I (I_{th})	Injection current (Threshold current)
$I_{1,2}$	Optical intensities inside the end mirrors
$I(y,z)$	Spatial distribution of optical intensity
J	Current density
$J_{th}^{fp,ur}$	Threshold current densities for FPSL and URSL
J_0	Transparency current density
k (k_0)	Wavevetor in material (in vacuum)
L	Laser cavity length
L_{eff}	Effective cavity length
L_{eq}	Equivalent cavity length
L_{ff}	Separation between a far-field plane and laser output mirror
L_{opt}	Optimum cavity length
M	Total resonator magnification
$M_{1,2}$	Forward, and backward resonator magnifications
M_s	Optical beam quality index

M1, M2	Laser end mirrors
N	Carrier density
N_{rt}	Number of round-trips needed to build up lasing action
$P_{1,2}$	Optical output power from two end mirrors
P_{op}	Total optical output power
$R_{1,2}$	Radii of curvature of laser end mirrors
$R_{s1,s2}$	Depth of Siegman centers
R_{sc} (R_{sf})	Siegman center depth from the curved (flat) mirror side
$R_{v1,v2}$	Apparent virtual source depths
$r_{1,2}$	Dimensionless parameters to measure the Siegman center depth
S	Scattering coefficient of a laser end mirror
S_a	Solid angle extended by an optical beam
$T(T_{1,2})$	Optical transmission coefficients (from two end mirrors)
W	Stripe width
W_{ff}	Far-field width (FWHM)
$y_{hm}(z)$	Transverse position for half maximum optical intensity
μ_e	Modal effective refractive index
ρ	Mirror reflectivity
$\rho_{1,2}$	Reflectivities of laser end mirrors
α	Linewidth enhancement factor
α_i	Internal optical loss
Γ	Optical confinement factor
η	Total power efficiency
η_d	External differential quantum efficiency
η_i	Internal differential quantum efficiency for stimulated emission
η_s	Internal quantum efficiency for spontaneous emission
γ	Light emission frequency in vacuum
β	A coefficient which is proportional to (dg/dJ)
μ_g	Group index
$\Delta\mu_c$	Carrier injection induced refractive index change
λ	Optical wavelength in vacuum
$\theta_{x,y}$	Lateral, and transverse divergence angles of a gaussian beam
$\theta_{\perp}$ ($\theta_{\parallel}$)	Transverse (lateral) divergence angle (FWHM)
$\omega_{(z)}$ ($\omega_{0x,0y}$)	Gaussian (lateral, and transverse) beam waists
σ	Wafer sheet conductivity

σ_{0i}	Spatial variance at an optical beam waist
σ_{si}	Variance in spatial frequency domain
τ_p	Photon lifetime
τ_s	Carrier lifetime
ξ	Root-mean-squared (RMS) roughness
ψ	Mirror wall tilt angle

List of Frequently Used Acronyms

Acronym	Full Name
COD	Catastrophic optical damage
FIBM	Focused-ion-beam micromachining
FPSL	Fabry-Perot type semiconductor laser
FWHM	Full width at half maximum
GRINSCH	Graded-index separate confinement heterostructure
HS-URSL	Half-symmetric unstable resonator semiconductor laser
MOPA	Master oscillator power amplifier
RAC	Refraction aberration corrected
SQW	Single quantum well
TIR	Total internal reflection
URSL	Unstable resonator semiconductor laser

ABSTRACT

Focused-Ion-Beam Micromachined Unstable Resonator Semiconductor Lasers

Zhuoyu Bao, Ph.D.

Oregon Graduate Institute of Science & Technology, 1995

Supervising Professor: Richard K. DeFreez

This dissertation presents geometrical analysis and experimental investigation of edge emitting unstable resonator semiconductor lasers (URSLs) with emphasis on the understanding of their lasing mechanisms and operating characteristics.

On the theoretical side, a geometrical URSL model is established to describe general device operating characteristics, such as the dependence of lasing threshold and efficiency on laser cavity length and resonator magnification. From the experimental side, investigations have centered on URSLs with circularly cylindrical end mirrors. For device fabrication, mirror processing technology based on focused-ion-beam micromachining (FIBM) has achieved nanometer levels of surface roughness. High performance URSLs have been fabricated from several types of III-V quantum well materials emitting at different wavelengths. For example, a 200 μm × 500 μm GaAs/AlGaAs single

quantum well triplet URSL can provide a total output power up to 2.0 Watts, and a nominal virtual source brightness as high as 430 MW/cm^2-Sr.

Comprehensive characterization procedures have been carried out for many of the FIBM URSLs. The experimental results obtained have enriched the understanding of fundamentals of URSLs. Curved subthreshold spatio-spectral patterns were observed for the first time to the author's knowledge. The virtual source width (FWHM) of an URSL usually reaches roughly diffraction-limited value around threshold, and then broadens with increasing injection levels. Streak camera results show that the delay between the formation of unstable resonator modes and the turn-on time of light emission is less than a few cavity round-trips. Further analyses of URSL temporal dynamics suggest that the broadening of the virtual source profiles can be correlated, at least in some cases, to the erratic dynamics of multiple lateral modes. Different lateral mode characteristics were observed for URSLs with different resonator magnifications.

URSLs with other types of resonator structures, such as self-collimated, refractive-aberration-corrected (RAC) mirror, hybrid, coreless, and dual curvature mirror, have also been studied. Although the devices do not perform as well as cylindrical half-symmetric URSLs, experimental observations have helped understanding lasing characteristics of unstable resonator semiconductor lasers.

Chapter 1

INTRODUCTION

For many practical applications, compact semiconductor lasers with high power, high brightness and high spatial coherence output beams are desired. Limited by the catastrophic optical damage (COD) level of the device facet, it is necessary to have large light emitting areas for these lasers. However, the transverse dimension of the semiconductor laser emitting area must be less than about 1 micron to ensure single transverse mode operation. For conventional semiconductor lasers with Fabry-Perot type resonator structures, furthermore, the filamentation phenomenon or regenerative self-focusing[1] appears when the stripe width exceeds about 10 μm. The positions of the individual filaments are unstable and shift around under current modulation. This filamentation effect seriously reduces the total power and the coherence of the output laser beam. To suppress filamentation, array structures consisting of multiple elements[2] which are narrow enough to be comparable to the size of filamentation were proposed.[3,4] After the investment of a tremendous amount of material and human resources, the resultant array lasers generally turned out to be spatially

incoherent, and temporally chaotic although stable operating characteristics could be observed occasionally. Another means of suppressing filamentation is to adopt the unstable resonator (UR) configuration.[5, 6] Although the advantages of unstable resonators for high gain semiconductor lasing media have been recognized and pursued for years,[6-10] it is only recently that URSLs with performance superior to devices with other designs have been fabricated.[11, 12]

The properties of unstable resonators have been described in the literature.[13] Unstable resonators can have high discrimination against higher order lateral modes, and unstable resonator modes are expected to be less sensitive to material non-uniformities than those of Fabry-Perot type resonators. They tend to suppress filamentation because of their magnifying abilities. They also possess large mode volumes,[5] which enables laser devices with unstable resonator configurations to efficiently utilize the gain medium. Details of relevant theoretical work will not be reviewed in this dissertation.

Restrained by material quality and facet processing technology, limited success was achieved in early URSL development.[6, 7, 9, 10] The main concern was to make cylindrical mirrors on the facets of GaAs/AlGaAs double heterostructure diode lasers to diverge the wave-front and to pursue output optical beams with high spatial coherence. In the design procedures, the gain/carrier characteristics of the the specific semiconductor active layers were either ignored,[9] or approximated with a rigid index step between the gain and loss regions.[14] The resonator magnifications were usually chosen to be larger than 5.0. The semi-empirical formula[8, 15] derived then for the

evaluation of URSL power characteristics did not provide a correct understanding of the operating characteristics necessary for designing high performance devices. As the consequence of all these factors, no significantly constructive results were achieved to confirm the advantages of UR configurations for semiconductor lasers, although a wide variety of resonator structures were tried.[10]

Recently, technologies for growth of quantum well heterostructure laser materials and fabrication of mirrors on the wafer facets were maturing. The growth of quantum well materials with low linewidth enhancement factors inspired numerical studies on laser devices.[16, 17] A research group in the Semiconductor Laser Branch in the Phillips Laboratory at Kirtland Air Force Base considered the combined effects of the diverging wave-fronts from the unstable resonator configuration and gain/carrier effects. After conducting numerical simulations using a *paraxial wave equation* (PWE) based algorithm, they suggested[16] that low magnification unstable resonators can sufficiently overcome the filamentation effects while maintaining efficiency. The joint research team of Phillips Laboratory and Oregon Graduate Institute fabricated URSLs with encouraging performance out of the graded-index separate confinement (GRINSCH) single quantum well (SQW) GaAs/AlGaAs materials.[11]

Being encouraged by the initial results, the joint team initiated a new program, which has expanded the research into a variety of quantum well materials with different emitting wavelengths, and scaled the devices to larger dimensions. To avoid any hot spots, which increase the possibility of

COD, inside the semiconductor laser media,[18] unstable resonators having no real focus inside the cavity are usually applied. The major design for this work, also the simplest configuration, is the half-symmetric unstable resonator, which consists of one cylindrical mirror and one flat mirror.

During the process of this study, the author conducted design, fabrication, and characterization tasks. The characteristics of URSL virtual source envelopes were investigated.[19] The brightness values of these virtual sources were evaluated,[12] and were found to be desirable for many practical applications. The temporal dynamics of URSL optical output were also studied using a streak camera. Following the successful CW operation of URSLs, the sub-threshold modal characteristics of URSLs were investigated, and lead to new observation of URSL spectral characteristics.[20] With the same geometrical device structures, it was later found that the efficiencies of AlGaInP quantum well lasers drop more dramatically than those of InGaAs and AlGaAs lasers after the fabrication of the cylindrical mirrors.[19] This observation led to the development of a modified geometrical theory, which considers the gain/carrier characteristics of the specific laser materials, and evaluates their general operating characteristics.[21] The solution to fabricating highly efficient AlGaInP URSLs is to increase the cavity length beyond a critical cavity length, which is dependent on the material characteristics.

With emphasis on understanding lasing mechanisms and operating characteristics, this dissertation presents geometrical analysis and experimental investigations of half-symmetric URSLs. The theoretical analysis and experimental procedures can also be readily extended to investigations of

URSLs with more complicated resonator structures. Indeed, URSLs have been fabricated with self-collimated confocal UR configurations, refraction-corrected mirrors, hybrid mirrors, laterally tilted mirrors, dual curvature mirrors, respectively. In parallel with this study, another research group has been working on URSLs with negative cylindrical regrown lens trains.[22-24]

This dissertation consists of six main chapters. In Chapter 2, a simple geometrical URSL model is presented and used to describe the general URSL operating characteristics.[25]

In Chapter 3, the general characteristics of quantum well laser materials are summarized. Material characterization procedures and results are included for several types of laser materials reported in this dissertation.

In Chapter 4, general procedures are summarized for fabricating cylindrical mirrors using focused-ion-beam micromachining (FIBM). An improved FIBM scanning strategy is introduced and applied to the fabrication of URSLs studied in this dissertation. The influence of mirror surface roughness and mirror wall tilt angle to mirror reflectivity and overall performance of the URSLs are also analyzed.

In Chapter 5, procedures for characterizing URSLs are briefly summarized, and the general operating characteristics of URSLs from various types of materials are presented. Results cover the near-field and virtual source spatial envelopes at different pumping levels, spatio-spectral mode patterns, spatial characteristics of different lateral modes, both near-field and virtual

source temporal behaviors, the sensitivity of URSL performance to the mirror wall tilt, and the cavity length dependence of URSL performance.

Chapter 6 summarizes the power characteristics of high performance URSLs from various types of materials. By defining a brightness figure for double-ended URSLs, the calculated values are presented, and compared with those of several Fabry-Perot type commercial devices. The data suggest that the URSLs do provide output beams with much higher brightness than those of Fabry-Perot type devices, and confirm the advantages of UR configurations for semiconductor lasers.

Chapter 7 presents the preliminary results and analysis of URSLs with a variety of resonator structures, which include self-collimated confocal, refractive-aberration-corrected, hybrid, coreless, and dual curvature resonators. Comparison with cylindrical URSLs are also made.

Chapter 8 includes the general conclusions of this dissertation and discussions for future research.

Chapter 2

GEOMETRICAL OPTICS ANALYSIS OF UNSTABLE RESONATOR SEMICONDUCTOR LASERS (URSLs)

In this chapter, a simple URSL model is established on the basis of geometrical resonator theory. It is then applied to the analysis of URSL operating characteristics, such as lasing threshold conditions and power characteristics. The half-symmetric unstable resonator is also analyzed.

2.1 Mode Formation in Unstable Resonators

Laser resonators consist of two reflectors placed in opposition. The curvature, separation, and size of these reflectors largely determine the field distributions and frequencies of the resultant oscillations. Resonators are conveniently characterized as either stable or unstable according to their geometric properties. In a stable resonator, a ray propagating from one reflector to the other remains confined, while all but the axial ray in an unstable resonator walk out of that resonator after a finite number of reflections. As shown in Figure 2.1, a resonator can be specified by the following parameters, the curvatures of the two end mirror as R_1 and R_2 (negative

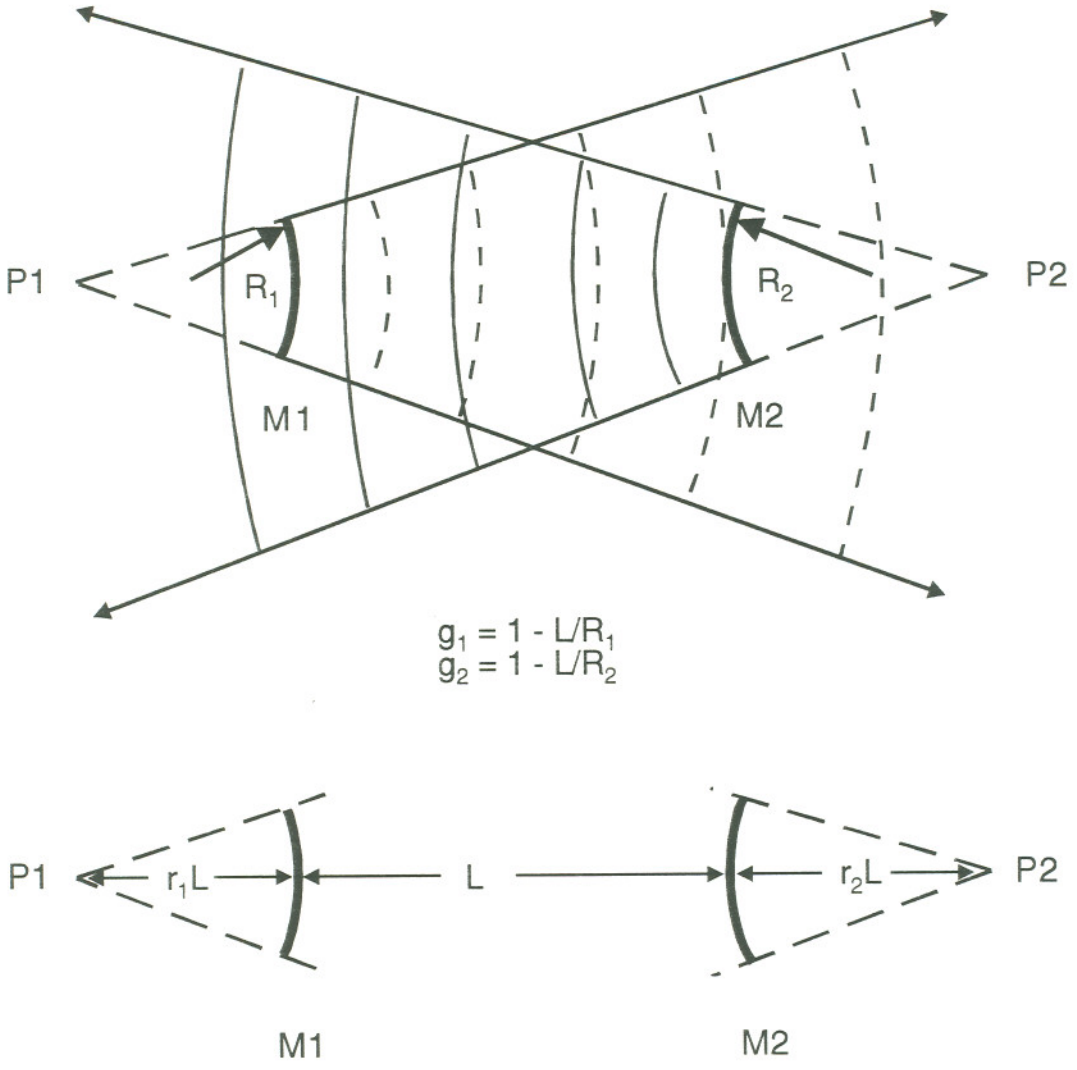

Figure 2.1 Geometrical approximation for the spatial mode pattern of an unstable resonator.

values for concave mirrors), and the mirror spacing as L. By defining parameters $g_1 = 1 - L/R_1$ and $g_2 = 1 - L/R_2$, an *ABCD* matrix for the resonator can be written as[13]

$$\begin{bmatrix} A & B \\ C & D \end{bmatrix} = \begin{bmatrix} 4g_1g_2 - 2g_1 - 1 & 2g_1L \\ (4g_1g_2 - 2g_1 - 2g_2)/L & 2g_1 - 1 \end{bmatrix}, \tag{2.1}$$

which will be used in the latter part of this section.

Geometrical analysis of unstable resonators was first made by Siegman.[5] The lasing mode of a hard-edge resonator with spherical mirrors consists of two opposite-going waves, which uniformly illuminate the in-coming mirror. These waves can be viewed as originating from two virtual sources (originally called "centers"), whose positions are determined by requiring self-consistency, i.e., by requiring that each virtual source be the image of the other upon reflection in the appropriate spherical mirror. The positions of the virtual sources P1 and P2 relative to the mirrors are measured in terms of the mirror spacing L by dimensionless distances r_1 and r_2. These quantities are taken positive for outward displacements, and negative for inward displacements such as appear in some forms of unstable resonators. According to the sign convention used in resonator analyses, the mirror radii of curvature R_1 and R_2 are negative numbers for outward curvatures, as the case shown in Figure 2.1. r_1 and r_2 are expressed as

$$r_1 = \frac{\sqrt{1 - (g_1g_2)^{-1}} - 1 + g_1^{-1}}{2 - g_1^{-1} - g_2^{-1}}, \tag{2.2}$$

and

$$r_2 = \frac{\sqrt{1-(g_1 g_2)^{-1}} - 1 + g_2^{-1}}{2 - g_1^{-1} - g_2^{-1}}. \tag{2.3}$$

For high power applications, it is desirable to have a large mode volume, and avoid any focused (hot) spots inside the resonator. To avoid internal focusing, which may initiate COD, only positive branch URs[13] are suitable for semiconductor laser applications. Typical examples are the symmetric UR (two equal convex mirrors) and half-symmetric UR (one convex and one flat), which have two virtual sources located outside of the resonator, i.e., r_1 and r_2 have positive values.

For semiconductor lasers, the refractive index of the laser medium is higher than that of the air. Due to refraction, as shown in Figure 2.2, the output laser beams can be traced back to different positions from those of virtual sources mentioned above, these new virtual point sources are called apparent virtual sources. Based on paraxial ray optics, the depths of the apparent virtual sources can be derived to be

$$R_{v1(2)} = \left[\frac{\mu_e}{(r_{2(1)} + 1)L} + \frac{(1-\mu_e)}{R_{1(2)}} \right]^{-1}, \tag{2.4}$$

where μ_e is the effective refractive index of the laser medium, the variables with subscripts "1" and "2" are the same as defined earlier in this chapter. For broad-area URSLs, the rays exiting at different lateral positions of the output mirror will have different backward crossing points on the resonator axis. This aberration effect results in diffused virtual sources which are undesirable for high brightness applications.

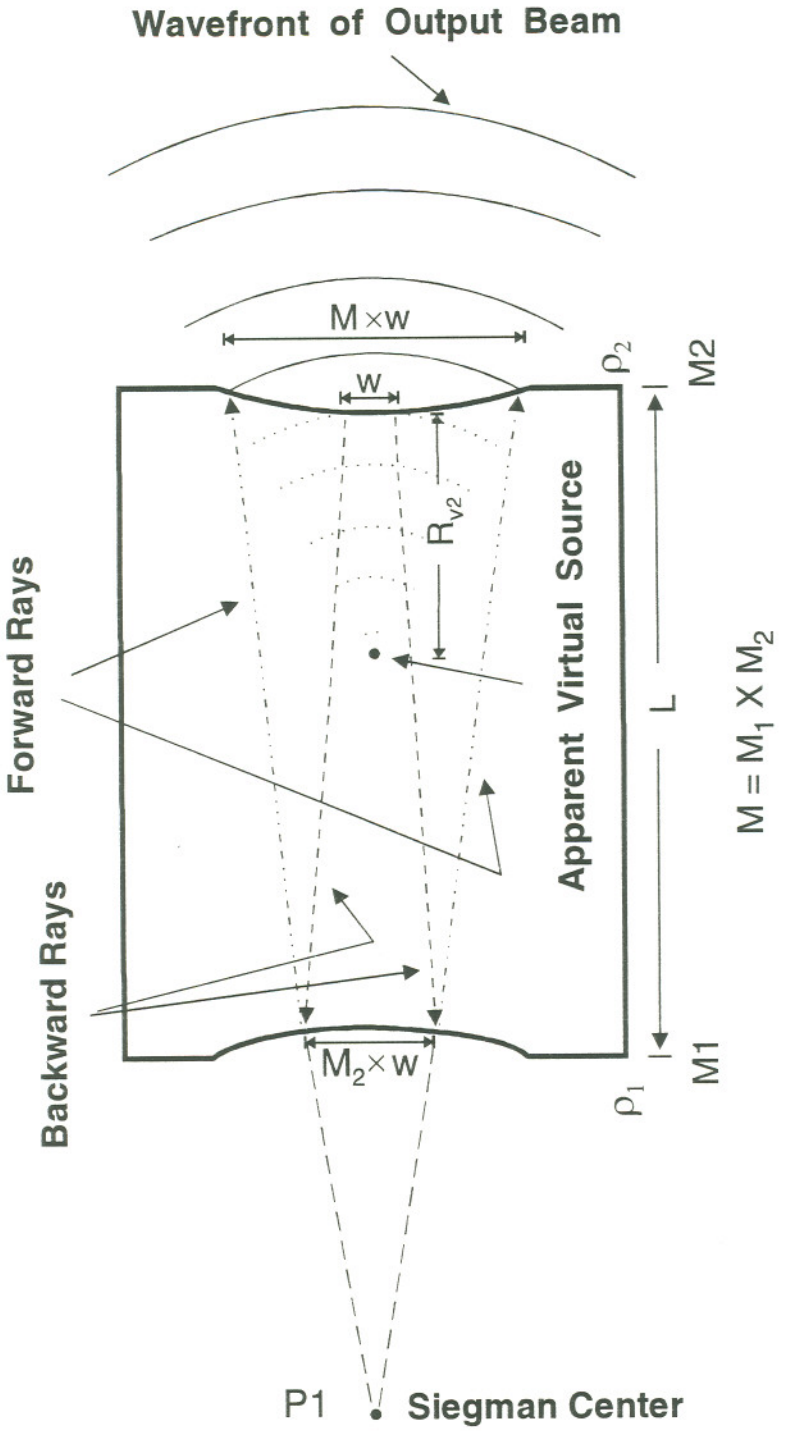

Figure 2.2 Schematic illustration of the beam propagation inside an unstable resonator, and the formation of apparent virtual sources.

For a beam of width w starting at mirror M2, as shown in Figure 2.2, it will be expanded to $M_2 w$ wide at the opposite mirror M1 after propagating along the cavity, and to Mw when returning to mirror $M2$ after one round-trip. The parameter M is defined as the resonator magnification which measures the resonator divergence, and is expressed as[13]

$$M = m + \sqrt{(m^2 - 1)}, \tag{2.5}$$

where

$$m = (A + D)2 = 2g_1 g_2 - 1. \tag{2.6}$$

The forward one way (from M1 to M2) magnification M_1 can be written as[13, 18]

$$M_1 = \frac{r_1 + 1}{r_1} = \frac{2Mg_1}{M + 1}. \tag{2.7}$$

Similarly, the backward (from M2 to M1) one-way magnification is

$$M_2 = \frac{r_2 + 1}{r_2} = \frac{2Mg_2}{M + 1}. \tag{2.8}$$

It is easy to verify that

$$M_1 M_2 = M. \tag{2.9}$$

For half-symmetric unstable resonator semiconductor lasers (HSURSLs), the flat mirrors are simply the cleaved crystal planes, the curved mirror can be formed through focused-ion-beam micromachining (FIBM)[11] or chemical etching.[7] The parameters defining the mode pattern of a HSURSL can be calculated from equations (2.2)-(2.3) with: $g_1 = 1$ and $g_2 = 1 - L/R$, where R is the radius curvature of the curved mirror, and has negative values. Expressions (2.2)-(2.3) can be simplified as

$$r_1 = \frac{M+1}{M-1}, \tag{2.10}$$

$$r_2 = \frac{2}{M-1}. \tag{2.11}$$

Equations (2.7) and (2.8) can also be simplified straightforwardly.

2.2 Lasing Condition and Efficiency

Theoretical expressions have been derived previously by others for the threshold and external differential quantum efficiency of URSLs.[8, 15] By converting the undetermined unstable resonator loss to either a modified mirror reflectivity,[8] or an equivalent mirror scattering loss,[15] the corresponding formulae from Fabry-Perot type semiconductor lasers (FPSLs) were directly adopted. In this section, new expressions for the URSL threshold and external quantum efficiency are derived.

Assume the optical intensities at the two mirrors are uniform, and defined as I_1 and I_2, respectively. For the forward propagation process (from M1 to M2), as shown in Figure 2.2, the field width is expanded from w to $M_1 w$. Accordingly, the power characteristics can be expressed as

$$I_2 = I_1(\rho_1/M_1)exp(g\Gamma-\alpha_i)L, \tag{2.12}$$

where L is the laser cavity length, ρ_1 is the power reflectivity of mirror M1, Γ is the optical confinement factor, g is the gain in the quantum well, and assumed to be homogeneous across the whole cavity here, and α_i is the internal loss of the URSL. Due to the nonplanarity of both the optical wavefront and the end mirrors, the mirror reflectivities are expected to have slight lateral nonuniformity. This minor effect is ignored here. Similarly,

the following expression can be derived for the backward propagation

$$I_1 = I_2(\rho_2/M_2)exp(g\Gamma-\alpha_i)L, \tag{2.13}$$

where ρ_2 is the power reflectivity of mirror M2. The combination of equations (2.12) and (2.13) give the following

Lasing condition:

$$\frac{\rho_1\rho_2}{M_1M_2}exp(g\Gamma-\alpha_i)L = 1, \tag{2.14}$$

Field intensity symmetry:

$$\frac{I_1}{I_2} = \left(\frac{M_1\rho_2}{M_2\rho_1}\right)^{1/2}, \tag{2.15}$$

Output power symmetry:

$$\frac{P_1}{P_2} = \frac{I_1T_1}{I_2T_2} = \frac{T_1}{T_2}\left(\frac{M_1\rho_2}{M_2\rho_1}\right)^{1/2}, \tag{2.16}$$

where P_1 and P_2 are the output powers, T_1 and T_2 are the optical transmission coefficients for mirrors $M1$ and $M2$, respectively. For a half-symmetric URSL, this power symmetry ratio can be simplified as

$$\frac{P_1}{P_2} = \frac{2}{M+1}\frac{T_1}{T_2}\left(\frac{M\rho_2}{\rho_1}\right)^{1/2}. \tag{2.16'}$$

Strictly speaking, only the counter-propagating paraxial rays overlap, so the very central region can be viewed as a lasing oscillator while the two side gain regions as amplifiers. In other words, the threshold condition — equation (2.14) — is only valid for the small, so-called, core-region. The

threshold gain can then be derived as

$$g_{th}\Gamma = \alpha_i + \frac{1}{2L}\ln(\frac{M}{\rho_1\rho_2}) = \alpha_i + \frac{1}{2L}\ln(\frac{1}{\rho_1\rho_2}) + \frac{1}{2L}ln(M). \qquad (2.17)$$

Casperson[26] derived expressions similar to (2.16) and (2.17) by solving steady-state rate equations, which were also established on geometrical assumptions.

Comparison of equation (2.17) with the corresponding expression for a Fabry-Perot laser reveals an extra term which depends on the resonator magnification but not on the specific details of the geometrical configuration. It is helpful to define an equivalent cavity length L_{eq} as[21]

$$L_{eq} = L\frac{ln(1/\rho_1^0\rho_2^0)}{ln(M/\rho_1\rho_2)}, \qquad (2.18)$$

where ρ_1^0 and ρ_2^0 are the reflectivities of the two cleaved end mirrors, respectively. It is obvious from equations (2.17) and (2.18) that the threshold gain of an URSL with cavity length of L is equivalent to that of an FPSL with shorter cavity length L_{eq} if the two devices have same end mirror reflectivities. As discussed in the following chapters, L_{eq} turns out to be an especially important parameter for the design of AlGaInP URSLs. For AlGaInP lasers, there exists a relatively large optimum cavity length. When the laser cavity is reduced to or below this value, the internal loss and reciprocal internal quantum efficiency increase dramatically with further decreases in the cavity length.[21] In practical URSL design, it is important to keep L_{eq} larger than this optimum cavity length in order to achieve high efficiency

operation.

With the assumption of a linear gain-current relation

$$g = b(J - J_0), \tag{2.19}$$

the threshold current density of an FPSL can be expressed as[27]

$$J_{th}^{fp} = J_0 + \frac{1}{b\Gamma}[\alpha_i^0 + \frac{1}{2L} ln\,(1/\rho_1^0\rho_2^0)], \tag{2.20}$$

where α_i^0 is the internal loss per unit length of the FPSL, J_0 is the transparency current density, b is the differential gain coefficient, respectively. Assumption (2.19) is correct only when the injected carrier density is relatively low. Assuming that parameters b, J_0 and Γ remain the same after fabrication of cylindrical mirrors, the threshold current density for an URSL can be written as

$$J_{th}^{ur} = J_0 + \frac{1}{b\Gamma}[\alpha_i + \frac{1}{2L} ln\,(M/\rho_1\rho_2)]. \tag{2.21}$$

For an FPSL without filamentation, the external differential quantum efficiency can be approximately expressed as[27]

$$\eta_d^{fp} = \eta_i^0 \frac{(1/2L)\,ln\,(1/\rho_1^0\rho_2^0)}{\alpha_i^0 + (1/2L)\,ln\,(1/\rho_1^0\rho_2^0)} \times \left[1 - \frac{S_1^0(\rho_2^0)^{1/2} + S_2^0(\rho_1^0)^{1/2}}{[1 - (\rho_1^0\rho_2^0)^{1/2}][(\rho_1^0)^{1/2} + (\rho_2^0)^{1/2}]} \right], \tag{2.22}$$

where η_i^0 is the internal differential quantum efficiency of the FPSL, and S_1^0 and S_2^0 are the light scattering coefficients of the two cleaved end mirrors,

respectively. Using the loss term introduced in equation (2.17), an empirical expression of the external differential quantum efficiency for an URSL can be derived as

$$\eta_d^{ur} = \eta_i \frac{(1/2L)ln(1/\rho_1\rho_2)}{\alpha_i + (1/2L)ln(M/\rho_1\rho_2)} \times \left(1 - \frac{S_1(\rho_2)^{1/2} + S_2(\rho_1)^{1/2}}{[1-(\rho_1\rho_2)^{1/2}][(\rho_1)^{1/2} + (\rho_2)^{1/2}]} \right), \quad (2.23)$$

where η_i is the internal differential quantum efficiency of the URSL. S_1 and S_2 are the light scattering coefficients of the two URSL end mirrors. Both η_i and α_i can be different from their counterparts of an FPSL. Limited by the cavity length dependence of quantum well materials, as explained in later chapters, equations (2.20) and (2.22) only apply to quantum well FPSLs with sufficiently long cavities; so do equations (2.21) and (2.23) to quantum well URSLs.

The total power efficiency of a semiconductor laser can be expressed as[28]

$$\eta = \frac{P_{op}}{(E_g + I/(LW\sigma))I}, \quad (2.24)$$

where E_g is the bandgap voltage of the active layer; σ is the wafer sheet conductivity; L and W are the cavity length and stripe width, respectively. Power consumption due to contact resistance was not included in equation (2.24). By ignoring the contribution of spontaneous emission, the total optical output power can be written in terms of η_d^{ur} as[29]

$$P_{op} = \eta_d^{ur}(h\nu/e)(I - I_{th}). \tag{2.25}$$

where $h\nu$ is the photon energy.

It was noticed earlier that a homogeneous gain was assumed in equations (2.12) and (2.13). For practical semiconductor lasers, the optical gain is directly related to the local optical field intensity. A nonhomogeneous intensity distribution would cause deviations from that assumption. At low injection levels, however, the optical intensity is weak, so the homogeneous gain is a convenient approximation, and the above expressions derived for URSL threshold and slope efficiencies are expected to closely approach actual operating characteristics.

2.3 Discussion

In reality, diffraction and interference effects may contribute to spatially nonhomogeneous distributions for the optical intensity and gain across the whole cavity. To closely monitor the spatial characteristics of an URSL, complicated models are needed to include the optical wave propagation and carrier injection related processes. The involved numerical analysis are usually very time-consuming. With emphasis on experimental work, relevant numerical simulations will not be covered in this dissertation. However, the geometrical URSL model presented in this chapter provides direct estimations of device operating characteristics. As will be mentioned in later chapters, these estimations indeed match closely to experimental observations and help to solve some practical design issues.

Chapter 3

QUANTUM WELL SEMICONDUCTOR MATERIALS AND LASERS

A conventional double heterostructure (DH) semiconductor laser[30] consists of a bulk active layer, which is typically 0.1 - 0.3 μm thick, sandwiched between two higher-bandgap cladding layers. This design, developed in the late 1970s and early 1980s, is now giving way to a more complex design in which the active layer is about an order of magnitude thinner than in the bulk DH design.[31] As the active layer thins down to the 10 nm regime, i.e. comparable to the de Broglie wavelength of carriers, the carrier (electron or hole) motion normal to the active layer in these new structures is restricted. As a result, the kinetic energy of the carriers moving in that direction is quantized into discrete energy levels similar to the well-known quantum-mechanical problem of the one-dimensional potential well, and the distribution of low energy, wave-like states available for electrons and holes confined to the active layer (potential well) changes from quasi-continuous to discrete.[32] Since laser action is generated by stimulating electron-hole recombination between these discrete (quantum well) states, devices with

this active layer design are called quantum well (QW) lasers.[31] In the last decade, the importance of the quantum well laser has steadily grown until it is preferred for most semiconductor laser applications today. While the first quantum well lasers operated at a wavelength of 0.8 μm, they have now been demonstrated from the visible through the infrared (0.49 - 10 μm).[33, 34]

In almost every respect, the quantum well lasers are better[31] than conventional lasers with bulk active layers. One obvious advantage is the ability to vary the lasing wavelength merely by changing the well thickness. A more fundamental advantage is that a quantum well laser delivers higher differential gain, gain per injected carrier, than conventional lasers, and results in lower threshold current and higher speed.[35] Another advantage is that quantum well lasers deliver gain with less change in refractive index than bulk lasers, i.e., have lower linewidth enhancement factor. To suppress filamentation effects, lower magnifications are needed for URSLs using quantum well active layers than those using bulk active layers. The splitting of the light- and heavy-hole valence bands by spatial quantization as well as the ability to grow quantum wells with compressive and tensile strain result in greater control over the optical polarization than in bulk lasers.[36] The differential gain, is even greater for a properly designed multi-quantum well laser than for a single quantum well laser.[35]

High quality quantum well material, in combination with advanced focused-ion-beam micromachining (FIBM) strategies, has contributed to the recent fabrication of high performance URSLs.[11, 12] In our research program, quantum well laser materials from several III/V families, which include

GaInP/AlGaInP, InGaAs/AlGaAs, and GaAs/AlGaAs, have been studied, and used to fabricate URSLs. In this chapter, the carrier injection related mechanisms and procedures for measuring the parameters of quantum well laser materials are reviewed, the general operating characteristics and relevant material parameters are summarized subsequently for all types of materials that we studied.

3.1 Carrier Injection Related Mechanisms of Quantum Well Materials

As mentioned in Chapter 2 (equation 2.22), the external differential quantum efficiency of a Fabry-Perot quantum well semiconductor laser (FPSL) with two ideal end mirrors is related to the laser cavity length L as $\eta_d = \eta_i/(1+\alpha_i L_{eff})$, where $L_{eff} = 2L/ln(1/\rho_1\rho_2)$ is the effective cavity length, ρ_1 and ρ_2 are facet reflectances, α_i is the internal optical loss per unit length, and η_i is the internal quantum efficiency. For constant η_i and α_i, the above expression gives a linear relation between $1/\eta_d$ and L_{eff}, just like the cases of bulk DH lasers.[37, 38] The direct effect of reducing the cavity length is the increase of carrier injection levels, the associated band filling effects increase the internal optical loss α_i[39] and enhance the nonradiative recombination processes.[40-42] The increase of α_i, in turn, directly leads to the decrease of η_d. The nonradiative recombination mechanisms[41, 43, 44] include Auger recombination, recombination in L-valleys, leakage current due to the carrier overflow out of the finite high wells, and nonradiative recombination from the Γ — conduction band. Enhancement of each of these processes could contribute to the increase of threshold current, and to the decrease of

internal quantum coefficiency η_i, and, in turn, decrease of the external quantum efficiency η_d. For quantum well materials with small bandgap offset, high injection levels of carriers causes noticeable carrier leakage through spilling over the cladding layers,[39] and reduces the internal quantum efficiency η_i. Analytical expressions have been derived to estimate the carrier dependence of the internal loss[39] and various nonradiative recombination rates,[41, 43] but will not be repeated here.

Figure 3.1, which was duplicated from an early publication,[41] plots the calculated threshold currents (I_{th}) versus cavity length (L) for a single quantum well (SQW) laser and a DH laser. The threshold current of the DH laser increases linearly with L as long as L is larger than 50 μm. For the SQW laser, however, I_{th} decreases dramatically with increasing L in the short cavity regime ($L < 300\ \mu m$). According to equation (2.20), this behavior means that the internal loss (α_i) decreases, while the gain coefficient b increases (i.e., passing through the gain saturation regime), with increasing L. That decreasing internal loss with increasing L can be explained by the weakening band filling effects. After the cavity length has reached a critical value, 300 μm for GaAs/AlGaAs SQW lasers, I_{th} of the SQW laser is almost independent on the cavity length. The flat I_{th}—L curve indicates that J_{th} is proportional to $1/L$. This critical cavity length, is also called as the optimum length L_{opt}. It was found that L_{opt} sets the lower limit for the equivalent cavity length (L_{eq}) of high performance URSLs.[21] In terms of optical loss, the fabrication of a curved mirror on to a FPSL is equivalent to a decrease of its cavity length, and causes the threshold

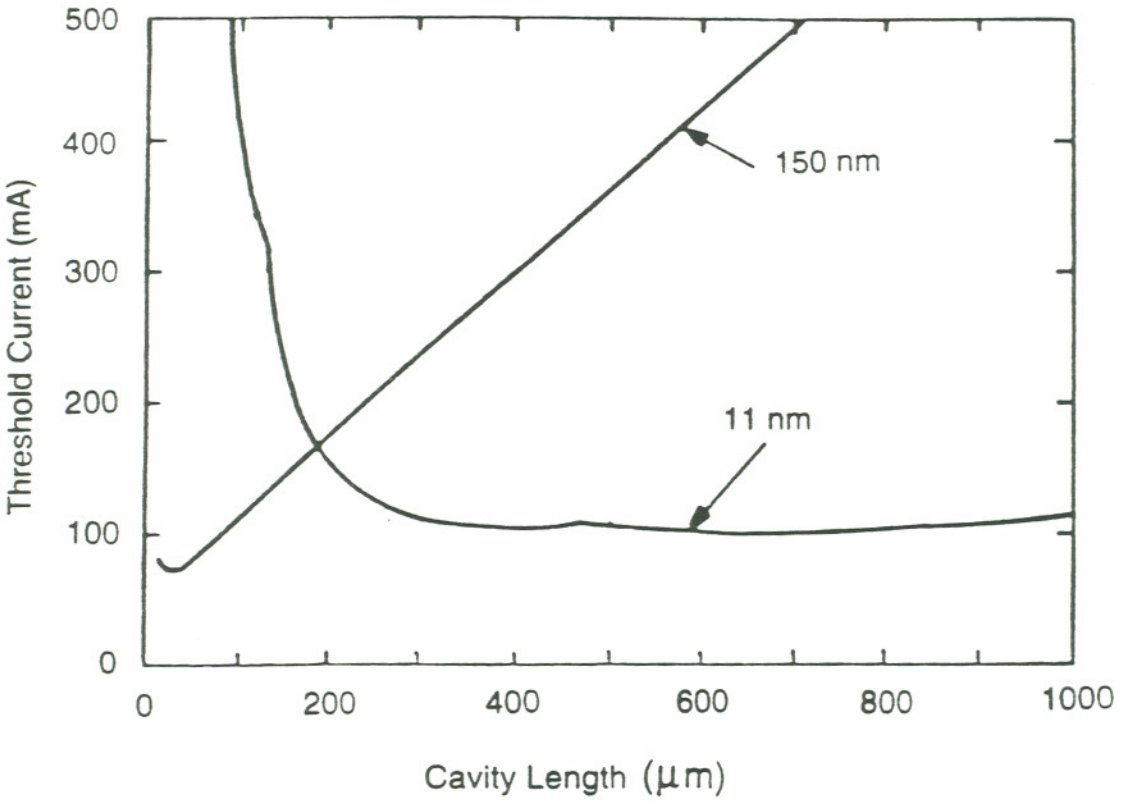

Figure 3.1 Calculated threshold current density versus cavity length for a) a 110 *Angstrom* single quantum well and a 1500 *Angstrom* bulk DH structure. Stripe width is 60 μm. [Ref. Reisinger *et al*][34]

change accordingly. When L is smaller than L_{opt}, the reciprocal external differential quantum efficiency η_d of the SQW laser is expected to increase with increasing of L due to the sharp decreasing of internal loss. When L is larger than L_{opt}, however, η_d will decrease with increasing of L since α_i is a constant now in equation (2.22).

Indeed, the theoretical analysis discussed above gives good explanation to early experimental observations for quantum well materials,[45, 46] and the measurements which will be presented in the next part of this chapter. When the quantum well laser length is reduced sufficiently, η_d reaches a maximum (threshold current density reaches minimum) at some optimum length (or critical length), and rapidly decreases (threshold current density increases) as the cavity length decreases further. Optimum cavity lengths are around 300 μm for InGaAs/GaAs and GaAs/AlGaAs GRINSCH SQW lasers, and 600 ~ 1000 μm for GaInP/AlGaInP SQW lasers.[21] The values of optimum length are usually smaller for multiple QW lasers than those for their counterparts with SQW structures.[39] In the next section, the experimental procedures for the operating characteristics and various material parameters will be briefly reviewed.

3.2 Experimental Characterization of Quantum Well Materials

Before the fabrication of URSLs from a specific type of material, characterization of the material properties was routinely conducted on corresponding FPSLs. Experimental techniques for characterizing the optical properties of quantum well materials have been well developed during last decade.[47-50]

Detailed tests include V-I and L-I curves, emission wavelength and longitudinal mode spacing, turn-on characteristics, temporal dynamics, near-field and far-field patterns, etc. Parameters that can be derived from these experimental data are series resistance, threshold current density, external differential quantum efficiency, internal quantum efficiency, internal loss, output beam divergence angles, optical confinement factor, emitting wavelength, longitudinal mode spacing, differential gain, carrier lifetime, and linewidth enhancement factor. The detailed procedures of data analysis were also well described elsewhere.[51, 52] In this section, only new and/or different understandings are addressed for several parameters.

The internal loss α_i and internal differential quantum efficiency η_i can be extracted by fitting the linear portion of $\eta_d(L)$ versus cavity length curve with the following expression[52, 53]

$$1/\eta_d(L) = 1/\eta_i[1 + 2\alpha_i L/ln(1/\rho_1\rho_2)]. \tag{3.1}$$

After knowing these two values, the differential gain coefficient b and transparency current density J_0 can be derived by fitting the straight portion of the J_{th} versus cavity length curve to expression (2.20).

A slightly different expression from equation (2.20) has also been used in the literature, where J_{th} is written as[52, 53]

$$J_{th} = \frac{1}{\eta_s}\left[J_0 + \frac{\alpha_i}{\Gamma\beta} + \frac{ln(1/\rho_1\rho_2)}{2L\Gamma\beta}\right], \tag{3.2}$$

where η_s is internal quantum efficiency for spontaneous emission only, and the linear gain $g(J)$ is defined with a different form of coefficient

$$g(J) = \beta(\eta_s J - J_0). \tag{3.3}$$

The only change is that the variable b in equation (2.20) is now replaced with the product of η_s and β, and J_0 by J_0/η_s. On the other hand, a simplified logarithmic gain-current density relation has been proposed for quantum well materials as[54, 55]

$$g(J) = G_0 ln(\eta_s J/J_0), \tag{3.4}$$

which considers the gain saturation behavior of quantum well materials at high injection current levels. It was claimed that this new expression describes accurately the gain characteristics of quantum wells.[54, 55] The detailed analysis concerning this logarithmic gain model will not be pursued in this dissertation. Actually, the first order approximation of equation (3.4) gives a linear relation in a similar form to equation (3.3). In other words, the two models agree at low injection levels, at which the threshold and quantum efficiency are usually evaluated. In the following context, only the linear gain model is considered.

The laser emitting wavelength, longitudinal mode spacing $\delta\lambda$, and spectral linewidth were all determined from the spectral measurements conducted with a 1.26 meter spectrometer. The group index[29, 37] $\mu_g = \lambda^2/(2L\,\delta\lambda)$ were derived thereafter. The refractive index change $\Delta\mu_c$ of the active layer with changes of drive current can be determined from the measured wavelength shift $\Delta\lambda$ of the individual longitudinal modes, both below and above threshold, through the relation[56]

$$\Gamma\Delta\mu_c/\mu_g = \Delta\lambda/\lambda. \tag{3.5}$$

The optical net gain G of a FPSL is usually obtained by measuring the

intensity modulation of the Fabry-Perot resonance spectra at various sub-threshold current levels.[57] The corresponding optical local gain is derived as

$$g = (G + \alpha_i)/\Gamma. \tag{3.6}$$

The current differential gain coefficient (dg/dJ) can then be calculated, so can the carrier density gain coefficient (dg/dN) after knowing the carrier life-time.[38, 50] Taking into consideration (3.5) and (3.6), the linewidth enhancement factor can be derived as

$$\alpha = -2k_0 \frac{d\mu_c/dN}{dg/dN} = -2k_0 \frac{\mu_g}{\lambda} \frac{\Delta\lambda}{\Delta G}, \tag{3.7}$$

where $k_0=2\pi/\lambda$ is the vacuum wavenumber. Due to the injection-dependent gain characteristics of quantum well materials, the values of α may be different for low injection levels from those for high injection levels. As will be discussed in Chapter 5, the sub-threshold spatio-spectral patterns of URSLs have curved structures.[20] The net gain of the central core region is expected to be different from those of the side regions.

The transverse and lateral divergence angles can be calculated from the axial variation of the output far-field patterns, which were usually recorded with a CCD camera at several different distances from the laser output mirror. By approximating the optical output with Gaussian beams, the values of beam waists (ω_{0x} and ω_{0y}) along the two perpendicular directions at the output mirror can be calculated from the divergence angles as[58]

$$\tan\theta_i = \frac{\lambda}{\pi\omega_{0i}}, \quad i = x, y. \tag{3.8}$$

For example, Figure 3.2a shows three transverse far-field patterns of a 200 μm × 500 μm GaInP FPSL recorded at three different distances from the output mirror. The FPSL was operated at twice threshold in pulsed mode. The measured values of far-field width W_{ff} (FWHM) were plotted in Figure 3.2b versus the far-field position L_{ff}. Then, the slope of the curve shown in Figure 3.2b can be used to calculate the transverse gaussian divergence angle as

$$\theta_y = \tan^{-1}\frac{\Delta W_{ff}/\Delta L_{ff}}{\sqrt{2ln\,2}}. \tag{3.9}$$

The data plotted in Figure 3.2 correspond to a transverse divergence angle of about 22°.

For nonideal optical beams, the right side of equation (3.8) needs to be multiplied by a coefficient M_s^2. According to the theory developed by Siegman,[59, 60] this coefficient is written as

$$M_s^2 = 4\pi\sigma_{0i}\sigma_{si}, \tag{3.10}$$

where σ_{0i}^2 is the minimum value of the spatial variance at the real-beam waist, and σ_{si}^2 is the variance of the beam in the angular or spatial frequency domain. However, the experimental procedures for measuring this M_s^2 parameter are quite complicated.[61, 62] Limited by the low spatial resolution used in the present work for the recording of virtual source envelope, this new method has not been used in the studies reported in this dissertation.

The experimental set-up for spectral measurements is schematically shown in Figure 3.3. Laser output is imaged onto the entrance slit of the spectrometer using a microscope objective. For intense optical beams, the

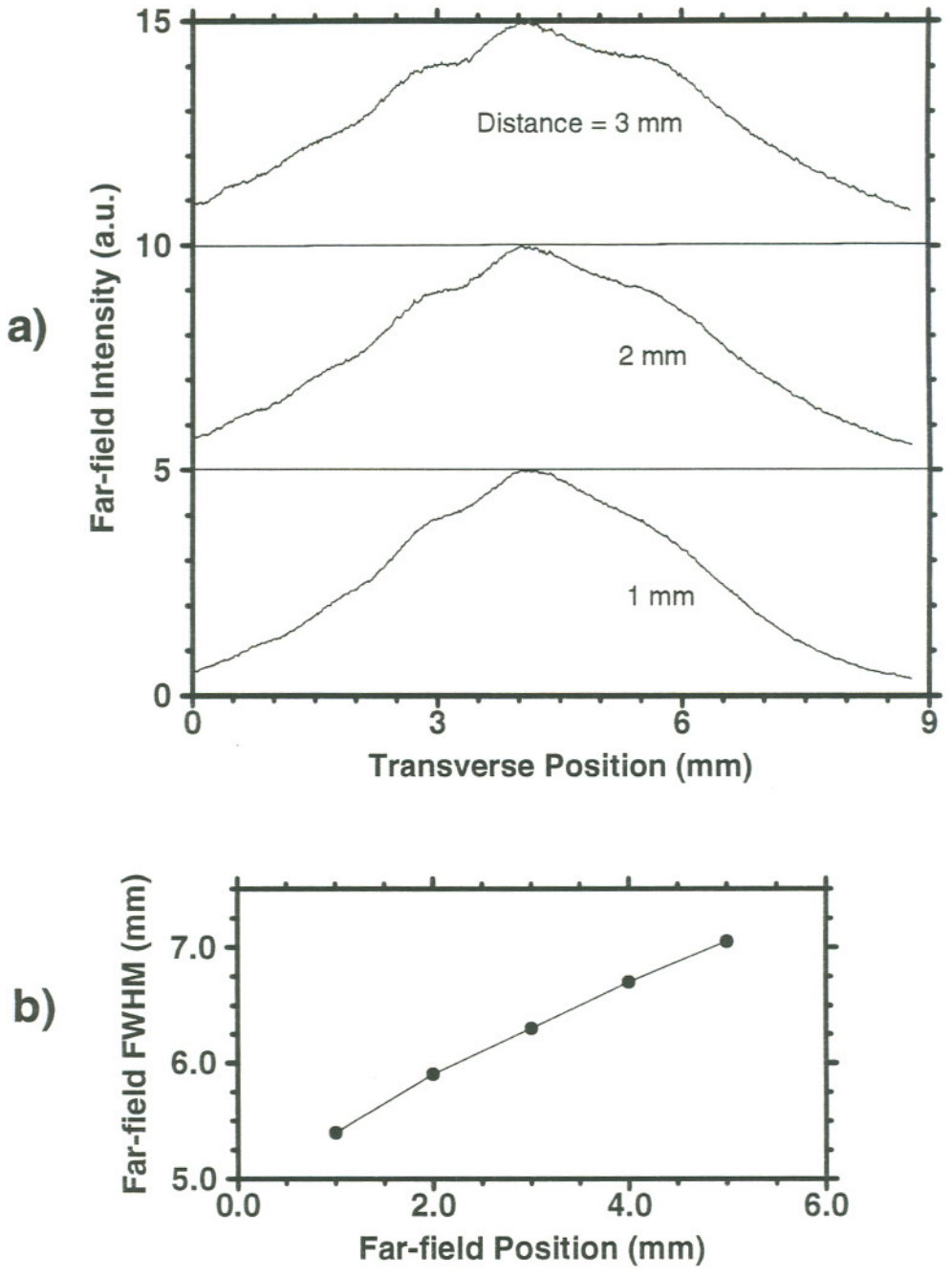

Figure 3.2 Transverse far-field characteristics of a 200 μm × 500 μm GaInP FPSL at $2\times I_{th}$, a) far-field patterns at three different distances from laser output mirror, b) far-field FWHM versus distance from the output mirror.

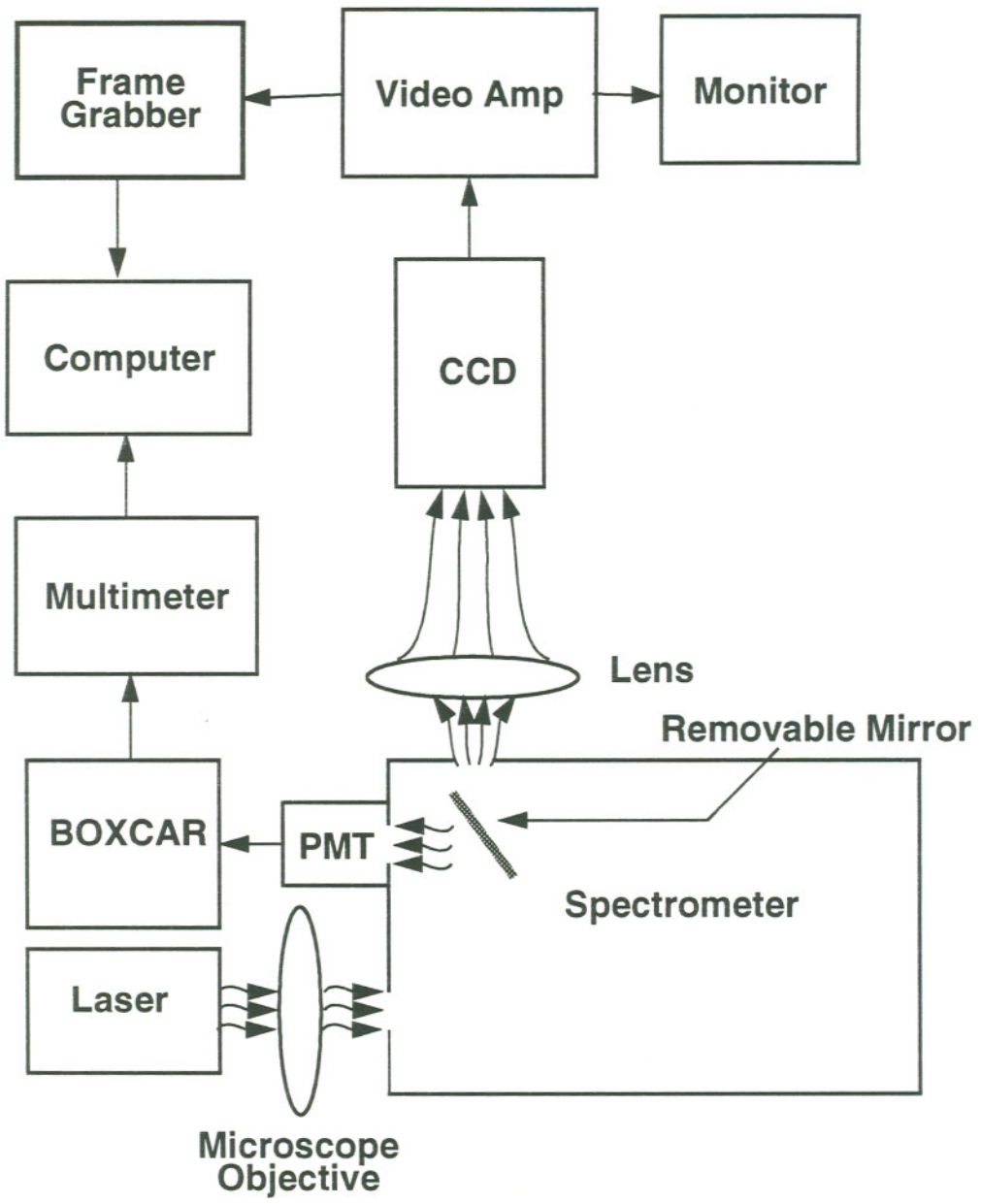

Figure 3.3 Experimental set-up for spectral measurements.

exit light can be recorded using a CCD camera and Frame Grabber system. For weak optical output, e.g., low duty cycle spontaneous emission, the exit light can be detected using a Photomultiplier Tube (PMT). The electrical output from the PMT can be processed using a Boxcar signal amplifier, and digitized/read through a multimeter/computer system. The data plotted in Figure 3.5 were measured using the latter method.

3.3 GRINSCH SQW GaInP/AlGaInP

Visible semiconductor lasers are attractive light sources for applications in optical information processing systems, such as high-density optical disk systems, high-speed laser printers, and bar-code readers etc. There have been several approaches under investigation, including high bandgap III-V and II-VI based compound materials. Among these, the greatest success has been achieved with the lattice-matched (to GaAs) GaInP/AlGaInP materials system.[63-66] Room temperature CW operation of AlGaInP bulk DH lasers was first accomplished in 1985.[67, 68] Later, CW operation at temperatures as high as 90-150 $^{\circ}C$ was found possible for AlGaInP bulk DH lasers.[69, 70] The operation of an AlGaInP quantum well laser was first reported in 1986.[71] Room-temperature CW operation has been achieved for quantum well AlGaInP lasers with emitting wavelength ranging from 610 nm to 697 nm.[72-81] Lower thresholds are expected for AlGaInP quantum well lasers than those for bulk DH lasers, since quantum confinement reduces the density of states in the active region and thereby lowers the number of injected carriers required to invert the population. General information regarding

the lattice properties, band structure, refractive indices, electrical properties, and growth of the GaInP/AlGaInP materials has been summarized by Bour.[65] Currently, AlGaInP lasers have become the choice for red compact light sources.

The values of optimum cavity length L_{opt} have been found to be in the range of 600 - 1000 μm for AlGaInP SQW lasers,[46, 82, 83] which are much larger than those of GaAs/AlGaAs SQW lasers ($\sim 300\ \mu m$),[39] and of InGaAs/AlGaAs GRINSCH SQW lasers ($< 300\ \mu m$).[52] The relatively large L_{opt} of AlGaInP lasers can be attributed in part to the low heterojunction band offsets, which leads to poor carrier confinement and low internal quantum efficiency. The maximum electron confinement available for GaInP/AlGaInP lasers is approximately only half of that available for GaAs/AlGaAs lasers, so the band filling effect is much more severe, and results in the large L_{opt}. The internal quantum efficiency for GaInP SQW FPSLs is in the range of 0.6 to 0.7, which is smaller than the typical values of 0.9 ~ 1.0 for GaAs/AlGaAs[53] and InGaAs/GaAs lasers.[52]

The GaInP/AlGaInP laser materials studied in this dissertation were grown by metalorganic chemical-vapor deposition (MOCVD), and have the well-known graded-index separate-confinement heterostructure (GRINSCH) strained single quantum well layer structure.[76, 82, 84] The composition and thickness of the cladding, confinement, and bounding layers were optimized to first order for both carrier and optical confinement of TE modes. The schematic illustration of the wafer cross section can be found in previous publications.[84] The n- and p-$(Al_xGa_{1-x})_{0.51}In_{0.49}P$ cladding layers were

doped with Si and Zn, respectively. A thin, Zn-doped *p–GaInP* layer was incorporated between the *p–AlGaInP* cladding layer and the p-GaAs contact layer to reduce the high barrier which can be present at such an interface.[85] The use of biaxial compressive strain in GaInP to lower the valence-band effective mass by increasing the In mole fraction causes the band gap to shift to longer wavelengths compared to GaInP lattice matched to GaAs.[86] On the other hand, the use of thin quantum well has the effect to shorten emission wavelength. In order to keep the wavelength in the range possible with unstrained GaInP, a 7 nm thick $Ga_y In_{1-y} P$ (y = 0.43) quantum well was used, and resulted in a lasing wavelength of about 660 nm for these materials compared to 691 nm previously reported for a 10 nm quantum well of similar composition in a nongraded, separate confinement structure.[74] The calculated confinement factor for this structure is 2.04%.[76]

A set of GaInP/AlGaInP (660 nm) lasers with cavity lengths ranging from 500 μm to 2500 μm were fabricated. FPSLs, with stripe widths of 300 μm, were mounted epi-up on heatsinks. Pulsed (200 ns, 1 kHz) light versus current characteristics were recorded for later comparison with URSLs fabricated from the same devices. The external quantum efficiencies and threshold current density for the FPSLs are plotted versus cavity length in Figures 3.4a and 3.4b, respectively. In general, these results suggest that L_{opt} is around 1000 μm for this GaInP SQW material.

By fitting a straight line to the data points of longer cavity (≥ 1000 μm) GaInP/AlGaInP FPSLs in Figure 3.4a (the lower solid line), the internal loss and internal quantum efficiency were determined to be 6.4 cm^{-1} and 0.69,

a)

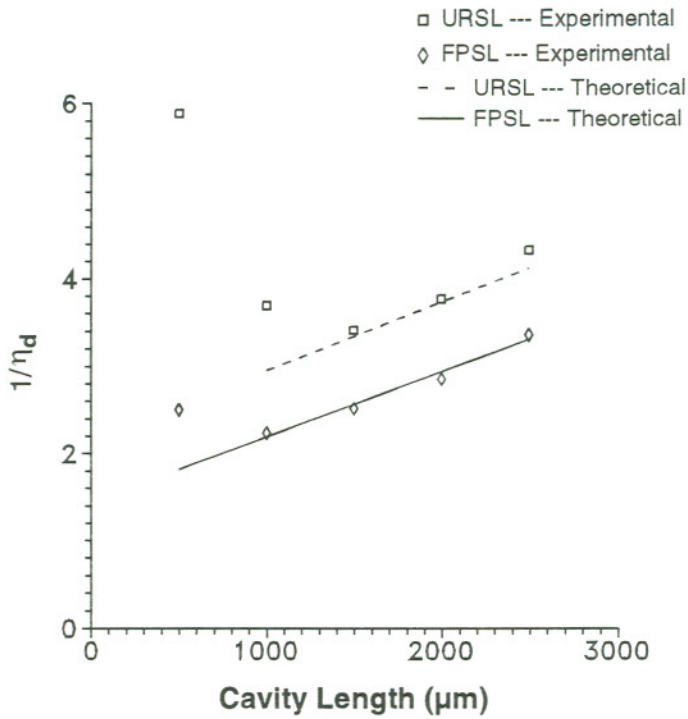

b)

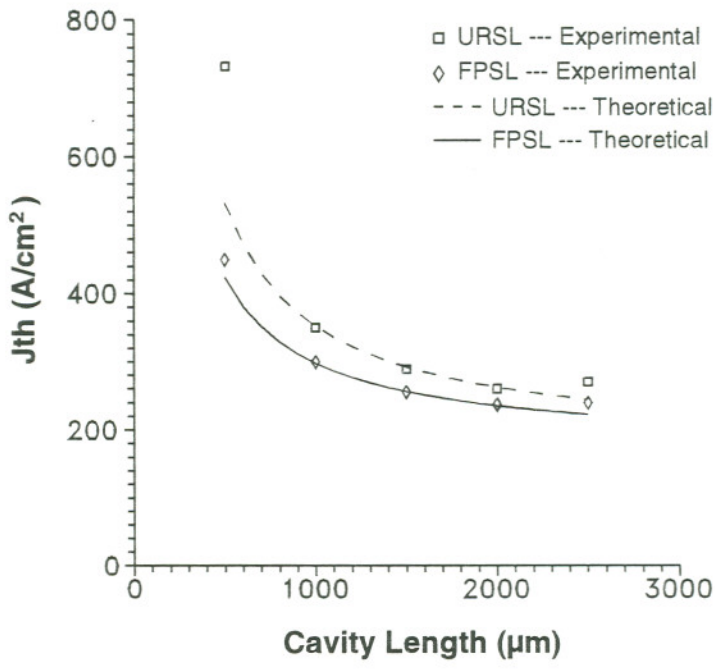

Figure 3.4 Cavity length dependence of the operating characteristics of the GaInP/AlGaInP GRINSCH SQW lasers, a) reciprocal external differential quantum efficiency, threshold current density.

respectively. In contrast, some early reports showed much higher internal loss by fitting the data points of very short FPSLs.[80, 87] The modal reflectivity was calculated to be 0.29 for a cleaved facet.

The threshold current density data for the four long FPSLs, as shown in Figure 3.4b, have been fitted to equation (2.20) by assuming that the cleaved end mirrors are perfect. Using the values of η_i, α_i obtained earlier and a calculated value of Γ (= 2.04%), J_0 and b were determined to be 107 A/cm^2 and 4.8 cm/A, respectively. The square symbols and dashed curves shown in Figure 3.4 represent the experimental data points and theoretical predictions for 2.5 magnification URSLs fabricated from those FPSLs. Detailed discussions will be given in Chapter 6.

To measure the differential gain coefficient, the linewidth enhancement factor, and the carrier lifetime, a 200 by 500 μm GaInP/AlGaInP laser was mounted epi-up for pulsed operation. The spectra were taken at current levels both below and above threshold. The values of net gain and wavelength shift versus current levels were then obtained, and plotted in Figures 3.5a and 3.5b, respectively. For the part below threshold, the experimental data points do not fit perfectly to a straight line. Experimental error, mainly jittering of pulsed operation, might contribute to the scattering of the data points for the net gain and wavelength length shift measurements. The average differential gain coefficient and differential wavelength shift were obtained by linearly fitting the respective parts of experimental data points below threshold. The average linewidth enhancement factor was then calculated. By measuring the turn-on delay time versus the

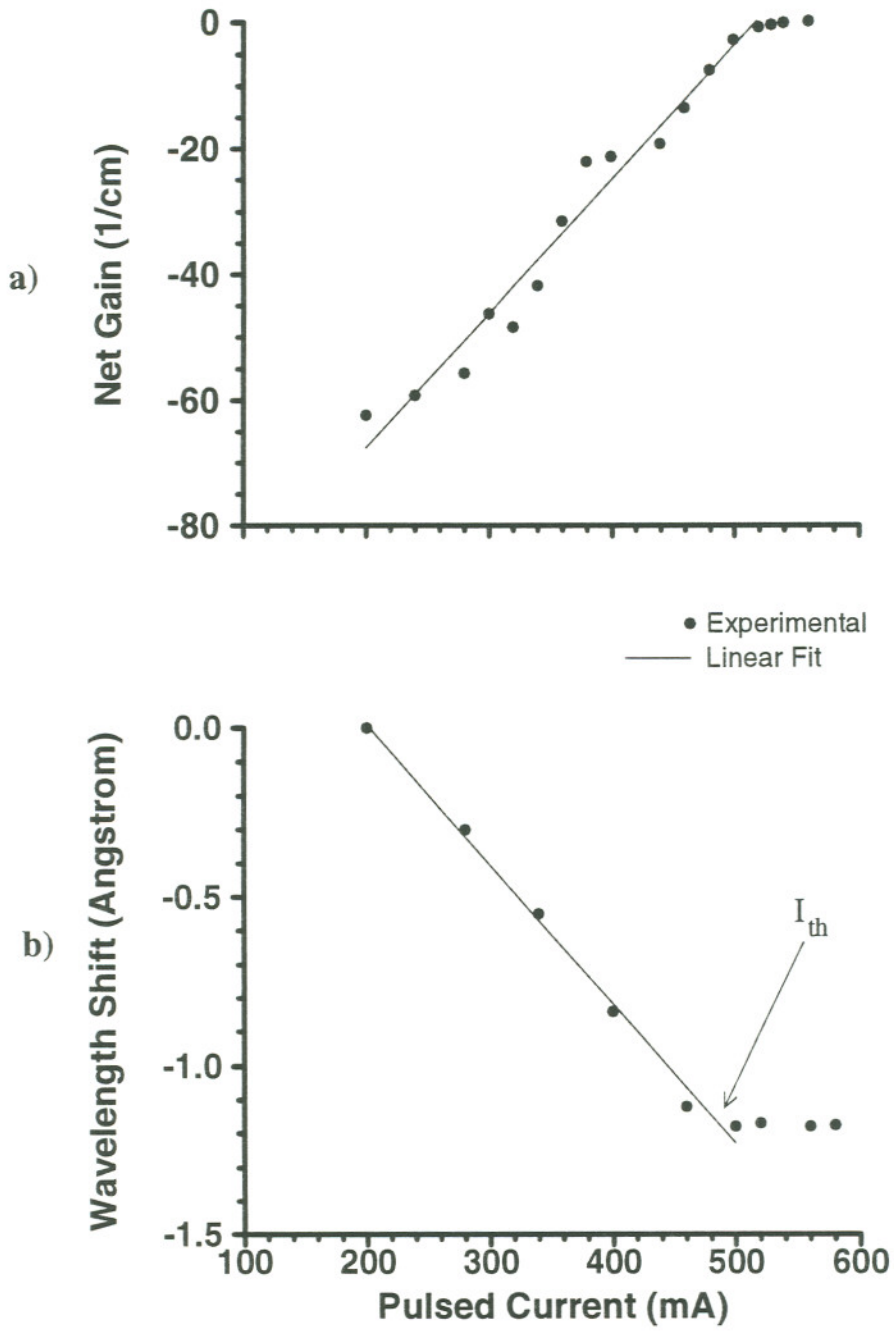

Figure 3.5 Carrier injection induced gain and spectral characteristics for a 200 μm × 500 μm GaInP/AlGaInP GRINSCH SQW Fabry-Perot laser, a) net gain versus injection current, b) wavelength shift versus injection current.

injection level, the carrier lifetime can be determined.[49] Table 3.1 summarizes the measured values of several device parameters. The gain, wavelength shift, and linewidth enhancement factor (α) measurements were repeated for several times. The scattering range of the measured α values was also quoted behind the average value in Table 3.1, as well as in Tables 3.2 and 3.3 latter in this chapter.

3.4 GRINSCH SQW InGaAs/AlGaAs

Semiconductor lasers incorporating a strained InGaAs quantum-well active layer and AlGaAs confining layers in heterostructures grown on a GaAs substrate offer many attractive applications, such as pumping rare earth-doped silica fiber amplifiers, and substituting for 1.06 μm wavelength emission of Nd:YAG lasers. Such InGaAs/AlGaAs strained-layer lasers with emission wavelengths extending from 870 nm to about 1100 nm have been reported by many researchers.[52, 88-92]

The strained-layer InGaAs/AlGaAs graded-index separate-confinement heterostructure single-quantum-well (GRINSCH SQW) laser material we studied was grown by organometallic vapor phase epitaxy (OMVPE) on Si-doped n^+-GaAs (100) substrates, tilted 2° toward the nearest (110) plane, with etch pit density of less than 2000 cm^{-2}.[52, 92] The wafer structures consist of the following layers: 20 nm thick n-GaAs buffer layer, 0.1 μm thick graded n-$Al_y Ga_{1-y} As$ layer (y linearly graded from 0.1 to 0.7), 1.1 μm thick n-$Al_{0.7}Ga_{0.3}As$ cladding layer, 0.15 μm thick undoped $Al_y Ga_{1-y} As$ confining layer (y linearly graded from 0.7 to 0.2 or 0.08), 10 nm thick GaAs bounding

Table 3.1 GaInP/AlGaInP GRINSCH SQW FPSLs

Stripe width (W)	200 μm
Cavity length (L)	500 μm
Optimum cavity length (L_{opt})	1000 μm
Wavelength (λ) - pulsed operation	660 nm
Group refractive index (μ_g)	4.2
Mirror reflectivity (ρ)	0.29
Confinement factor (Γ)	2.04%
Threshold current density (J_{th})	480 Acm^{-2}
External differential quantum efficiency (η_d)	0.37
Internal loss (α_i)	6.33 cm^{-1}
Internal quantum efficiency (η_i)	0.69
Transparency current density (J_0)	107 Acm^{-2}
Carrier lifetime (τ_s)	3.1 ns
Photon lifetime (τ_p)	4.3 ps
dg/dN	5.5×10^{-16} cm^2
dG/dI	212 $cm^{-1}A^{-1}$
Gain coefficient (dg/dJ)	10.7 cmA^{-1}
$d\lambda/dI$	$2.7 \times 10^{-8} cmA^{-1}$
Linewidth enhancement factor (α)	1.6 ± 0.4 *
g_{th}	1524 cm^{-1}
Transverse divergent angle (FWHM) ($\theta_{\perp}$)	44^o
Lateral divergent angle (FWHM) ($\theta_{\parallel}$)	10^o

*: Pulsed operation led to a large uncertainty for the measurements of spectral shifts.

layer, 7 nm thick undoped $Al_xGa_{1-x}As$ active layer ($0 \leq x \leq 0.25$ depending on the wavelength requirements), another 10 nm thick GaAs bounding layer, 0.15 μm thick undoped $Al_yGa_{1-y}As$ confining layer (y linearly graded from 0.2 or 0.08 to 0.7), 1.1 μm thick p-$Al_{0.7}Ga_{0.3}As$ cladding layer, 0.1 μm thick graded p-$Al_yGa_{1-y}As$ layer (y linearly graded from 0.7 to 0.1), and 0.1 μm thick p^+-GaAs contact layer. The n- and p-type doping levels in the cladding layers were varied from 10^{18} down to $10^{17}cm^{-3}$ toward the GRIN layers to reduce the optical loss due to free-carrier absorption. The incorporation of GaAs bounding layers causes a marked reduction of the threshold current density, and increase of the internal quantum efficiency for the InGaAs-AlGaAs lasers.[52] The material emits at a wavelength around 0.97 μm.

To fabricate broad-area lasers, 200 to 500 μm wide stripes were defined on the p-side of the wafer with 200 μm margin separations. To study the optical properties of the wafer materials, the cavity length dependence of the operating characteristics was investigated. The wafer was cleaved into bars ranging from 500 to 1700 μm, and soldered epi-up to a copper heat sink for pulsed operation. The reciprocal external differential quantum efficiency $1/\eta_d$ and threshold current density J_{th} are plotted versus laser cavity length L in Figures 3.6a and 3.6b. Both sets of data are comparable to the results reported earlier,[92] and fit to straight lines. These data also suggest that the optimum length for this InGaAs/AlGaAs GRINSCH SQW material is smaller than 500 μm. Material parameters were obtained through the same analysis procedures as for GaInP/AlGaInP quantum well materials in

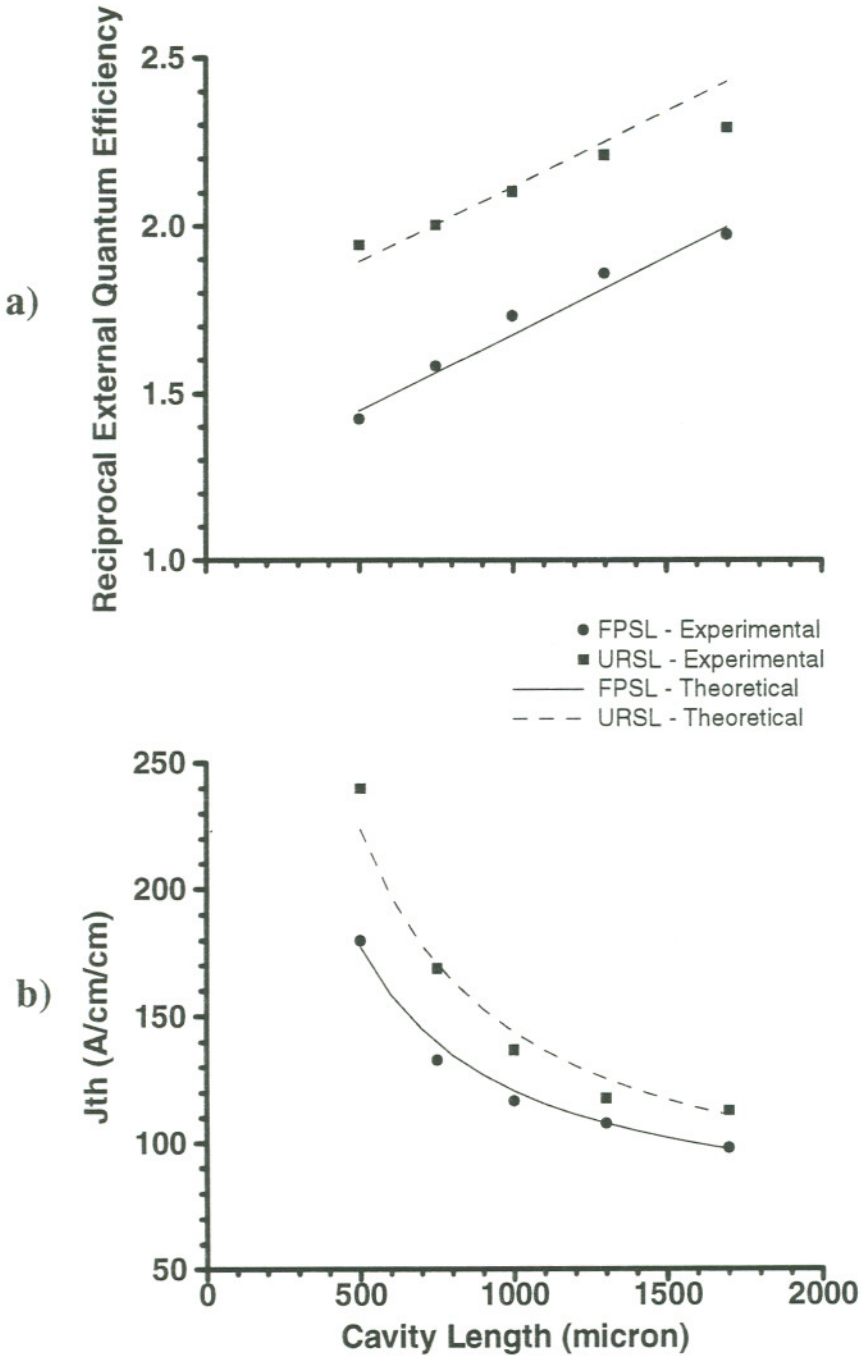

Figure 3.6 Cavity length dependence of the operating characteristics of the InGaAs/AlGaAs GRINSCH SQW lasers, a) reciprocal external differential quantum efficiency, b) threshold current density.

previous section, and summarized in Table 3.2. The filled square symbols and dashed curves shown in Figure 3.6 were obtained for 2.5 magnification URSLs fabricated from those FPSLs. A more detailed discussion on cavity length dependence of URSLs will be given in Chapter 6.

3.5 GRINSCH SQW GaAs/AlGaAs

Ever since the invention of semiconductor lasers,[93-96] the GaAs/AlGaAs material system, emitting in the range of 0.68 ~ 0.85 nm, has been playing a dominant role. All the early unstable resonator research activities were carried out on GaAs/AlGaAs materials with bulk double heterostructures.[6, 7, 10] The first quantum well laser was also fabricated from the GaAs/AlGaAs material system.[97] The emission wavelength of a quantum well heterostructure laser can be varied by the well thickness, as mentioned earlier in this chapter. The physical characteristics, growth and processing technologies of GaAs/AlGaAs quantum materials are also the best developed, and can be found in many publications.[31, 98]

The GaAs/AlGaAs material used in our URSL program has a GRINSCH SQW layer structure, and emits at a wavelength of 853 nm. To characterize the material performance characteristics, a set of six Fabry-Perot devices each with stripe width of 300 μm were cleaved out at various cavity lengths, and mounted epi-up on a copper heat-sink. From the pulsed L-I data, the external quantum efficiencies and threshold current densities were obtained, and fitted to expressions (2.18) and (2.20) to derive the values for such

Table 3.2 InGaAs/AlGaAs GRINSCH strained-layer SQW FPSLs

Stripe width (W)	200 μm
Cavity length (L)	450 μm
Optimum cavity length (L_{opt})	≤ 300 μm
Wavelength (λ) - pulsed operation	969 nm
Wavelength (λ) - CW operation	973 nm
Group refractive index (μ_g)	3.8
Mirror reflectivity (ρ)	0.29
Confinement factor (Γ)	2.5%
Threshold current density (J_{th})	150 Acm^{-2}
External differential quantum efficiency (η_d)	0.7
Internal loss (α_i)	4.5 cm^{-1}
Internal quantum efficiency (η_i)	0.82
Transparency current density (J_0)	43 Acm^{-2}
Carrier lifetime (τ_s)	5.0 ns
Photon lifetime (τ_p)	4.3 ps
dg/dN	$9.4 \times 10^{-16} cm^2$
dG/dI	706 $cm^{-1}A^{-1}$
Gain coefficient (dg/dJ)	29.4 cmA^{-1}
$d\lambda/dI$	$2.0 \times 10^{-7} cmA^{-1}$
Linewidth enhancement factor (α)	1.5 ± 0.3
g_{th}	1170 cm^{-1}
Transverse divergent angle (FWHM) ($\theta_{\perp}$)	44^o
Lateral divergent angle (FWHM) ($\theta_{\parallel}$)	10^o

parameters as the internal quantum efficiency, gain coefficient, and transparency current density. Once again, perfect surfaces were assumed for the cleaved end mirrors. Other material parameters can also be obtained through the same procedures introduced for GaInP/AlGaInP materials. The optimum cavity length was found to be smaller than 500 μm. The material parameters are summarized in Table 3.3.

3.6 "Manifold" Triplet GRINSCH SQW GaAs/AlGaAs

It is well-known that the catastrophic optical damage (COD) level sets the highest power density achievable at the output facets of a semiconductor laser. In other words, increasing the light emitting area will increase the highest achievable total output power. In the early stages of semiconductor laser development, designs of large optical cavity (LOC) lasers, in which the injected carriers are confined to a narrow part of the total region in which the light is confined, were proposed to increase the source size and thus the COD power level.

Later, monolithic stacking of injection lasers was investigated.[99, 100] This alternative offers higher emitter density, less complexity and lower cost as compared to a conventional stack of separated lasers. Multiple integrated bulk DH lasers were also fabricated.[99-102] In all those designs, either Shockley diode behavior[99, 100, 102] or nearly ohmic behavior[101] resulted from the reverse-biased junction which separated the light-emitting junctions. In the latter case a high-quality tunnel junction was used to achieve low operating voltages. However, CW operation was not attained due to insufficient heat

Table 3.3 GaAs/AlGaAs GRINSCH SQW FPSLs

Stripe width (W)	200 μm
Cavity length (L)	500 μm
Optimum cavity length (L_{opt})	~300 μm
Wavelength (λ) - pulsed operation	853 nm
Group refractive index (μ_g)	4.0
Mirror reflectivity (ρ)	0.32
Confinement factor (Γ)	(~2%)
Threshold current density (J_{th})	300 Acm^{-2}
External differential quantum efficiency (η_d)	0.60
Internal loss (α_i)	9.9 cm^{-1}
Internal quantum efficiency (η_i)	0.86
Transparency current density (J_0)	37.2 Acm^{-2}
Carrier lifetime (τ_s)	3.6 ns
Photon lifetime (τ_p)	4.0 ps
dg/dN	$3.4 \times 10^{-16} cm^2$
dG/dI	150 $cm^{-1}A^{-1}$
Gain coefficient (dg/dJ)	7.63 cmA^{-1}
$d\lambda/dI$	$4.5 \times 10^{-8} cmA^{-1}$
Linewidth enhancement factor (α)	2.0 ± 0.5
g_{th}	1634 cm^{-1}
Transverse divergent angle (FWHM) ($\theta_\perp$)	40^o
Lateral divergent angle (FWHM) ($\theta_{\|\|}$)	10^o

dissipation in these high-current-density DH lasers. In subsequent work,[103] the tunnel junction was eliminated by keeping the spacing between active regions under 3 μm. Viable devices were demonstrated, but again, CW operation was precluded by the current requirement.

Recently, CW operation has been achieved for a stack of a pair and of a triple of GaAs single quantum-well lasers separated by a single p-n junction, called "manifold" lasers.[104, 105] A typical device structure is shown schematically in Figure 3.7. Each laser section is identical to a high-performance GRINSCH structure. It consists of a (nominal) 10 nm wide GaAs quantum well flanked by (linear) compositional $Al_xGa_{1-x}As$ regions with $0.30 < x < 0.60$, which, in turn, is surrounded by $Al_{0.6}Ga_{0.4}As$ cladding regions. For those structures, a 177% improvement in the CW catastrophic optical damage (COD) power level was realized for the triplet[105] compared with the single-quantum-well case. In pulsed operation, the corresponding factor is 130%.[105] The CW operation was enabled by utilizing a low threshold current-density GRINSCH SQW structure.[41, 53, 106]

The differences between the present "manifold" structure and those early stacking ones can be described in the following way. The quantum well spacings here are large (on the order of diffusion lengths), the wells exist in distinct (albeit weakly coupled) waveguide regions. While the carrier wave-functions in separate wells are decoupled and the optical field distribution may or may not couple, what the several wells do share is a common space-charge region. As a consequence, operating voltages are not increased when compared to a standard GRINSCH although threshold

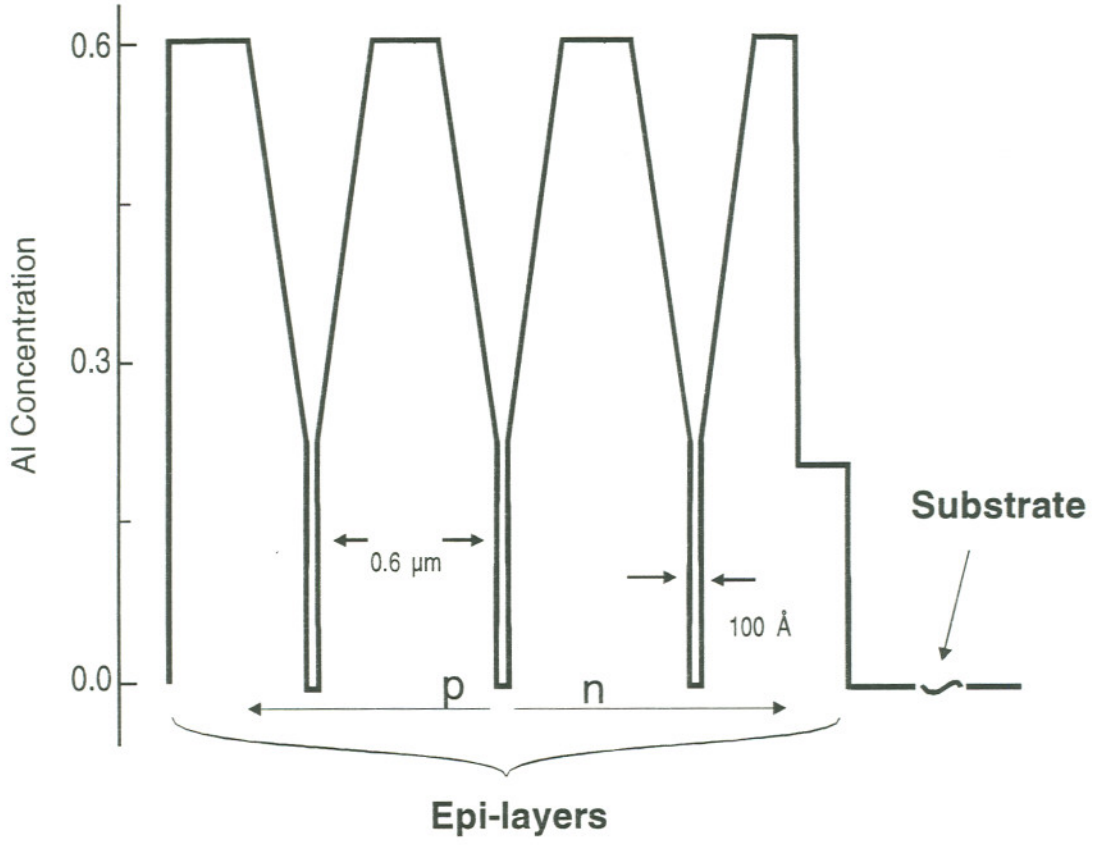

Figure 3.7 Schematic illustration of a "manifold" laser with a triplet GRINSCH SQW structure.

currents will increase due to increased carrier volume.

The "manifold" laser structure was optimized to provide a single-lobed transverse far-field and increased COD power levels, while maintaining the same output efficiency as single quantum well lasers, and keeping the threshold as low as possible.[105] The quantum well spacing of 0.6 μm was found to be large enough to generate single-lobed far-field and maintain the slope efficiency at the same level as the single quantum well lasers. With that well spacing, the threshold current density for a triplet "manifold" lasers is about twice that of a single quantum well laser.[105] The triplet lasers showed higher COD levels than the doublet ones, although they had slightly lower slope efficiencies. And the pulsed COD levels are more than twice larger than those for CW operation.[105] Due to the large emitting area, the transverse diverging angle of the output beam from a triplet "manifold" laser is only about 10° at FWHM.

The materials used for the URSL program are those with triplet structures. The device parameter such as internal loss, internal quantum efficiency, and transparency current density, were measured the same way as for other types of materials. The values of these parameters, along with the operating characteristics of a typical FPSL with 200 μm by 500 μm stripe dimension, are summarized in Table 3.4.

Table 3.4 GaAs/AlGaAs GRINSCH SQW Triplet Stack FPSLs

Stripe width (W)	200 μm
Cavity length (L)	500 μm
Optimum cavity length (L_{opt})	≤ 300 μm
Wavelength (λ) - pulsed operation	842 nm
Group refractive index (μ_g)	4.0
Mirror reflectivity (ρ)	0.32
Confinement factor (Γ)	($\sim 3 \times 2.0\%$)
Threshold current density (J_{th})	440 Acm^{-2}
External differential quantum efficiency (η_d)	0.65
Internal loss (α_i)	1.6 cm^{-1}
Internal quantum efficiency (η_i)	0.7
Photon lifetime (τ_p)	5.4 ps
Transparency current density (J_0)	121.6 Acm^{-2}
dG/dI	575 $cm^{-1}A^{-1}$
Gain coefficient (dg/dJ)	9.58 cmA^{-1}
$d\lambda/dI$	$1.1 \times 10^{-7} cmA^{-1}$
Linewidth enhancement factor (α)	1.4 ± 0.5
g_{th}	406 cm^{-1}
Transverse divergent angle (FWHM) ($\theta_\perp$)	17^o
Lateral divergent angle (FWHM) ($\theta_{\parallel}$)	10^o

Chapter 4

URSL FABRICATION USING FOCUSED-ION-BEAM MICROMACHINING

4.1 Introduction

Focused-ion-beam micromachining (FIBM) is a relatively new technique for forming optical quality surfaces in semiconductor laser materials.[107-110] This technique makes use of a tightly focused beam of 15 to 25 keV Ga^+ ions derived by field evaporation from a bright liquid gallium source.[111] The beam of ions emitted by the liquid metal source is apertured and focused in an ion-optical column which, depending on the design, can provide a focal spot ranging from 25 to 250 nm.[112-114] Current densities of the order of 1 A/cm^2 are readily achieved. The focused beam of ions can be deflected under computer control with a precision much smaller than the spot size. This allows the removal of material by sputter-etching to form features with optically smooth surfaces. Sputtering yield is usually dependent on the composition of the material to be machined, and typically of the order of 1 $\mu m^3/nAs$. A significant advantage of FIBM is that it is completely maskless

process. Mounted and partially packaged devices can be modified without adverse interactions with packaging materials. The ability to deflect the ion beam under computer control provides added flexibility for producing features with arbitrary surface profiles.

In recent years, it has been proven that FIBM[107, 110, 112, 115] can provide smoother surfaces than conventional mechanical polishing,[6] wet chemical etching,[7, 10] or reactive-ion etching.[116] Though with the drawback of not being suitable for mass-production applications, FIBM is the most effective method, from every other aspect, for fabricating prototype optical mirrors with desirable structures in semiconductor materials,[110] and was used to fabricate all the URSLs for this study.

Slightly different device fabrication procedures are used for different applications. The wafer materials, which were grown and processed by other groups, usually contain metal stripes of 100 ~ 400 μm wide. After receiving the wafer materials, Fabry-Perot laser dice were always cleaved out first. The top part of Figure 4.1 schematically shows how the cleaving was performed. A narrow region without metallization is always left on the end where FIBM is to be done. FIBM of metallization needs to be avoided, as will be discussed in a later section. For pulsed operation, the dice were mounted junction side up on copper heat-sinks with conductive epoxy, and wire-bonded to the p-metal contact. Fabrication of the cylindrical mirror was performed after testing the operating characteristics of the FPSLs. The lower portion of Figure 4.1 schematically shows the geometrical structure of a FIBM half-symmetric URSL. For CW operation, the cylindrical mirror was

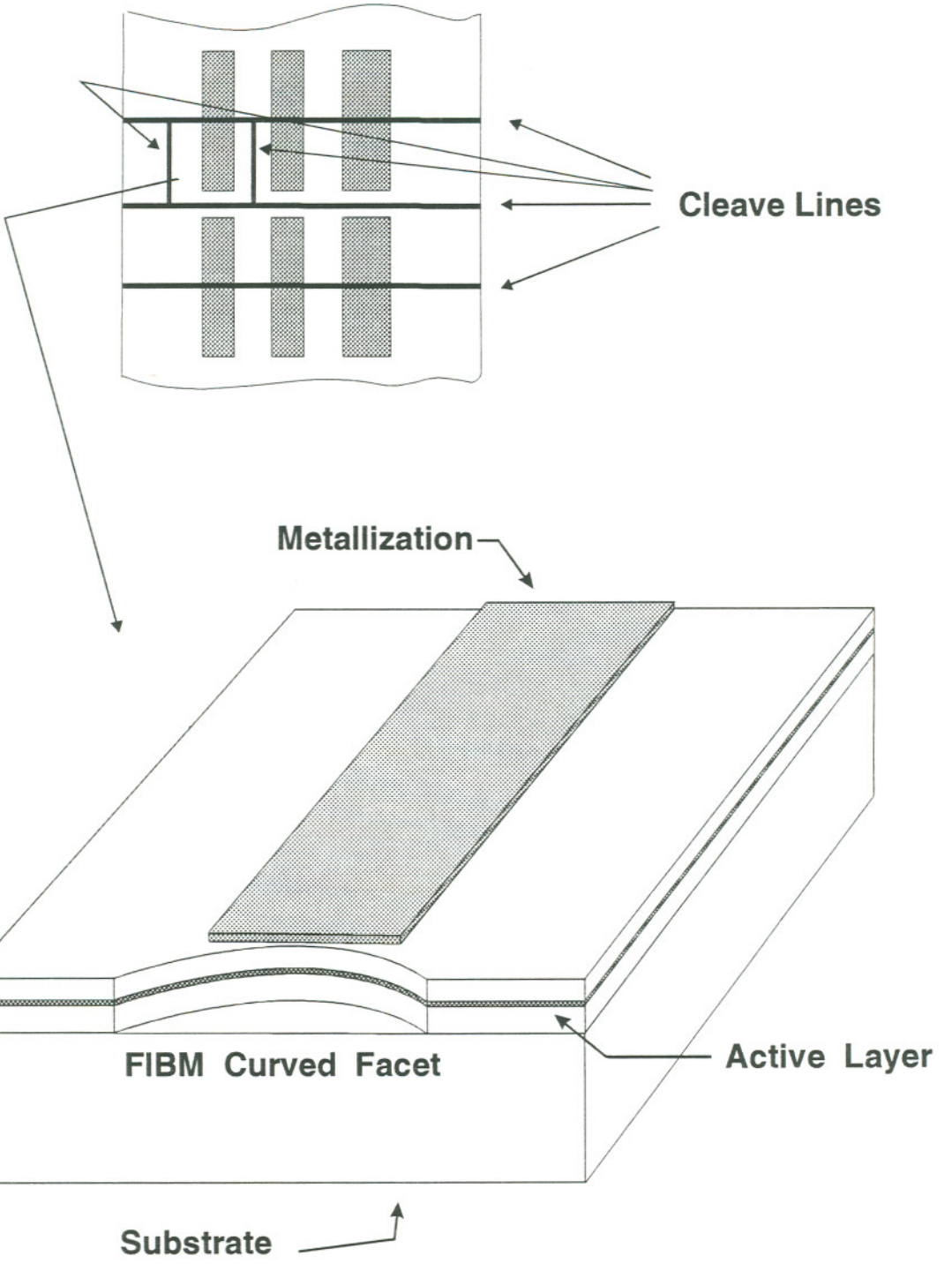

Figure 4.1 Schematic illustrations of the original wafer pattern and the geometrical structure of a FIBM half-symmetric URSL.

fabricated first, and then the laser was mounted junction side down onto the copper heat-sink with indium solder, and wire-bonded to the n-metal. End mirrors for high performance URSLs are expected to meet the following requirements: low surface roughness, small deviation from the desired shape, and small mis-orientation (or wall tilt angle).

A few fabricated mirror surfaces were examined, by co-workers at Rockwell Power Systems, using a Laser Interferometric Microscope (Maxim 3D Model 5700)[117] built by Zygo Corporation. This microscope determines 3-dimensional surface topography by measuring the interference pattern generated by reflecting a laser beam off a flat reference onto the sample. It consists of laser source and optics, microscope head, data acquisition and analysis system, and accessories. The vertical (perpendicular to the surface under examination) resolution of the Maxim 3D is about 0.5 Å, regardless of the optical magnification used. The lateral resolution is about 20 μm at 20 × optical magnification, and 0.5 μm at 1600 × magnification.

In this chapter, the procedures for fabricating high quality cylindrical mirrors are briefly presented. The effects of residual mirror deviations, such as surface roughness and mirror wall tilt, are discussed.

4.2 Focused-ion-beam Micromachining

Two different methods can be used to scan the ion beam, *raster scanning* and *vector scanning*. In *raster scanning*, the initial and final positions are specified, and the ion beam scans at constant rate between them. FIBM is usually conducted by scanning a series of overlapping rectangular sputter

craters. Since the variation of ion dose with position depends on the overlap,[107, 115] complicated surface contours can be created by varying the area of the micromachined flat bottomed crater on subsequent raster scans. For example, a V-shaped groove can be formed by rastering the ion beam over a sequence of successively narrower rectangles on a common center.[110, 118]

In *vector scanning*,[118] the ion beam moves from one pixel to the next pixel. The dwell time at each pixel is controlled by the computer. By controlling the dwell time distribution along the scan, the depth of the sputter profile can be varied.[119, 120] With the same dwell time, the depth of sputter profiles are approximately proportional to the number of scanning cycles. Usually, the FIBM of a surface feature requires more than one scanning cycle. Therefore, it is necessary to find the most suitable dwell time and number of scanning cycles to fabricate a feature with certain depth and desirable surface quality.

A significant amount of the research effort towards development of the liquid metal ion sources and FIBM applications was initiated and accomplished at OGI. The current FIBM system consists of a Amray Model 1830 SEM, a FEI twin-lens FIB gun, ion beam control circuitry and computer. The detailed information concerning the system itself, and results concerning the machining of several types of semiconductor materials and devices can be found in a large collection of journal publications,[107, 108, 110, 118, 121, 122] and dissertations/theses[123-126] written by previous graduate students. Therefore, it will not be repeated here. Factors such as ion dose and energy, sputter crater size and shape, crystal

orientation (which affects the probability of ion channeling), beam scan velocity, and angle of incident ion beam, have found to be more or less relevant to the micromachining speed.[124] The relevant conclusions therein are: (1) Repeated fast scanning of the ion beam gives more uniform machined profiles than a single slow scan, (2) the stability of the ion beam current is critical to achieving of high quality surface structures. The ion beam energy used in those studies was usually smaller than 30 keV.

A so-called high resolution circuit,[126] which was developed by previous group members, has been used to improve the milling and alignment resolutions. The circuit, as shown schematically in Figure 4.2, can be connected in series between two digital-to-analog converters (DACs) and one signal generator (for either "x" or "y"). The output from one DAC is reduced by a adjustable voltage divider to produce the high resolution signal. This signal is added to a second, undivided DAC, so that the high resolution is available to the entire field. The combined output is then sent to the signal generator controlling the selected (either the "x" or "y") offset signal. The effective positioning resolution along the selected direction can be a fraction of a pixel size.

4.3 Convex Cylindrical Mirrors

The FIBM of convex cylindrical mirrors was initiated in this group.[11, 126] Mirror fabrication was performed previously by other group members utilizing the raster scan method. The raster scanning was carried out through

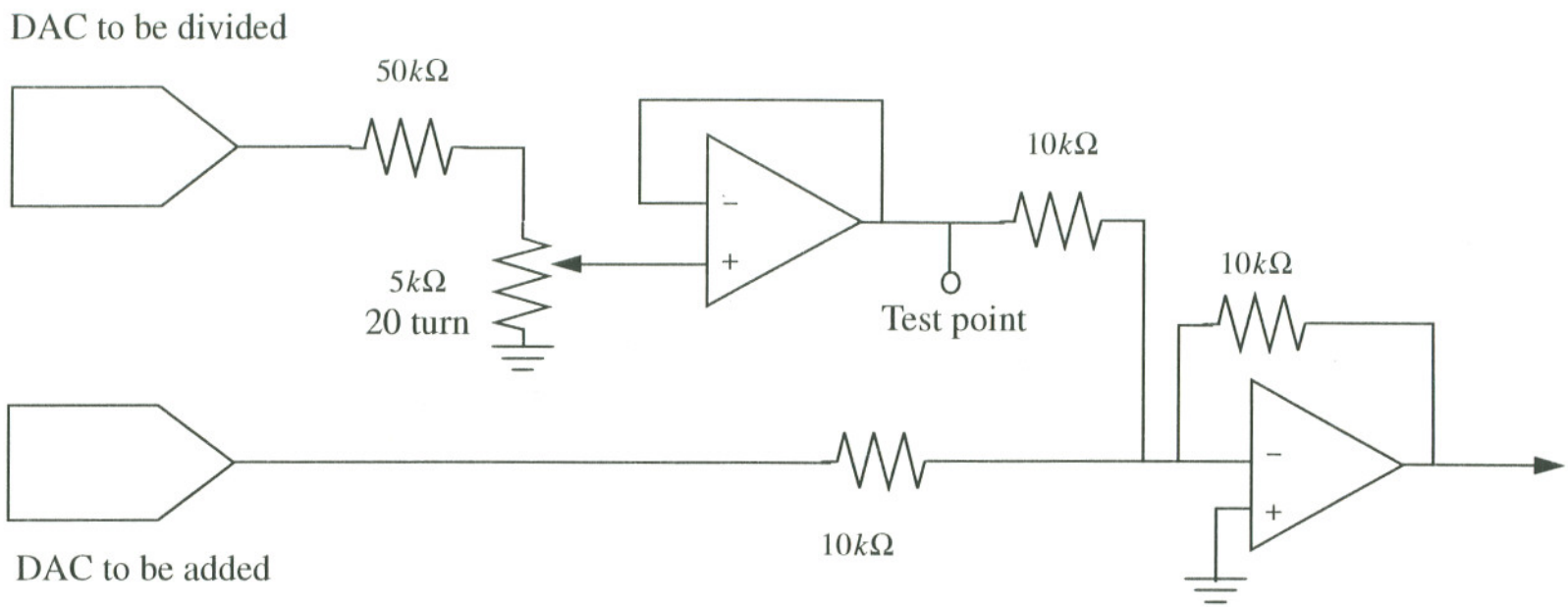

Figure 4.2 Schematic illustration of the high resolution voltage divider circuit.

two ramp generators, which were controlled by a VAX LAB computer to generate high frequency ramp pulses. That early work led to the demonstration of URSLs with promising operating performance, and served as the stimulus for the on-going URSL program and this dissertation.

Although those early FIBM mirrors had low surface roughness, they had "seagull" deviations from the desired cylindrical shapes, as shown in Figure 4.3. The curve shown in Figure 4.3 was obtained from a Zygo microscope by sampling a lateral line (2-D) across an early cylindrical mirror. This undesired deviation was later found to be caused by the slight distortion of the ramp pulses from the ramp generators, which were not worthy of being repaired. Each of the distorted ramp pulses had a short ($< 10\ \mu s$) platform at the starting point, as shown in Figure 4.4, which would cause more milling on one side of the mirror than what was desired. The dashed curve at the bottom of Figure 4.4 represents the desired circular contour. The solid curve represents the FIBM contour, which is slightly wider than the circular one. After being aligned to their centers to perform the best fitting, as shown in Figure 4.4, the difference of those two curve will give a "seagull" profile.

To achieve more accurate FIBM mirrors for the on-going program, a Tektronics AT bus PEP301 16MHz 80386/80387 PC with a Metrabyte DDA06 DAC board, which can directly generate a fast vector scan, has been used to replace the two ramp generators and the VAX computer system. The inset of Figure 4.5 schematically shows the signal generated by the DDA06 DAC board. The ion beam scan routine was deliberately designed to be

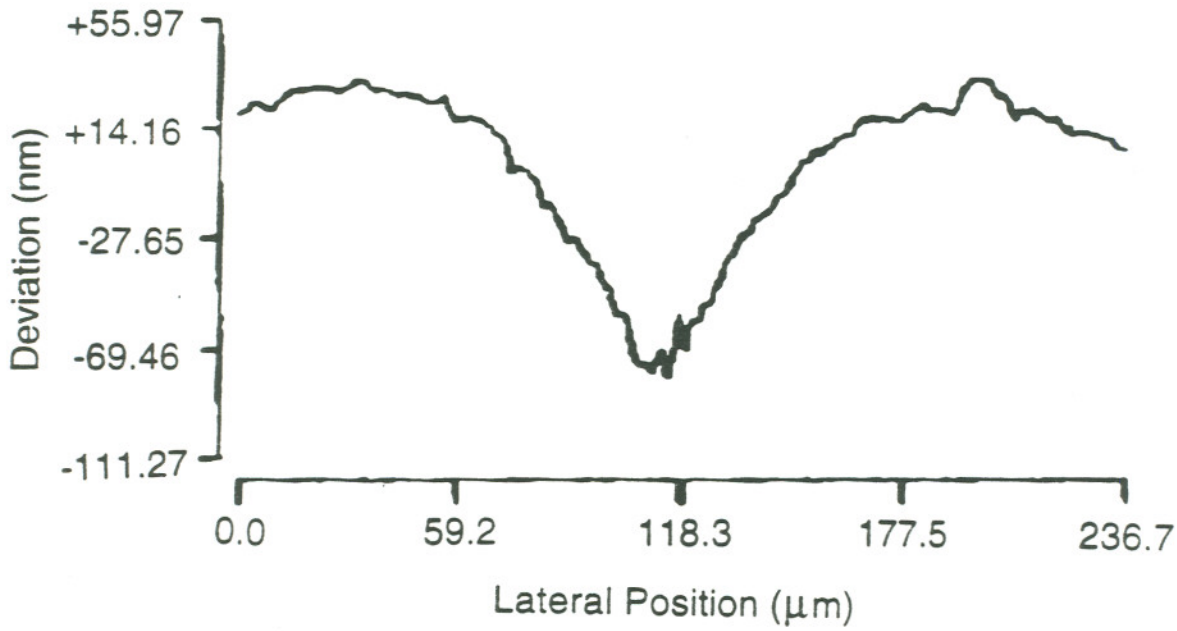

Figure 4.3 Early FIBM curved mirrors had "seagull"-type departures from the desired cylindrical surfaces.

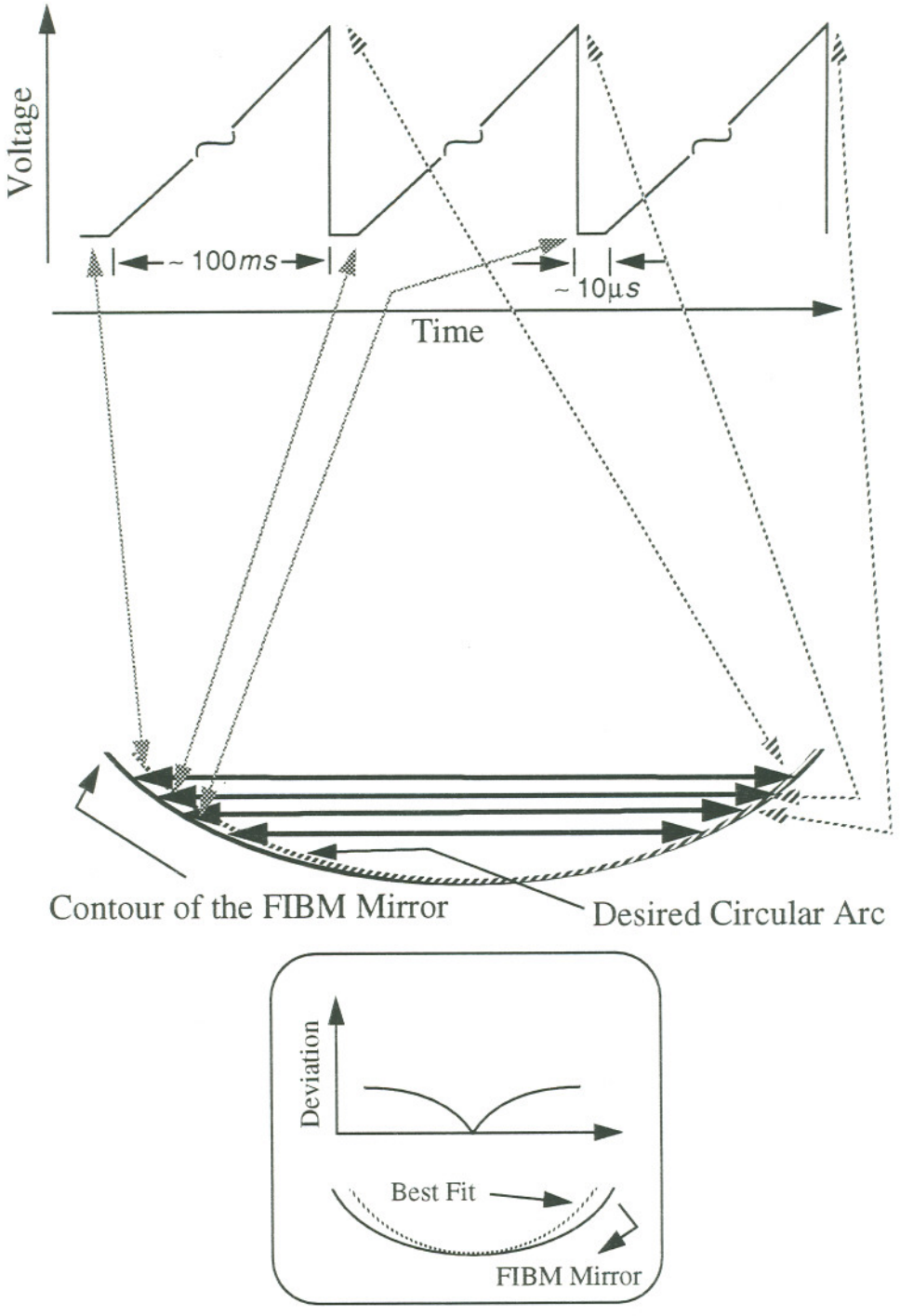

Figure 4.4 Schematic illustration of the distorted ramp pulses and the formation of a distorted FIBM mirror. The inset shows the formation of "seagull"-type departure (not in scale).

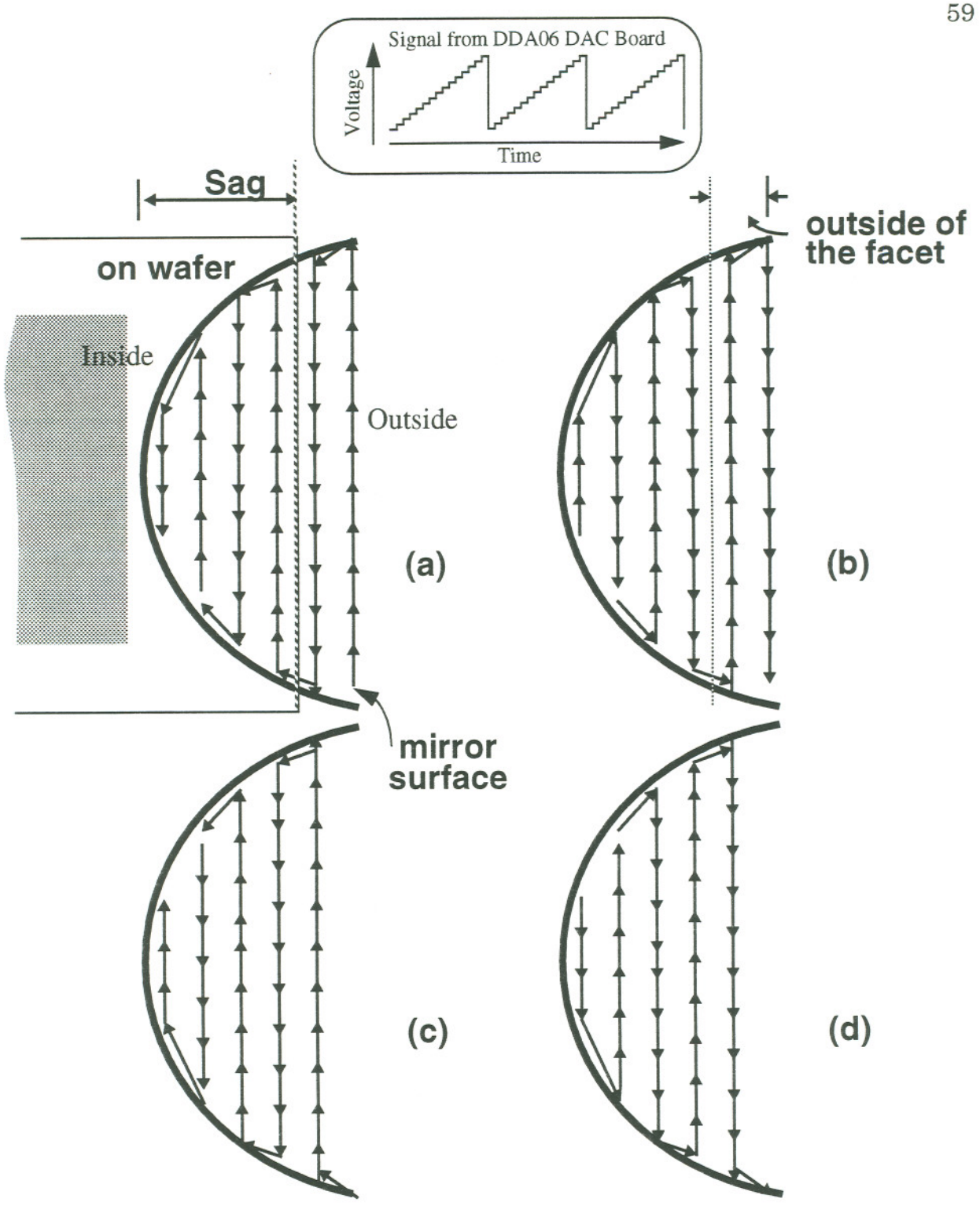

Figure 4.5 Schematic illustration of scan routine designed for the FIBM of high quality convex cylindrical mirrors. **a)** scan from outside to inside; **b)** scan from inside to outside along the same path of phase **a**; **c)** shift one line towards the inside and scan from outside to inside; **d)** scan from inside to outside along the same path of phase **c**.

symmetric vector scanning. It was speculated that symmetric scanning could lead to symmetric sputtering. The scanning routine can be monitored through an oscilloscope, and is schematically shown in Figure 4.5. The scanning routine covers both the mirror sag region, which is defined in this Figure, and a region beyond the originally cleaved wafer facet to ensure a complete mirror coverage. In the FIBM controlling code, the positions of the end points of each line are then calculated. The ion beam dwells at each pixel for the same amount of time, and moves along the lateral lines in patterns shown in Figure 4.5. Each scan cycle can be divided into four phases. In the first phase, the ion beam is first scanned along one direction from the outer most line to the inner most line. Then the scanning direction is reversed in the second phase, and the ion beam is scanned from the inner most line to the outer most line. The third phase continues from the last line of last phase, the ion beam is scanned along the same direction from the outside to inside, and then the scanning direction is reverted again in the fourth phase for the ion beam to go from inside back to outside. The combination of this scan routine and the correctly functioning signal generator enables uniform and symmetric coverage of the whole arc of the mirror by ion beam milling. The outer most line is milled two passes less than the others, which are all milled four passes. Since this line is always outside of the wafer, it does not cause any problem.

Generally, beam scanning during micromachining is accomplished with an address grid size less than or equal to one beam radius to ensure a uniform dose distribution. In the case of FIBM cylindrical mirrors, the

requirement would be that the address grid along the arc of the cylindrical surface is less than or equal to one beam radius. For the FIBM system used to fabricated virtually all the URSLs described in this dissertation, the maximum numbers of pixels along both directions are equal to 4094, the radius of the beam spot is around 250 nm. Therefore, an URSL mirror arc length should be designed to be less than 4094 *pixels* $\times$ 0.25 $\mu m/pixel$ = 1023.5 μm. In practice, a feature to be milled (e.g., the arc for the case of a cylindrical mirror) is always aligned to be within 3/4 of that maximum value, since the astigmatism of the lens column might be stronger when the ion beam is reaching the outer regions in the pixel map. The high resolution circuit[126] was used to increase the positioning resolution along the longitudinal direction, i.e., along the sag defined by the cylindrical mirror, and to increase the accuracy of mirror alignment. At low longitudinal positioning resolution, i.e., less than 400 scan lines per micron, the FIBM mirror usually has high surface roughness, which would result in a broad virtual source envelope.

Limited by the significant amount of wafer material needed to be removed, all URSL mirrors (from all types of materials) were fabricated at the highest available beam current ($\sim$ 4000 pA). To minimize the wall tilt angles of the FIBM mirrors,[126] the cleaved facets to be machined were tilted about 2.0° towards the incident direction of ion beam, i.e., the angle between the normal of the cleaved facet and the ion beam was about 88°. The FIBM control code reads in mirror parameters — such as radius of curvature and sag, and milling resolution — scanning lines per micron of the sag region. For a 200 μm $\times$ 500 μm URSL with resonator magnification of

2.5 (corresponding to 2222 μm of radius of curvature for the mirror) and mirror aperture width of 300 μm, it took about two hours to machine through an arc region with a sag of 5.0 μm and vertical (perpendicular to the junction plane) depth of about 15 μm. To minimize the sputtering of epi-layers by backscattered ions from the bombardment of the mirror bottom, mirrors were usually fabricated with vertical depths (typically around 15 μm) much larger than the active layer depth (~ 2 μm), and showed fairly smooth surfaces. Mirrors fabricated from a few particular wafers, as will be mentioned later in this chapter, were found to be very rough. For devices requiring the removal of larger volume of materials, the machining time will scale up. After conducting trial and error, the optimal scanning resolution, dwell time, and number of scanning cycles were found to be about 400 lines per micron sag, 90 μs, and 7 cycles, respectively. This set of parameters gave the best mirror surfaces, which are about 15 μm deep in the vertical direction. For a mirror with sag larger than 5 μm, the scanning resolution available will be lower than 400 lines per micron sag since the maximum number of scanning lines across the sag is about 2047, i.e., one side of the pixel space. The other side of the pixel space is reserved for scanning lines outside of the wafer facet. However, the ion beam dwell time and the number of scanning cycles can be set to any values.

Mirror structures were also milled by using a smaller beam current (~ 1000 pA). From SEM pictures, these mirror surfaces are as smooth as those milled using the highest beam current. However, they took a longer time (about 4 times longer) to mill, although they usually showed less rounded

top edges than the mirror structures milled using the highest beam current.

According to the Zygo interferometry measurements, the "seagull"-type deviations were not evident with the new cylindrical mirrors. Figure 4.6 plots the Zygo data of a typical new FIBM mirror from a GaInP/AlGaInP URSL. This plot suggests a surface root-mean-squared (RMS) roughness as low as 4 nm for that FIBM mirror. The peak-to-valley deviation is about 10 nm for this particular mirror. As a comparison, the lattice constant for GaInP crystal is about 0.6 nm. These observation confirmed the original objective that symmetric vector scanning can provide accurate milling. Actually, features with lateral dimensions smaller than 0.5 μm, which is the lateral resolution of the Zygo microscope, were not accurately sampled in this measurement. On the other hand, those types of small features are not expected to be significant on our FIBM mirror surfaces since the ion beam size (diameter) is also close to 0.5 μm. Both the longitudinal line spacing ($\sim$ 25Å) and the lateral pixel separation ($<$ 0.2 μm) were selected to be smaller than the ion beam size when those URSL mirrors, actually all of our mirrors, were fabricated. Thus, this author considers Zygo measurement to be a reasonable means to examine our FIBM mirror surfaces.

For non-cylindrical convex mirrors, e.g., refractive-aberration corrected mirrors, hybrid mirrors, and dual curvature mirrors, a similar ion beam control routine can be used. Different algorithms are needed for different types of mirrors to calculate the positions of the end points of each lateral line.

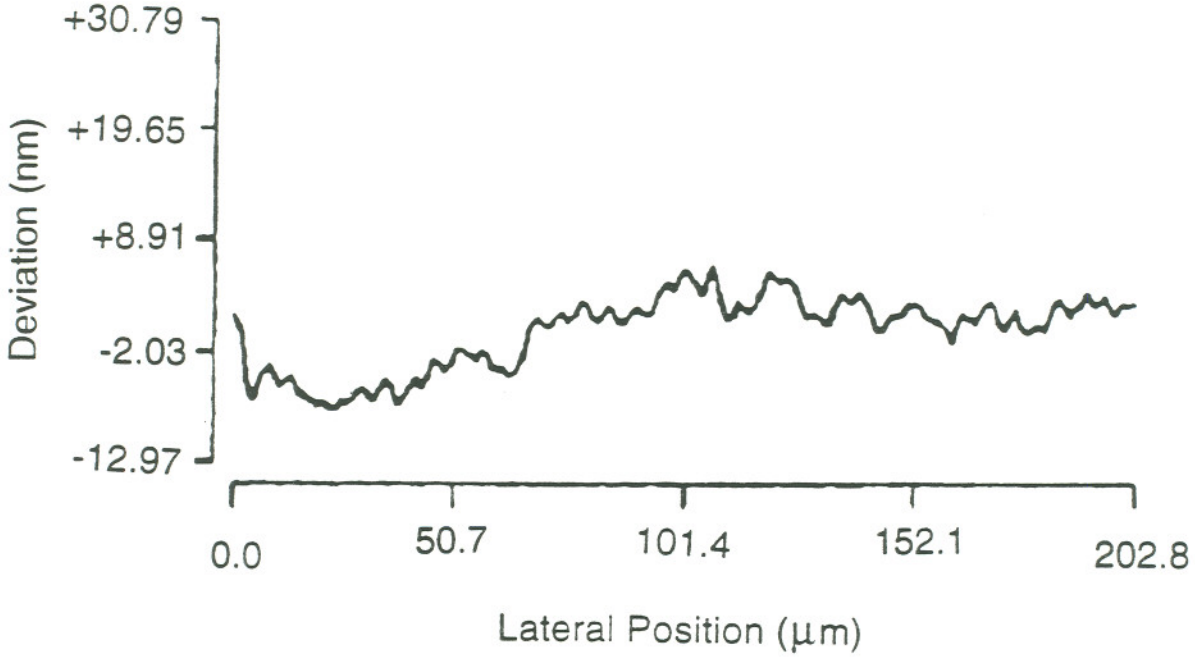

Figure 4.6 Differential surface profile of a GaInP/AlGaInP GRINSCH SQW URSL mirror - Zygo data.

4.4 Concave Cylindrical Mirrors

For half-symmetric URSLs, only a single convex mirror is needed. For URSLs with other types of resonator structures, such as self-collimated URSLs, however, fabrication of concave mirrors are required. The control code for FIBM convex mirrors was modified to specify scan routines for the concave mirrors. In principle, a similar scanning strategy to that of convex mirrors can be utilized for concave mirrors, i.e., the ion beam is scanned along straight lines. When scanning across the sag region, as shown in the inset of Figure 4.7, the straight lines need to be broken into two parts — one on each side of the sag region. However, undesired milling might occur to the sag region when deflecting the ion beam directly from one side of the sag to the other side. For that reason, such a straight line scanning strategy was not used.

Instead, a different strategy was designed to scan the ion beam along arc lines (or partial circles) of constant extending angle. This strategy is easier to execute in a symmetric manner. After specifying the values of mirror radius, the maximum sag, and mirror aperture, the total number of consecutive arcs and their extending angle can be determined in consideration of the milling resolution. All the consecutive arc lines are also scanned with the same number of points, where the ion beam will dwell for the same amount of time. The separation between two neighboring points on each arc line may be a fraction of a pixel size. The total number of dwell points and the total number of arcs can be optimized through experimental trial

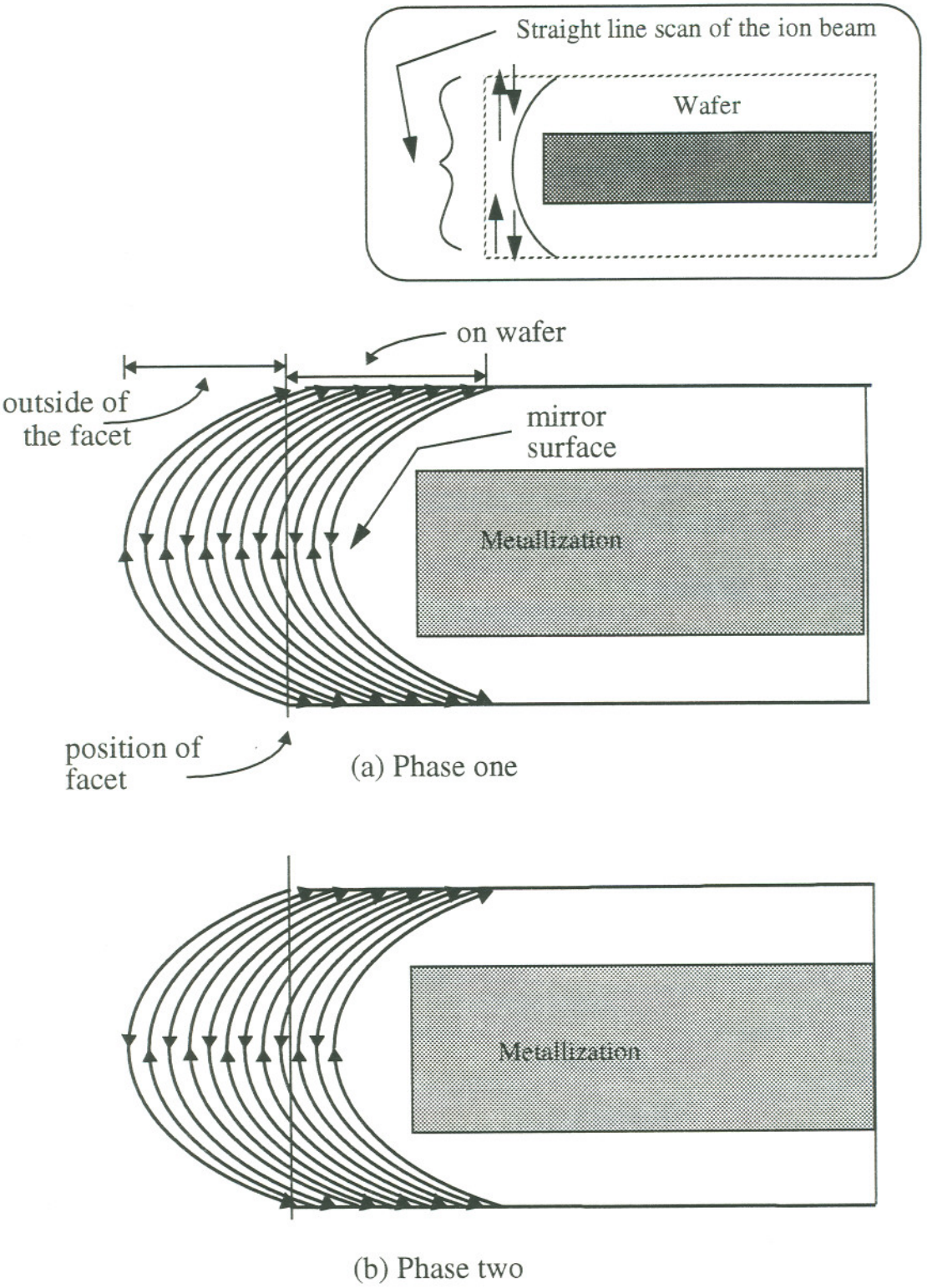

Figure 4.7 Schematic illustration of the circular scanning routines for the FIBM of concave cylindrical mirrors. Inset: undesirable straight scan routine.

and error. The scan of the ion beam starts from the outer most arc, and covers each arc in both of the two opposite directions. Figure 4.7 schematically shows the scan routine. After the scan of the inner most arc is finished, the ion beam moves back to the outer most arc, and the next milling cycle starts.

The micromachining was also conducted using the largest beam current. It took about three hours to machine a concave mirror (with aperture width 340 μm, radius of curvature 2300 μm, and a vertical depth of 20 μm) out of InGaAs/AlGaAs wafer material. Zygo measurements were not conducted for the FIBM concave mirrors. For mirrors that were started from cleanly cleaved facets, no significantly rough features/defects were observed under the examination of a scanning electron microscope (SEM). Unfortunately, the SEM that we used can not provide quantitative measure for mirror surface roughness. The pictures taken from that SEM did not have as high resolutions, along both vertical and lateral directions, as Zygo measurements did.

In principle, this scanning strategy can also be used for FIBM convex mirrors. Being satisfied with the quality of convex mirrors fabricated by using the method described in section 4.3, unfortunately, experimental work has not been pursued in further exploring this circular scanning strategy.

4.5 Mirror Quality and Optical Properties

The FIBM cylindrical mirror profiles can be sampled using the Zygo Maxim 3D laser interferometric microscope. By subtracting the best-fit

circular arc from the measured one-dimensional profile, the undesired deviations can be obtained. The deviations of a FIBM mirror from the desired structure can be classified into three categories, the surface roughness, the mirror wall tilt, and the overall deviation of the mirror shape (e.g., "seagull"-shape). An ideal mirror would be perfectly smooth and perpendicular to the junction plane. In practical fabrication processes, however, it has been noticed that impurities and nonuniformities associated with the original facets will be retained (or even magnified, depending on the specific case) during the FIBM processes. For example, a piece (as small as a few microns in diameter) of debris setting in the area to be machined will leave a relief behind. The lateral dimensions of the relief are close to that of the original debris. FIBM was usually conducted in areas not covered by the metal stripes. If a mirror was aligned through part of the metallization, the resulted surface would be very rough due to the polycrystalline structure of the metallization. Detailed study about the last topic was reported by a separate research group,[127] and showed that mirror surface roughness can be reduced by depositing tungsten on top of the device metallization prior to FIBM. Vibrations of ion gun column and the specimen stage may cause drift of the ion beam positions relative to the milling areas, and generate undesired rough features on the mirror surfaces. The tail-effect[128] of the Gaussian profiled ion-beam and the uncertainty of wafer tilt alignment may lead to a slight angle between the FIBM mirror wall and the desired perpendicular plane.

The surface roughness and mirror wall tilt directly contribute to the reduction of mirror reflectivity, and affect the URSL operating characteristics. Simple analyses will be given below to describe these two effects. It was predicted that the overall mirror shape deviation may affect the lasing mode properties.[14] The overall mirror shape deviation (usually on the order of tens of nanometers) is much smaller than the cylindrical mirror sag (on the order of microns) for the FIBM mirrors.

4.5.1 Surface Roughness

The parameter that measures the overall surface smoothness is usually defined by the root-mean-squared (RMS) roughness ξ, which is given by the formula[129, 130]

$$\xi = \left[\sum_{i=1}^{n} y_i^2 / n \right]^{1/2}, \tag{4.1}$$

where y is the deviation from the ideal surface profile, n is the number of points in the one-dimensional vector y.

Depending on the quality of the original facet, and the specific stability of the FIBM system during the process of milling, the deviation patterns differ significantly from one device to another. Mirrors with RMS roughness as low as 36 Å, as shown in Figure 4.6, and as large as 200 Å have been fabricated. The surface roughness can be minimized by starting with clean and smoothly cleaved facets, and by conducting the milling process while the FIBM system is in a stable status. Both vibration and beam current stability were carefully monitored by looking at the secondary-ion

image of the sample surface. The milling process would not be started until no obvious image shift was observed over a certain period of time, e.g., half a hour.

Low surface roughness is essential to maximizing facet reflectivity, and minimizing scattering loss. For a FIBM cylindrical mirror, residual surface roughness tends to degrade its optical characteristics. The mirror reflectivity ρ, transmission coefficient T and scattering coefficient S can be approximately expressed in the following way[8, 131]

$$\rho = \rho_0[1 - (4\pi\xi/\lambda)^2], \tag{4.2}$$

$$T = T_0[1 - [2\pi\xi(1 - \mu_e)/(\lambda\mu_e)]^2], \tag{4.3}$$

$$S = 1 - \rho - T, \tag{4.4}$$

where λ is the lasing wavelength inside the cavity, μ_e is the modal effective refractive index, and ρ_0 and T_0 are the reflectivity and transmission coefficients for smooth mirrors ($\rho_0 + T_0 = 1$). This wavelength sensitivity means that the scattering effect is more severe for AlGaInP lasers (660 nm) than GaAs, InGaAs and InGaAsP lasers. Assuming an RMS surface roughness of 60Å for the FIBM AlGaInP mirror,[19] S is calculated to be about 7%. The effects on device performance due to a increased S will be discussed in Chapter 6.

Mirror surface roughness may also have effects on spatial coherence of URSL optical output beams. It has yet to be investigated how severe those effects are.

4.5.2 Mirror Wall Tilt

Iga *et al* analyzed the dependence of mirror reflectivity on the mirror wall tilt angle by treating the optical modes as Gaussian type waves along the transverse direction, and found the following expression[132]

$$\rho = \rho_0 exp\,[-2k^2\omega_{0y}^2\tan^2(\psi)], \tag{4.5}$$

where ρ_0 is the modal reflectivity for an untilted mirror, ω_{0y} is the transverse spot size of the Gaussian beam,[58] $k = 2\pi\mu_e/\lambda$ is the effective guide propagation constant, and ψ is the mirror wall tilt angle. The mode spot size can be expressed in terms of the effective refractive index and the transverse divergence angle as

$$\omega_{0y} = \frac{\sqrt{2ln\,2}\,\mu_e}{k\tan(\theta_\perp/2)}, \tag{4.6}$$

the relevant derivations are given in Appendix A. Equation (4.5) can then be re-written as

$$\rho = \rho_0 \exp\left[-(4ln\,2)\mu_e^2\frac{\tan^2(\psi)}{\tan^2(\theta_\perp/2)}\right] \tag{4.7}$$

where μ_e is the modal effective refractive index, $\theta_\perp$ is the full divergence angle (FWHM) in the transverse direction. Equation (4.7) shows that the reflectivity change due to a non-zero mirror tilt angle is dependent on the beam divergence and the mirror tilt angle, both of which can be measured, and the effective index of the waveguide, which can be calculated after knowing the device structure. Incidentally, since all the different types of GRINSCH SQW materials we studied had transverse divergence angles

(FWHM) around 44°, it would be expected that they face essentially the same sensitivity to the mirror wall tilt.

By purposely tilting the original cleaved facet 2 ~ 4° towards the ion beam, i.e., the angle between the normal of the cleaved facet and the ion beam is about 86~88°, the wall tilt angles have been controlled within 1.5°. To measure the facet tilt, a high-resolution circuit,[126] as described in section 4.2, was used to stretch the image along the direction perpendicular to the facet. The 2 ~ 4° cleaved facet tilt angle could be calculated from the projected width of the facet, and the known facet height (i.e., wafer thickness). The projected width of the facet was measured in the FIB system by comparing with an adjacent feature of given size. Mirrors with larger wall tilt angles were also fabricated. Table 4.1 lists the cleaved facet tilt angles and the resulting mirror wall tilt angles for three URSL mirrors fabricated on the same bar. When the facet was tilted 1° away from the ion beam, the mirror wall tilt angle increased to 7.5°. Only one data point was collected for each mirror with a large wall tilt angle. Considering the low positioning precision achievable from the FIBM stage, those data might contain significant error. As will be discussed in chapter 5, a mirror wall tilt angle of 2.9° would cause significant power efficiency drop for a typical low magnification URSL. Figure 4.8 shows the data points for a total of eleven mirrors. By setting the facet tilt angle at 3.5°, the resulting URSL mirror wall tilt angles were measured to be in the range of 0.8°~1.5°. Those uncertainties may be attributed partly to the errors associated with the angle measurements.

Table 4.1 Mirror wall tilt angle versus facet tilt angle for three mirrors fabricated on the same InGaAs wafer bar

Facet tilt angle (degree)	Mirror wall tilt angle (degree)
3.5	0.9
2.0	2.9
-1.0	7.5

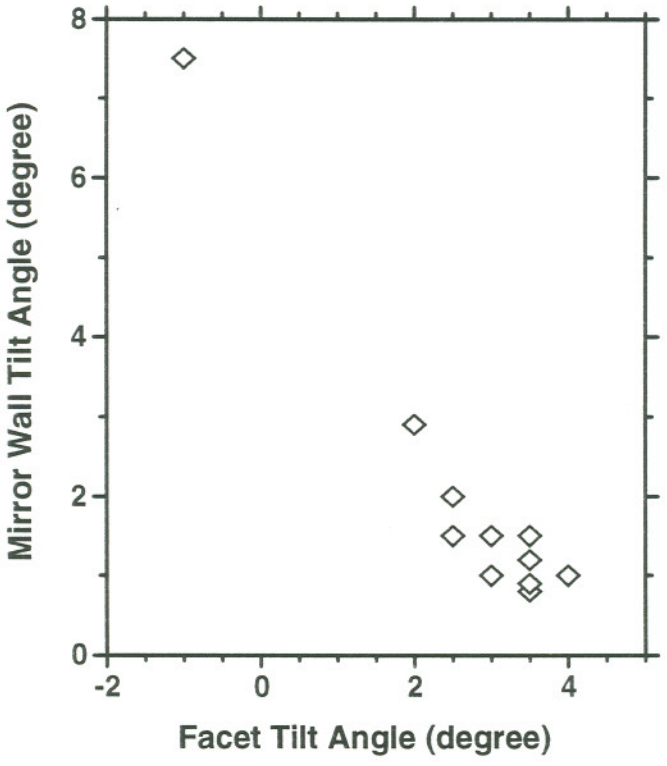

Figure 4.8 Mirror wall tilt angle versus facet tilt angle for total of eleven URSL mirrors.

4.6 Summary and Discussion

4.6.1 Summary

To fabricate curved mirrors with high quality surfaces and precisely the desired shapes, investigations have been conducted for finding suitable FIBM strategies. By deliberately arranging a symmetric *vector scanning* routine, cylindrical mirrors with RMS roughness as low as 40 Å were fabricated. Through careful mirror alignment with the help of a high resolution circuit, mirror wall tilt angles could be controlled within 1.5°. As discussed above and confirmed by experimental results in chapter 5, URSL performance has strong dependence on the surface roughness figure and mirror wall tilt angle of its curved mirror.

4.6.2 Discussion

Associated with the Ga^+ ion sputtering processes, there are also some potential effects such as the formation of altered layer, and amorphization at the sputtered material surface when it is about perpendicular to the ion beam incidence direction.[123, 124] For the particular Ga^+ ion and GaAs target combination, altered layers formation was observed quite readily in the form of *Ga* rich droplets on the bottom of the sputtered areas.[123] However, most part of the sputtered surface that is about perpendicular to ion beam incidence direction is the bottom of the cylindrical mirror, and far below the laser active layer. The side effects on the mirror bottom, which is usually very rough, has no direct influence on the device performance. So, the study of those side effects on the bottom surface profiles has not be

pursued. The other concern would be about the mirror surface, which is also subjected to ion radiation. A beam of ions incident on a surface at a given point will penetrate to a certain depth along the incidence direction. Since the milling itself is proceeding along the incidence direction, the penetration depth is not relevant to our concern. Due to collisions with the lattice atoms, the ions will also be scattered along transverse directions (i.e., perpendicular to the incidence direction) in a distribution with half width ΔR_t, called transverse straggle. At a beam energy of 25 keV, it was projected[133, 134] that the average values of transverse straggle for Zn^+, Se^+, Cd^+, and Te^+ into a GaAs substrate are around 40 Å. Since the mass of a Ga atom is about the average mass of a Zn atom and a Se atom, the transverse straggle of our 25 keV Ga^+ beam might also be around 40 Å, which is less than ten times the crystal lattice constant. Side effects, if there is any, would be limited to a very thin layer at the mirror surface. The direct effects may include slight decreasing the mirror reflectivity, reducing the threshold for optical COD, and increasing the diode leakage current.[135] Perhaps coincidentally, the estimated transverse straggle matches the 40 Å RMS surface roughness reported for one of our FIBM mirrors.

If ion channeling significantly affects the sputtering yield, ion dose can affect the yield through a change in channeling probability associated with target amorphization. For FIBM of GaAs and Si, it was reported[124] that the crystallinity of the target does not significantly affect the sputtering yield, so channeling may not be a major factor there. The sputtering rate was estimated by monitoring the milling time and the volume of a sputtered

mirror, which could be calculated from the measured mirror depth, sag, and aperture width. Table 4.2 summarizes some milling parameters for four different types of materials we studied.

4.6.3 Future Work

It would be very helpful for finding the answers to the uncertainties discussed above by conducting more specific studies on all these types of III-V ternary and quaternary compound materials. For example, features with the same patterns could be machined on a variety of substrates with different dopants/doping levels, and different crystal orientations. The analysis of the resulting surfaces should provide correlations between surface quality and material characteristics. It would be highly desirable to selectively grow laser materials that are suitable for FIBM.

To examine the dependence of mirror surface roughness upon ion beam scanning strategies, it would also be interesting to try raster scanning by using sharp rising ramp pulses, and compare the resulting mirror surfaces with those from using vector scanning. Unfortunately, relevant experiments have not been pursued due to the lack of suitable ramp pulse generators.

Table 4.2 Parameters used for milling 300 micron wide convex cylindrical mirrors from four different types of materials*

Material*	Beam Voltage (kV)	Nominal Beam Current (nA)	Dwell Time (μs)	Beam Diameter (nm)	Sputtering Rate# $(\frac{\mu m^3}{s \bullet nA})$
GaInP/ AlGaInP	25	4.0	90	500	1.07 ± 0.09
InGaAs/ AlGaAs	25	4.0	90	500	1.05 ± 0.09
AlGaAs/ GaAs	25	4.0	90	500	1.0 ± 0.1
GaAlAsSb /GaSb	25	4.0	90	500	0.5 ± 0.07

* Scanning routine shown in Figure 4.5 was adopted.

\# The listed values were obtained by averaging the measurements for several different mirrors. The error values quoted in this table cover the scattering range of sputtering rates measured for several different mirrors. The error was considered to be mainly from the measurements of mirror sag depths, which were sensitive to the alignment of mirror walls relative to the electron beam of a SEM.

Chapter 5

OPERATING CHARACTERISTICS OF HALF-SYMMETRIC URSLs

Earlier URSL studies[6-8, 10, 11] have concentrated on the power characteristics and spatial coherence of the output beams. Parameters, such as output power, quantum efficiency, the fringe visibility and others, were usually measured. On the other hand, limited information was obtained to help in the understanding of URSL lasing mechanisms and characteristics of the output beams. During last two years, numerous URSLs were fabricated and characterized for this URSL program. The experimental results have helped to reveal some fundamental characteristics such as sub-threshold spatio-spectral patterns, virtual source formation and evolution, and temporal dynamics of the output beams. Some of these observations were not widely noticed (or investigated) in early studies of "macro-"unstable resonator lasers. Some of them are phenomena unique to URSLs.

In this chapter, the operating characteristics of a variety of half-symmetric URSLs are summarized. The results presented are just a small

part of the experimental data that we have collected during this URSL program. However, they do provide an overview of the operating characteristics of URSLs.

5.1 Experimental Procedures for Device Characterization

After the fabrication of cylindrical mirrors, URSLs were always examined by measuring their power, near-field and virtual source envelopes. For some URSLs, their spectral and temporal characteristics were also studied. Power measurements were conducted by simply recording the L-I data, and the relevant set-up will not be discussed here.

Near-field patterns directly provide useful information about laser devices. The spontaneous emission near-field patterns may be used to evaluate the quality of laser facets (or FIBM mirrors for URSLs). For lasers with perfect facets (mirrors), the lasing near-field patterns illustrate how severe filamentation effects may be. Figure 5.1 schematically shows the experimental set-up for characterizing near-field patterns. The near-field patterns are usually magnified through a microscope objective, and recorded using a CCD camera. For broad-area URSLs, the divergence angles (FWHM) of the output beams along both the lateral and transverse directions may be as large as 40°, as we will see later in this chapter. To alleviate vignetting effects, the numerical aperture of the microscope objective needs to be large enough to fully cover a solid angle filled by the output laser beam. To fully resolve the fine structures on the near-field patterns, the optical magnifica-

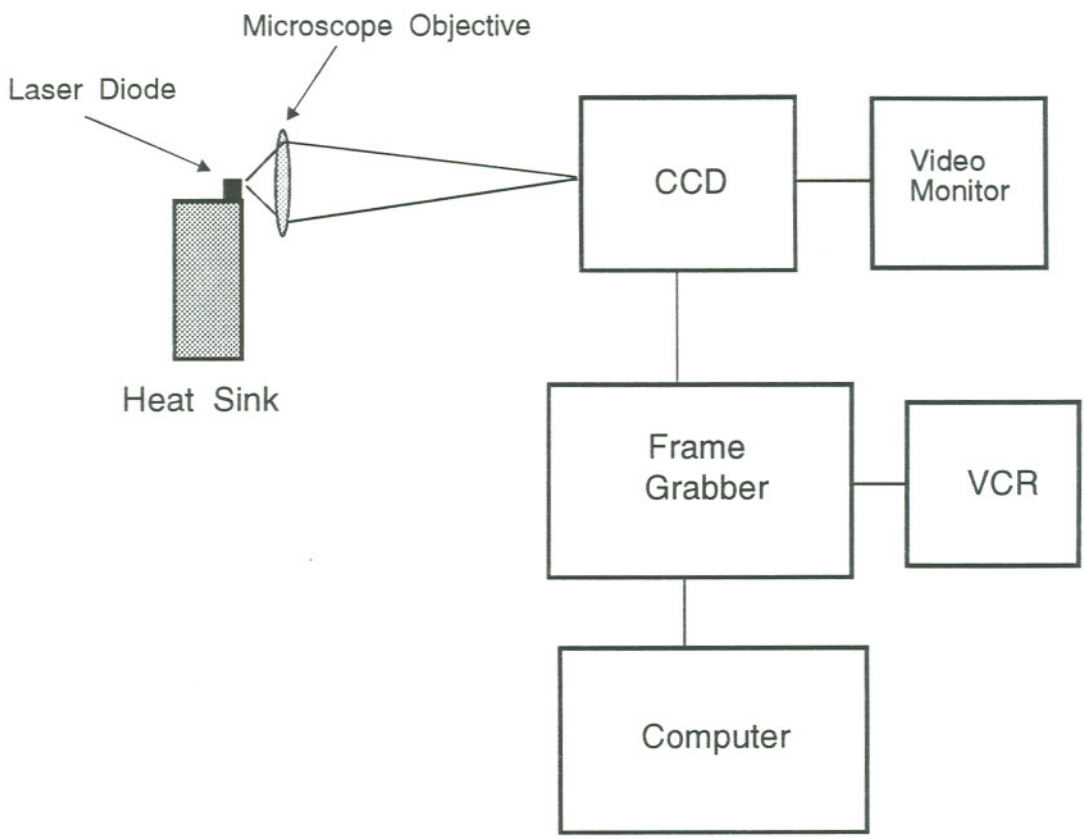

Figure 5.1 Block diagram of the experimental set-up for characterizing URSL near-field and virtual source envelopes.

tion needs to be adjusted accordingly for the specific URSLs.

The same experimental set-up for characterizing near-field patterns can be used to study URSL virtual source envelopes. Since the cylindrical FIBM mirrors only diverge the optical phase-front in the lateral direction while that along the transverse direction remains the same as FPSLs, the URSL output beams are strongly astigmatic. Due to this astigmatic nature, the single microscope objective can only focus the beams along one direction at a time. When the objective is focused at the position of the virtual source, i.e., the lateral circular phase-front is focused to the image position of the virtual source, while the transverse phase-front is out of focus. (Note: The direction perpendicular to the junction plane has also been referred as "vertical" or "vertical transverse", which is equivalent to "transverse" used in this dissertation. The direction that is parallel to the junction plane and perpendicular to the "transverse" direction is referred as "lateral" in this dissertation.) So the virtual source images appear as vertical line patterns. By adding a cylindrical lens along the transverse direction, the virtual source may be imaged into spot patterns. Once again, the lateral optical magnification needs to be high enough to fully resolve the fine lateral structures of virtual sources. At low lateral optical magnifications, what can be recorded are just actually virtual source envelopes. Considering that the 20× optical microscope objective we used was calibrated with an image distance of 16 cm, many of our early virtual source related experiments were conducted under those calibrated conditions (with 20× optical magnification). More detailed discussion will be given in section 5.3.

Spectral measurements were conducted by imaging either the near-field or the virtual source onto the entrance slit of a 1.26 meter spectrometer. For spectral studies presented in this chapter, a CCD camera was used to detect the spectrally expanded output light from the exit slit, as shown in Figure 3.4. Through proper alignment of the system, the spatial and spectral characteristics of the URSL output light can be simultaneously recorded in a two-dimensional configuration, which provides a means to examine the spectral correlations between different parts of the URSL resonator.

The temporal behavior of URSL optical output can be studied using a streak camera[136] by imaging either the near-field or the virtual source at the entrance slit of the camera. The Hamamatsu streak camera system used here consists of a C1587 Temporal Disperser, an M1952 High Speed Streak Unit, an M2567 Synchronous Blanking Unit, and a C1000 Camera Head. The experimental set-up is schematically shown in Figure 5.2. The diode laser was driven by an Avetech-2-C pulser with a typical pulse risetime of 2.0 ns and a pulse width up to 50 ns. It is possible to observe approximately 5 ns of the time-evolution of the laser output anywhere within the 50 ns pulse. Detailed experimental procedures are similar to those described in previous publications,[50, 51, 137] and will not be repeated here. The spatio and temporal characteristics can be recorded simultaneously in a two-dimensional configuration. The dynamic lasing build-up and stability of optical output from different parts of the resonator can be investigated through these two-dimensional recordings.

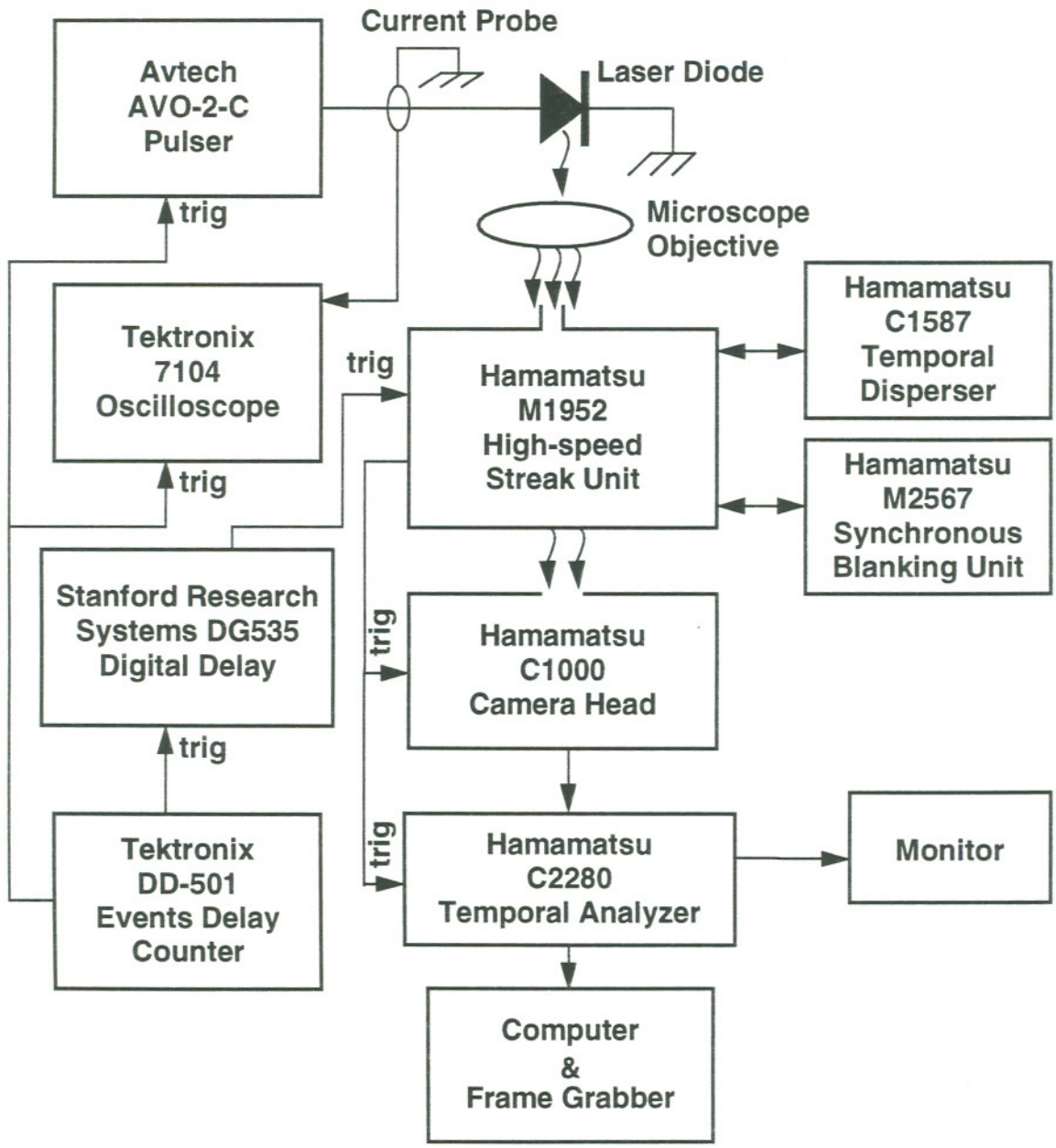

Figure 5.2 Block diagram of the experimental set-up of the streak camera system.

5.2 Evolution of Near-field Pattern with Injection Current

As the injection current increases, the output light changes from spontaneous emission to stimulated emission, and the near-field pattern is expected to vary accordingly. Near-field profiles were taken and analyzed for some devices at various injection levels. Figure 5.3 shows a set of near-field patterns recorded from the FIBM mirror of a InGaAs/AlGaAs URSL with a magnification of 2.5 and dimension of 200 μm $\times$ 500 μm. The smooth envelope of the spontaneous emission pattern suggest that there is no major defects on the FIBM mirror. As the current exceeds threshold, the general smoothness remains almost the same although the overall envelope changes slightly. For current levels higher than threshold, there are ripple-like modulations embedded on the profiles. As the current level increases, the amplitudes and lateral sizes of those ripples also increase slightly.

For high magnification URSLs, the lateral divergence angles of the output beams can be so large that the reduction of reflectivities at the side regions of the mirror relative to that of the core region may be significant. The extreme situation is that total internal reflection (TIR)[8] may occur at the two side regions of the output mirrors. Theoretical considerations of the TIR limit and lateral reflectivity variations are given in Appendix B and C.

URSLs with magnification as high as 6.0 have been fabricated for this work, and the near-field patterns from both end mirrors were recorded. Figure 5.4 shows a set of near-field patterns from the flat mirror of a InGaAs/AlGaAs URSL with magnification of 6.0 and stripe dimension of 200

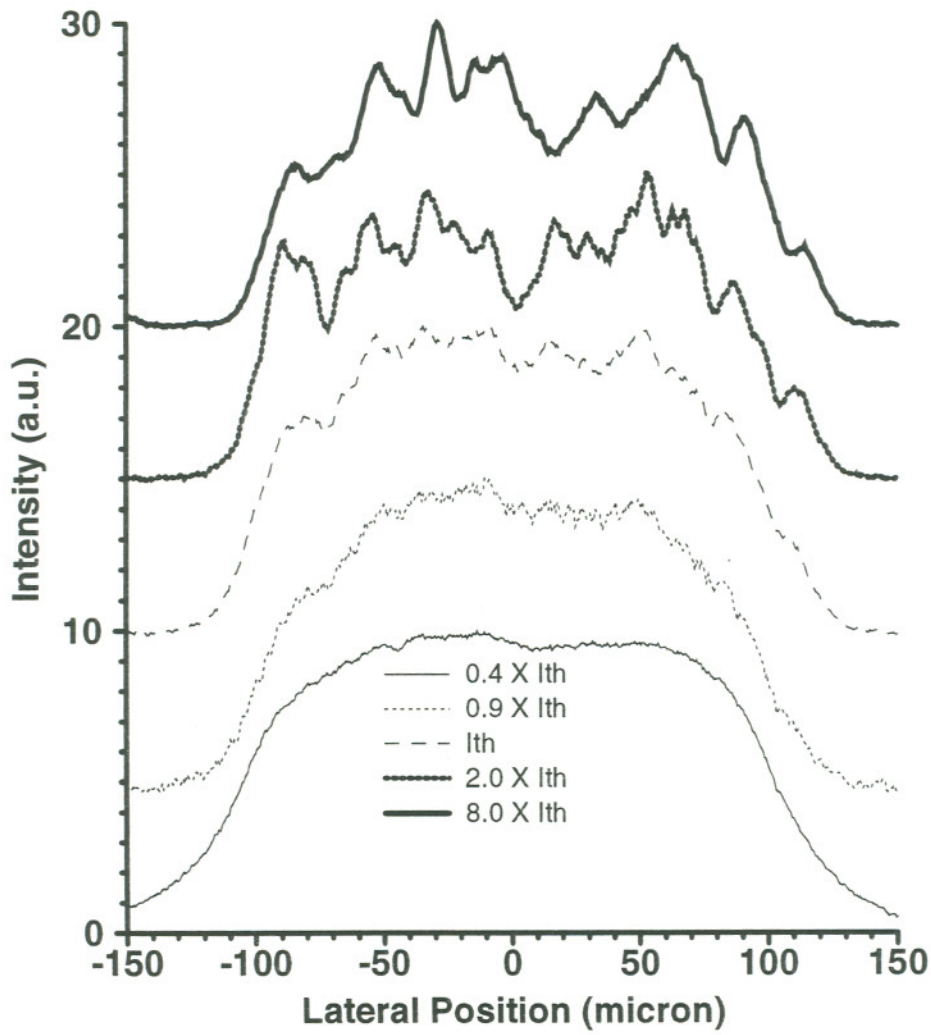

Figure 5.3 Near-field patterns of a 2.5 magnification InGaAs/AlGaAs GRINSCH SQW URSL at various injection levels; stripe dimension is 200 $\mu m \times 500\ \mu m$.

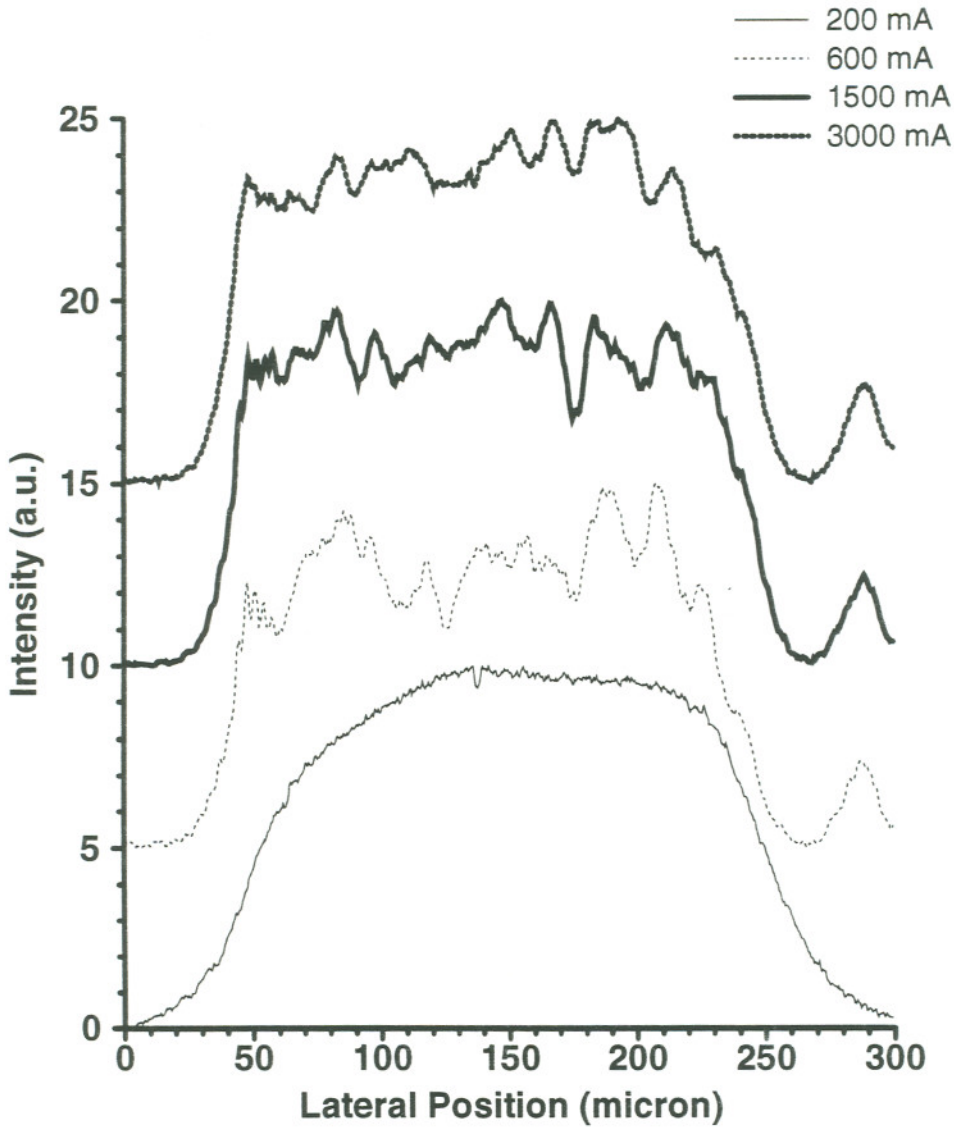

Figure 5.4 Near-field patterns from the flat (cleaved) mirror side of a high magnification (6.0) InGaAs/AlGaAs GRINSCH SQW URSL. The stripe dimension is 200 μm × 500 μm, and threshold current is about 300 mA.

μm × 750 μm. The microscope objective that was used has a numerical aperture (NA) of 0.4, which corresponds to a full acceptance angle of about 47°. The threshold of that URSL is about 300 mA, as will be shown in Figure 6.4. The spontaneous emission pattern at $0.3\times I_{th}$ shows a relatively smooth profile. As the injection current increases, the lasing near-field patterns show similar behavior as those shown in Figure 5.3. No nulls were observed for any of the curves. The appearance of a single lobe in the far right side of each lasing near-field is not fully understood.

As calculated in Appendix B, TIR does not occur until the stripe width increases up to 311 μm for such an URSL. For the URSL with 6.0 magnification, its apparent virtual source depth (R_{v2}) from the curved mirror side was measured to be 195 μm. The calculated R_{v2} is also 195 μm when an effective refractive index of 3.35 is used. The full divergence angle of the output beam from the curved mirror side could be as large as 54°, which is larger than the acceptance angle of the objective. Thus, the near-field patterns from the curved mirror side, unfortunately, could not be recorded properly using the objective with 0.4 NA.

For that same 6.0 magnification URSL, the apparent virtual source depth (R_{v1}) from the flat mirror side is about 315 μm, which gives a full divergence angle of 35° for its output beam. The calculated R_{v1} is about 313 μm with an effective refractive index of 3.35. So the microscope objective with NA = 0.4 can efficiently image the near-field from the flat mirror side.

It is very interesting to notice that URSLs have wider near-field profiles

than FPSLs. The width values of lasing near-field profiles of URSLs, especially those shown in Figure 5.4, are comparable to those of spontaneous emission patterns. However, the near-field profiles of FPSLs are obviously narrower than the spontaneous emission patterns. Figure 5.5 shows the spontaneous emission and lasing near-field patterns for a 200 μm $\times$ 750 μm InGaAs FPSL. The near-field widths (measured at 10% of maximum intensity) for 1.0$\times$ and 4.0$\times$ I_{th} injection levels are slightly smaller than or equal to the stripe width, while the width of a spontaneous emission pattern at 0.25$\times I_{th}$ is slightly larger than the stripe width. Those observations could be explained by spatial hole burning, which occurs when injection level is above threshold, in the gain profile. For URSLs, the light that escapes away from the gain region may not be totally absorbed, and contributes to the near-fields that are slightly wider than the metal stripe.

The spontaneous emission curves plotted in Figures 5.3 — 5.4 show that light emissions could be observed from regions outside the metal stripe. Those light emissions can be attributed to lateral diffusion of carriers.[37] For a broad-area gain-guided laser at an injection level below threshold, the carrier density distribution has rounded edges, and an effective width (FWHM) comparable to the metal stripe width. In other words, the carrier densities at metal stripe edges are about half the maximum density across the stripe. That explains the strong spontaneous emission observed at, and beyond, stripe edges. The characteristics of the rounded edges are dependent on the carrier diffusion length. The detailed analysis will not be repeated here.

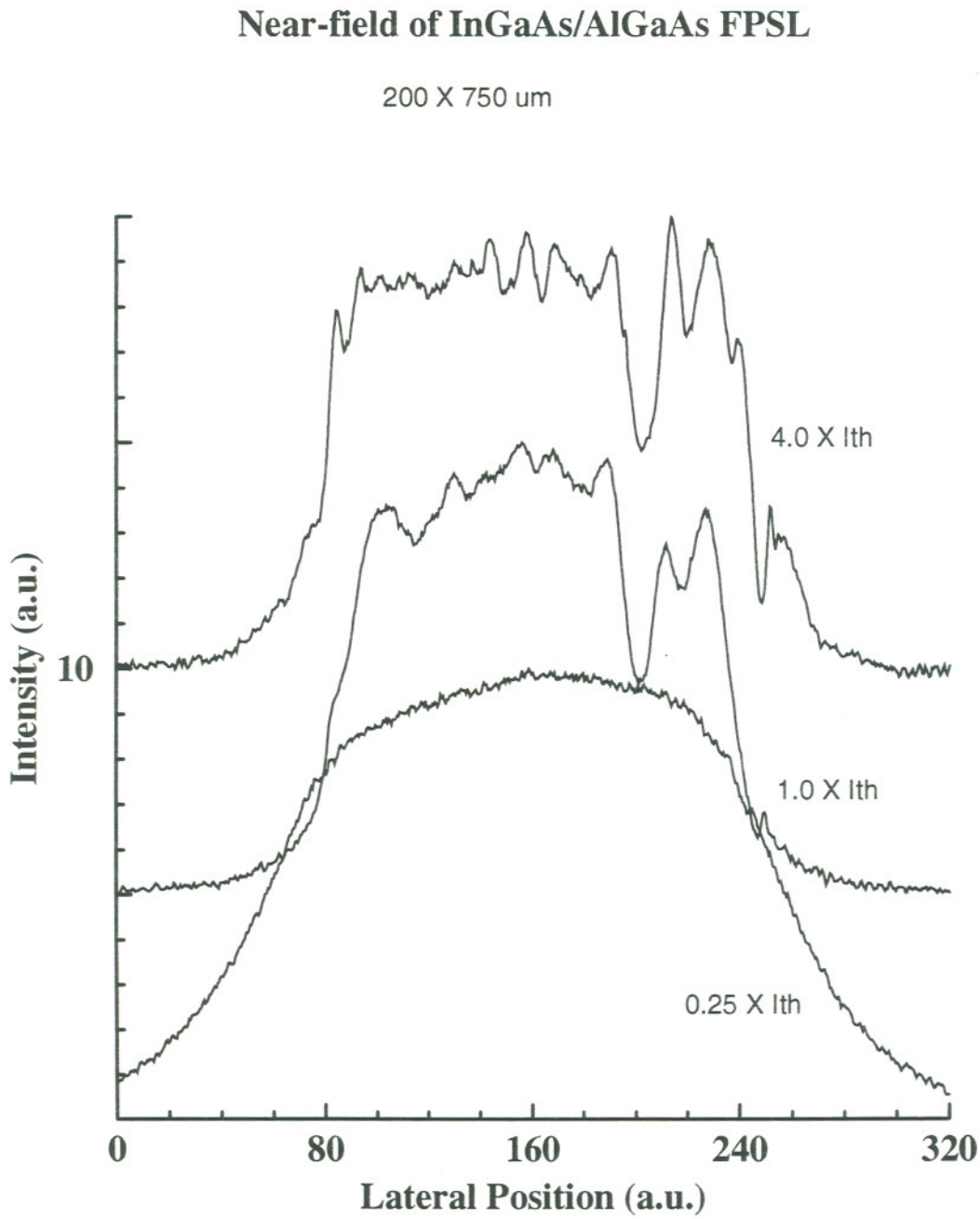

Figure 5.5 Near-field patterns for a 200 μm x 750 μm InGaAs/AlGaAs GRINSCH SQW FPSL.

5.3 Virtual Source Envelope Width versus Injection Current

URSL virtual source patterns contain information, as will be discussed in later sections, regarding the spatial coherence of the optical output, and the lasing modal characteristics. To quantify the spatial intensity distribution, the URSL virtual source was imaged onto a CCD camera through a 20×, 0.4 NA microscope objective, and then digitized for computer processing. The cell size of the CCD camera is 17 μm × 13 μm. To resolve a 1.0 μm size feature with this CCD, it would be necessary for the optical magnification to be larger than 17×.

Several renormalized virtual source envelopes are shown in Figure 5.6a for a 200 μm × 500 μm GaAs/AlGaAs SQW triplet URSL with 3.0 magnification, and in Figure 5.6b for a 200 μm × 750 μm InGaAs URSL with 2.0 magnification. Both devices were operated in pulsed mode. It can be seen that the virtual source starts to form at sub-threshold injection levels,[19] as the curves corresponding to $0.8 \times I_{th}$ show in Figure 5.6, although its peak intensity is relatively weak in comparing with the spontaneous emission background. The virtual source envelope usually shows a very sharp peak at low injection current levels (a few times of threshold), and a broadened peak at high injections. For some URSLs, their virtual source envelopes break into multiple lobes at high injection levels. That behavior is consistent with the modulation observed in the near-field profiles. The separations between different lobes may be small, and can be resolved only when high enough optical magnifications are used. On the other hand, diffraction

a)

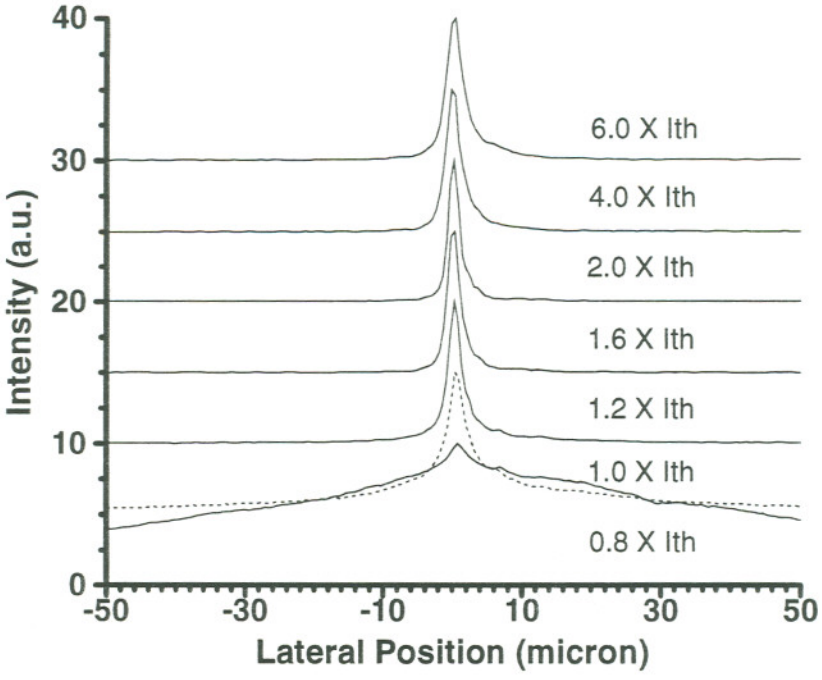

b)

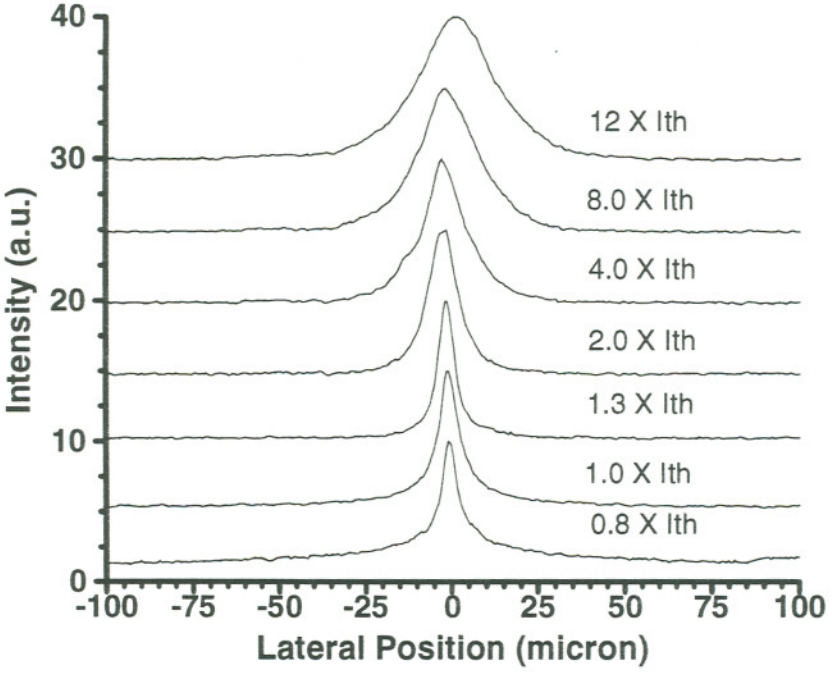

Figure 5.6 Virtual source envelopes at various injection current levels, a) a GaAs/AlGaAs SQW triplet URSL with 3.0 magnification and 200 μm × 500 μm stripe, b) an InGaAs GRINSCH SQW URSL with 2.0 magnification and 200 μm × 750 μm stripe.

effects impose a spatial resolution limit to a imaging system. For an microscope objective with numerical aperture NA,[131] the diffraction-limited resolution can be expressed as

$$x_{DL} = 0.61\lambda/NA, \tag{5.1}$$

where λ is the optical wavelength. For example, with $NA = 0.4$, x_{DL} values will be about 1.0 μm, 1.28 μm, and 1.48 μm at wavelengths of 0.66 μm, 0.84 μm, and 0.97 μm, respectively. The higher the optical magnification is, the more accurate the virtual source envelope is sampled. The optical magnifications that were used are 25× for Figure 5.6a, and 35× for Figure 5.6b. The corresponding spatial resolutions are diffraction-limited for both cases. The broadening behavior of the virtual source at high injection levels varies from one device to another. Streak camera results shown in a later section suggest that the mechanism behind the virtual source broadening phenomena is erratic modal dynamics.

The lateral envelope size, called virtual source envelope width, was measured as the full width at half maximum (FWHM) of the lateral intensity envelope at the plane of the virtual source. Figure 5.7 plots the virtual source envelope width versus drive current for a 300 μm × 1500 μm AlGaInP URSL with resonator magnification of 2.5. The virtual source starts to form at current levels far below threshold, and has a width equivalent to the stripe width. As the current increases, the virtual source envelope width decreases rapidly, and reaches the minimum value of 2.0 μm at threshold, then increases slightly with drive current. The inset curve shows a virtual source envelope, which corresponds to an injection level right above

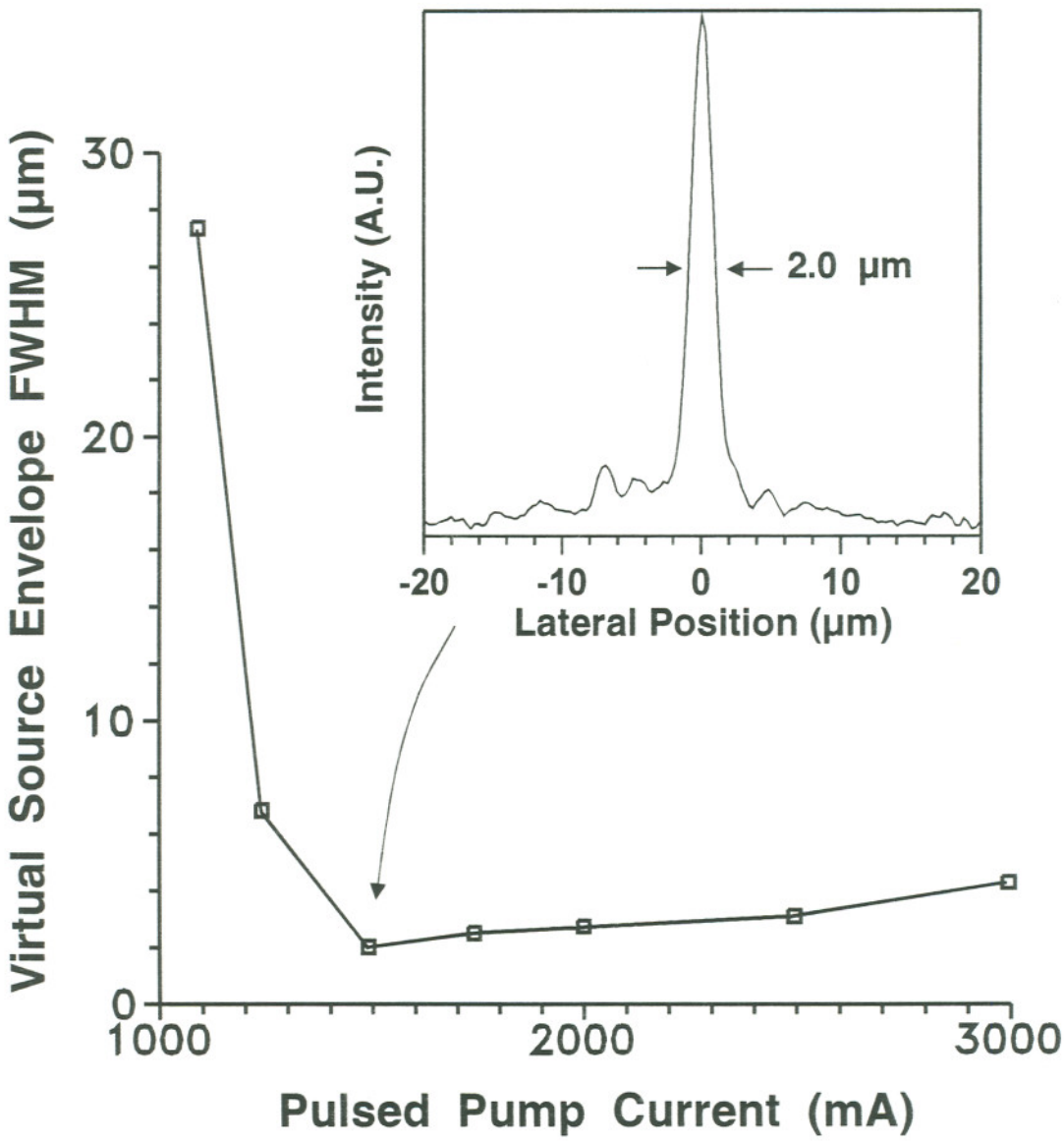

Figure 5.7 Virtual source envelope width versus injection current of a 300 μm × 1500 μm GaInP/AlGaInP URSL in pulsed operation. I_{th} = 1300mA.

threshold. There are small ripples spreading around the main lobe.

The virtual source envelope characteristics of other URSLs were also tested, and show similar behavior as those of Figure 5.6. The minimum source width achievable varies from one type of material to another. The smallest virtual source envelope width was observed from a 200 μm × 500 μm GaAs/AlGaAs URSL with triplet GRINSCH SQW wafer structure and a resonator magnification of 2.5. The virtual source characteristics of this device are plotted in Figure 5.8. The minimum virtual source envelope width measured for this device is about 1.8 μm. The smallest virtual source envelope width measured is about 2.0 μm for GaInP/AlGaInP GRINSCH SQW lasers, and 2.5 μm for InGaAs/AlGaAs GRINSCH SQW lasers. According to analysis based on diffraction theory, as shown in Appendix D, the diffraction limited virtual source envelope width is proportional to the lasing wavelength. It would be reasonable that InGaAs/AlGaAs URSLs had wider virtual sources envelope since they lase at longer wavelengths. However, the GaInP/AlGaInP URSLs did not have much smaller virtual source envelope width than the GaAs/AlGaAs triplet SQW devices although they had shorter lasing wavelengths. For URSLs with stripe width equal to, or larger than, 200 μm, the diffraction limited virtual source envelope widths are less than 1.5 μm for all three lasing wavelengths, i.e., 0.66 μm, 0.84 μm, and 0.97 μm, respectively. In practical operations, measured virtual source envelope widths are always close to these diffraction limited values for near threshold operations. For some URSLs, virtual source envelope sizes remained essentially constant as injection current increased. For some other

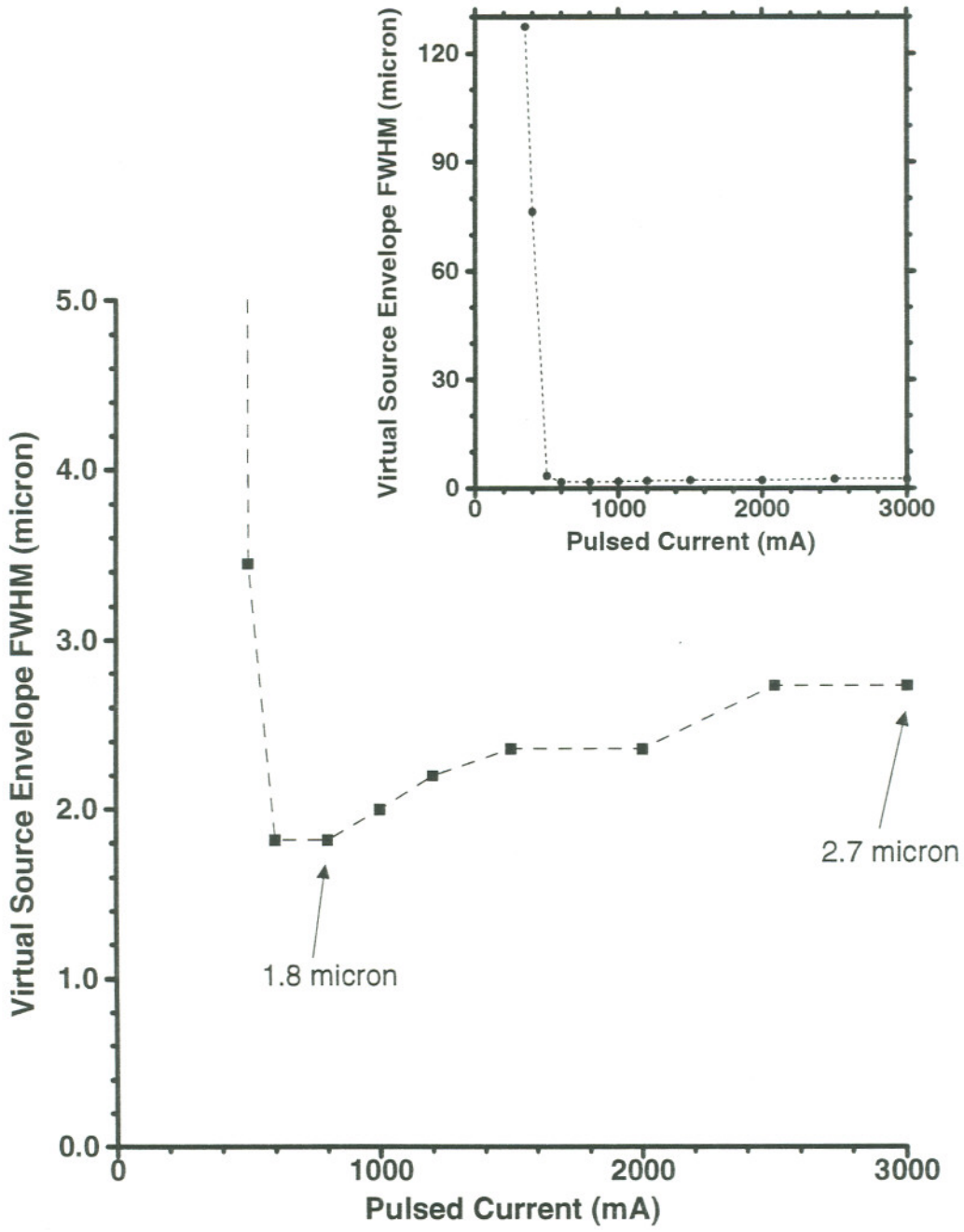

Figure 5.8 Virtual source envelope width versus injection current of a 200 μm × 500 μm triplet GaAs/AlGaAs GRINSCH SQW URSL in pulsed operation.

devices, the envelope widths increased to a few times of diffraction-limited values at high injection levels.

5.4 CW Operation and Evolution of Sub-threshold Near-Field Spatio-spectral Patterns

CW operation has been achieved for the InGaAs/AlGaAs GRINSCH SQW URSLs.[20] The devices had stripe dimensions of 200 μm × 500 μm, and magnifications around 2.5. The lateral source size of a particular CW URSL was measured and plotted in Figure 5.9, with filled circle symbols, versus injection current. The threshold current density of this URSL is about 240 A/cm^2. The source width decreases rapidly from the FWHM of spontaneous emission pattern far below threshold, to 2.8 μm at threshold, then increases to 9.0 μm at injection current of 2.0 A. The source depth was measured to be 350 μm with less than 2% shift through the full range of tested injection currents. This device was also tested in pulsed operation. The virtual source depth was also measured to be around 350 μm with no obvious shift as the injection current went up to 2000 mA. The pulsed virtual source size data were also plotted in Figure 5.9, with filled square symbols. When the injection level was around threshold, the source size for pulsed operation was very close to that of the CW one. As the injection levels went beyond $2.0\times I_{th}$, the source width for pulsed operation was slightly larger than that of the CW one although both increase with increasing injection level. At high injection levels ($I > 6.0\times I_{th}$), however, pulsed operation gave slightly smaller source size than in CW. These observations suggest

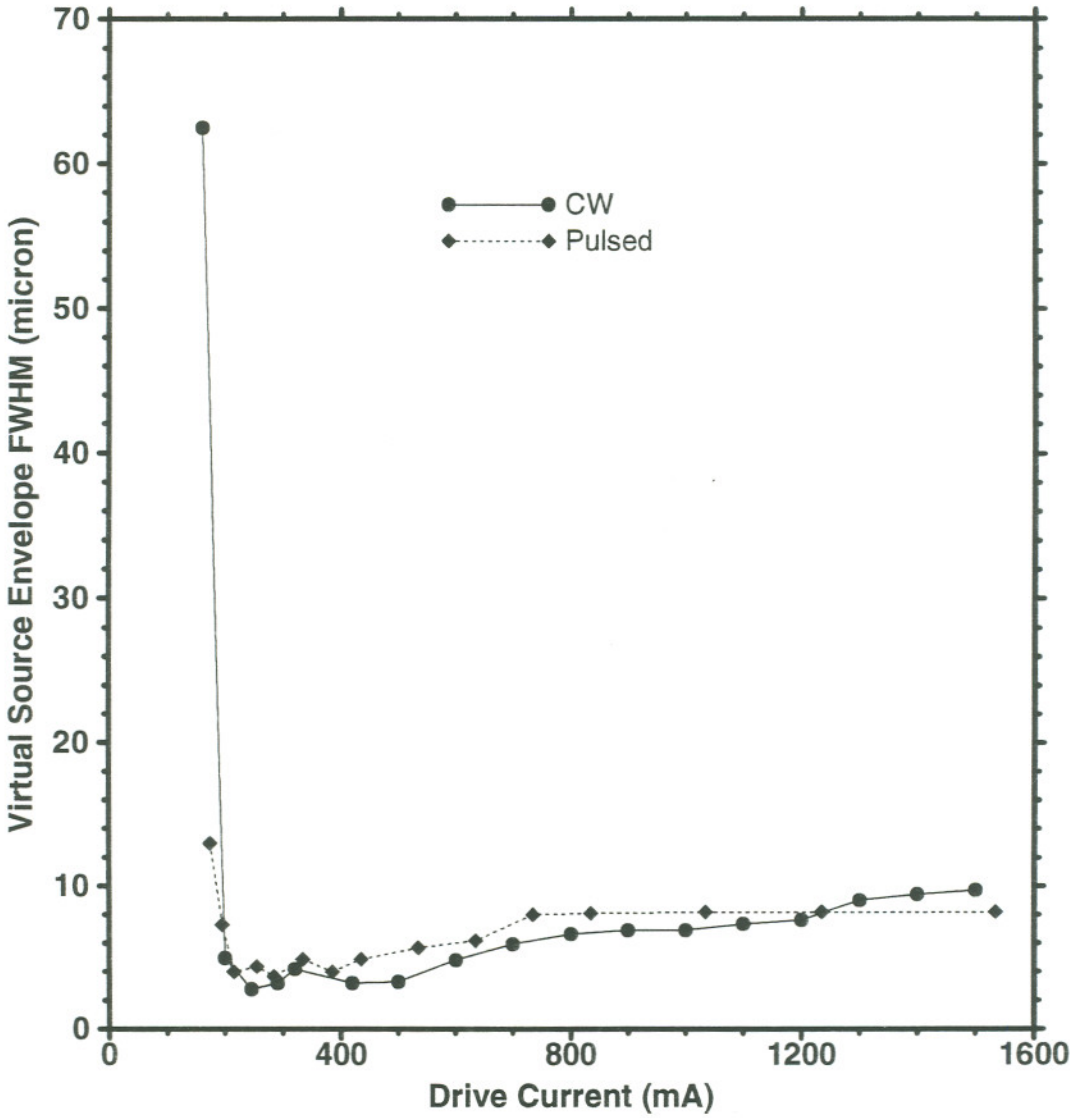

Figure 5.9 Virtual source envelope characteristics of an epi-down bonded 200 μm × 500 μm InGaAs URSL under CW and pulsed operation. I_{th} = 230mA for both pulsed and CW operation.

that thermal lensing effects are insignificant, at least for moderately high injection levels.

The URSL spectral characteristics were investigated for both below and above lasing threshold operation. Near-field spatio-spectral patterns[20] were recorded from the curved mirror side at various injection levels. Figure 5.10 shows half-tone pictures of the corresponding patterns at three different injection levels. At low injection levels, e.g., the case of $0.75 \times I_{th}$ shown in Figure 5.10a, all the longitudinal mode patterns appear as curved structures. As the pump level increases, the optical intensity in the central region — call it the core-region — increases relative to those in the side regions, as shown in Figure 5.10b for the case of $0.9 \times I_{th}$ injection level. For each curved pattern, there is a straight line extending out from the center, indicating that the side regions begin to spectrally lock to the core-region and form the unstable resonator modes. At threshold, as shown in Figure 5.10c, the straight line patterns extend over the whole stripe domain, and dominate in intensity. In other words, the whole URSL lases at the longitudinal mode wavelengths of the core-region. The curved spatio-spectral patterns shown in Figure 5.10 are characteristic of all URSLs we have studied. For pulsed operations with low duty cycles ($< 1.0 \times 10^{-4}$), the sub-threshold patterns might be too dim to record, depending on the sensitivity of the CCD camera used.

An unstable resonator may be viewed as a parallel combination of many narrow Fabry-Perot resonators, whose cavity lengths are determined by the mirror curvature and their lateral positions. By calculating and mapping the

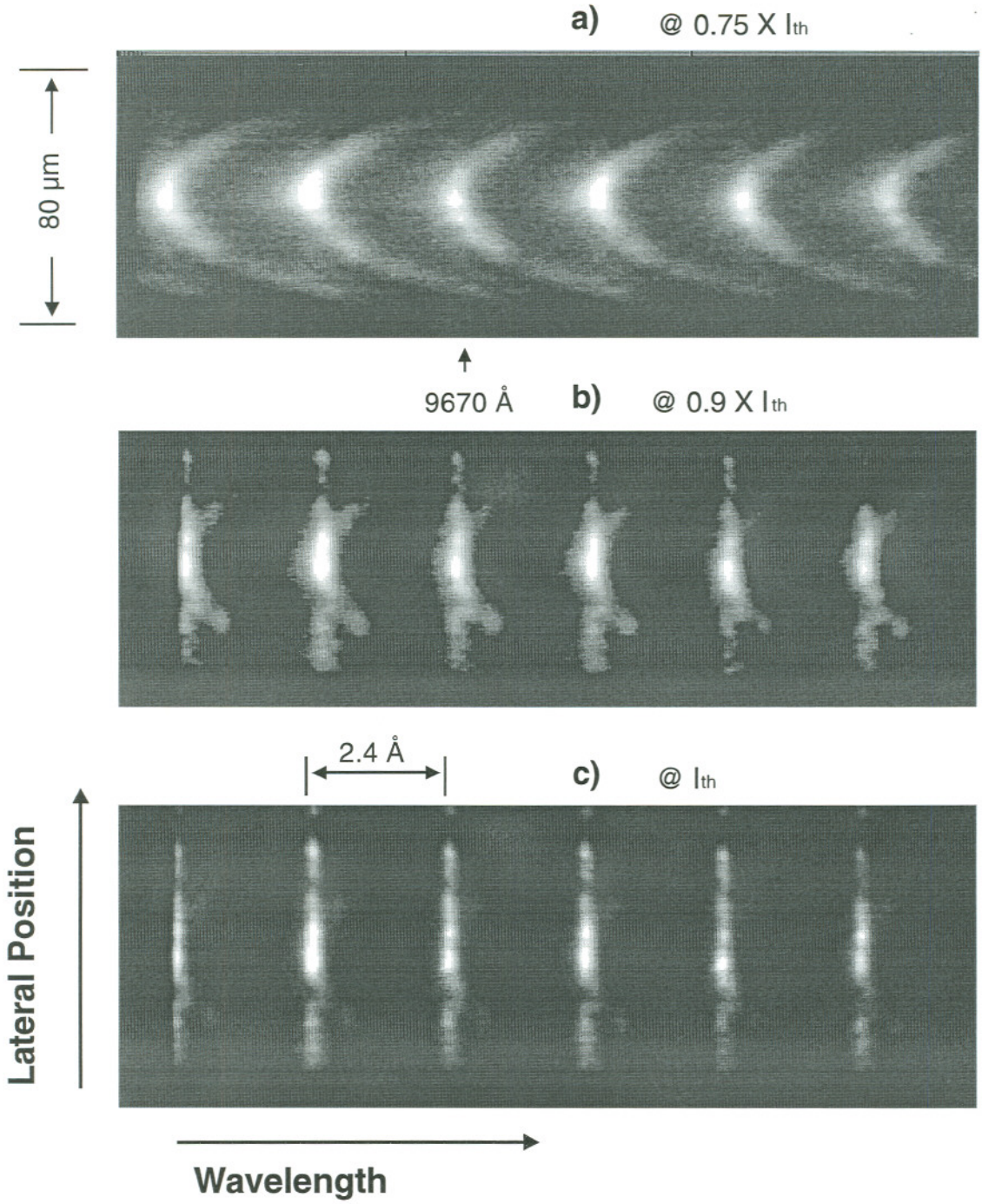

Figure 5.10 Spatio-spectral patterns of an InGaAs/AlGaAs URSL at three different CW injection levels, a) 0.75 I_{th}, b) 0.9 I_{th}, c) I_{th}.

wavelengths of the cold-cavity resonant modes for all of these narrow Fabry-Perot resonators, the curved patterns can be obtained, and fit very well to the experimental observations. Figure 5.11 shows the calculated spatio-spectral pattern for an URSL with the same geometrical structures as that of the CW URSL. Group index of 3.9, effective refractive index of 3.35, and wavelength of 0.97 μm were assumed in the calculation. The detailed algorithm derived for this simple calculation is presented in Appendix E.

A simple core-amplifier model is proposed to describe the evolution of URSL spatio-spectral patterns with injection current. The narrow, nearly flat, core-region forms a Fabry-Perot type master oscillator. When the injection level is far below threshold, both the core and side regions operate in local Fabry-Perot resonant modes. As the pump level increases, the core-region approaches threshold first. And the side regions effectively serve as amplifiers of the diffracted optical wave from this narrow core laser.

A more complex regenerative amplifier model[138] has also been proposed to numerically simulate these curved spatio-spectral patterns. In that analysis, an integral equation was set up between the field distribution at one end mirror and the field distributions inside the cavity, and solved using Neumann series expansion and numerical iterations. It was found that the calculated numerical results were in close agreement with our experimental observations.

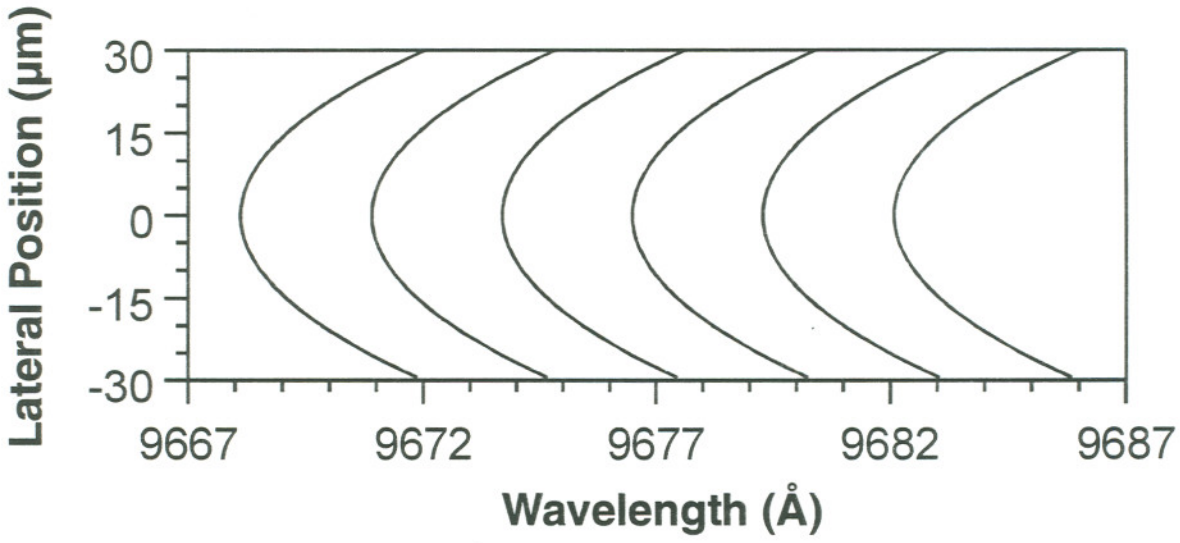

Figure 5.11 Calculated spatio-spectral patterns for the CW InGaAs/AlGaAs URSL (magnification = 2.5, μ = 3.35, μ_g = 3.9, λ = 0.97 μm). The patterns match closely those shown in Figure 5.10a.

5.5 URSL Near-Field Spatial Mode Patterns

The spatial characteristics of different lateral modes have been studied in their near-fields. Low magnification URSLs usually operate in a single lateral mode around threshold, e.g. the spatio-spectral pattern shown in Figure 5.10c. As the injection current reaches about two or three times threshold, each longitudinal mode splits into multiple lateral modes. The spatial profiles of the lateral modes usually differ from each other, and may change with increasing injection levels. The lateral modes keep broadening as the injection current further increases, and eventually fill the space between the adjacent longitudinal modes. The specific spatial profiles of individual lateral modes vary from case to case. Figure 5.12 shows two half-tone spatio-spectral patterns for a GaAs/AlGaAs SQW URSL with magnification of 2.5 and dimension of 200 μm $\times$ 350 μm. The first pattern shows single lateral mode operation at threshold. The second one shows three lateral modes operating around twice threshold. The separations between the lateral modes are larger than those of URSLs with slightly longer cavities, including the CW InGaAs URSL discussed earlier. It is not clear what mechanism contributed to this lateral mode separation.

For high magnification URSLs, the lateral mode behavior is more clearly recognized. At low injection levels, each longitudinal mode consists of only one lateral mode, although different longitudinal modes might still have different lateral intensity profiles. A group of longitudinal modes with similar lateral profiles can be separated from another group of longitudinal modes

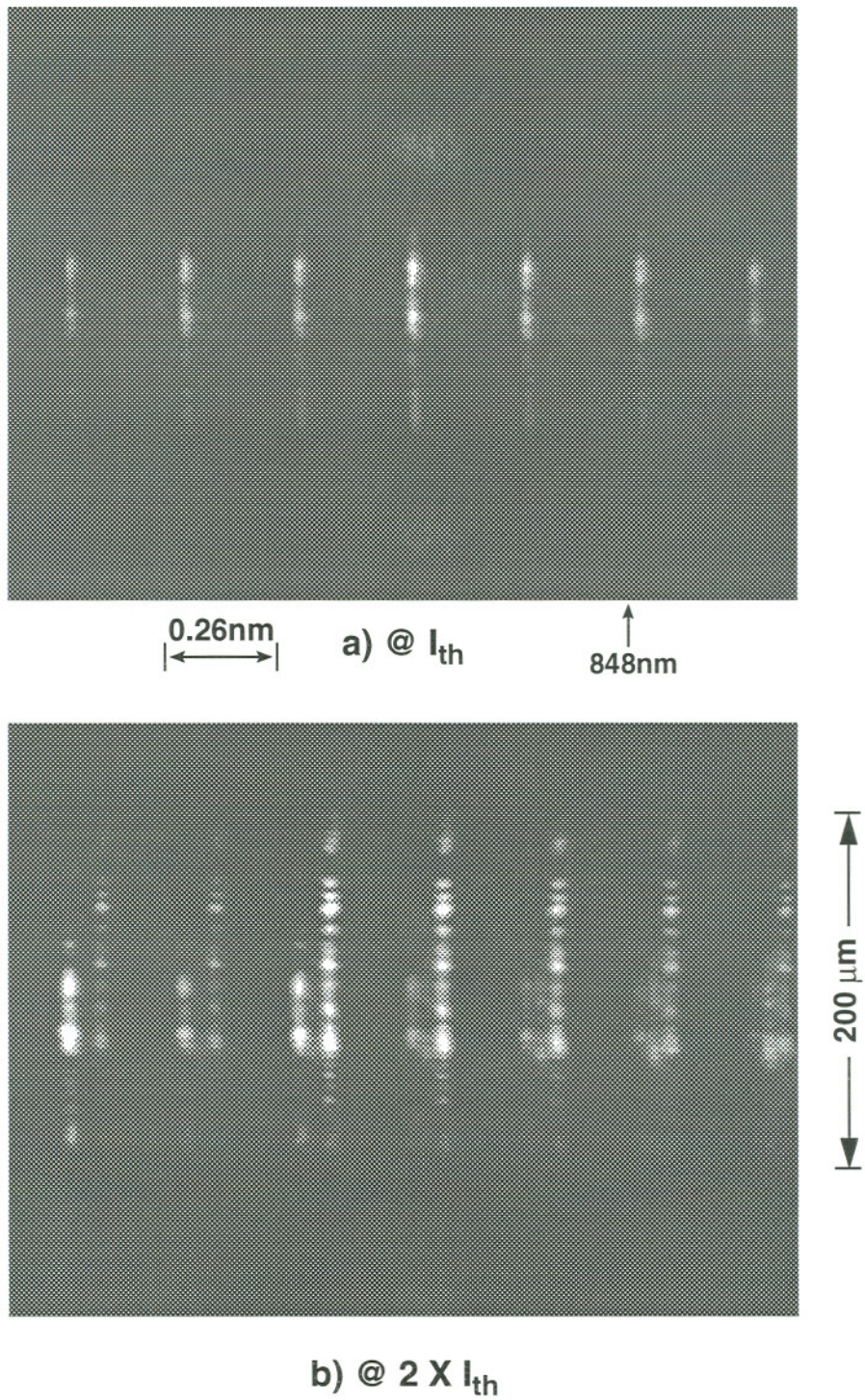

Figure 5.12 Spatio-spectral mode patterns of a GaAs/AlGaAs SQW URSL with 2.5 magnification and 200 μm × 350 μm dimension, a) at threshold, b) around twice threshold.

with different lateral patterns. As the injection current increases, each single longitudinal mode broadens, and the differences between the lateral profiles of different groups of modes become less obvious.

Interesting characteristics of the lateral modes were recorded for a InGaAs/AlGaAs GRINSCH SQW URSL with magnification of 6.0. Two obviously different groups of modes were observed for this device. Figures 5.13a and 5.13b show the half-tone pictures of the spatio-spectral patterns of two typical lateral mode bands at three times of threshold, respectively. Inside each band, all the different longitudinal modes have roughly same lateral profiles — with an intensity maximum in the center for the first band, and a minimum in the center for the second band. Rogers and Erkkila's numerical predictions[13, 139] showed that the near-field of the lowest URSL mode has the maximum intensity in its center, and that of a higher order URSL mode has either a null or a dip in the center. The separation between the centers of these two bands is about 50 Å at this specific injection level. The modes in the second band have shorter wavelength than those in the first band. Figure 5.14 plots the digitized data of the lateral intensity profiles of typical longitudinal modes in the two bands shown in Figure 5.13, respectively. The two curves more clearly show the differences between the two types of lateral modes. Neither of the two curves matches the near-field patterns described in section 5.2. However, they do look similar to some of the mode patterns observed for early high-power gas unstable resonator lasers.[140-143] As the injection current keeps increasing, the differences between the two bands become less

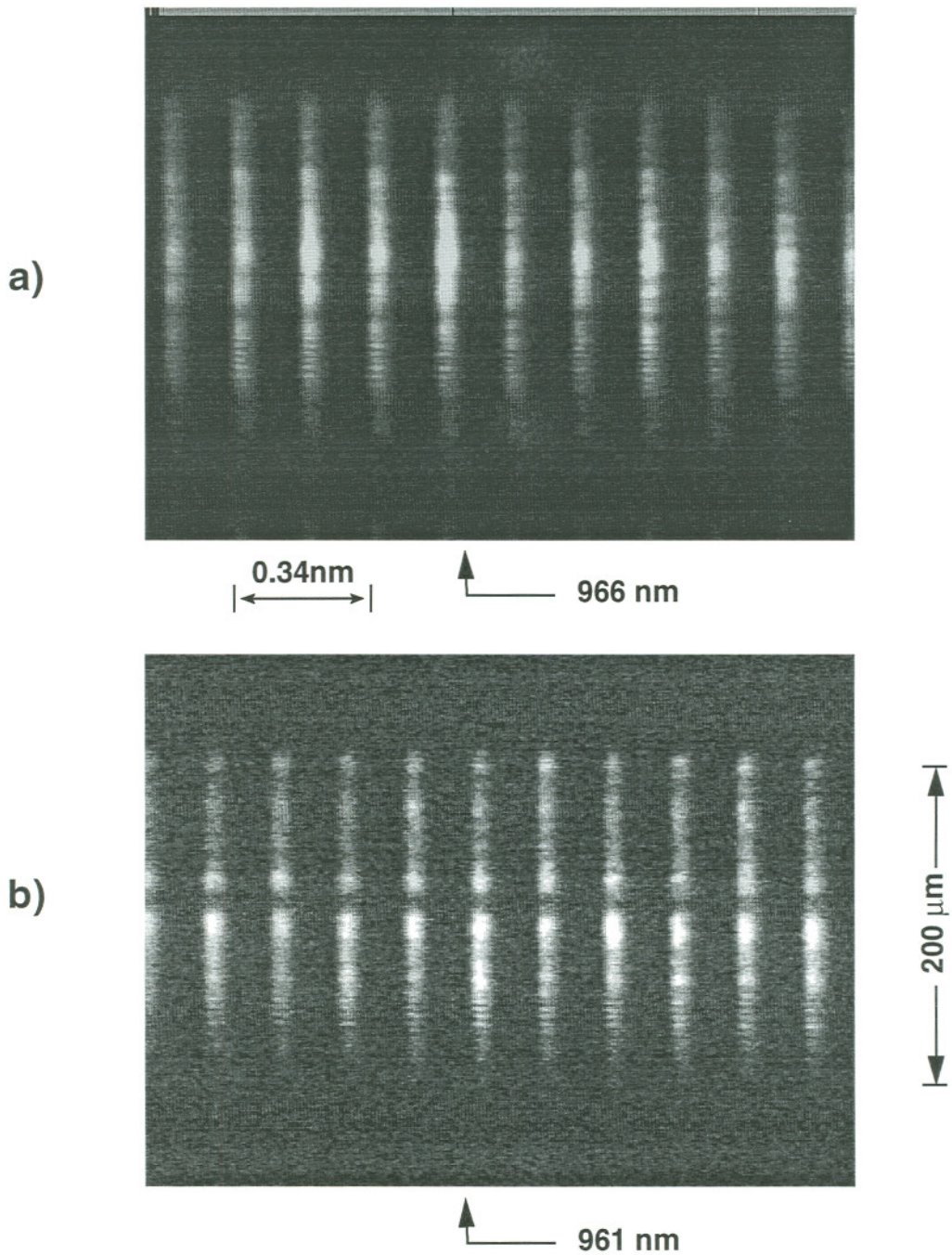

Figure 5.13 Two types of mode patterns observed for a high magnification (6.0) InGaAs/AlGaAs URSL at three times of threshold, a) first band, b) second band. Stripe dimension is 200 μm × 750 μm. Mode spacing = 1.7*angstrom*, center wavelength = 9640*angstrom*.

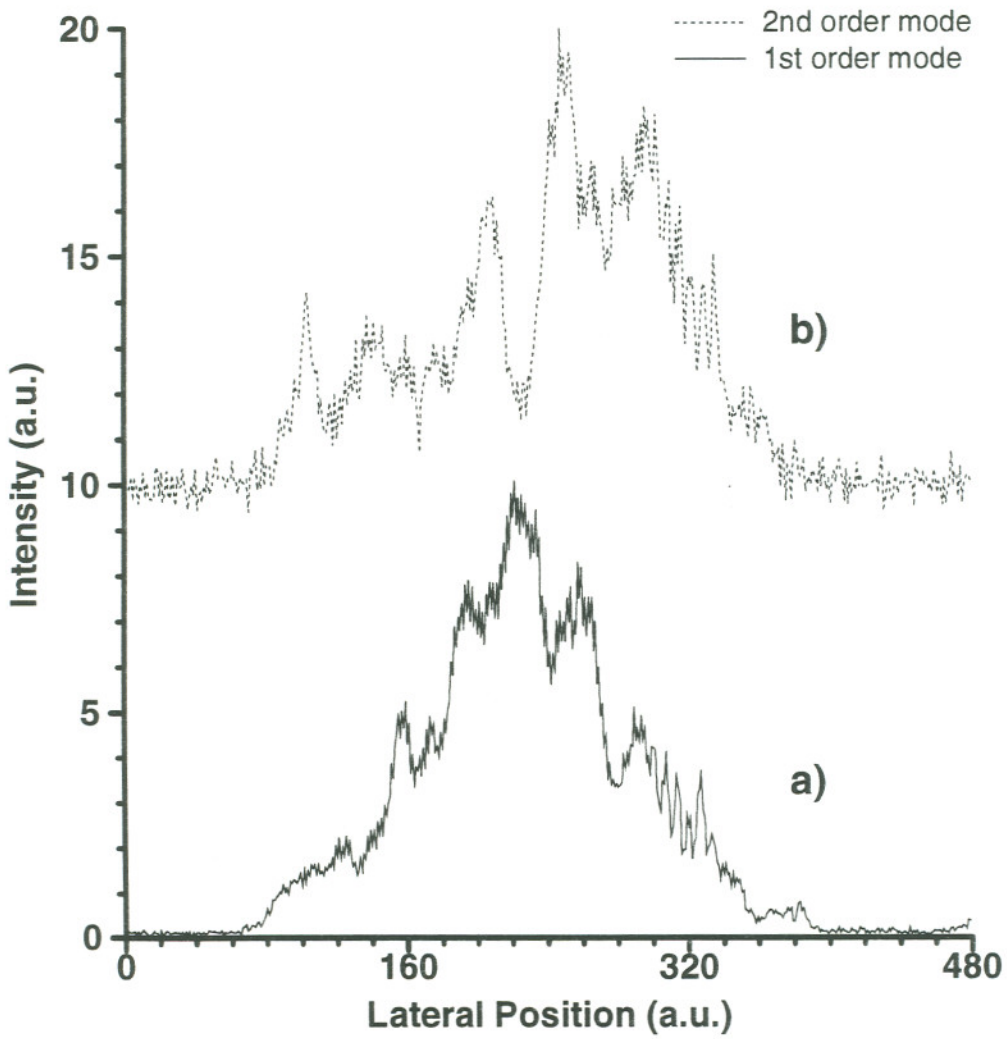

Figure 5.14 The curves showing the digitized spatial intensity distribution for the central portions of the two strongest spectral modes of the 6.0 magnification InGaAs URSL, a) one with maximum intensity in the center, b) the other with a dip in the center.

obvious. Figure 5.15 shows the spatio-spectral patterns of the two spectral bands at five times threshold. The spectral lines broaden significantly, and the spatial profiles of the two bands look more alike each other than those shown in Figure 5.13. At even higher injection levels, each individual spectral line broadens to such a degree that the spectral separation between adjacent modes is filled in a continuous pattern, e.g. the case of injection at ten times of threshold shown in Figure 5.16.

The spectra of two other InGaAs/AlGaAs GRINSCH SQW URSLs (with magnification of 4.0 and 5.0, respectively) were also studied, and found to be similar to each other. These two devices also lased in single lateral mode at injection levels of a few times of threshold, and total optical output power levels up to 2 Watts. But the linewidth of each mode increased more rapidly with increasing current than that of the 6.0 magnification URSL. In the whole lasing spectral regime, all modes had almost identical lateral profiles. And the lateral mode profiles changed very slightly with increasing current. The power efficiencies of these high magnification URSLs are smaller than those of devices with 2.5 magnification.

5.6 Temporal Dynamics

The temporal characteristics of URSL optical output beams, during pulsed operation, were studied using a Hamamatsu streak camera by focusing the near-field or virtual source onto the entrance slit of the camera. After the turn-on relaxation oscillation, which is always visible from both the near-field and virtual source of every URSL, devices show a variety of

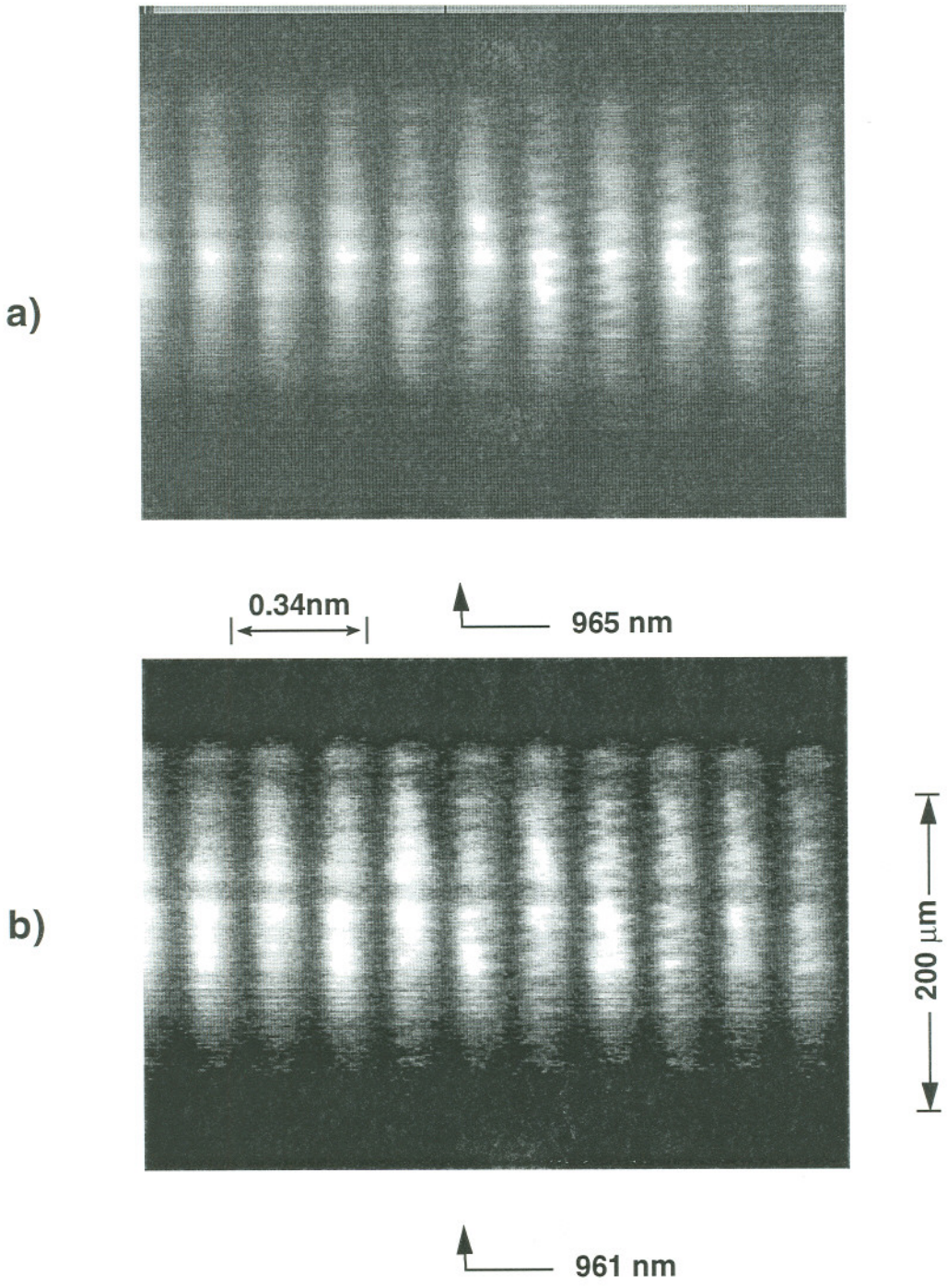

Figure 5.15 Spatio-spectral patterns of the two spectral bands of the high magnification URSL at five times of threshold, a) first band, b) second band. The spectral and spatial scales are the same as in Figure 5.13.

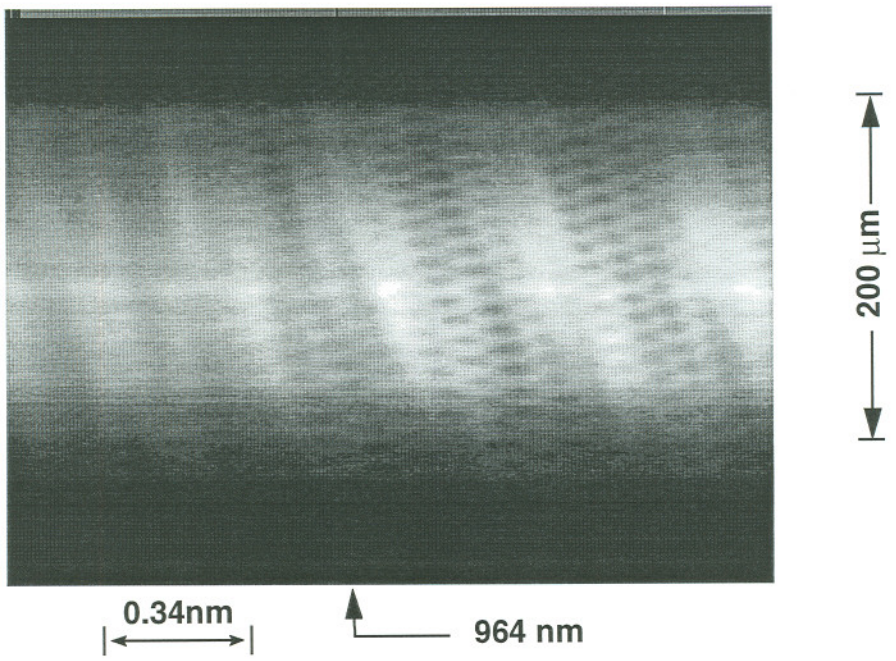

Figure 5.16 Spatio-spectral patterns of the high magnification InGaAs/AlGaAs URSL at ten times threshold - almost continuous spectral structure. The spectral and spatial scales are the same as in Figure 5.13a.

behaviors. Very stable, uniform temporal behavior has been observed for some URSLs. However, many other devices showed very erratic temporal patterns.

The stable streak traces of a 200 μm × 500 μm GaInP/AlGaInP URSL with 2.5 magnification are shown in Figure 5.17. The first two half-tone pictures (Figures 5.17a and 5.17b) correspond to the first several nanoseconds of temporal traces of the virtual source at injection levels of threshold and twice threshold, respectively. Similar to the observations from virtual source size measurements, the operation at twice threshold gave a wider trace than that around threshold. However, both traces show stable patterns. Figure 5.17c shows the first several nanoseconds of temporal trace of the near-field (at $2\times I_{th}$), which also has a stable pattern. This stable behavior was found to continue along the whole course of injected current pulses. In contrast, the traces of a 400 μm × 1000 μm InGaAs/AlGaAs URSL in Figure 5.18 show erratic patterns. Figure 5.18a is the temporal evolution of the virtual source, and Figure 5.18b is that of the near-field at an injection level of twice threshold.

The power spectrum[50] of those two URSLs were also recorded, and plotted in Figure 5.19, and 5.20, respectively. The curves were obtained by averaging the discrete Fourier transform (DFT) of 20 streaks of 5.8 ns length taken at 20 ns after the initiation of lasing. The two curves shown in Figure 5.19 for the GaInP/AlGaInP URSL exhibits no significant features at frequencies higher than 2 GHz. Spectra for the 400 μm × 1000 μm InGaAs/AlGaAs URSL show only frequency features around relaxation resonance peak,

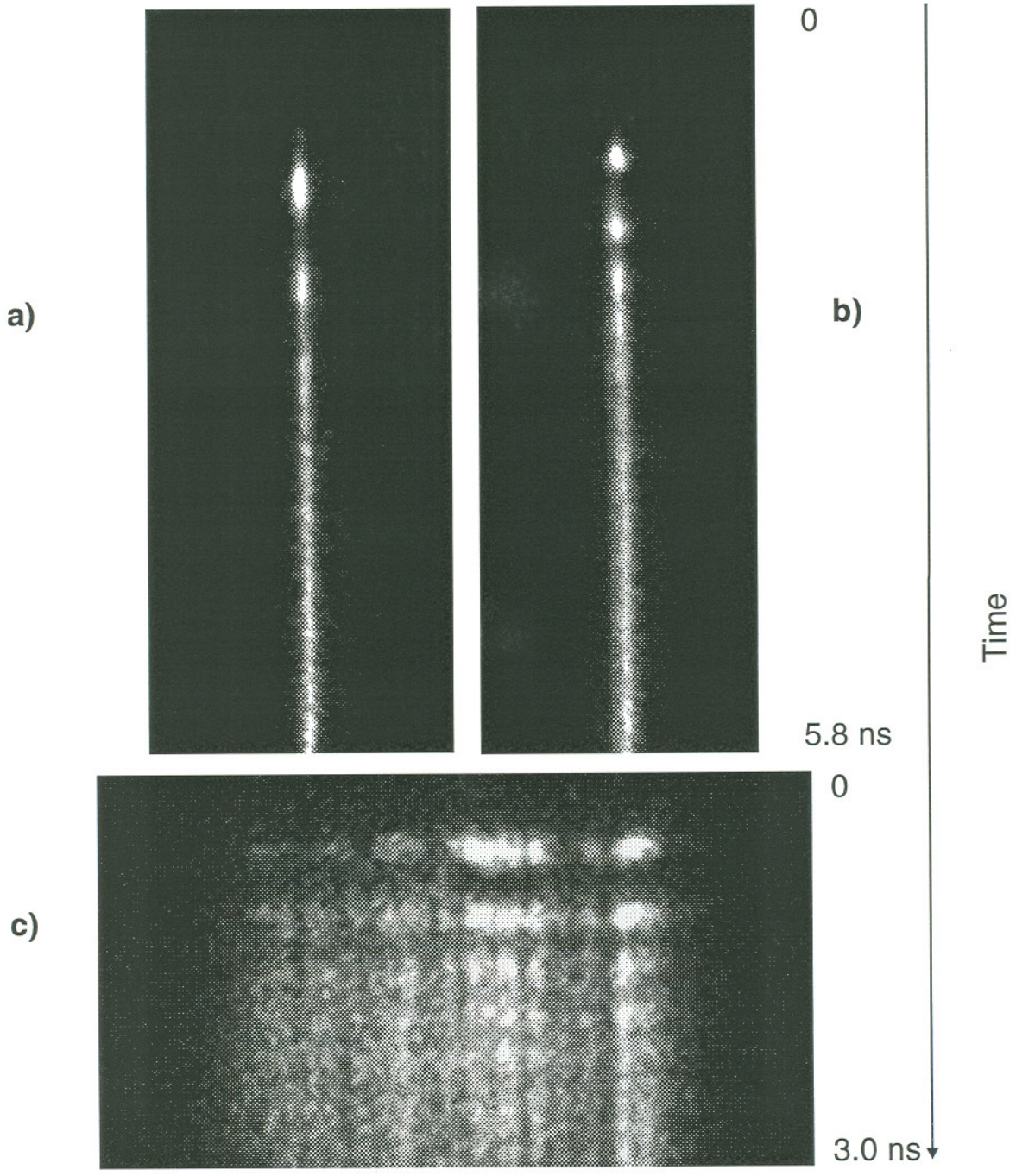

Figure 5.17 Half-tone pictures showing the turn-on characteristics of the output from a 200 μm × 500 μm GaInP URSL, a) virtual source trace slightly above threshold injection level, b) virtual source trace at twice threshold injection, c) near-field trace at twice threshold injection.

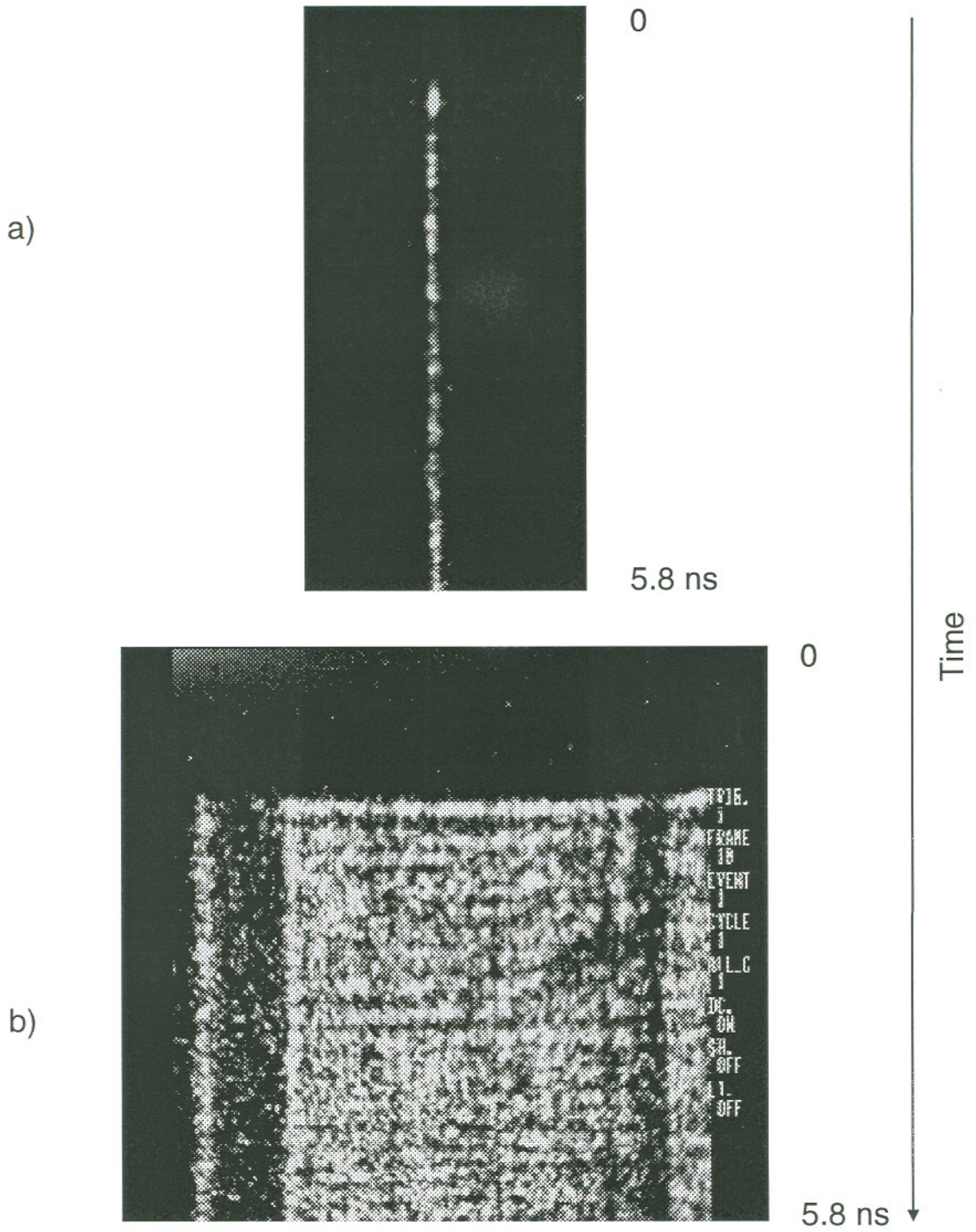

Figure 5.18 Half-tone pictures showing the turn-on characteristics of the output from a 400 μm × 1000 μm InGaAs URSL, a) virtual source trace at twice threshold injection, b) near-field trace at twice threshold injection.

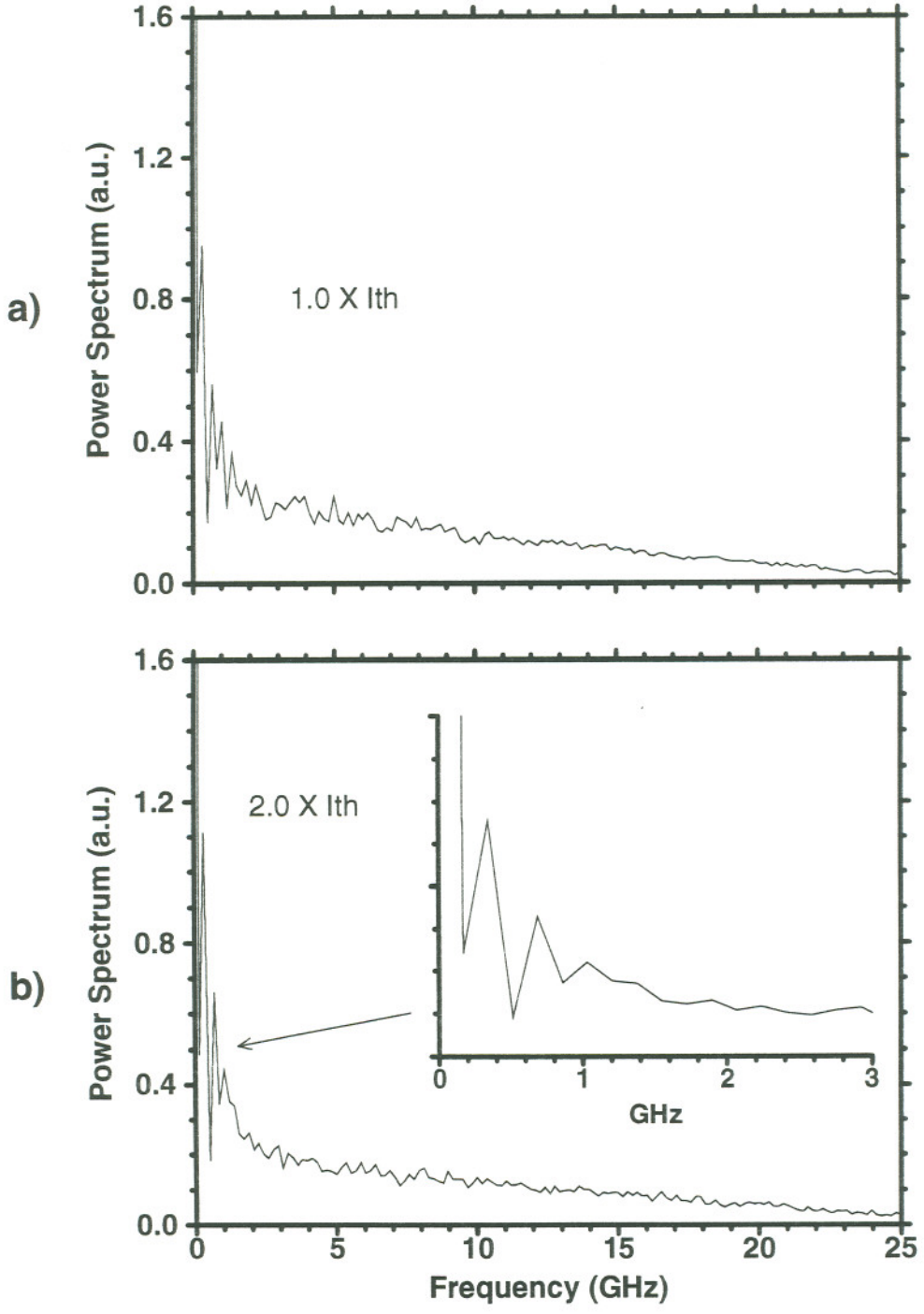

Figure 5.19 Averaged power spectrum recorded for the virtual source of a 200 μm × 500 μm GaInP URSL, a) around threshold, b) at twice threshold. The inset shows the beginning part of spectrum b).

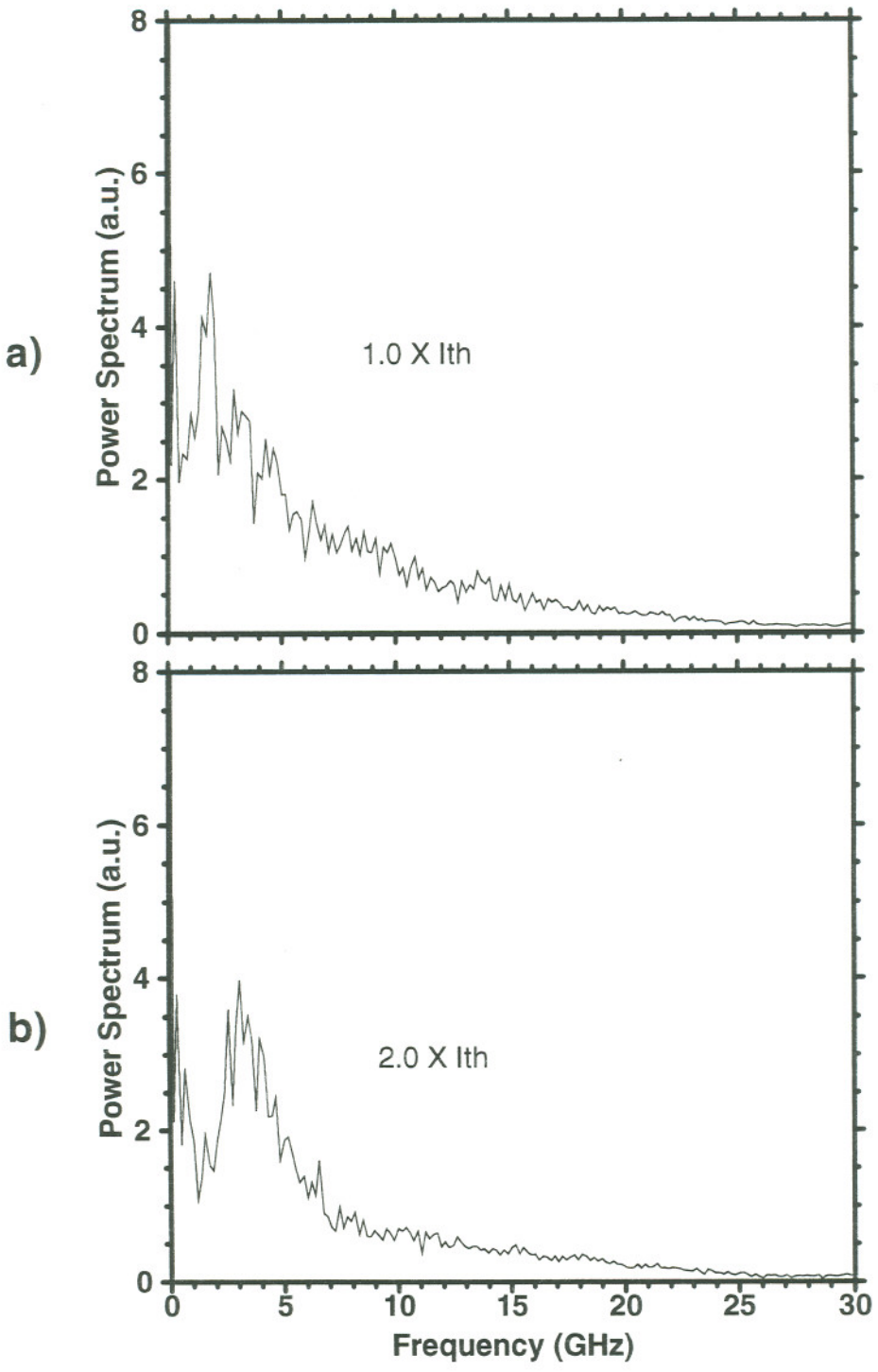

Figure 5.20 Averaged power spectrum recorded for the virtual source of a 400 μm × 1000 μm InGaAs URSL, a) around threshold, b) at twice threshold.

which is in the range of 2 ~ 5 GHz depending on the injection level.

The virtual source formation and temporal evolution also indicates the stability of the URSL mode phase-front. Examples of the time evolution trace can be seen in Figure 5.17a, the temporal trace of the virtual source for the stable 200 μm × 500 μm AlGaInP URSL, and in Figure 5.18a for the 400 μm × 1000 μm AlGaAs URSL. As the time evolves, the position of the virtual source shown in Figure 5.18a keeps bouncing slightly back and forth along the lateral direction. Considering the measured small source width for the former, and the large width for the latter, it is reasonable to attribute the widening of virtual source to the modal dynamic characteristics. It is not clear yet what mechanisms control the erratic mode characteristics. As discussed in the last two sections, virtual source broadening behavior is associated with multiple spatial mode operation and/or spectral broadening of a single spatial mode. The erratic evolution trace of the virtual source shown in Figure 5.18a may suggest that there is lateral mode competition.

Figure 5.21 shows the virtual source formation of a 400 μm × 1000 μm InGaAs/AlGaAs URSL at a high temporal resolution. The resonator magnification of this URSL is about 3.2. The virtual source formation time is less than the time to the relaxation peak (≤ 70 picosecond), and indicates that the circular wave-front is fully established in the first several round-trips. According to early theoretical analysis, the number of round-trips for virtual source formation N_{rt} is approximately expressed as[13, 144]

$$N_{rt} = ln(a^2/L\lambda)/ln(M), \tag{5.2}$$

where a is the laser output aperture width, L is the resonator length, M is

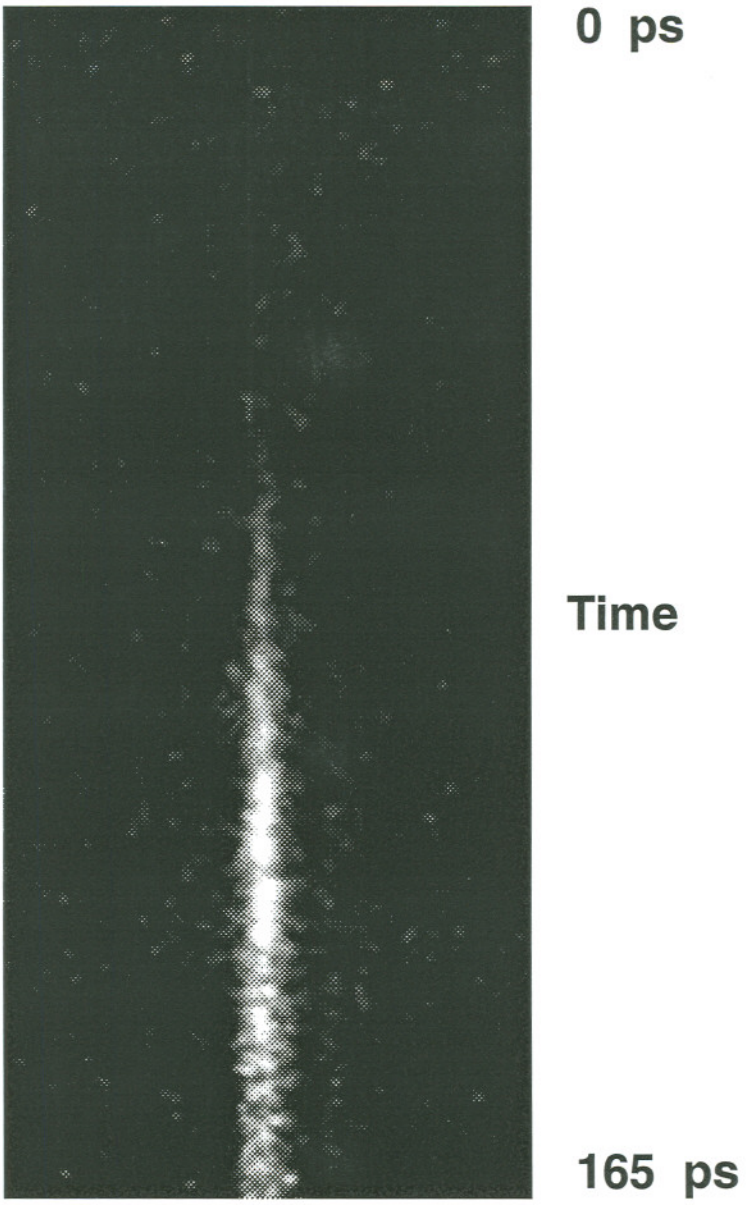

Figure 5.21 Half-tone picture of the virtual source formation process of the 400 μm × 1000 μm InGaAs URSL at high temporal resolution scale with twice of threshold injection.

the resonator magnification. The calculated value of N_{rt} for the 400 μm × 1000 μm InGaAs URSL is about 4.4, which corresponds to a time of 100 picoseconds. The calculated value is much larger than that of our measurement.

5.7 Effects of Mirror Wall Tilt

Non-zero wall tilt angle of an FIBM cylindrical mirror could lead to decreasing mirror reflectivity and increasing URSL lasing threshold. To investigate the direct effects of this tilt angle, URSLs were purposely fabricated with several degrees of mirror wall tilt. To minimize the experimental error in measuring FIBM mirror tilt angles, three InGaAs/AlGaAs devices on the same wafer bar were selected for this study. Each device has a dimension of 200 μm × 500 μm.

To measure its tilt angle, a mirror surface was first viewed from a direction perpendicular to the originally cleaved facet to determine its wall height. Then, the mirror was viewed from top of the wafer, i.e., perpendicular to the metal plane, to determine the mirror wall width. The tilt angle can be calculated from the mirror wall width and wall height. With the same wall height, the larger the tilt angle, the larger the wall width. More detailed description can be found in an early publication.[126] The FIBM mirror tilt angles were measured to be 1.0°, 2.9°, and 7.5° for the three URSLs, respectively. The L-I curves were recorded both before and after the fabrication of the mirrors, and plotted in Figure 5.22a (FPSLs) and 5.22b (URSLs), respectively. The FPSLs had comparable L-I performances. For

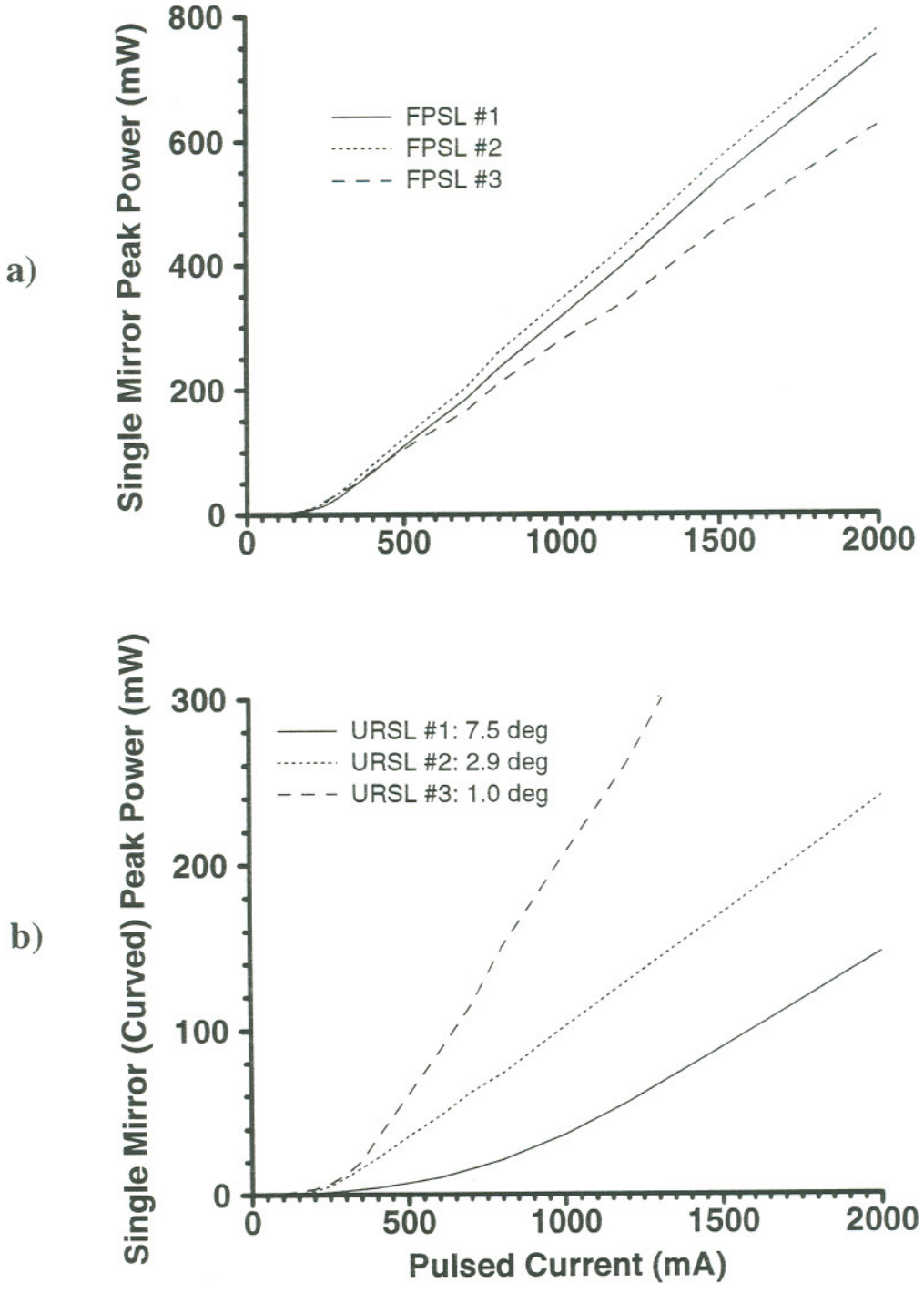

Figure 5.22 L-I curves of 200 μm × 500 μm InGaAs lasers, a) FPSLs, b) URSLs with curved mirrors having several different tilt angles.

URSLs, the one with large mirror tilt angle (7.5°), however, has a drastically increased threshold in comparison with the other two with smaller mirror tilt angles.

Assuming a Gaussian intensity profile for the optical output beam, the reflectivity can then be estimated using equation (4.7). Figure 5.23 plots the relative reflectivity (R/R_0) versus mirror wall tilt angle for three different transverse beam diverging angles (HWHM), where the modal refractive index was taken as 3.35. The curve obtained with 22° diverging angle (HWHM) is expected to match the case of InGaAs/AlGaAs GRINSCH SQW lasers, whose reflectivity almost drops to zero at a tilt angle around 8.0 degree. Smaller diverging angles give rise to steeper curves. The curve with 8.5° diverging angle (HWHM) corresponds to the case of GaAs/AlGaAs triplet GRINSCH SQW devices.

Substituting the material parameters in table 4.2 into equations (4.7) and (2.21), the dependence of threshold current density on the single mirror wall tilt angle can be calculated. Both measured and calculated J_{ur}/J_{fp} values are plotted versus mirror wall tilt angle in Figure 5.24. Both sets of data suggest that URSL performance may degrade significantly if the mirror wall tilt angle is larger than a few degrees. However, experimental data indicate that threshold current density of the URSL with 7.5° mirror tilt increases more than the calculated curve predicts. This discrepancy can be explained by the significantly increased resonator loss. Considering the reduced mirror reflectivity, as plotted in Figure 5.23, the resonator loss for an URSL with a 7.5° tilted mirror is estimated to be more than twice that of a 200 μm

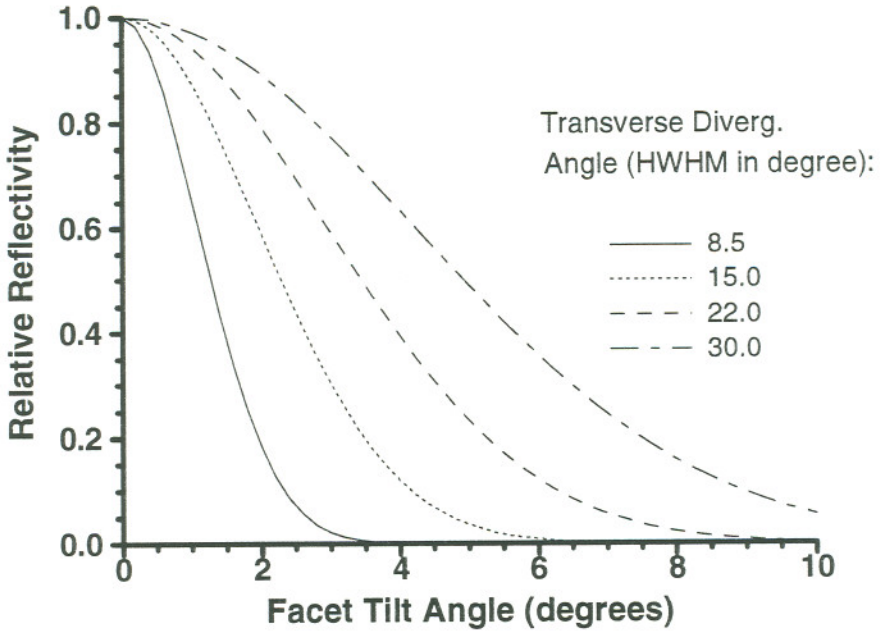

Figure 5.23 Relative reflectivity of a Gaussian beam versus the mirror tilt angle (μ = 3.35).

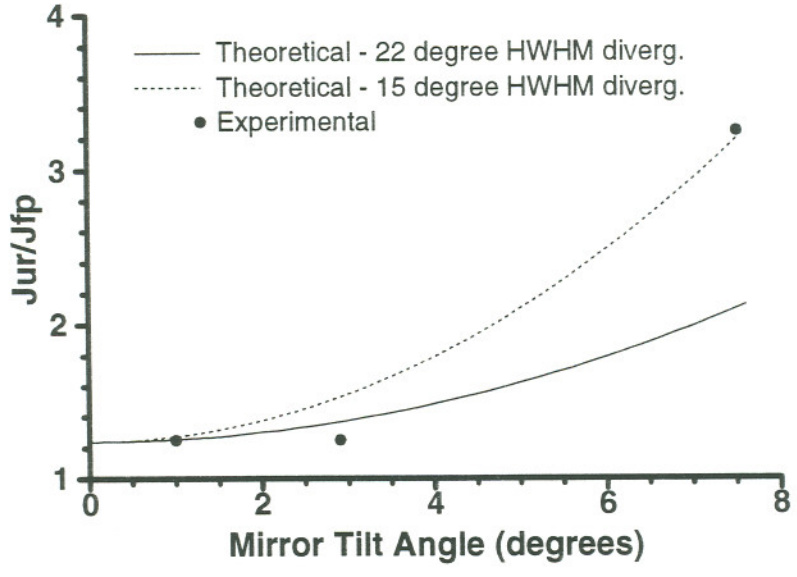

Figure 5.24 Mirror wall tilt angle dependence of threshold current density ratio (J_{th}^{ur}/J_{th}^{fp}) for 200 μm $\times$ 500 μm URSLs.

$\times$ 500 μm FPSL. In other words, the equivalent cavity length of that URSL is about 250 μm (i.e., half of the FPSL cavity length), and is close to, maybe shorter than, the optimum cavity length of the InGaAs quantum well material used. The associated gain characteristics, as mentioned in section 3.1, lead to the larger increase of threshold than that predicted by the simple geometrical URSL model. For comparison, the curve calculated by assuming 15° divergence angle (HWHM) is also plotted in Figure 5.24, and fits well to the experimental data point of 7.5° mirror tilt angle.

When these three URSLs were being fabricated, it was not desired to collect the light emission from the back (flat) mirrors. Therefore, the total power efficiency was not available.

Chapter 6

BRIGHTNESS, AND POWER CHARACTERISTICS OF HALF-SYMMETRIC URSLs

Half-symmetric unstable resonator semiconductor lasers (HS-URSLs) are the prototypes of positive branch URSLs and provide bright optical sources. The equivalent optical power densities of the virtual sources can be much higher than the limiting values causing material damage for both inside the cavity and at the mirror surfaces.[145] For FPSLs, in contrast, the near-field patterns at the facets have about the maximum brightness values achievable from the output beams. Ideally, if a FPSL and an HSURSL, having same device dimensions, operate at same diffraction-limited optical output power levels, the brightness values for the two devices are expected to be comparable. In reality, however, a FPSL is more vulnerable to high order lateral mode formation and filamentation effects than an URSL. The brightness values for HSURSL virtual sources can be much higher than those at the facets of practical FPSLs with same device dimensions. This unique characteristics of HSURSLs may lead to practical applications which have critical

requirements of high brightness optical beams. In the process of the current URSL program, both high optical output power and high virtual source brightness have been pursued. This chapter summarizes the power and brightness characteristics of HSURSLs.

6.1 Nominal Brightness of URSLs

The brightness of an optical source (or beam) is usually defined as[131]

$$Brightness = \frac{P_{op}}{AS_a}, \tag{6.1}$$

where P_{op} is the total output power, A is the light emitting area (or area of the cross section of the output beam), S_a is the solid angle extended by the output beam. The right side of equation (6.1) has also been defined as radiance in some text books.[146] For a semiconductor laser beam with its astigmatism corrected, the effective light emitting area can be defined as the product of the beam sizes (FWHM) along the two perpendicular directions, i.e.

$$A = h_{||}h_{\perp}, \tag{6.2}$$

where $h_{||}$ is the lateral virtual source size (FWHM), which can be directly measured, and $h_{\perp}$ is the transverse beam size (FWHM). $h_{\perp}$ can be calculated from the measured transverse beam divergence angle. The relevant formulae used for the calculation are presented in Appendix A. Equation (6.2) is used in this dissertation to approximate the emitting areas of URSL virtual sources, which are not corrected for their astigmatism. The solid angle can be approximated as

$$S_a = 2\theta_{||}\theta_{\perp}/\pi, \tag{6.3}$$

where $\theta_{||}$ is taken as the divergence angle extended from the virtual source to the laser stripe edge, and $\theta_{\perp}$ is the transverse divergence angle (FWHM).

For commercial applications, URSLs are expected to have one end mirror coated for high reflection (HR) and the other coated for low reflection (LR). The power characteristics from the LR coated mirrors are usually comparable to the total power characteristics of double-ended emission from URSLs with uncoated mirrors. In other words, the brightness value measured using the double mirror output power of an uncoated URSL is close to the brightness achievable from an HR/LR coated URSL, and can be defined as the nominal brightness of the uncoated URSL. For example, the 200 μm × 500 μm GaAs/AlGaAs URSL described in Table 4.4 gives a nominal brightness of 431 $MWcm^{-2}sr^{-1}$ at the injection level of 3.0 Ampere, which corresponds to a double mirror output power of 2.0 Watts.

For practical URSLs, one issue that may be raised is what effects, if any at all, the HR/LR coatings would have on the virtual source sizes. Unfortunately, we could not pursue the answer to this question due to the lack of coating facilities. On the other hand, as long as the effects are not significant, the concept of nominal brightness is always a reasonable measure for the brightness value achievable from an URSL.

6.2 GRINSCH SQW GaInP/AlGaInP URSLs

The threshold gain of an URSL with magnification M and cavity length L, as described in Chapter 2, is equivalent to that of a FPSL with shorter cavity length of L_{eq}. If L_{eq} falls below L_{opt}, the increased threshold gain of

an URSL will lead to a significantly higher threshold carrier density and a lower external differential quantum efficiency. To maintain good device performance, it is necessary to keep L_{eq} near L_{opt}. It was already found, in Chapter 4, that the L_{opt} is around 1000 μm for the GaInP/AlGaInP materials we used. In other words, URSL cavity lengths need to be longer than 1000 μm in order to achieve efficient optical output.

At the beginning of this URSL program, we fabricated[19] half-symmetric URSLs with magnifications of 2.0~3.0 on several GRINSCH-SQW materials using focused-ion-beam micromachining. The lasers were designed to have cavity lengths around 500 μm. For InGaAs/GaAs (970 nm)[19] and GaAs/AlGaAs (840 nm)[11] lasers, the threshold current density increased less than 15%, and slope efficiency dropped less than 25% as the result of machining the cylindrical mirrors. But for AlGaInP (660 nm) lasers, the threshold almost doubled, and the slope efficiency decreased more than 50%.

A set of five URSLs were fabricated from those Fabry-Perot AlGaInP lasers described in Chapter 3. The half-symmetric URSLs were designed to have a nominal magnification of 2.5. The performance of short cavity ($\leq$ 1000 μm) URSLs showed the same characteristics as in our earlier observations. For lasers with longer cavities ($\geq$ 1500 mm), however, the L-I and virtual source characteristics approached that of InGaAs/GaAs and GaAs/AlGaAs URSLs. After fabricating the cylindrical mirror, the threshold increased only slightly, and the external differential quantum efficiency dropped less than 25%. In Figure 6.1, the L-I curves of 1500 μm long lasers

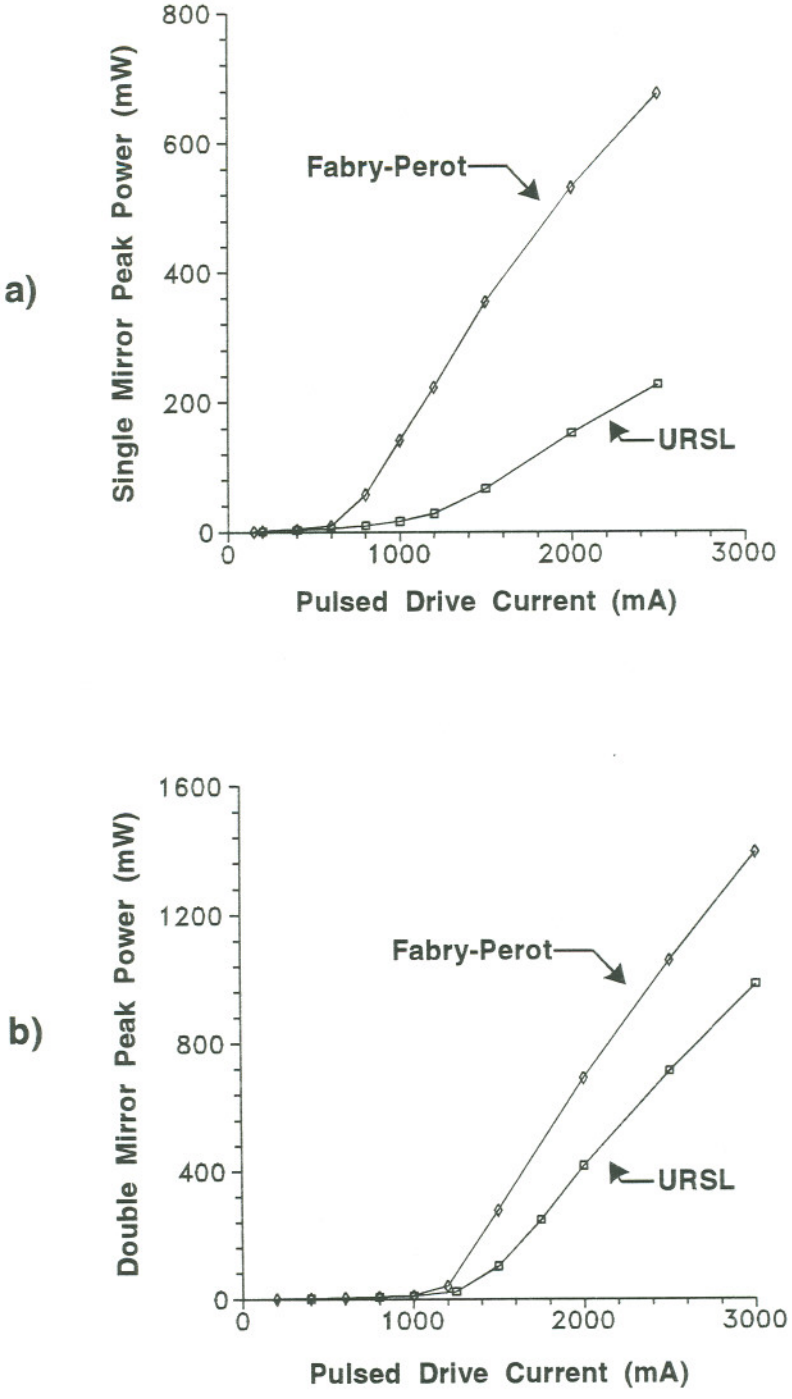

Figure 6.1 L-I curves for two GaInP/AlGaInP GRINSCH SQW URSLs of 2.5 magnification and with a) 300 μm × 500 μm stripe, b) 300 μm × 1500 μm stripe, respectively.

are shown in comparison with those of 500 μm long lasers. The external differential quantum efficiencies and threshold current density for these URSLs are also plotted versus cavity length in Figures 3.4a and 3.4b, respectively. In general, these results suggest that L_{opt} is around 1000 μm for this GaInP/AlGaInP SQW material.

Assuming an RMS surface roughness of 60Å for the FIBM AlGaInP mirror,[19] as discussed in chapter 4, the scattering coefficient S was calculated to be about 7%. The dashed line in Figure 3.4a shows the external differential quantum efficiency calculated from equation (2.23) by considering this mirror roughness and the material parameters. It fits well to the three points for long cavity URSLs. Both the 2500 μm long FPSL and URSL had slightly lower performance than the curves predicted, which may be caused by material nonuniformity. The threshold current densities for the URSLs were also calculated from equation (2.21), and were found to fit well to the experimental data for long cavity lengths in Figure 3.4b. As mentioned earlier, the derivation of the nominal threshold, expressed by equation (2.21), was based on the core-region.

The total power efficiencies of the URSLs were calculated according to equation (2.24) from their corresponding L-I data and measured sheet conductivity of the wafer material. For each URSL, there exists a peak value for the power efficiency. These peak values are plotted in Figure 6.2 versus URSL cavity length. The highest peak efficiency was obtained from the URSL with a cavity length of 1500 μm. The calculated L_{eq} of this URSL is about 1100 μm, which is comparable to the value of L_{opt}. The sheet

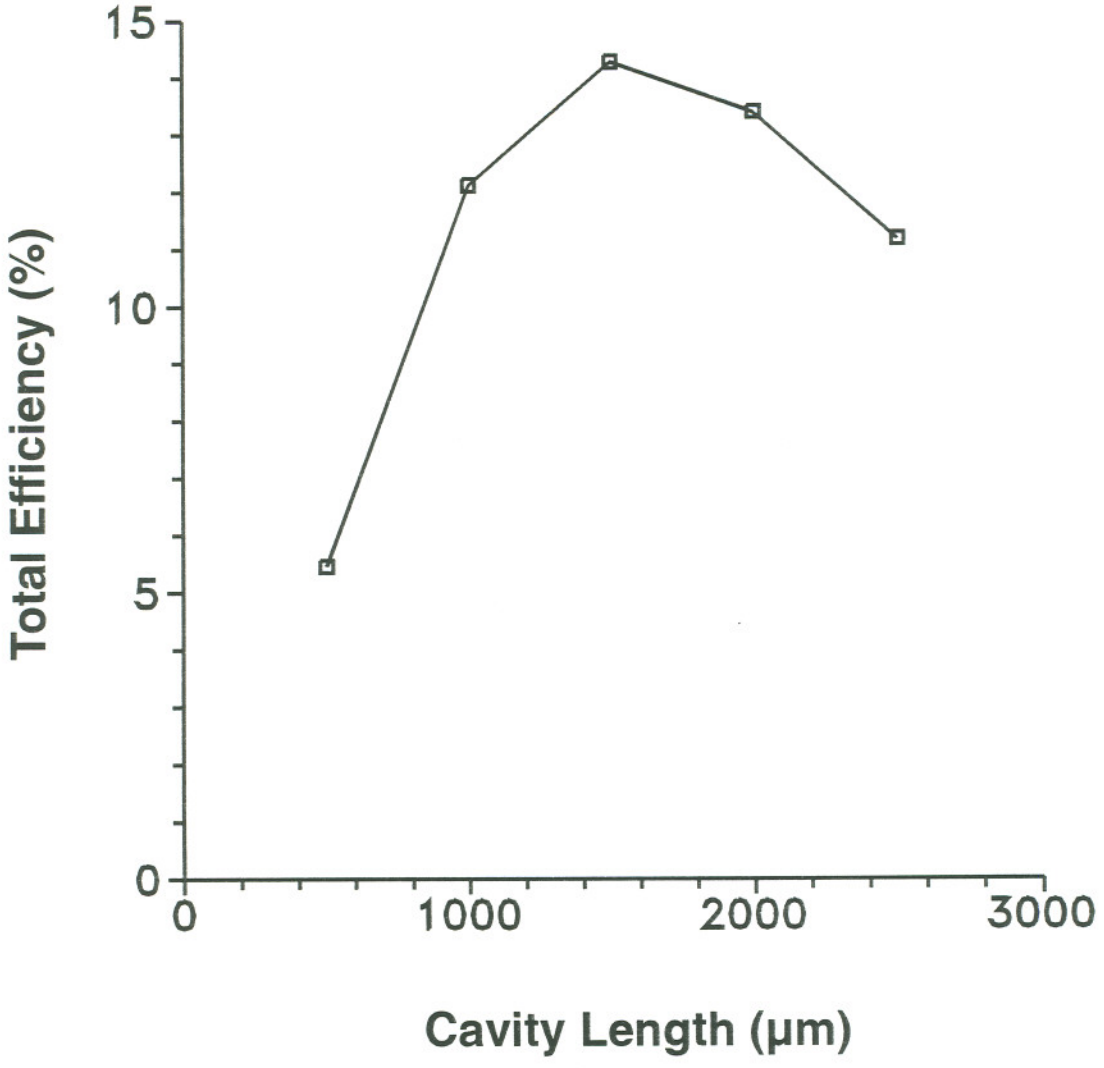

Figure 6.2 Peak power efficiencies versus the cavity lengths for the GaInP/AlGaInP URSLs.

conductivity of the wafer material was measured to be $1.1\times10^{3}\ \Omega^{-1}cm^{-2}$. Although it is more desirable to directly measure the power consumed by the whole device package when calculating the power efficiency, the power consumed by the heatsink and bonding layer usually varies from case to case, and complicates the analysis for the low resistance, broad-area laser structures described here.

For the 300 μm × 1500 μm URSL at 3000 mA — the highest current tested — the double mirror optical output power reaches 1 W, which corresponds to a nominal brightness of 320 $MWcm^{-2}sr^{-1}$.

6.3 GRINSCH SQW InGaAs/AlGaAs URSLs

URSLs with 2.5 magnification were also fabricated from the set of InGaAs/AlGaAs Fabry-Perot devices whose threshold and efficiency properties are summarized in Figure 3.6. The cavity length ranges from 500 μm to 1700 μm. URSL operating characteristics were measured, and shown in Figure 3.6 with filled square data points. The dashed curves shown in Figure 3.6 were calculated from equations (2.21) and (2.23) by considering the parameter values summarized in Table 3.2. Considering the wavelength difference, the surface roughness dependence of mirror reflectivity is less severe for these URSLs than for GaInP/AlGaInP ones. Furthermore, the mirrors fabricated from these InGaAs/AlGaAs devices are usually very smooth. So the FIBM mirror surface roughness effect was ignored in the calculations. Generally speaking, the theoretical curves fit well to the experimental data points.

A set of five InGaAs/AlGaAs FPSLs with same dimension of 200 μm × 750 μm were mounted and the pulsed L-I data were recorded. Five devices with comparable slope efficiencies and thresholds were then selected to fabricate half-symmetric URSLs. The resonator magnifications were chosen to be in the range of 2.0 to 6.0. Pulsed L-I data from the URSLs were collected from both of the front and back mirrors. The threshold current densities and external differential quantum efficiencies are calculated and plotted in Figures 6.3a, 6.3b, respectively. The threshold current density increases rapidly with increasing resonator magnification. The measured slope efficiency from the curved mirror decreases slightly with increasing resonator magnification, while that from the flat mirror decreases much more rapidly. The ratio between the slope efficiency from the flat mirror to that from the cylindrical mirror is defined here as *power symmetry*. The power symmetry values of these URSLs were plotted in Figure 6.3c. The data points show that the power symmetry value decreases as the magnification increases. With limited material resources, no attempt has been made to reproduce the performance of high magnification (> 3.0) URSLs.

Due to the smaller radius of curvature, cylindrical mirrors for a high magnification URSL has a large sag. For example, with 750 μm long cavities and 260 μm wide mirror apertures, the sag value is about 2.54 μm for an URSL with 2.5 magnification, and 11.83 μm for an URSL with 6.0 magnification. As discussed in chapter 4, the optimal FIBM scanning density is about 400 lines per micron. Since the maximum number of lines for the FIB milling region is about 3000, i.e., three quarters of the total number of lines

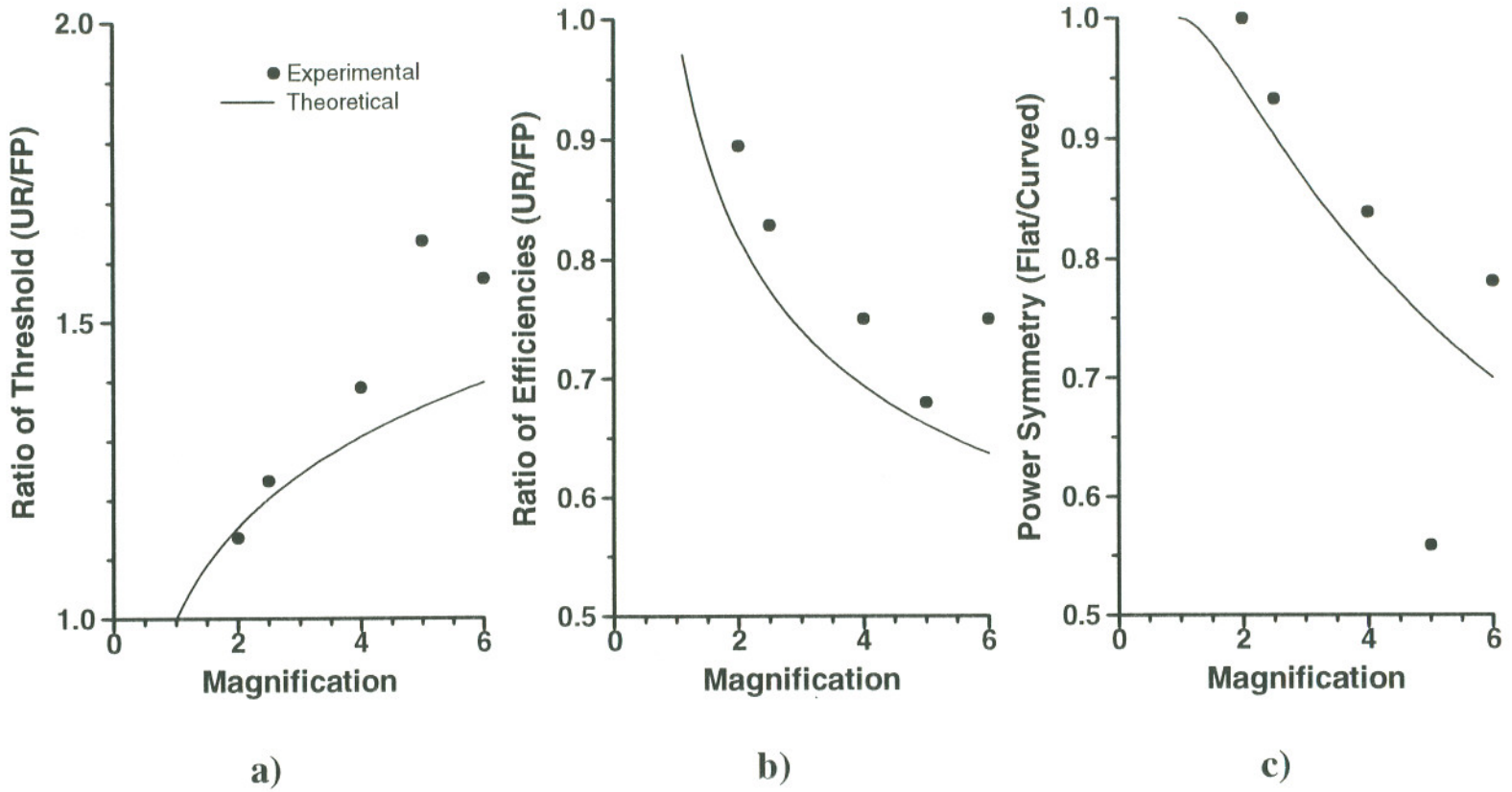

Figure 6.3 Resonator magnification dependence of the operating characteristics of the 200 μm x 750 μm InGaAs URSLs, **a)** ratio of the thresholds of URSLs to the original FPSLs, **b)** ratio of slope efficiencies, **c)** power symmetry.

available, the scanning resolution for the 6.0 magnification URSL would be lower than the optimal one. For that reason, the mirror surfaces of higher magnification URSLs looked slightly rougher under a scanning electron microscope (SEM), or even a high magnification optical microscope.

With the material parameters summarized in Table 3.2, numerical results were calculated from equations (2.21), (2.23), and (2.16'), and also plotted in Figure 6.3. Mirror roughness was ignored in the calculations due to the lack of relevant information for these InGaAs mirrors. Experimental data points for three low magnification URSLs agree with the numerical results in the general trend. However, the data points of the two high magnification (5.0 and 6.0) URSLs deviate obviously from the calculated curves. Those discrepancies may be caused by the stronger mirror surface roughness of the higher magnification URSLs. Stronger surface roughness would lead to higher lasing threshold. The equivalent cavity lengths of those two high magnification URSLs (about 448 μm and 428 μm, respectively) are still larger than the optimum cavity length of the InGaAs quantum well materials. Thus, cavity length shall not be a concern here. In general, the calculated total efficiencies are slightly lower than the measured values. These discrepancies may be attributed to the assumption, which was used in the calculations, of 100% loss for light escaped away from the gain region. Actually, the near-field profiles were found to be slightly wider than those of FPSLs, and wider than the metal stripes. When the measurements were done, some of the diffracted light was collected by the power meter, and led to higher efficiencies than the calculations. The measured power symmetry

values for the fabricated URSLs are also slightly higher than the calculated curves. Again, the ignored mirror surface roughness may be attributed to the deviations. Rough cylindrical mirrors would have lower output efficiencies than the perfect ones assumed in the calculation.

Figure 6.4 shows the L-I curves of the URSL with a resonator magnification of 6.0 and its original FPSL. The two L-I curves from the front (curved) and back (flat) mirrors give the same threshold, and have smaller slope efficiency than the original FPSL. The power symmetry can be obviously seen from the difference of the slopes of these two curves.

Figure 6.5 shows the L-I curve of a 200 $\mu m \times 500\ \mu m$ URSL with 2.5 magnification under CW operation. The threshold current density is 240 A/cm^2, which is about 20% larger than that of a typical cleaved facet FPSL from the same wafer.[12] The total output power increases almost linearly up to 1.2 W at an injection level of 2.0 A, which is the highest drive current level tested. Its peak external differential quantum efficiency is 50%, and peak power conversion efficiency is 30%. The nominal brightness value at the high injection level is about 92 $MW/cm^2\text{–}sr$.

6.4 GRINSCH SQW GaAs/AlGaAs Triplet "Manifold" URSLs

The GaAs/AlGaAs triplet manifold material has also enabled the fabrications and operations of high performance URSLs. The large bandgap offset of the GaAs/AlGaAs GRINSCH structures and the multiple active layers contribute to its relatively small optimum optical cavity length ($< 300\ \mu m$).

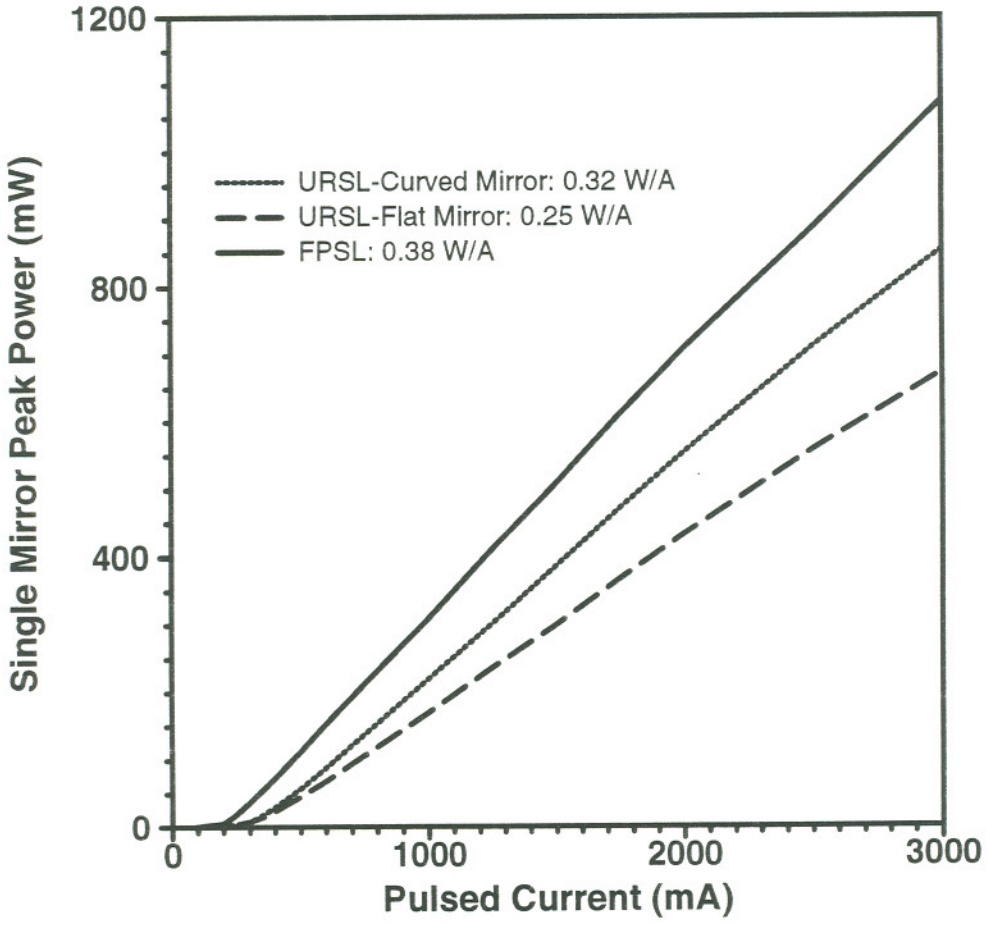

Figure 6.4 L-I curves of lasers with dimension of 200 μm × 750 μm; the URSL has a magnification of 6.0.

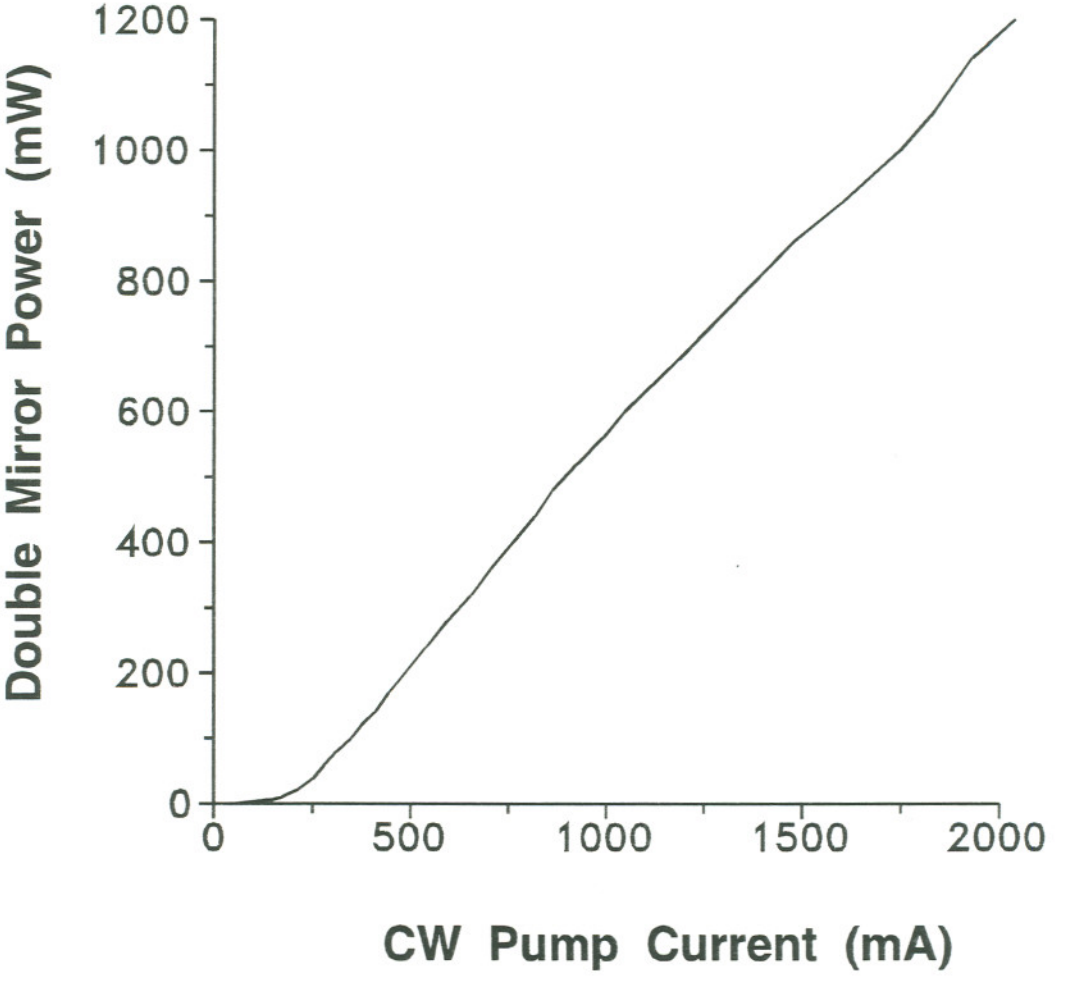

Figure 6.5 L-I curve of a 200 μm × 500 μm InGaAs URSL under CW operation.

The devices were tested under pulsed operations with 200 ns pulse width, and 1 kHz pulse repetition rate. For a typical 500 μm long URSL with a smooth cylindrical mirror and magnification around 2.5, both its threshold and slope efficiency are very close to their counterparts of the FPSL. The virtual source width usually increases less than 50% as the injection current increases from threshold to six times threshold. Figure 6.6 shows the L-I curves of a 200 μm × 500 μm URSL with magnification 2.5 and the original FPSL. The total double mirror peak power output of the URSL was about 2.0 Watts at an injection level of 3000 mA. The virtual source width of that URSL was plotted versus injection current in Figure 5.8. The virtual source stays in the range of 1.8 ~ 2.7 μm for lasing operations up to $6.0 \times I_{th}$, which is highly desirable for high power applications. The lateral brightness for that URSL is calculated to be as high as 10 kW/cm-rad, which is attributed to the small lateral virtual source width at high output power levels. The nominal source brightness is estimated to be about 431 $MWcm^{-2}sr^{-1}$ for that particular URSL at an injection level of 3000 mA.

Due to the limited amount of material available, the investigations of the cavity length dependence, resonator magnification dependence, and the dynamic characteristics were not pursued.

6.5 Discussion

The parameters describing the output beam characteristics are summarized in Table 6.1 for several typical URSLs. The nominal brightness values are calculated for all these devices using equations (6.1) — (6.3). Up to the

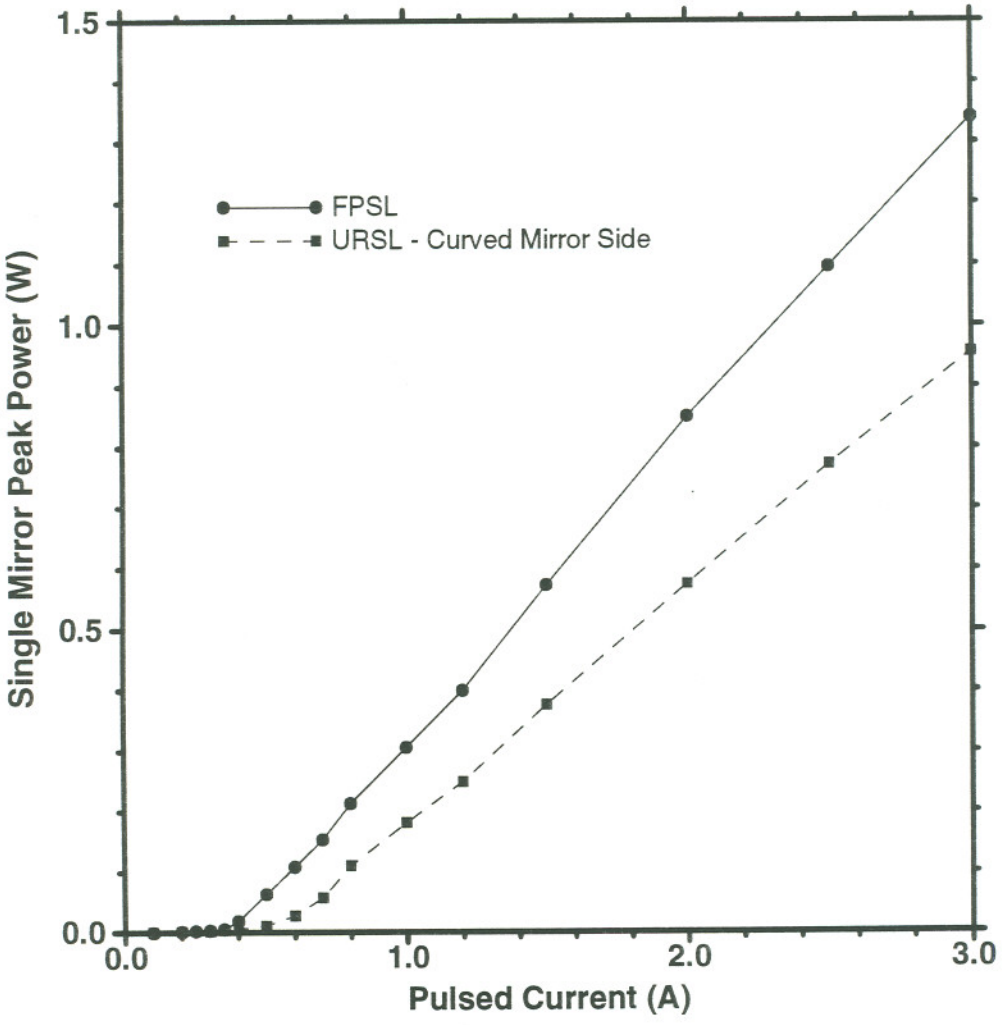

Figure 6.6 L-I curves of a 200 μm × 500 μm GaAs/AlGaAs triplet SQW URSL and the original FPSL. Magnification = 2.5.

Table 6.1 Summary of FIBM URSL results and comparison with some commercial devices

Material/ Device ID	Structure/ Comment	λ	Operation mode	FWHM Spot size	FWHM Diverg.	FWHM Spot size	Full Diverg.	Maximum Power	**Lateral Brightness**	**Brightness**
		μm		μm	degrees	μm	degrees	Watts	**$kWcm^{-1}rad^{-1}$**	**$MWcm^{-2}sr^{-1}$**
GaInP/ AlGaInP	GRINSCH -SQW	0.66	Pulsed	0.36	44	5.3	18	0.92	**5.5**	**323**
GaAs/ AlGaAs	Triplet GRINSCH SQW	0.84	Pulsed	1.24	17	2.7	42	2.00	**10**	**431**
InGaAs/ GaAs	GRINSCH -SQW	0.97	Pulsed	0.53	44	15	44	6.0	**5.2**	**201**
InGaAs/ GaAs	GRINSCH -SQW	0.97	CW	0.53	44	9	32	1.20	**2.4**	**92**
							FWHM Diverg.			
SDL5762*#	MOPA	0.98	CW	2500	0.06	2500	0.06	0.75	**3.0**	
SDL2480*	Arrays	0.81	CW	1	40	500	10	3.00	**0.3**	
SDL5410*	Diffraction -limited	0.83	CW	1	30	3	10	0.10	**1.9**	
SDL2370*	High Brightness	0.81	CW	1	30	200	10	2.00	**0.6**	
LD324Z**	High Density	0.81	CW	1	30	200	10	1.80	**0.5**	

(1) **Lateral Brightness** = Power/(lateral spot size)/ (lateral FWHM Divergence angle in Radians)
(2) **Brightness** = Power/(multiplication of spot sizes)/(solid angle extended by the beam)
(3) Double mirror optical power used here and for nominal brightness calculations.
(4) FWHM approximates the lateral full beam divergence angles.
* Data taken from Spectra Diode Labs catalog.
# Collimating optics was used in the output end.
** Data taken from SONY Advanced information data sheet.

tested injection levels shown in the table, the GaAs/AlGaAs GRINSCH SQW triplet URSL gives the highest brightness — 431 $MWcm^{-2}sr^{-1}$. The CW operated InGaAs/GaAs GRINSCH SQW URSL has the lowest brightness. Since none of these devices were driven hard enough to reach the COD limit, higher power and brightness values are expected to be achievable from all of them by going to higher current levels.

Values of lateral brightness were also calculated for the four particular URSLs and five Fabry-Perot type of commercial devices, and included in Table 6.1. Again, the GaAs/AlGaAs SQW triplet URSL gave the highest lateral brightness. Devices having higher nominal brightness also have higher lateral brightness. And the values for our URSLs are about one order of magnitude larger than the five commercial devices. Although these commercial devices might be advantageous in some other respects, their lateral brightness figures are quite lower than those of our URSLs, except for the most recent product, SDL's single mode master oscillator optical amplifier (MOPA).[147] These data confirm that unstable resonators are desirable designs for semiconductor lasers for high brightness and high power applications.

Many practical applications can be envisioned for using the bright optical output from these positive branch URSLs. In nonlinear optical processes, a higher intensity pump source usually generates higher yield. The efficiency for harmonic generation could be higher when pumped by URSLs than by FPSLs at the same pump power level. High power, and high brightness URSLs should also be excellent pump sources for diode

end-pumped solid-state lasers. High quality URSLs may provide output beams to be used in remote energy (or signal) delivery, such as free space communication etc.

Chapter 7

URSLS WITH NOVEL RESONATOR STRUCTURES

7.1 Introduction

Devices with resonator structures other than half-symmetric URs have also been fabricated during the process of our URSL program. The optical output beams from half-symmetric URSLs usually have elliptical divergence, i.e., the transverse divergence angles are different from the lateral ones. With properly designed optical elements, these output beams can be either focused to provide bright optical spot sources or collimated to be paraxial beams.

For some applications, it may be desirable to have collimated output beams directly from diode lasers. To achieve laterally self-collimated output beams, a design of a self-collimated unstable resonator was previously proposed for semiconductor lasers.[18] One such device was fabricated for this dissertation, and its operating characteristics will be presented in this chapter.

Before our sub-threshold spatio-spectral patterns observations,[20] a

core-amplifier model was speculated[148] to explain the lasing mechanism of URSLs. Based on this core-amplifier model, a variety of simple resonator structures have been proposed to create divergent wave fronts to increase spatial coherence and overcome/alleviate filamentation. Resonator structures that have been studied include hybrid, coreless, and dual curvature unstable resonators. Only one end mirror was modified from the cleaved facet for each of these structures. The FIBM mirror of a hybrid URSL consists of a narrow ($2 \sim 10$ μm) flat region in the center and one linearly tilted region on each side. The FIBM mirror of a coreless URSL, i.e., the width for the flat region (core) is zero, is simply a flat mirror with a few degrees of tilt relative to the originally cleaved facet. The coreless URSL design is reminiscent of the "tilted stripe" lasers studied in 70's[149, 150] and "tilted mirror" lasers studied in 80's.[151] A dual curvature URSL has one end mirror with two different radii of curvature.

For broad-area URSLs, the cylindrical mirrors usually have noticeable refractive aberration effects, which cause the broadening of the apparent virtual source envelopes. Attempting to reduce the drawbacks of virtual source broadening effects, refractive aberration corrected mirrors were designed to match "ideal" URSL modes.[148]

The fabrication and operating characteristics of these novel devices will be summerized here and compared with those of half-symmetric URSLs.

7.2 Self-collimated URSLs

Most URSLs fabricated to date have exhibited laterally divergent far fields, which stem from the divergent nature of the beam inside a positive-branch UR and the magnification of that divergence by refraction across the index discontinuity at the output mirror. In an attempt to directly achieve collimated output beams, confocal URSLs[152] were previously fabricated. Each of those confocal URSLs consists of one resonator section and two planar output couplers, which are separated from the feedback mirrors. The three sections are electrically isolated from each other. When both output couplers were pumped, however, these types of devices generated very complicated interference far-field patterns, which are very undesirable for practical applications.

Recently, Lang[18] proposed a design for a self-collimated URSLs. A self-collimated URSL consists of only the resonator section itself, and couples the optical output from the feedback mirrors. In principle, a device with this new design can provide a collimated and diffraction-limited output beam from a single emitting area. Figure 7.1 schematically shows the configuration of a self-collimated URSL. With a cavity length of L, resonator magnification of M, and resonator effective refractive index of μ_e, the radii of curvatures of the two end mirrors can be expressed as[18]

$$\frac{R_1}{L} = \frac{4M}{(M-1)[M(\mu_e - 1) + (\mu_e + 1)]} \tag{7.1}$$

for the left end mirror, and

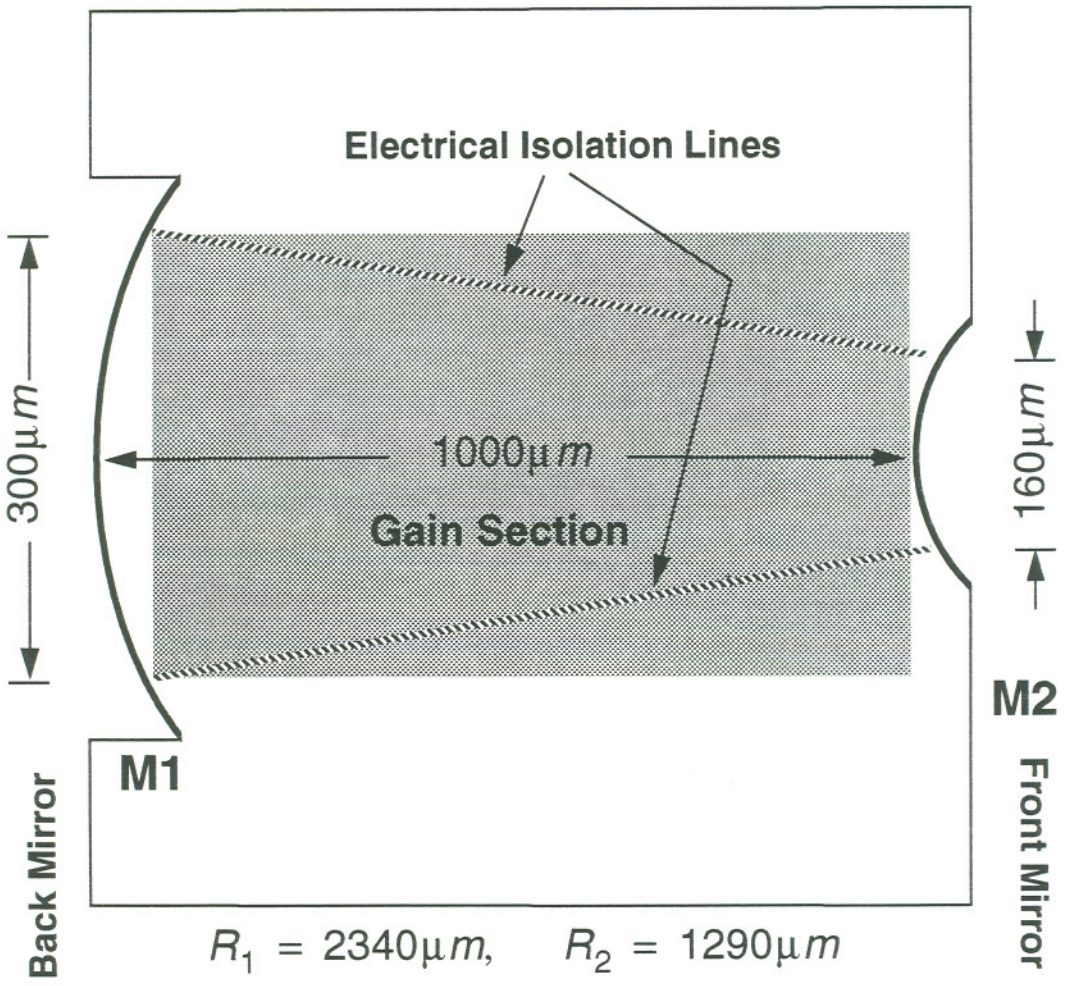

Figure 7.1 Schematic diagram of a self-collimated URSL with magnification =1.3.

$$\frac{R_2}{L} = \frac{M(\mu_e - 1) - (\mu_e + 1)}{\mu_e (M - 1)} \tag{7.2}$$

for the right end mirror. Negative (positive) radius of curvature represents a convex (concave) mirror. To avoid any real internal focal spots, the following condition needs to be satisfied:

$$1 \leq M \leq \frac{\mu_e + 1}{\mu_e - 1}. \tag{7.3}$$

For a typical case of μ_e = 3.35, the right side of equation (7.3) is about 1.85. For magnifications higher than 1.85, no self-collimating geometry is possible without an internal focal spot.

A self-collimated URSL was fabricated from InGaAs/AlGaAs quantum well material, which was described in Chapter 3. The laser cavity length is 1000 μm, resonator magnification is 1.3. The radii of curvatures of the right concave mirror and the left convex mirror are about 1255 μm and 2305 μm, respectively. The metallization was originally patterned to be 300 μm × 1000 μm in dimension. Two straight electrical isolation lines (about 1 μm deep) were formed using FIB micromachining to separate the extra parts of metallization in the two side regions. The resonator gain section is 160 μm wide in the right end, and 300 μm wide in the left end. The device was mounted p-up, and tested in pulsed operation with pulse width of 200 ns and repetition rate of 1 kHz.

Figure 7.2a shows the L-I curves for the original 300 μm × 1000 μm FPSL, and the self-collimated URSL. Although the collimated beam from the front mirror has a lower overall slope efficiency than that from the back

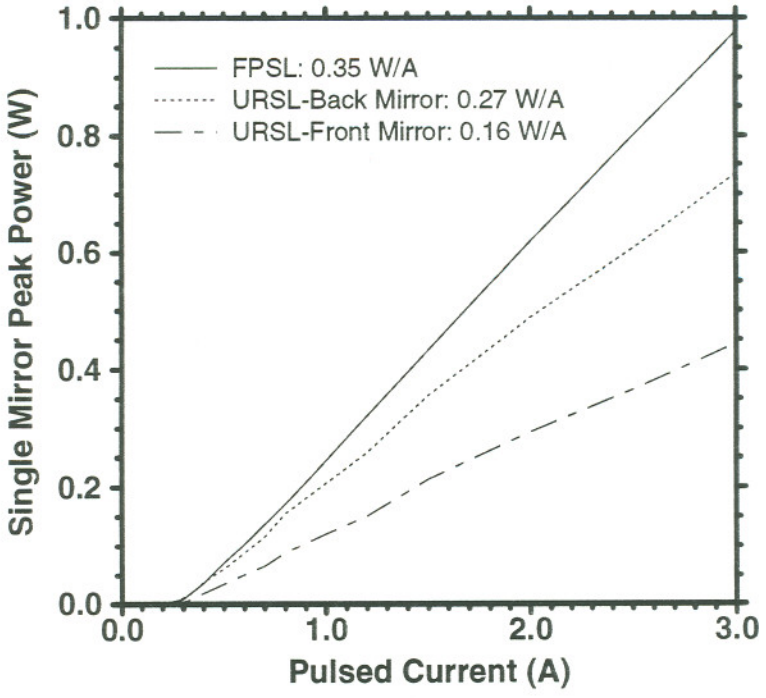

Figure 7.2a L-I curves of a self-collimated URSL, magnification = 1.3.

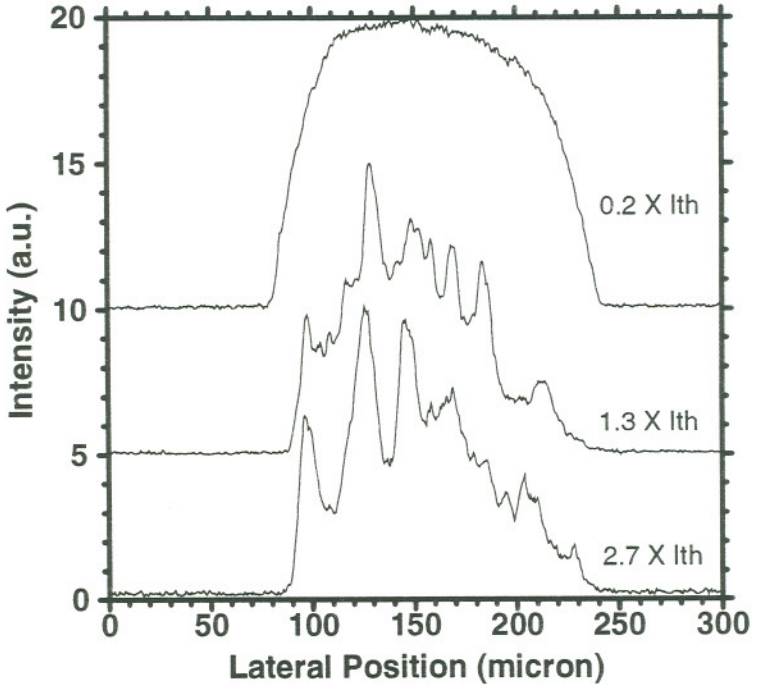

Figure 7.2b Near-field patterns of a self-collimated URSL (magnification = 1.3) at three different injection levels.

mirror, its spatial optical intensity is actually slightly higher due to its narrower emitting width. The total power efficiency of this URSL is lower than that of the original FPSL. This power degradation may be attributed to the slightly increased resonator loss and potential side effects of the FIB processing of the electrical isolation lines and end mirrors.

Near-field patterns were recorded from the narrower mirror end ("front" mirror), and plotted in Figure 7.2b. A smooth spontaneous emission profile (at $0.2\times I_{th}$) was observed. The lasing near-field patterns, however, were modulated with multiple ripples, and slightly narrower than the spontaneous emission pattern. The latter has a width matching closely to the stripe width on that mirror end.

The far-field patterns were also recorded for the collimated output beams at several different injection levels, and plotted in Figure 7.3a. The first curve corresponds to an injection level of 350 mA, which is slightly higher than the threshold (300 mA). That far-field curve consists of one strong center lobe and four relatively weaker side-lobes. The lateral divergence angle of the center lobe was measured to be about 0.6° at FWHM, which is almost twice the diffraction limited value of 0.31° for an 160 μm wide hard edge. The non-uniform near-field profiles may be attributed to part of the deviations. As the injection current increases, multiple lateral modes were observed, and the side-lobes grow rapidly to level up with the original central lobe. So the overall beam divergence also increases with the increasing of injection level. At high injection levels (above four times of threshold), the far-field pattern settles down to one big lobe, and the

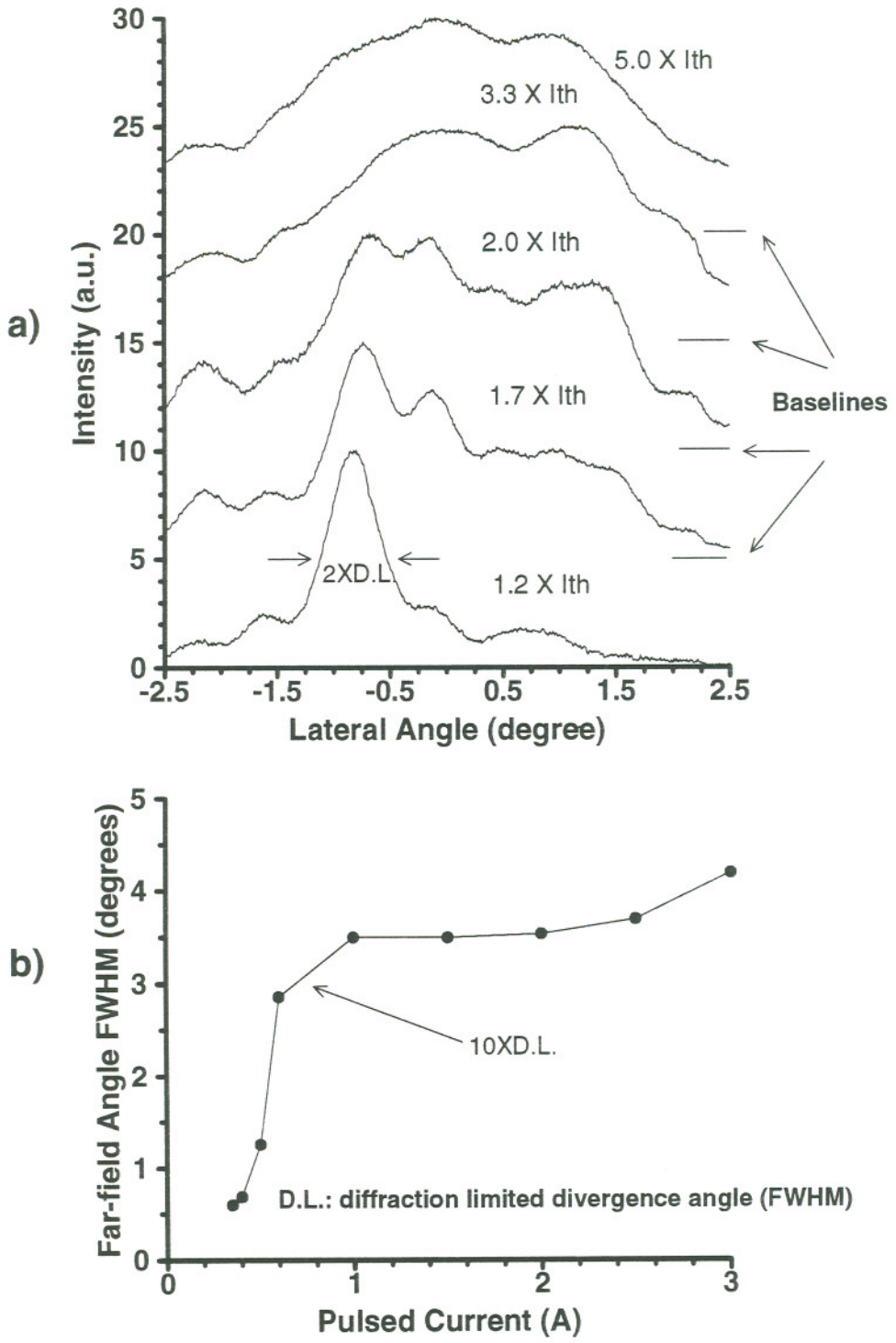

Figure 7.3 Far-field data for a 1.3 magnification self-collimated URSL, a) far-field profiles at five different injection levels, b) FWHM divergence angle versus injection current.

divergence angle increases only slightly with the injection current. Figure 7.3b plots the lateral divergence angle versus injection current. Slight beam steering was observed. It is not clear how this phenomenon happened.

The performance of the device discussed above only provided a rough demonstration of the original objective of self-collimated URSL design. By directly patterning the desirable tapered metal stripes and improving the precision of mirror fabrication, devices with better performance would possibly be achievable. On the other hand, the upper bound of the resonator magnification may restrain the self-collimated URSL design from applications that utilize materials having even moderate antiguiding parameters.

7.3 Refractive-aberration-corrected (RAC) Half-symmetric URSLs

From the point view of geometrical optics, the marginal rays in the resonator of a broad-area URSL deviate more and more severely from the paraxial approximation as the stripe width and/or magnification increases. The non-paraxial rays will contribute circular refractive aberration when they are refracted through the URSL end mirrors. This aberration effect will lead to the broadening of apparent virtual source width. To illustrate the aberration effect of a 200 μm $\times$ 500 μm URSL with 2.5 magnification, numerical analyses were conducted for the virtual source from the curved mirror side using both diffraction and ray tracing methods. The results were plotted in Figure 7.4. By propagating (using FFT) a uniform circular wave with 200 μm wide aperture back to the position of the apparent virtual source, the pure diffraction-limited source profile is derived as the dashed

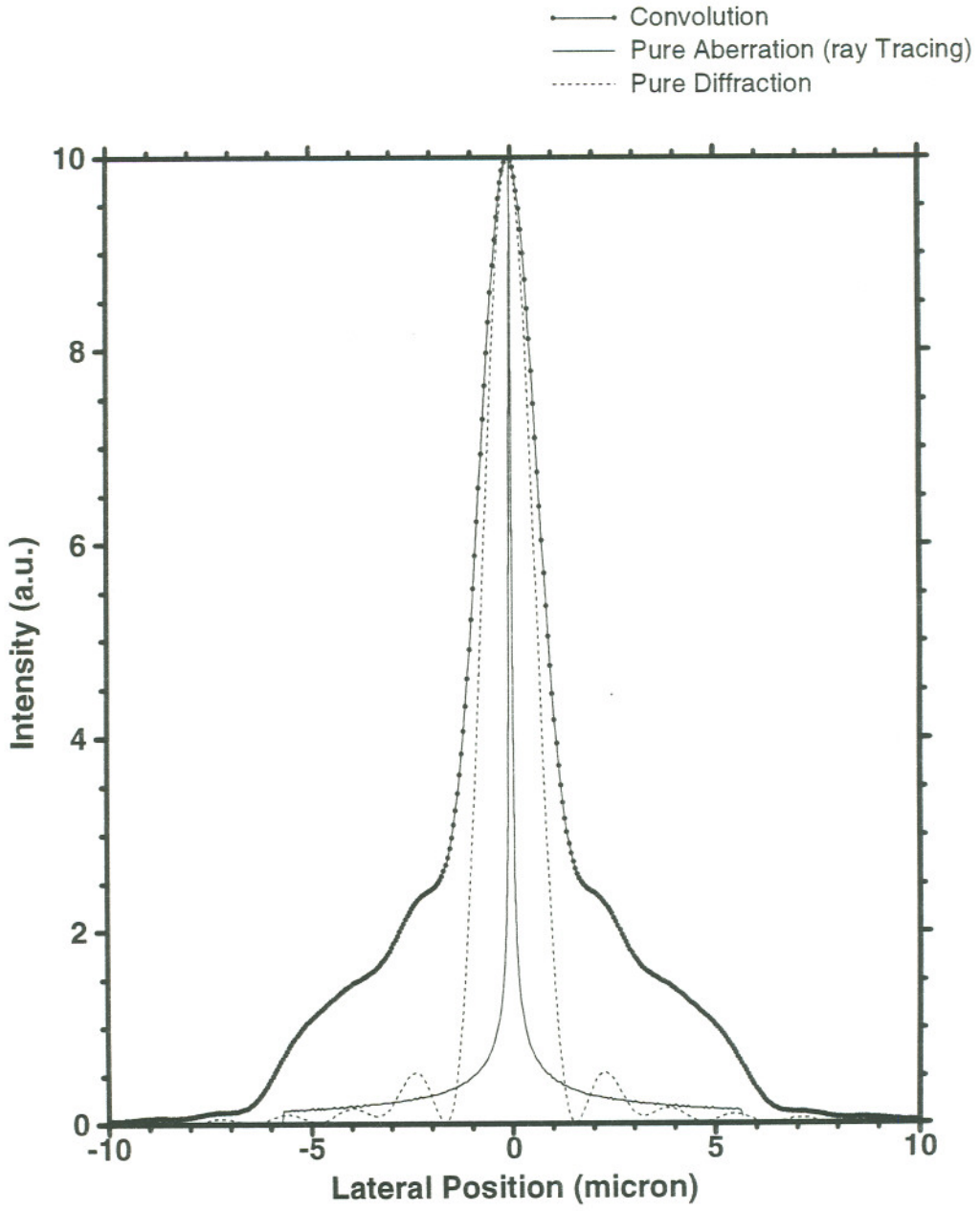

Figure 7.4 Circular aberration effect on the virtual source envelope of a 200 μm × 500 μm URSL with 2.5 magnification.

curve shown in Figure 7.4. Starting with angularly uniform ray distribution from the Siegman center (see Figure 2.2), a ray tracing method was used to calculate the direction of each refracted ray and its crossing position at the apparent virtual source plane. Detailed ray tracing analysis and computer programs can be found in Appendix D. The solid curve shown in Figure 7.4 shows the lateral ray density at that apparent virtual source plane. The convolution of these two curves gives the dot-dashed curve, and represents the overall profile of the apparent virtual source. It can be seen that aberration effect contributes broadening of the center lobe and enhancing of the platform in comparison to the pure diffraction-limited profile. In an attempt to achieve sharp virtual source profiles, curved mirrors were designed to alleviate potential aberration effects.

One simple design of refractive-aberration-corrected URSL mirrors was carried out by assuming that a half-symmetric URSL has a perfect lasing mode, which corresponds to perfect point virtual sources (or "Siegman" centers). With a specified resonator magnification, the positions of virtual sources can be determined. To the first-order approximation, the curvature of the cylindrical mirror can be calculated by assuring a perfect point apparent virtual source after the refraction of laser beam out of the curved mirror. The detailed analytical analysis is provided in the following.[148]

As shown in Figure 7.5, the left "Siegman" center P1, is assumed to be a perfect point source. To ensure a perfect apparent virtual source, each refracted ray from the curved mirror must be traced back to the same single point VS on the resonator axis, i.e., the optical path shall be constant for

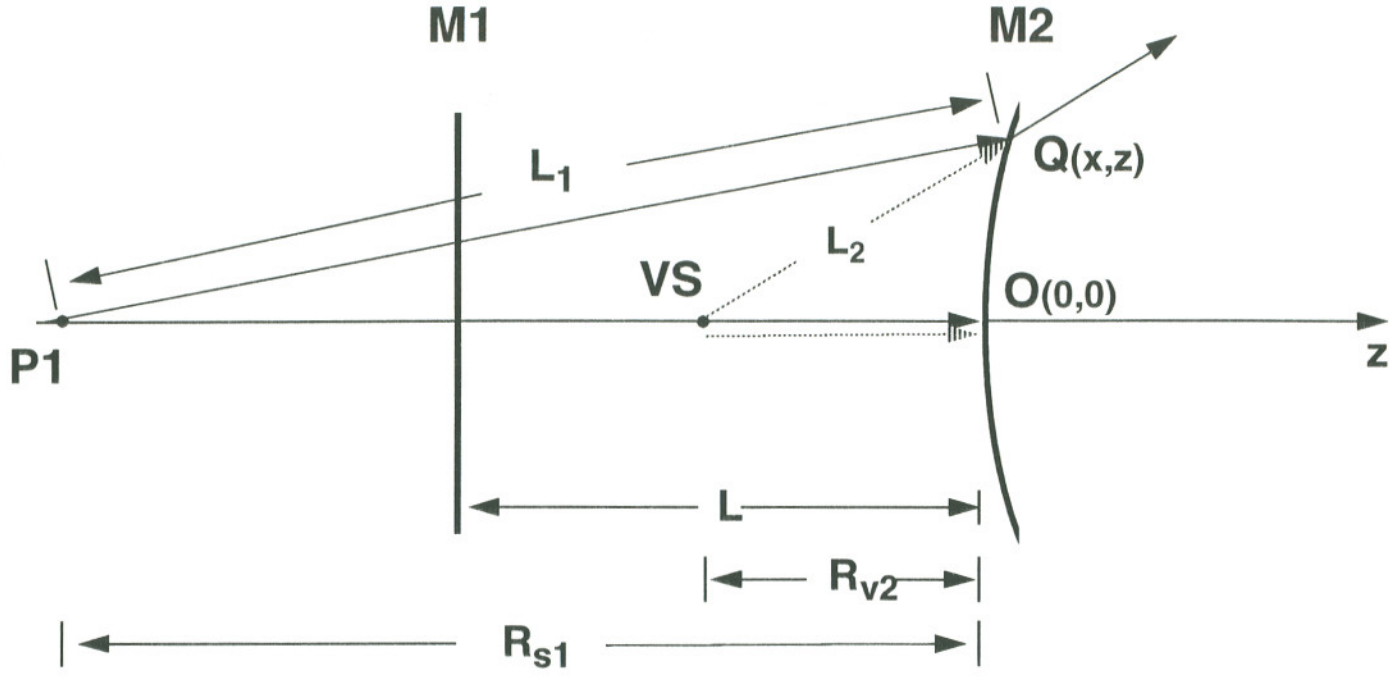

Achieving point source VS from Point source P1 requires:

$$\mu_e L_1 - L_2 = \mu_e R_{S1} - R_{V2}$$

Figure 7.5 Design of a refractive-aberration-corrected cylindrical mirror for a half-symmetric URSL.

each single ray propagating from P1 to VS. The mathematical expression is

$$\mu_e L_1 - L_2 = \mu_e R_{s1} - R_{v2}, \tag{7.4}$$

where μ_e is the modal effective refractive index, L_1 is the distance from the "Siegman" center to the crossing point Q on the curved mirror, L_2 is the distance from the apparent virtual source to the crossing point Q, $R_{s1} = (r_1 + 1)L$ is the depth of P1, and r_1 and R_{v2} are the parameters that were defined in Chapter 2. With the coordinates specified in Figure 7.5, we have

$$L_1 = \sqrt{x^2 + (R_{s1} + z)^2} \tag{7.5}$$

and

$$L_2 = \sqrt{x^2 + (R_{v2} + z)^2}. \tag{7.6}$$

By substituting expressions (7.5) and (7.6) into equation (7.4), the following implicit relation between x and z can be derived as

$$x = \left[\frac{B + C(1+D)}{A}\right]^{1/2}, \tag{7.7a}$$

where

$$A = \mu_e^2 - 1 - \frac{\mu_e R_{s1} - R_{v2}}{R_{v2} + z}, \tag{7.7b}$$

$$B = (\mu_e R_{s1} - R_{v2})^2 + (R_{v2} + z)^2 - \mu_e^2 (R_{s1} + z)^2, \tag{7.7c}$$

$$C = 2(R_{v2} + z)(\mu_e R_{s1} - R_{v2}), \tag{7.7d}$$

and

$$D = \left[1 + \left(\frac{x}{R_{v2} + z}\right)^2\right]^{1/2} - 1 - \frac{x^2}{2(R_{v2} + z)^2}. \tag{7.7e}$$

With a given value of z, the corresponding x can be calculated by

numerically iterating expressions (7.7a) - (7.7e) until a satisfactory accuracy is achieved. As an example, Figure 7.6a shows the calculated mirror curvature for a half-symmetric URSL with 2.5 magnification and 200 μm by 500 μm stripe dimension. For comparison, plotted in Figure 7.6a is also the curvature of a circular mirror, which is slightly more curved than the refractive-aberration-corrected (RAC) one. Figure 7.6b shows the difference of the two curves shown in Figure 7.6a.

By using the above algorithm in FIBM code, URSLs with RAC mirrors were fabricated from the InGaAs/AlGaAs GRINSCH strained-layer SQW materials, which were already described in a previous chapter. Optical power, spatial, and spectral characteristics were tested for these devices in pulsed operation (PW: 200 ns, and PRF: 1 kHz). Both the threshold and slope efficiency of this RAC URSL are comparable to a conventional circular mirror URSL. Figure 7.7 shows the L-I curve of a typical RAC URSL, which has a nominal resonator magnification of 2.5, and that of the original FPSL. The increase in the threshold and decrease of slope efficiency are close to what were reported in previous chapters for conventional circular mirror URSLs.

The near-field characteristics for RAC URSLs were found to be very similar to those of conventional URSLs. Figure 7.8a shows the near-field profiles of a particular RAC URSL at three different injection levels. Sharp virtual source envelopes were always observed for RAC URSLs when the injection levels were around threshold. However, the lateral virtual source width increases, unexpectedly, more dramatically with injection current

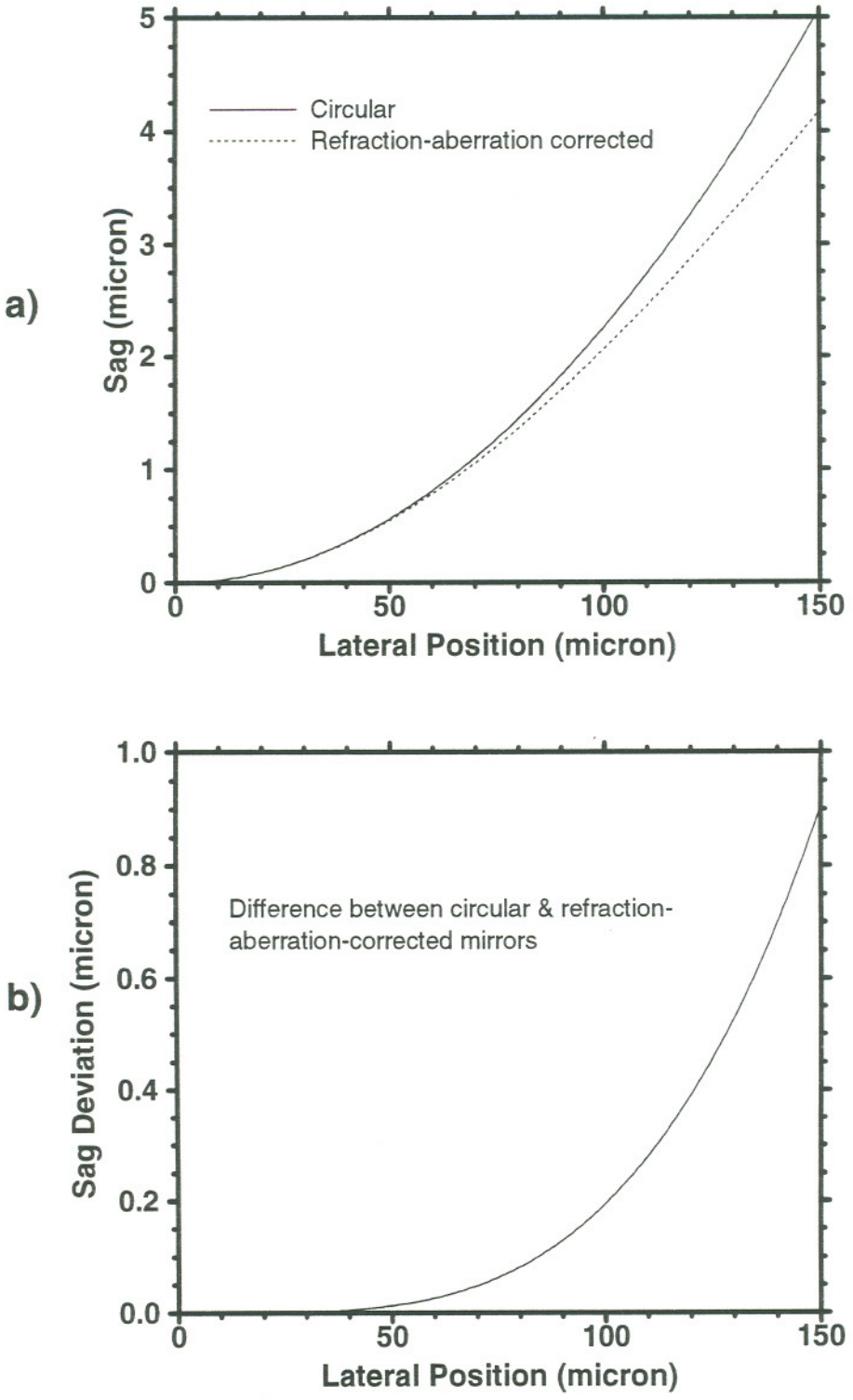

Figure 7.6 Comparison of circular mirror and aberration-corrected mirrors, a) mirror profiles, b) deviation of a circular mirror from a refraction-aberration-corrected mirror.

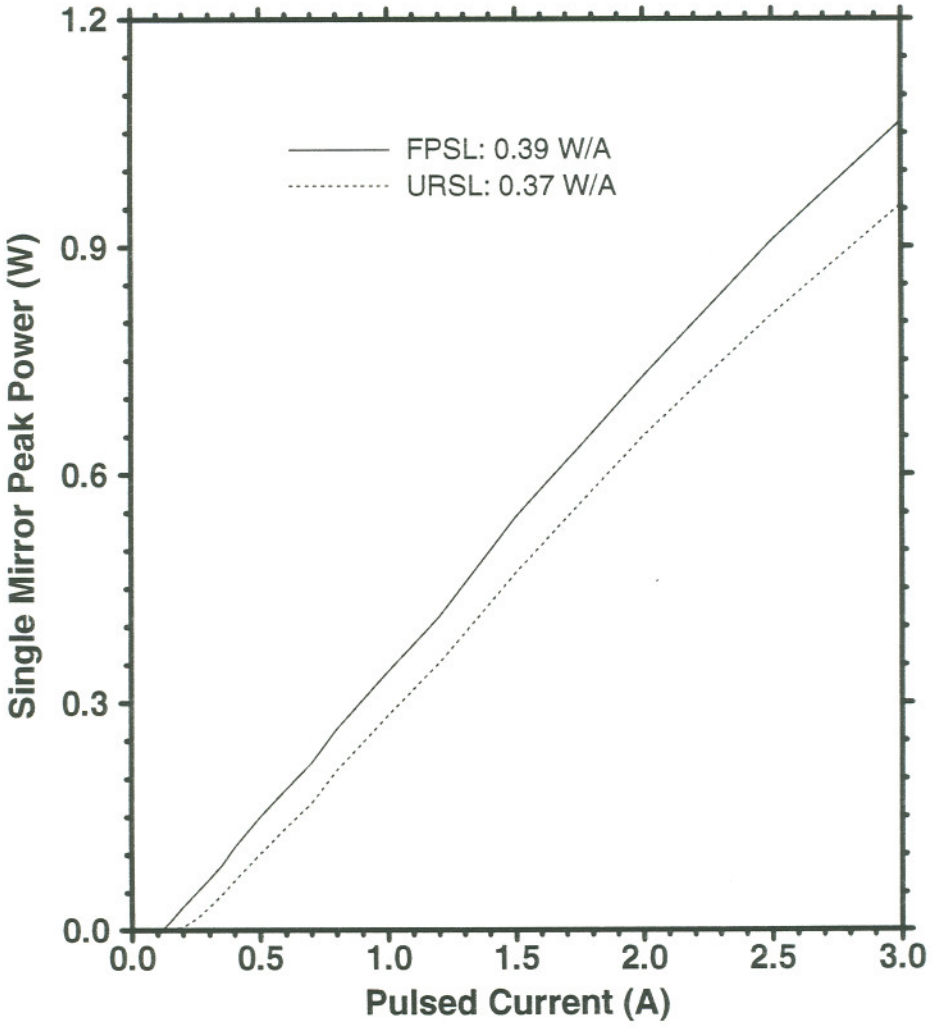

Figure 7.7 L-I curves of a 200 μm × 500 μm RAC URSL with 2.5 magnification, and a FPSL.

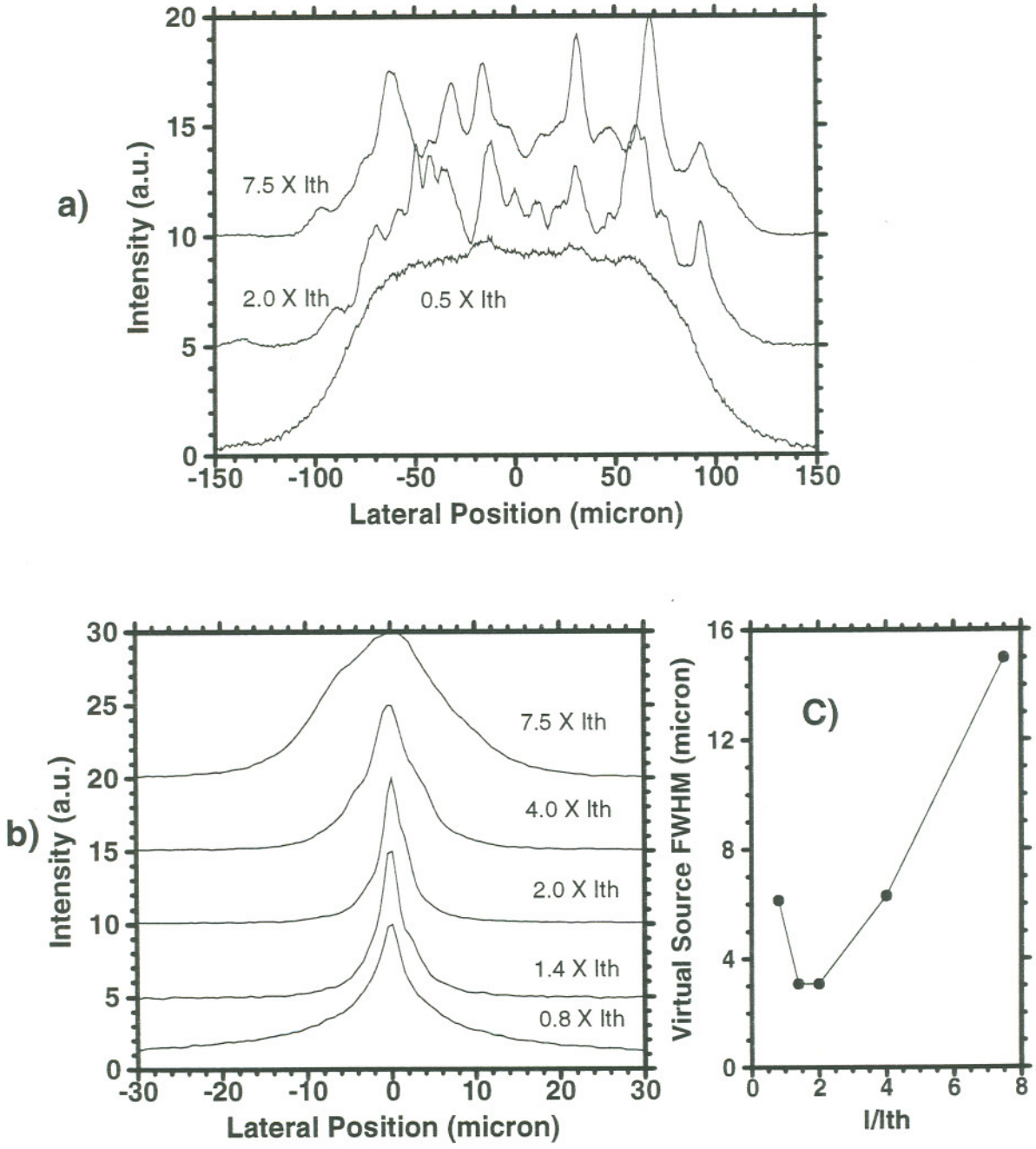

Figure 7.8 Near-field and virtual source characteristics of a 200 μm × 500 μm RAC URSL with 2.5 magnification, a) near-field profiles, b) virtual source envelopes, c) virtual source width versus injection level.

than that of circular mirror URSLs. The virtual source envelopes of the same RAC URSL were plotted in Figure 7.8b for five different injection levels. The virtual source width was also plotted versus the injection level in Figure 7.8c. The spectral mode pattern usually broadens rapidly with the virtual source as the injection current increases. Figure 7.9 shows half-tone pictures of spatial-spectral patterns of that RAC URSL at several different injection levels. At low injection levels, i.e., $1.5\times I_{th}$ shown in Figure 7.9a, each longitudinal mode consists of only one sharp lateral mode. Each longitudinal mode broadens as the injection level increases, as shown in Figure 7.9b. However, no lateral mode splitting was observed for that RAC URSL. At injection levels higher than $10\times I_{th}$, i.e., shown in Figure 7.9c, each longitudinal mode is so broad that it occupies about half of the inter-longitudinal mode separation.

With the same design guideline, RAC URSLs were fabricated with different resonator magnification and stripe dimensions. Generally speaking, these devices have worse virtual source characteristics than the conventional URSLs. One explanation is that the RAC mirrors severely enhance the reflection aberrations although the refractive aberration is corrected. Since the formation of lasing modes depends strongly upon the reflection processes off the end mirrors, the enhanced reflection aberration will definitely cause deviations of the lasing modes from those with ideal spot sources.[5] So the correction of refractive mirror aberration does not necessarily shrink the apparent virtual source envelope.

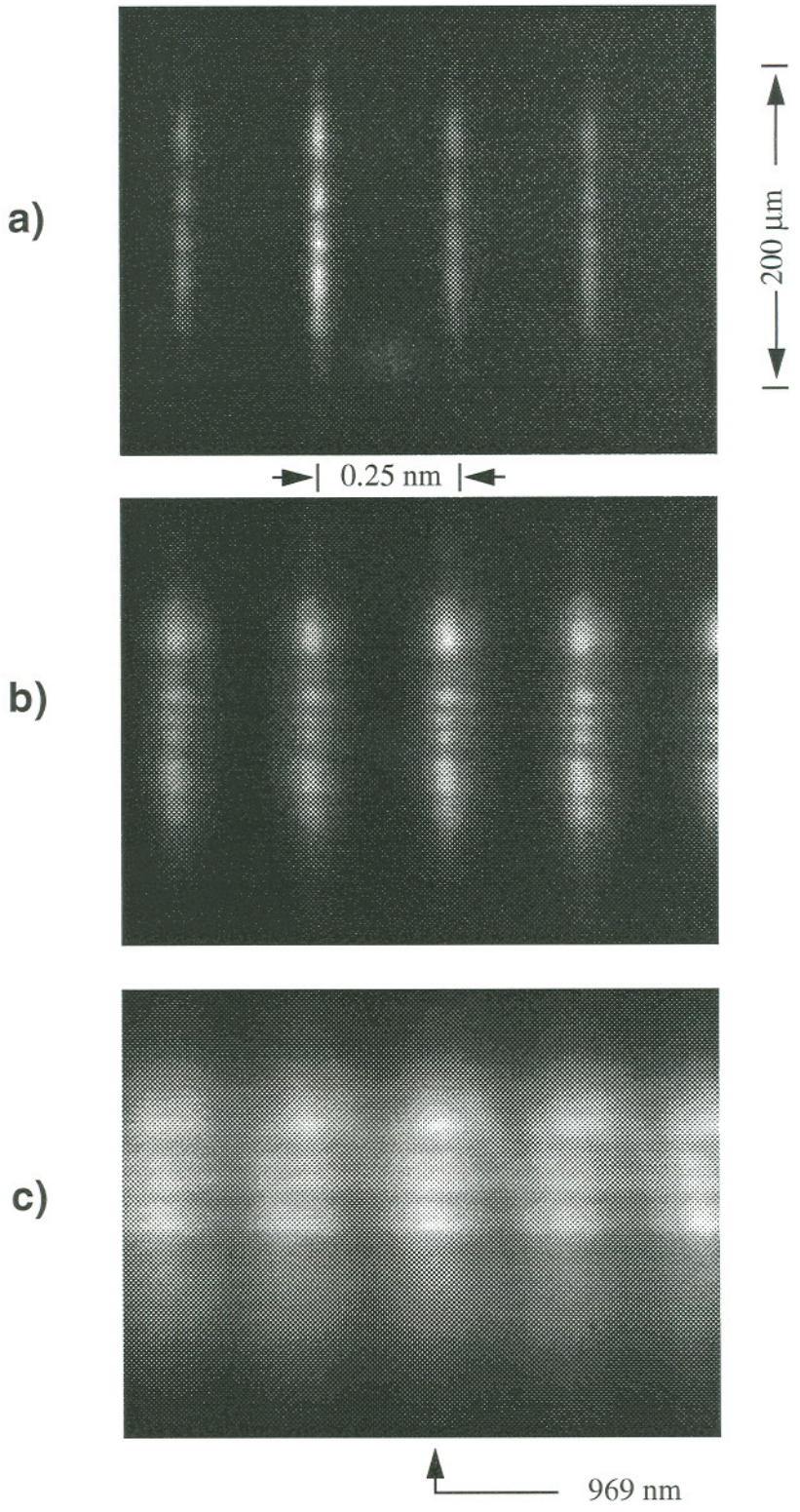

Figure 7.9 Spatio-spectral near-field patterns of an 200 µm x 500 µm InGaAs/AlGaAs RAC URSL, a) 1.5 x I_{th}, b) 3.0 x I_{th}, c) 12 x I_{th}. Magnification = 2.5.

7.4 Hybrid URSLs

Based on the core-amplifier URSL model, a type of device structure, called a hybrid URSL (also "stealth URSL"), was proposed by Dente and co-workers in 1992.[148] The schematic diagram of a typical device structure is shown in Figure 7.10. One end of the device is still the original cleaved facet. The other end mirror has a narrow flat central region to serve as a core oscillator region. The two side regions are symmetrically tapered with a tilt angle, which is called the "wing angle" here, relative to the cleaved facet. With the objective of achieving optical output efficiencies that are comparable to those of FPSLs, wing angles were limited to less than or equal to 2° for this study. The width of the core region is usually chosen to be in the range of 1 μm to 6 μm, which is smaller than the estimated filament width.[37] In principle, the narrow core region shall be able to act as a master oscillator. The side regions with non-parallel mirrors act as amplifiers for the diverging (due to diffraction) light from the center master oscillator.

This type of device was also fabricated from InGaAs/AlGaAs GRINSCH SQW laser materials by FIBM of the end mirrors, and tested under pulsed (PW: 200 ns, PRF: 1 kHz) operation. In comparison with original FPSLs, the slope efficiencies for hybrid URSLs with 1 ~ 6 μm core width and 1~2° wing angle usually drop 10 ~ 30%, which is close to those of URSLs with cylindrical mirror. Figure 7.11 shows the typical L-I curves for two different hybrid URSLs and those of the original FPSLs. URSLs with larger wing

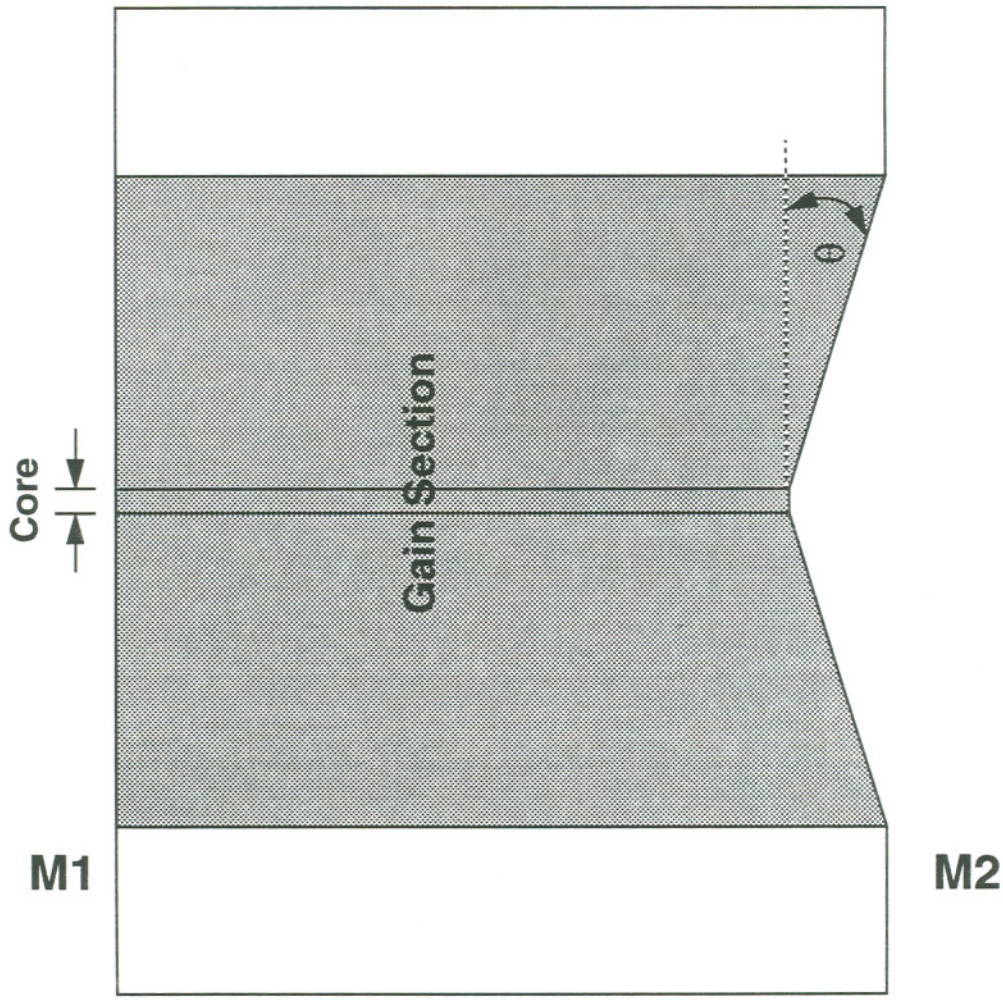

$\theta = 1° \sim 2°, \quad Core = 1 \sim 6\mu m$

Figure 7.10 Schematic diagram of a hybrid (or "stealth") URSL.

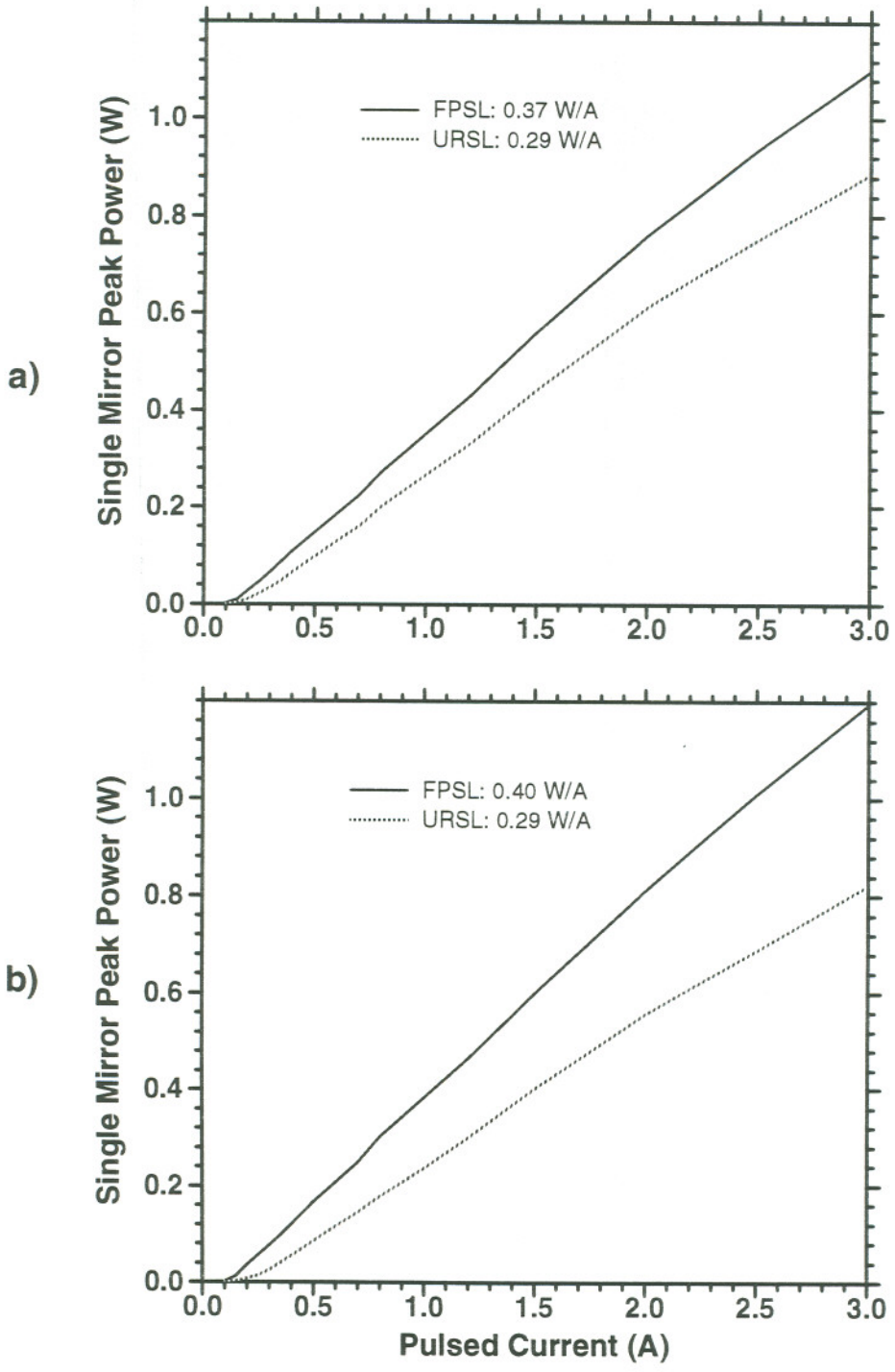

Figure 7.11 L-I curves of two hybrid URSLs and their original FPSLs; a) URSL with 1.0 μm wide core and 1.5° wing angle, b) URSL with 6.0 μm wide core and 2.0° wing angle. Stripe dimensions are 200 μm x 500 μm.

angle usually have larger slope efficiency drop, e.g., the efficiency of the device shown in Figure 7.11b dropped slightly more than that of the one in Figure 7.11a. On the other hand, our experimental data do not show consistent correlation between the core widths ($1 \sim 6 \mu m$) and the L-I characteristics.

The near-field patterns of hybrid URSLs were studied. For a device with very narrow core regions, i.e., 1 or 2 μm, there are usually three lobes covering the two sides and the center of a near-field pattern, as shown in Figure 7.12a for a device with 1 μm core and 1.5° wing angle. As the core width increases, the intensity of the center lobe grows stronger than the two side ones, e.g., the curves shown in Figure 7.12b for a device with 6 μm core and 2.0° wing angle. Theoretically speaking, the smaller the core, the larger the diffraction angle, which controls the coupling efficiency between the core/master oscillator and the side amplifiers. A smaller core may correspond to a larger coupling efficiency. All the data plotted in Figure 7.12 were recorded from the FIBM mirror ends. The near-field patterns viewed from the flat mirrors show similar behavior.

The near-field of these hybrid URSLs cannot be laterally imaged to a virtual source due to their non-cylindrical phase fronts. When directly viewing the output far-field from the URSL emitting end, the recorded intensity profile consists of two main branches, which are separated from each other by a large angle. The angles are about 35° for two devices with 1.5° wing angle, and with 1.0 μm and 2.0 μm core, respectively. The region in between the two branches in the far field is very dim. It is not clear how

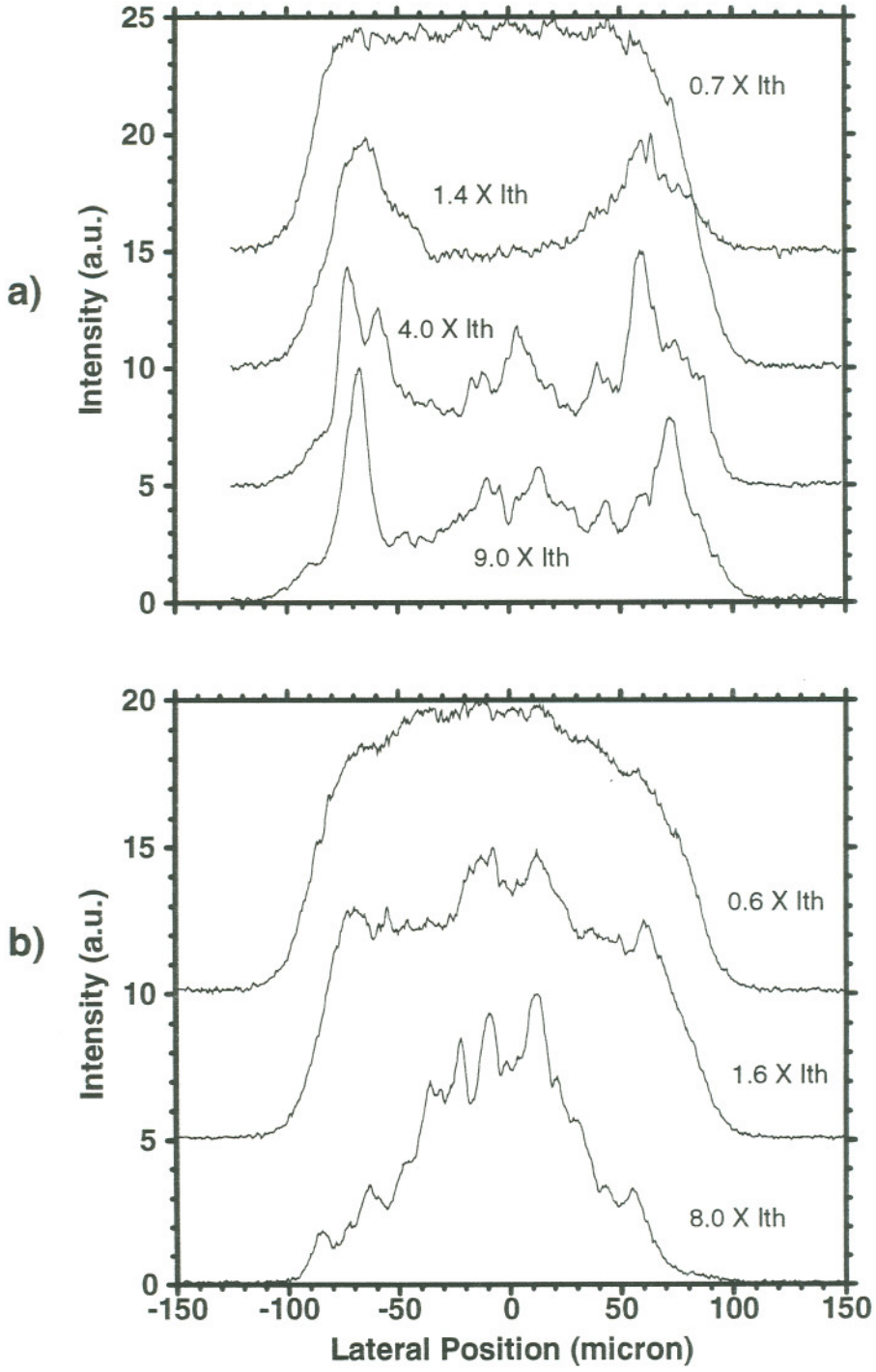

Figure 7.12 Near-field profiles of two 200 μm × 500 μm hybrid URSLs, a) 1.0 μm core and 1.5° wing angle, b) 6.0 μm core and 2.0° wing angle.

this separation was built up. One mechanism may be the diffraction effect associated with the whole cavity defined by the core region. In comparison, the diverging angle (FWHM) of the central lobe of the diffraction pattern from a sharp aperture of width δl is about $2\tan^{-1}(0.4429\lambda/\delta l)$, which is about 48° for $1.0\mu m$ wide aperture, and 8.5° for 6.0 ~ μm wide apertures ($\lambda = 1.0\mu m$). It needs to be pointed out that the diffraction effect associated with the core region is far from sharp edge diffraction. On the other hand, the wing angle may also contribute partly to this angular separation. These types of diverging far-field patterns represent their irregular phase-fronts. Many practical applications may not be realized with these devices since complicated optics would be needed to collimate the output beams.

The spectral characteristics of hybrid URSLs were also studied. Multi-lateral modes operation was observed for all devices tested. From the concern of spectral merit, the hybrid URSL design is no better than cylindrical URSL ones. Also, the performance of these hybrid URSLs do not fit well to the projections of the core-amplifier URSL model. It was speculated[153] that larger wing angles may be needed for hybrid URSLs to lase as MOPAs.

Unlike URSLs with cylindrical mirrors, there is no such a parameter as geometrical resonator magnification for hybrid URSLs. To compare the divergence of a typical hybrid URSL with that of a cylindrical URSL, the tangential angles of a cylindrical mirror are analyzed. For a 200 μm × 500 μm cylindrical URSL with magnification of 2.5, the tangential angle of the mirror surface increases almost linearly with the lateral displacement (from the center point), as shown in Figure 7.13. The tangential angle at the

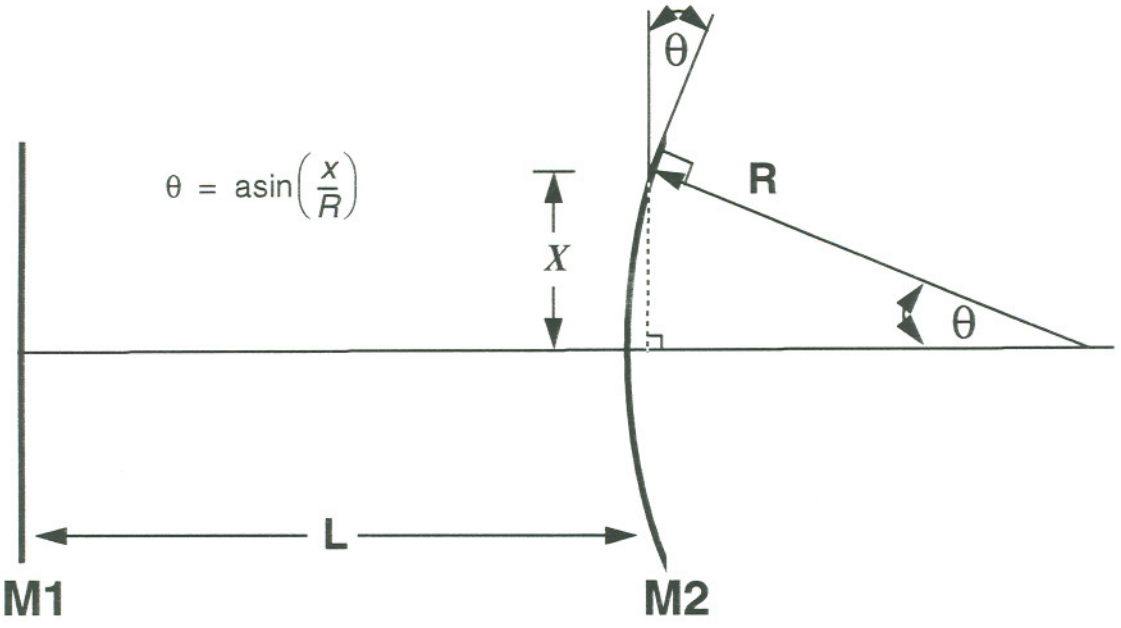

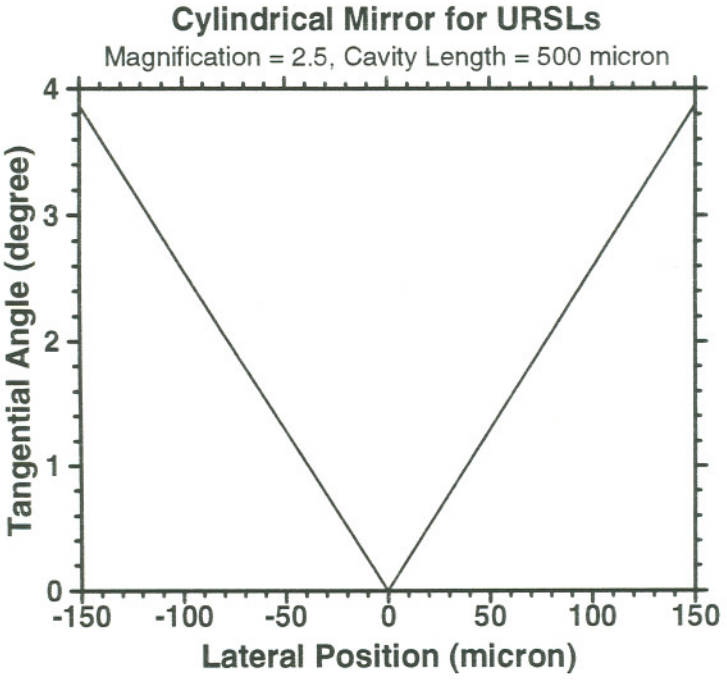

Figure 7.13 Tangential angle versus lateral position for the cylindrical mirror of an URSL, a) schematic diagram, b) calculated results.

stripe margins is about 2.6°. From this point of view, the resonator loss of an URSL of 2.5 magnification is comparable to that of a hybrid URSL with 1.0~2.0° wing angle.

7.5 Coreless URSLs

Another attempt at extending the core-amplifier URSL model is the proposal[148] of the so-called coreless URSL structure. This new design is almost identical to what was studied previously, the tilted-mirror semiconductor laser,[151] which simply consists of a tilted flat mirror on one end and a cleaved mirror on the other end of the cavity. The only difference is that a small (~ 1 μm) scattering seed, which is simply a FIBM dip, is positioned at the crossing point of the tilted mirror and the stripe margin towards the shorter cavity side. The idea of this design is that the small scattering seed serves as the source of a diverging wave-front, which, in turn, will be amplified by the rest of the gain section. For this study, the tilted mirrors and the scattering seeds were fabricated using focused-ion-beam micromachining. The tilt angles, relative to the cleaved facet, were chosen to be either 1° or 2°.

From the point view of geometrical optics, this coreless structure is also an unstable resonator. With the parameters specified in Figure 7.14, ray-tracing analysis can easily be conducted. First, let's trace an optical ray starting from the flat mirror at the shorter cavity side, and assume the ray is parallel to the normal of the flat mirror at the beginning. When the ray is reflected back to the flat mirror after one "round-trip", it is displaced

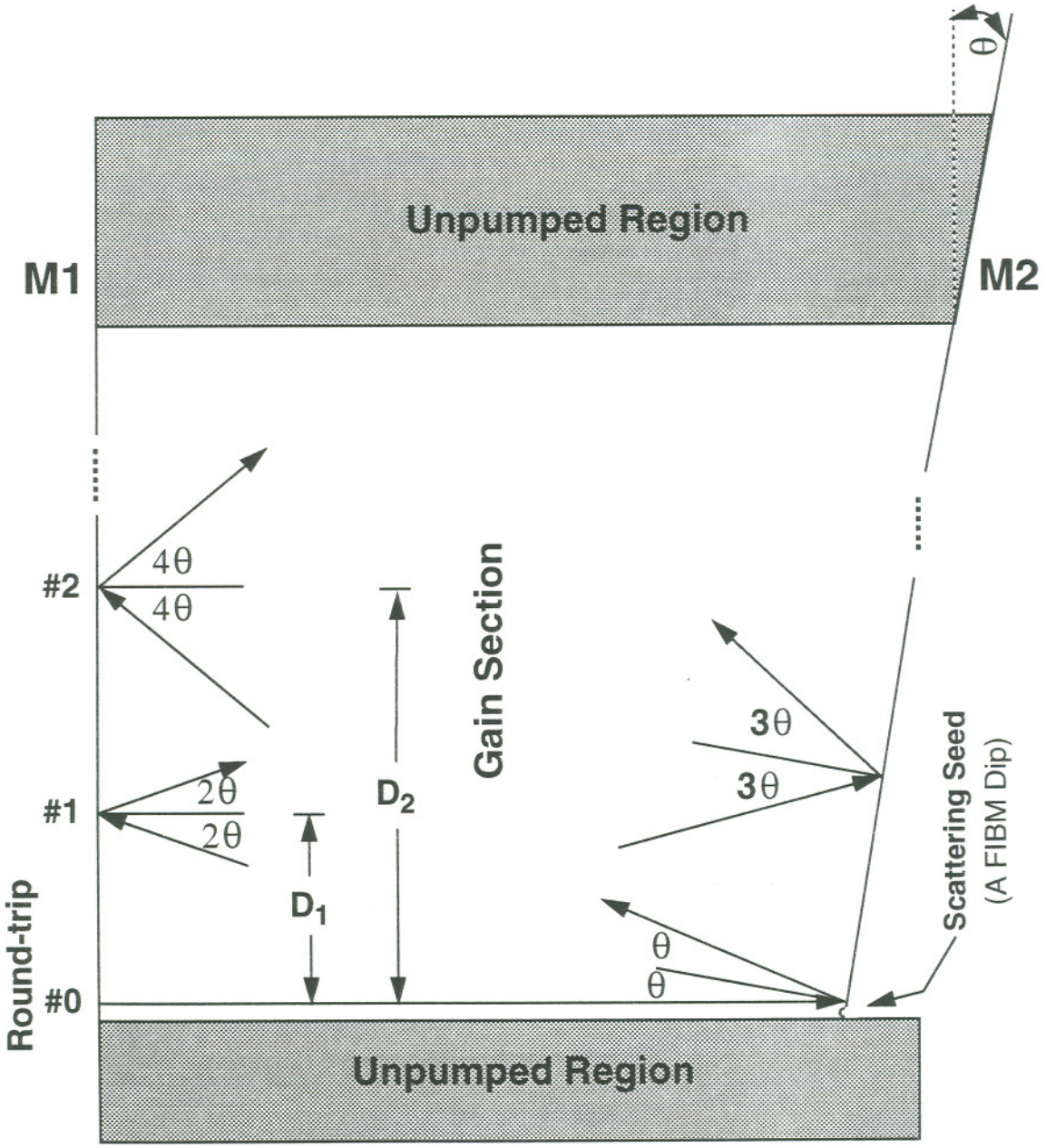

$$D_1 = 2\theta L;\ D_2 = D_1 + 2\theta L + 4\theta L = 8\theta L$$

Figure 7.14 Schematic diagram of a coreless URSL.

approximately in the lateral direction by

$$D_1 = 2\theta L, \tag{7.9}$$

where θ is the mirror tilt angle, L is the average cavity length. Actually, the ray can never come back to its starting point. After the second "round-trip", the lateral displacement from the starting point will be

$$D_2 = 2\times 2\theta L + 4\theta L = 8\theta L.$$

Straightforwardly, the displacement after N "round-trips" can be derived as

$$\begin{aligned} D_N &= 2\times(2\theta + 4\theta + \ldots\ldots + (N-1)2\theta)L + 2N\theta L \\ &= 2N^2\theta L. \end{aligned} \tag{7.11}$$

The ray will eventually escape away from the resonator at the longer cavity side after going through a maximum number N_m "round-trips". N_m is determined by the following equation

$$2N^2\theta L = W, \tag{7.12}$$

where W is the stripe width. Most devices that we studied have stripe dimensions of 200 μm $\times$ 500 μm. The values of N_m are less than 4 for a mirror tilt angle of 1°, and less than 3 for a tilt angle of 2°. This analysis suggests that a coreless URSL has to build up its lasing action in only a few "round-trip"s.

Every coreless URSL that we have fabricated lases. Figure 7.15 shows the L-I curves of two devices with mirror tilt angles of 1° and 2°, respectively. For the device with 1.0° mirror tilt angle, the threshold increased by roughly 8% in comparing with that of the original FPSL, while the slope efficiency dropped by only 5%. For the device with 2.0° mirror tilt angle, the threshold increased by almost 50%, while the slope efficiency dropped

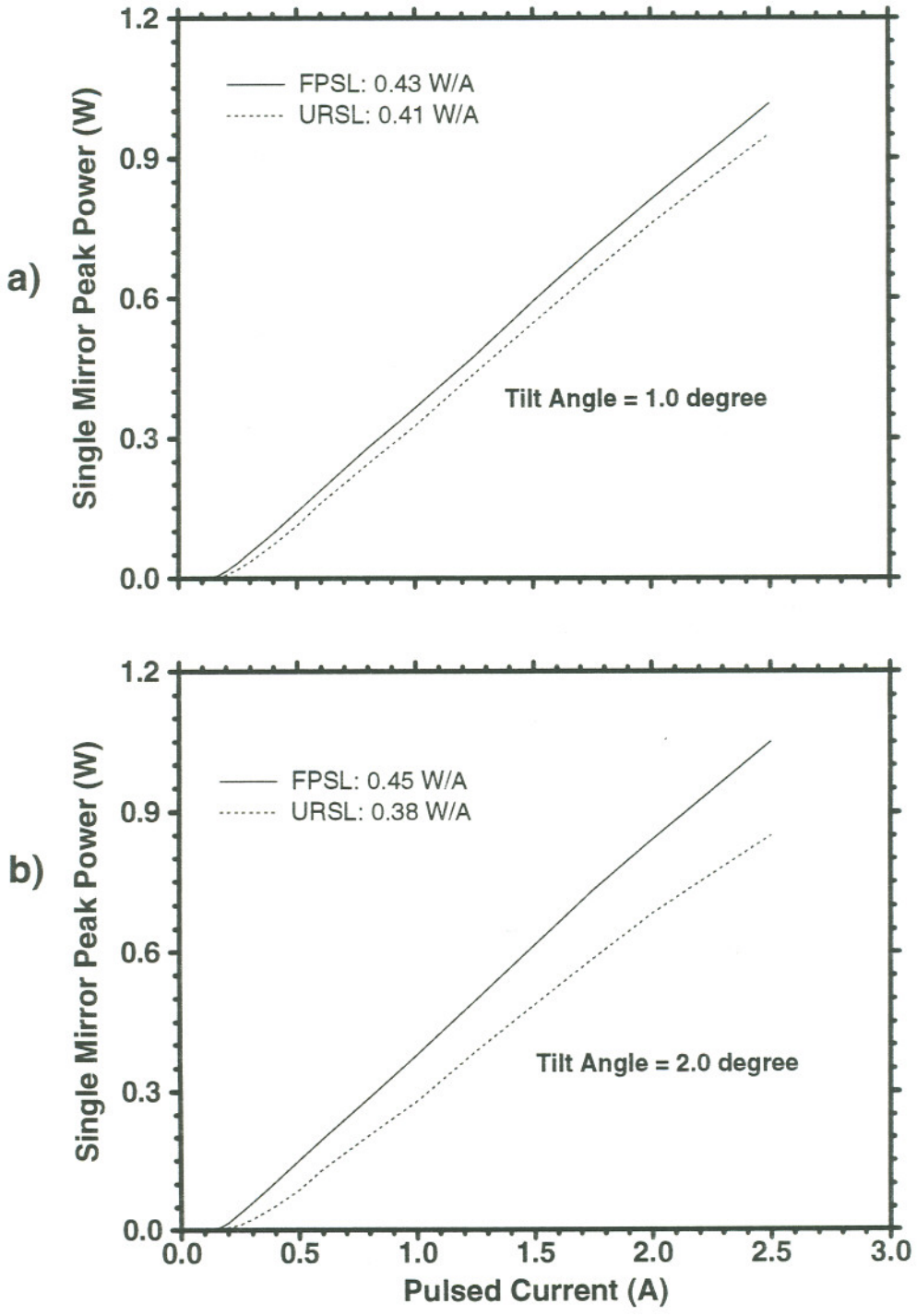

Figure 7.15 L-I curves of two 200 μm × 500 μm coreless URSLs, a) 1.0° mirror tilt angle, b) 2.0° mirror tilt angle.

by 16% after the tilted mirror was fabricated. These results are comparable to early observations.[151] L-I curves of other devices were also studied, and it has been noticed that the threshold always increases more rapidly than the reciprocal slope efficiency as the mirror tilt angle increases.

The near-field patterns of the two devices were also recorded, and plotted in Figure 7.16. Even when the injection level is far below threshold, e.g., 0.2 times threshold, the spontaneous emission pattern shows asymmetric behavior, with the longer cavity side having stronger optical intensity. As the injection current increases, the optical intensity grows faster at the longer cavity side than that at the shorter cavity side, i.e., the effective emitting area shrinks. For the device with 2° mirror tilt angle, as shown in Figure 7.16b, the near-field biases more severely towards the longer cavity side than that of the device with small tilt angle. Almost all the light was emitted from a region smaller than half of the stripe. The far-field is usually steered towards the longer cavity side with several degrees of angle. The spatially biased near-field and steered far-field are not particularly good for any practical application, and were not systematically recorded.

The lasing spectral characteristics of coreless URSLs were also studied. Figure 7.17 shows parts of the spectra of two devices, which had mirror tilt angles of 1.0° and 2.0°, respectively. A coreless URSL typically lases in single lateral mode up to 3 ~ 4 times of threshold, with intensity distribution identical to the near-field profile; then, each longitudinal mode broadens significantly, and the intensity of the whole spectrum decreases.

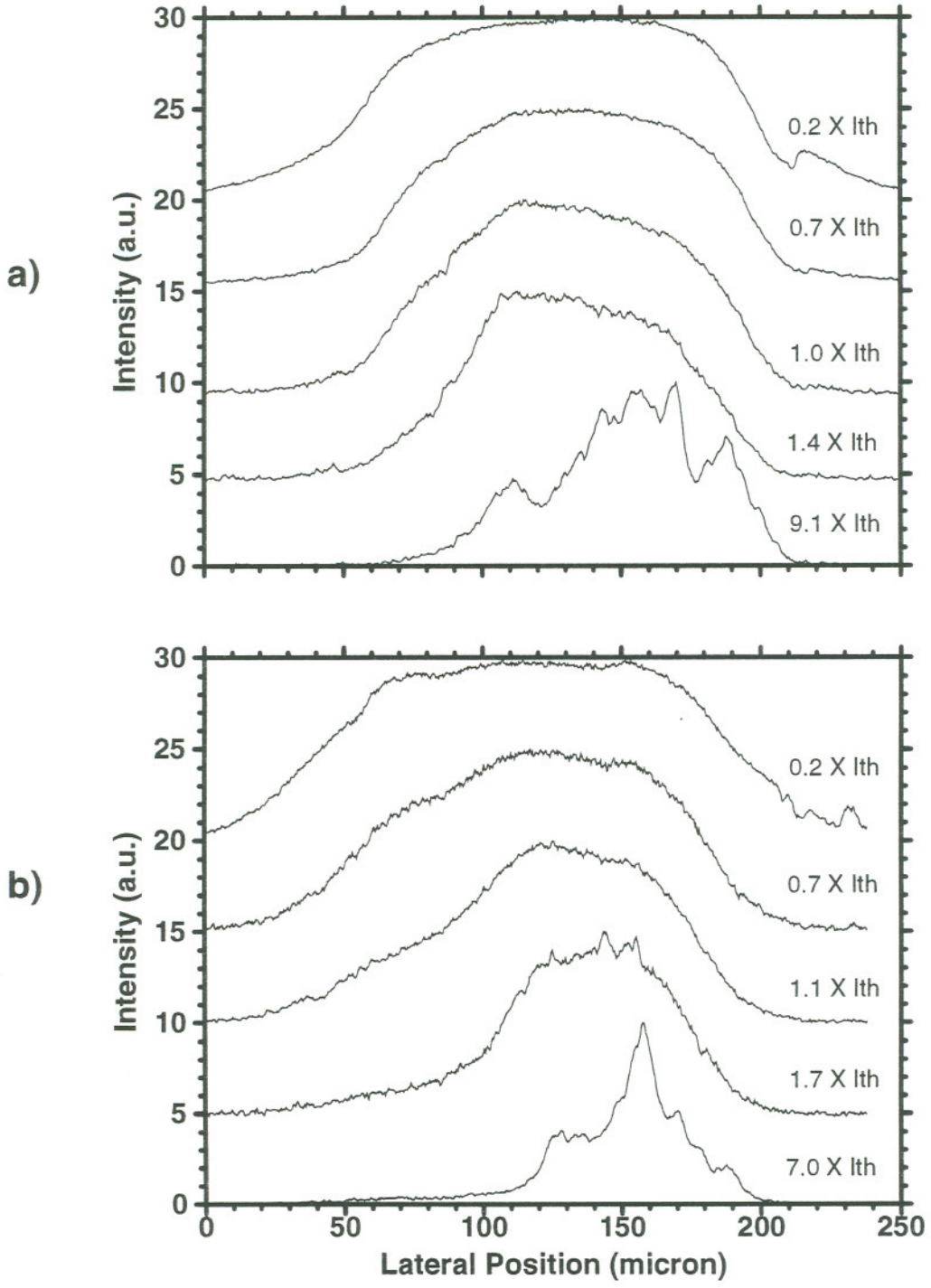

Figure 7.16 Near-field profiles of two 200 μm × 500 μm coreless URSLs, a) 1.0° mirror tilt angle, b) 2.0° mirror tilt angle.

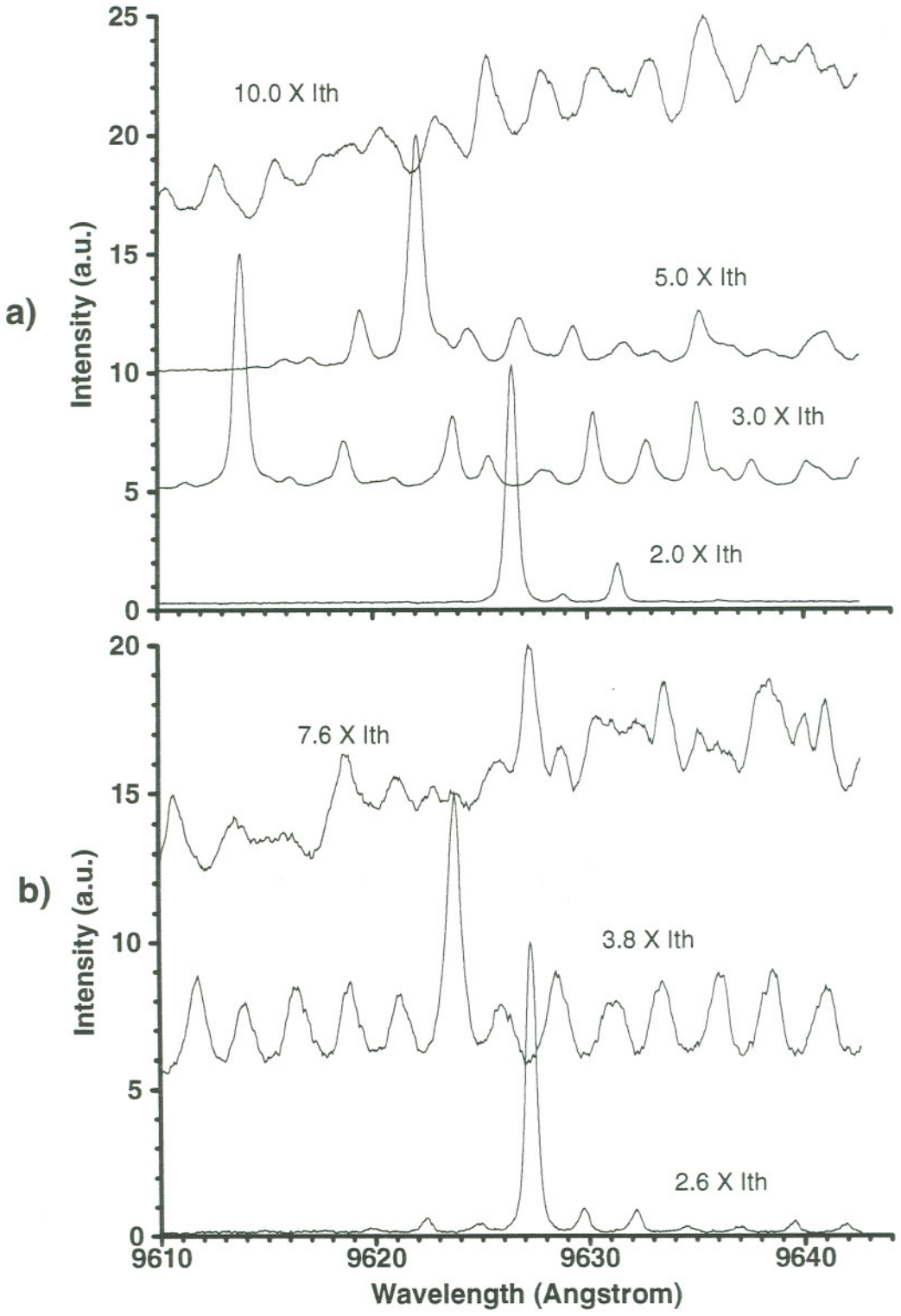

Figure 7.17 Spectral characteristics of two 200 μm × 500 μm coreless URSLs, a) 1.0° mirror tilt angle, b) 2.0° mirror tilt angle.

The performance of these coreless URSLs may not be very attractive for any practical application. As mentioned at the beginning of this chapter, the goal of fabricating these prototypes of devices is to understand the lasing mechanism of unstable resonator semiconductor lasers. For cylindrical mirror URSLs, the observed sub-threshold spatio-spectral patterns suggest that the central core-regions build up feedback processes. For coreless URSLs, however, the general principles of geometrical optics cannot project any feedback mechanism. It is anticipated that gain guiding plays a critical role in mode formation of coreless URSLs. An optical ray can only stay in the cavity for a few "round-trip"s. In a previous study, lasing operations of 100 $\times$ 300 μm devices with mirror tilt angle as large as 15° were observed.[151] As the mirror tilt angle goes up to 10°, optical rays could survive no more than one "round-trip" inside the cavity.

Diffraction effects should be important but have been ignored in the geometrical analysis presented above. Based on the principles of wave optics, it may be speculated that a coreless URSL can be viewed as the lateral combination of many narrow "FPSL"s, which can always build up feedback process, no matter how weak it may be, to lase. The direct effect of the tilted mirror is the build-up of a tendency for the light from each "FPSL" to be steered towards the longer cavity side. That explains how the one-side-biased near-field patterns were generated.

7.6 A Half-symmetric URSL with Dual Curvature Mirror

In an attempt to examine the effect of mirror curvature changes on URSL modal behavior, cylindrical mirrors with dual curvatures were designed and fabricated on devices using FIBM. The central part of the cylindrical mirror has larger curvature, as shown in Figure 7.18, and is expected to initiate a strongly diverging wave-front. The outer regions of the mirror have a smaller curvature. So the outer parts of the resonator can be viewed as amplifier of the diverging waves from the central region.

Such devices were fabricated from InGaAs/AlGaAs GRINSCH strained SQW material, with the parameter values specified in Figure 7.18. The metal stripe has a dimension of 300 μm × 500 μm. The outer mirror has a radius of curvature of 2200 μm, and gives a magnification of 2.5 for the outer part of the resonator. The inner part of the mirror corresponds to a radius of curvature of 293 μm, which gives a resonator magnification of about 8.7. The total sag of the whole mirror is about 4.1 μm. The aperture of the inner part of the mirror was designed to be 38 μm, which corresponds to a sag of about 0.62 μm.

Devices were tested under pulsed operation (PW: 200 ns, PRF: 1 kHz). Figure 7.19 shows the L-I curve for a dual curvature URSL and that of the original FPSL. After FIBM of the dual curvature mirror, the threshold increased by almost 50%, while the slope efficiency decreased by less than 12%. In comparing with conventional cylindrical URSLs, the relatively large threshold increase can be attributed to the strong divergence of the central

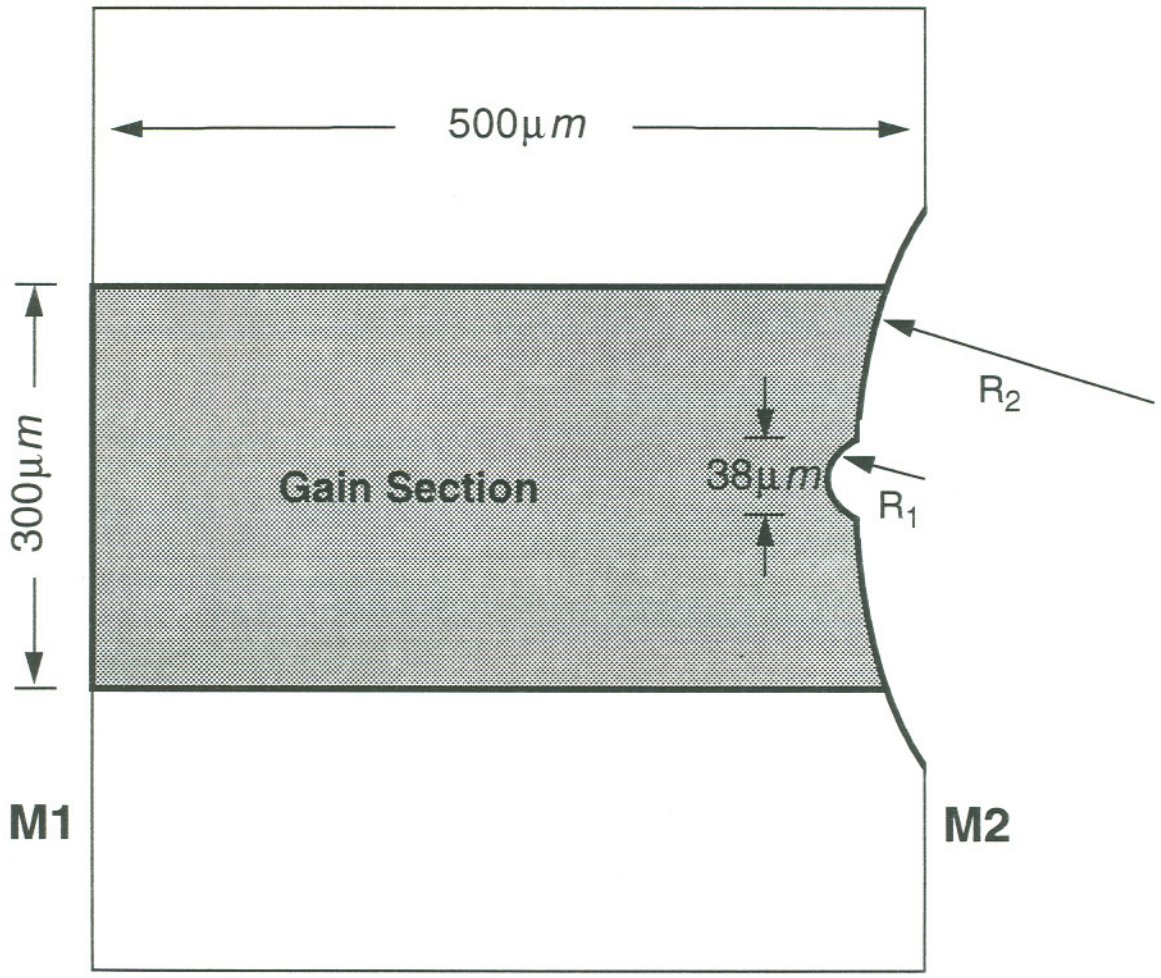

$R_1 = 293\mu m, \quad R_2 = 2200\mu m$

Figure 7.18 Schematic diagram of a dual curvature URSL with magnifications of 8.7 and 2.5.

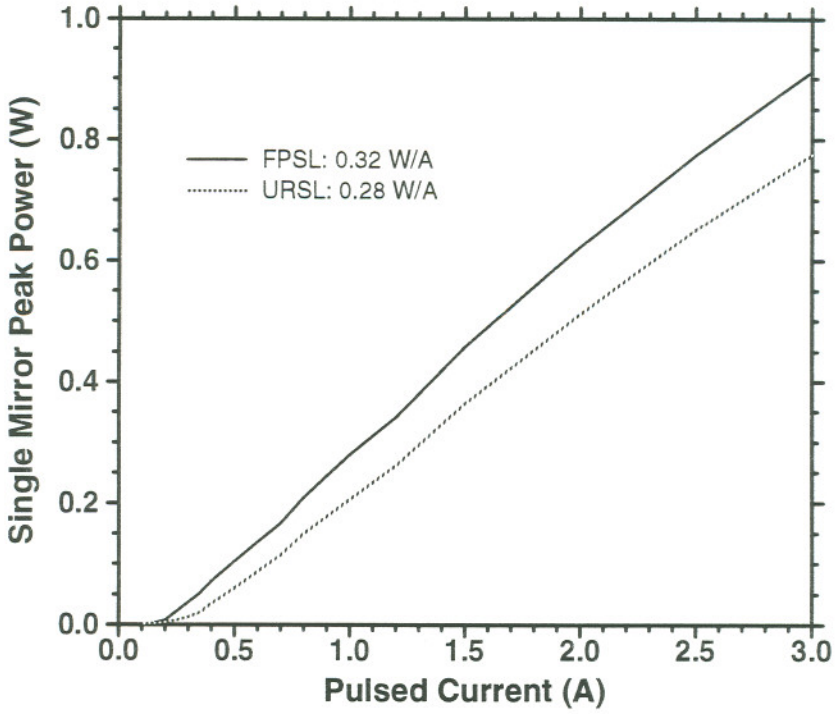

Figure 7.19 L-I curves of a dual curvature URSL and its original FPSL.

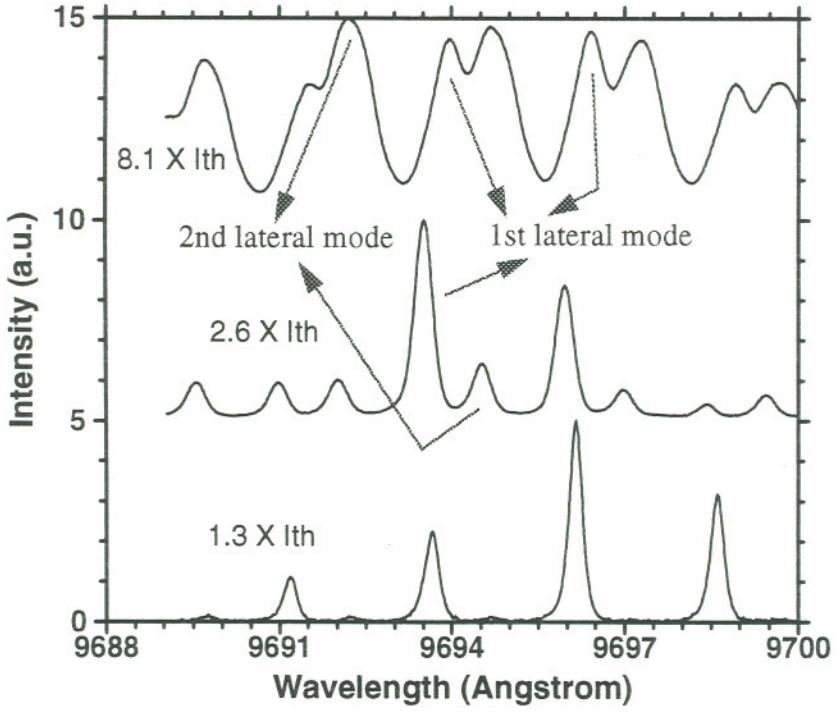

Figure 7.20 Spectral characteristics of a dual curvature URSL with magnifications of 8.7 and 2.5.

region of the curved mirror. However, the optical waves diverging from the center region will not escape the resonator but be amplified by the side regions. In other words, the total resonator loss is dependent mainly on the outer regions, which have low magnification values in the current case. Therefore, the device output efficiency is expected to be close to values observed for conventional low magnification URSLs.

As a result of the dual nature of the curved mirror, this type of URSL does not have a sharp virtual source any more (FWHM width is consistently larger than 30 μm). The strongest portion of the spectrum was recorded for the same device, and plotted in Figure 7.20. Single lateral mode operation was observed around threshold injection. As the injection level increases, a second lateral mode appears, and its intensity gets stronger as the injection level increases further. In the same time, the spectral lines of both modes keep broadening. The separation of the two lateral modes is about 1.0Å at $2.6\times I_{th}$, and 0.7Å at $8.1\times I_{th}$.

Once again, the design/fabrication of this dual curvature URSLs provided additional information towards the understanding of general mechanisms of URSLs although the devices themselves did not generate sharp virtual sources.

7.7 Discussion

In this chapter, preliminary work on URSLs with several different resonator structures has been presented. All the device structures, except the self-collimated URSL, evolved, more or less, from the half-symmetric URSL

with a cylindrical mirror. In terms of device performance, none of these modified structures could compete with the original circular cylindrical URSLs. The latter ones could provide output beams with sharper virtual sources and more uniform near-field profiles. By illustrating both positive and negative effects caused by the structure modifications, however, investigations of these new structures helped in the understanding of the lasing mechanisms of URSLs with cylindrical mirrors, and in the design of cylindrical URSLs with improved performance.

The attempt of shrinking the apparent virtual source envelopes by correcting the refractive aberration of output beams from cylindrical URSLs turned out to be a failure. The reflection properties of cylindrical mirrors are more essential for resonators to generate lasing modes with sharp virtual sources than it is to modify their own potential drawbacks, e.g., refractive aberration effects.

The study of coreless URSLs showed that a laser, with one mirror tilted a few degrees towards the other one, can always lase. This observation may suggest the following picture for describing the lasing action of conventional URSLs with cylindrical mirrors. By dividing a cylindrical URSL into many small longitudinal strips, each strip can be viewed as a narrow coreless URSL, and each strip has the potential to lase on its own as long as the injection level is high enough. The combination of those narrow strip lasers contributes one competition mechanism, which is between the self-lasing of each tilted strip resonator and its amplification of the traveling light from neighboring resonators. As the injection level increases, narrow strip

resonators in the core of the cylindrical URSL, i.e., having relatively small mirror tilt angles, will reach their thresholds first. The overall effect is the broadening of every individual longitudinal mode. More and more of the outside narrow strip resonators will also be able to lase on their own as the injection level increases further. So, an URSL with a cylindrical mirror has the potential to lase in multiple frequencies, which may be the major obstacle for developing high power and high spatial coherence URSLs. Single and sharp lateral mode operation can only be maintained up to very limited injection levels. For a cylindrical URSL having higher magnification, single lateral mode operation may be maintained up to higher injection levels, however, the output power efficiency will be lower. There exists a trade-off between lasing mode quality and optical output power efficiency.

The same analysis can also be applied to a hybrid URSL, which may be viewed as consisting of two coreless URSLs and a narrow FPSL. Obviously, a hybrid URSL would also, as it did, operate in multiple frequencies as injection level increases.

Only prototype devices were fabricated using the self-collimated URSL design. The collected results can serve only as qualitative reference when evaluating the potential performance of devices with that design. Preliminary results of the self-collimated URSL did confirm the original objective of the resonator design — generating laterally collimated output beams. However, the output beam quality degraded as the injection levels increased. To achieve better performance, metal stripe patterning and mirror alignment may need to be improved.

It is anticipated[154] that the simple core-amplifier URSL model will break down when the coupling between the core and side regions of the URSL is strong. In that circumstance, there are only modes of the whole resonator. Plane wave expansion technique would be more suitable for optical wave propagation analysis than the ray tracing method used in this dissertation. As injection level increases, hole burning effects will eventually become strong enough and break the resonator (of an URSL) apart as it does in a FPSL at lower injection levels. The hole burning effects may contribute to the spectral broadening of individual modes and the spatial broadening of lateral virtual source profiles.

Chapter 8

CONCLUSIONS AND SUGGESTIONS FOR FUTURE WORK

8.1 Summary and Discussions

Developments in both theoretical and experimental studies of unstable resonator semiconductor lasers have been presented in this dissertation. Theoretical analysis have been carried out for a geometrical URSL model, which provides evaluations of device power characteristics and simple optimization design guidelines. By refining cylindrical mirror processing technology, high performance URSLs were fabricated from several different types of III/V quantum well laser materials. Operating characteristics of URSLs with a variety of structures have been studied. The advantages of URSLs in potential applications have also been discussed.

In the theoretical aspect, a geometrical URSL model was introduced to describe device operating characteristics such as the dependence of lasing threshold and efficiency on laser cavity length and resonator magnification. By introducing the concept of equivalent cavity length, the unstable resonator loss was equated to that of a Fabry-Perot resonator with this equivalent

cavity length, which is shorter than the URSL cavity length. In an attempt to optimize the device efficiency and impose mode selection capability, metal stripes can be designed to match the resonator mode patterns. The details will be presented later in this chapter.

In the aspect of device fabrication, focused-ion-beam micromachining (FIBM) has been used to fabricate curved mirrors. Cylindrical mirrors have been fabricated with an RMS surface roughness in nanometer levels. In principle, an atomic force microscope (AFM) would be a better instrument for characterizing surface roughness than a Zygo laser interferometric microscope because of its higher lateral resolution. The lateral resolution is in the range of tens of Angstroms for the former, and slightly less than half a micron for the latter one. However, laser interferometric microscopes are more efficient than AFMs in measuring the overall mirror contour with a dimension of hundreds microns. The maximum field of view, corresponding to minimum lateral resolution, of an AFM is less than 100 micron. The mirror quality dependence of device performance was discussed, and applied to the analysis of GaInP URSL performance. Micromachining strategies were also designed for mirrors other than convex cylindrical structures. Several different types of mirrors were fabricated for URSLs having self-collimated, refractive-aberration-corrected, hybrid, coreless, and dual curvature resonator structures.

Investigations have been extended to cover several different types of III/V quantum well laser materials. The relevant optical and electrical properties of these materials were characterized. Performance differences

between different materials were also discussed. Some simple design guidelines were established. In order to maintain efficient operation, the equivalent cavity length of an URSL was required to be slightly larger than the optimum cavity length of the laser material structure.

In the aspect of device characterization, experimental results of this study have helped in the understanding of the fundamentals of URSLs. Observation of the curved subthreshold spatio-spectral patterns led to the proposal of a core-amplifier URSL model. The virtual source width (FWHM) of an URSL usually approaches a diffraction-limited value around a lasing threshold, and then broadens with increasing injection levels. A low magnification (< 4.0) URSL usually operates in single lateral mode at low injection levels, and in multiple lateral modes as injection goes beyond four or five times of threshold. High magnification URSLs were found to lase in either single lateral mode or multiple isolated lateral mode bands. As the injection level increases, lateral mode broadening was observed for all types of URSLs that were tested. Furthermore, streak camera results showed that the broadening of virtual source envelopes also corresponds to the erratic dynamics of lateral modes. The virtual source broadening behavior could vary from one device to another, even though nominally the same device geometry was used. This observation may indicate that material non-uniformity is still a critical factor leading to inconsistent performance of URSLs.

The other, and one of the most important, findings of this work is that the positive branch URSLs, such as half-symmetric URSLs, can provide

optical point sources with brightness values much higher than those achievable from Fabry-Perot type laser devices. This unique feature makes URSLs promising candidates for many applications, e.g., pumping sources for solid-state lasers and harmonic generation, free space communications, remote optical detonation, etc.

URSLs with non-circular cylindrical mirror resonator configurations have provided important additional information. Circular cylindrical mirrors contribute circular aberrations in both reflection and refraction processes. The former would directly cause the deviations of resonator modes from those described by the geometrical URSL model. Fortunately, in the geometrical limit, this reflection aberration effect is negligible for half-symmetric URSLs covered in this dissertation. In an attempt to achieve sharper (or brighter) virtual sources, designs were carried out for refraction-aberration-corrected (RAC) end mirrors,[148, 155] which turned out to be less curved than cylindrical mirrors. However, the fabricated half-symmetric RAC URSLs did not show any improved performance. On the contrary, the virtual sources broadened much faster than those of URSLs with cylindrical mirrors. Considering that the RAC mirrors lead to stronger reflection aberration than the circular cylindrical mirrors, one speculation that might be drawn here is that enhanced reflection aberration may strongly affects the stability of URSL modes.

Devices with hybrid and coreless resonator structures were also fabricated. Based on the observed lasing characteristics, questions were raised about the lasing mechanism of these devices with tilted end mirrors. It is

not clear how the formation of lateral modes can be related to the specific resonator parameters of these types of devices. Other resonator structures that have been studied include self-collimated confocal URSLs, and dual curvature URSLs. Since only limited efforts were devoted to this task, and limited results were achieved, the author cannot draw definite conclusions, but in general, no improvements with respect to the circular cylindrical mirror URSL evolved.

The spectral coherence properties of the output beams have not been evaluated for many of the URSLs described in this dissertation. The URSL spectrum usually consists of multiple longitudinal modes, and broadens with increasing injection current. Since the temporal coherence length of the output beam is inversely proportional to the spectral bandwidth,[131, 156] URSLs with cylindrical mirrors clearly do not achieve as high temporal coherence as those single frequency devices, such as DFB lasers.[38]

Spatial coherence properties[131, 156] are related to the emitting area of the source and the divergence characteristics of the optical beam. Full spatial coherence can be achieved with a circular wavefront, which is associated with a line source. Near circular waves can be focused to a line size approaching finite wavelength limits, or collimated to travel with minimal divergence. The smallest source size is the so-called "diffraction limited" size, which is described in Appendix D for URSLs. The virtual source sizes measured for all the URSLs are nearly diffraction-limited around threshold, and often several times diffraction-limited at high injection levels. For some GaAs/AlGaAs triplet SQW URSLs, the virtual source sizes were found to be

only about twice of the diffraction-limited value at injection levels as high as $6.0 \times I_{th}$. Undesired deviations from the "diffraction-limited" values are directly linked to mode broadening/splitting behavior and dynamic instability.

Recently, exciting results have also been achieved from broad-area semiconductor master oscillator optical amplifiers (MOPAs).[157-161] 11.6 W diffraction-limited peak power was reported for a diode-to-diode optical amplifier.[162] And 21 W near-diffraction-limited peak power was achieved for a Ti: Sapphire laser pumped single pass GaAlAs traveling wave amplifier.[163] CW output power up to 3.5 W and 4.5 W have been reported for a tapered traveling wave amplifier and a laser with tapered gain region, respectively.[164] However, all the amplifiers still have to face the same problem as URSLs do, i.e., the beam quality degrades as the injection level increases. Scaling of the device cavity is limited due to gain saturation. The taper angle, which determines the lateral scaling range, is limited by the width of the master oscillator to only a few degrees. The formation of filaments was predicted by theory, and directly demonstrated in the operation of a broad-area active grating amplifier (MOPA).[165, 166] For the tapered lasers, the small uncoated back facet is practically at the focal point of the lasing mode, and the optical power density there reaches the COD limit quite easily.[164] In comparison with URSLs, tapered amplifiers/lasers have demonstrated better simultaneous spatial and spectral (single frequency) coherence at $1 \sim 2$ Watts of output power levels. The junction between master oscillator and tapered region can be equivalently taken as the real source for the output

beam from a tapered device, i.e., the master oscillator width sets the low limit (5 ~ 8 μm) for the lateral source sizes. On the other hand, URSLs may enjoy larger scaling flexibility. At this point, it is hard to declare which of the two designs, the URSL or the amplifier (MOPA), is better for future development of high power and high brightness optical sources.

8.2 Suggestions for Future Work

Simple analysis based on geometrical optics can be applied to the design of URSL metal contact patterns to improve the device performance. As shown in Figure 8.1a, the geometrical unstable resonator mode pattern ($A_1C_1B_1B_2C_2A_2$) is confined by the four marginal rays, which start at the Siegman centers (P1 or P2) and end at the opposite margins (B_1B_2 or A_1A_2) of the metal stripe. In principle, any optical rays that fall beyond this mode area will be absorbed by the wafer material, so only the optical gain inside this defined mode area can be efficiently utilized. In other words, the power efficiency can be optimized by matching the metal contact to the mode area.

Unknown parameters needed to define the shaded area shown in Figure 8.1a can be determined in the following way. Assuming that the mirror aperture widths are $2a_1$ and $2a_2$, the angles between the marginal rays of the two counter-going waves and the resonator axis can be expressed as

$$\theta_1 = \tan^{-1}\frac{a_2}{(r_1 + 1)L} \tag{8.1}$$

and

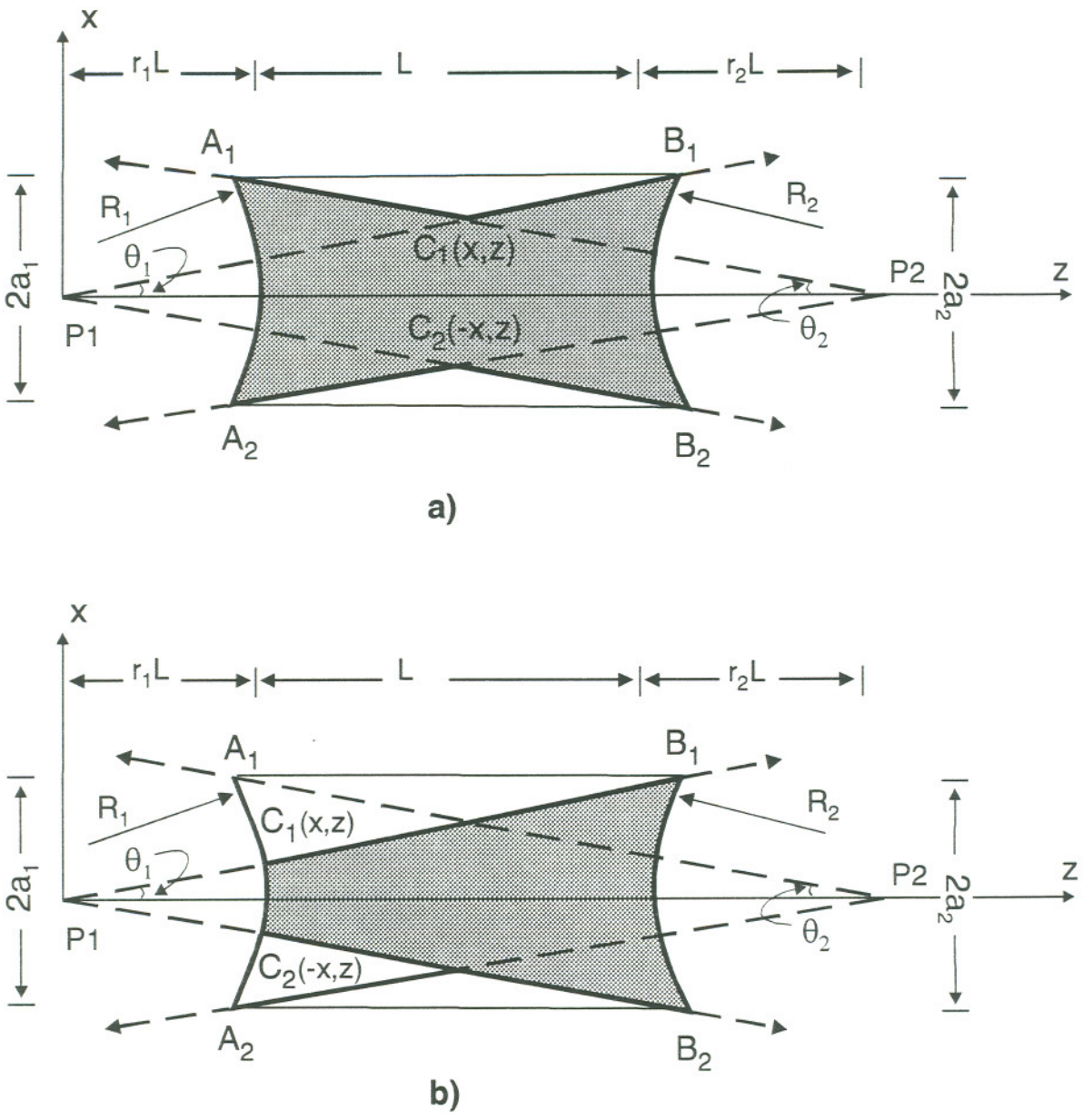

Figure 8.1 Efficient Design of metal contacts for unstable resonator semiconductor lasers, a) with both end mirrors uncoated, b) with left end mirror high-reflectivity (HR) coated.

$$\theta_2 = \tan^{-1}\frac{a_1}{(r_2 + 1)L}, \tag{8.2}$$

respectively. Furthermore, assuming that the origin of the two-dimensional Cartesian coordinate system is at the position of the left virtual source, then a straightforward geometrical derivation leads to the following expressions for the coordinates of $C_1(x,z)$ and $C_2(-x,z)$ as

$$x = \frac{(r_1 + r_2 + 1)a_1a_2}{(r_2 + 1)a_2 + (r_1 + 1)a_1}, \tag{8.3}$$

$$z = \left(\frac{(r_1 + 1)(r_2 + 1)a_1 - r_1(r_2 + 1)a_2}{(r_2 + 1)a_2 + (r_1 + 1)a_1} + 1\right)L. \tag{8.4}$$

It is possible to achieve efficient pumping by matching the metal contact patterns with the resonator mode structures. For typical uncoated URSLs, the two symmetric triangular regions $A_1B_1C_1$ and $A_2B_2C_2$, as shown in Figure 8.1a, can be left unmetallized. Then the metalization can be patterned in the shape of the shaded area shown in Figure 8.1a instead of a rectangular stripe for a Fabry-Perot type laser. In practical applications, the URSLs would usually be high-reflection (HR) coated with one mirror, e.g., left one, and low reflectance coated with the other one. The metallization pattern can be even further shrunk to a tapered shape, as schematically shown in Figure 8.1b. The metal contact needs only to match the outgoing mode pattern, i.e., the shaded region defined by $C_1B_1B_2C_2$. The coordinates of positions $C_1(x,z)$ and $C_2(-x,z)$ are simply

$$x = r_1L\tan\theta_1 = \frac{r_1a_2}{r_1 + 1}, \tag{8.5}$$

$$z = r_1 L. \tag{8.6}$$

In principle, this tapered metal contact provides the maximum gain-guiding to the spatial mode that diverges from the geometrical virtual source, i.e., has certain mode selection capability[153].

Considering the simplest case, the metal contact of a half-symmetric URSL is designed to have same aperture width at the two end mirrors, i.e., $a_1 = a_2 = a$, as shown in Figure 8.1a. Then, the total area of the regions that are beyond the mode pattern can be derived as

$$A_{idle} = (a - x)L = \frac{aL}{r_1 + r_2 + 2}$$
$$= \frac{A_0}{2(r_1 + r_2 + 2)} = \frac{M - 1}{2(3M + 1)} A_0, \tag{8.7}$$

where A_0 is the total area of the rectangular stripe. It is interesting to note that the ratio of A_{idle} to A_0 depends only on the resonator magnification. Further numerical calculations showed that this ratio is about 10% for resonators with 2.5 ~ 4.0 magnification and 500 μm ~ 1000 μm long stripes. From the perspective of geometrical optics, this metal contact will reduce the threshold current, and increase the total efficiency by roughly 10%. When the left mirror is HR coated, as shown in Figure 8.1b, the metal contact can be shrunk by a larger area

$$A_{idle} = (a - x)L = \frac{aL}{r_1 + 1} = \frac{1}{2(r_1 + 1)} A_0 = \frac{M - 1}{4M} A_0. \tag{8.8}$$

For devices having 2.5 magnification, about 15% of the original rectangular stripe can be left unmetalized. It is also speculated[153] that this optimized metal design may enhance lateral mode discrimination since it provides gain

guiding only to a region that matches the geometrical mode pattern.

It was noticed, in both our own observation and a separate report,[167] that half-symmetric URSLs with higher magnifications usually provide sharper virtual sources, but lower output power efficiencies due to the higher resonator losses. Higher magnification leads to stronger mode discrimination. A low magnification URSL always lases in multiple lateral modes as injection current increases to certain level. On the other hand, lower magnification URSLs have higher power efficiencies. Ideally, a low magnification URSL with enhanced mode discrimination would be able to provide output beam with sharp virtual source and high power efficiency. Recently, the design of URSL resonator structure has also been extended to include extra longitudinal mode discrimination mechanism. To achieve single frequency operation, i.e., to increase the temporal coherence, a grating URSL design was proposed.[155] Another recent proposal[153] is to incorporate a narrow grating in the core-region of a conventional cylindrical mirror URSL. Based on the core-amplifier URSL model, the whole device has the potential to lase in the same single frequency of the DFB oscillator in core region. Experimental work is now underway to demonstrate this latter idea.

In conclusion, this dissertation provides simple theoretical tools for the design of URSLs, observations helpful to the understanding of lasing mechanisms and general operating characteristics of URSLs, and encouraging experimental results that confirm the potential high power and high brightness applications of positive branch URSLs. These results are also expected to be helpful to conducting future designs of (or the extensions of

UR concepts to) semiconductor laser devices. Yet, there are still many issues left unsolved about URSLs. Major issues are related to the formation of lateral mode(s), control of mode broadening and splitting behavior, and dynamical instability. From a theoretical point of view, most of the issues may have to be handled in a way more complicated than the geometrical model. From a technical point of view, answers to these issues may be approached by studying devices with more complicated structures, such as grating URSLs and tapered URSLs, which provide enhanced mode discrimination. In reality, the material quality might still be the key factor in limiting the performance of URSLs. Desirable technologies would be those that enable the growing of high quality semiconductor epi-layers up to millimeter dimension, and maintaining the quality during the device fabrication and handling process.

References

1. P. A. Kirkby, A. R. Goodwin, G. H. B. Thompson, and P. R. Selway, "Observations of self-focusing in stripe geometry semiconductor lasers and the development of a comprehensive model of their operation," *IEEE J. Quantum Electron*, vol. QE-13(8), pp. 705-719, August 1977.
2. D. R. Scifres, R. D. Burnham, and W. Streifer, "High power coupled multiple stripe quantum well injection lasers," *Appl. Phys. Lett.*, vol. 41(2), pp. 118-120, 15 July 1982.
3. D. R. Scifres, W. Streifer, and R. D. Burnham, "High-power coupled-multiple-stripe phase-locked injection laser," *Appl. Phys. Lett.*, vol. 34(4), pp. 259-261, 15 February 1979.
4. D. R. Scifres, W. Streifer, and R. D. Burnham, *IEEE J. Quantum Electron.*, vol. QE-15, p. 917, 1979.
5. A. E. Siegman, "Unstable optical resonators for laser applications," *Proc. IEEE*, vol. 53, pp. 277-287, March 1965.
6. A. P. Bogatov, P. G. Eliseev, M. A. Man'ko, G. T. Milaslyan, and Y. M. Popov, "Injection laser with an unstable resonator," *Sov. J. Quantum Electron.*, vol. 10 (5), pp. 620-622, May 1980.
7. R. Craig, L. Casperson, D. Stafsudd, J. Yang, G. Evans, and R. Davidheiser, "Etched mirror unstable resonator semiconductor lasers," *Electron. Lett.*, vol. 21 (2), pp. 62-63, 17 Jan 1985.
8. R. R. Craig, "Unstable Resonator Semiconductor Lasers," *Ph.D. Dissertation*, University of California, Los Angeles, Los Angeles, California, 1985.
9. R. Lang, M. Mittelstein, A. Yariv, and J. Salzman, "Unstable resonator semiconductor lasers I-Theory," *IEEE Proc. J.*, vol. 134 (1), pp. 69-75, Feb 1987.
10. J. Salzman, T. Venkatesan, R. Lang, M. Mittelstein, and A. Yariv, "Unstable resonator semiconductor lasers II-Experiment," *IEEE Proc. J.*, vol. 134 (1), pp. 76-86, Feb 1987.
11. M. L. Tilton, G. C. Dente, A. Paxton, J. Cser, R. K. DeFreez, C. Moeller, and D. Depatie, "High power, nearly diffraction-limited output from a semiconductor laser with an unstable resonator," *IEEE J. Quantum Electron.*, vol. QE-27(9), pp. 2098-2108, September 1991.
12. R. K. DeFreez, Z. Bao, P. D. Carleson, M. K. Felisky, and C. Largent, "High-

brightness unstable resonator semiconductor lasers," *Proc. SPIE, Laser Diode Technology and Applications V*, vol. 1850, pp. 75-83, 1993.

13. A. E. Siegman, *Lasers* , Chapters 22 & 23, University Science Books, Mill Valley, California, 1986.
14. R. J. Lang, J. Salzman, and A. Yariv, "Modal analysis of semiconductor lasers with nonplanar mirrors," *IEEE J. Quantum Electron.*, vol. QE-22(3), pp. 463-470, March 1986.
15. J. Salzman, R. Lang, and A. Yariv, "Efficiency of unstable resonator semiconductor lasers," *Electron. Lett.*, vol. 21(18), pp. 821-823, 29 August 1985.
16. M. L. Tilton, G. C. Dente, and A. H. Paxton, "Mode control of broad area semiconductor lasers using unstable resonators," *Proc. SPIE, Laser-Diode Technology and Applications II*, vol. 1219, pp. 423-434, 1990.
17. G. R. Hadley, J. P. Hohimer, and A. Owyoung, "Comprehensive modeling of diode arrays and broad-area devices with applications to lateral index tailoring," *IEEE J. Quantum Electron.*, vol. QE-24(11), pp. 2138-2152, November 1988.
18. R. J. Lang, "Geometric formulation of unstable-resonator design and application to self-collimating unstable-resonator diode lasers," *Opt. Lett.*, vol. 16(17), pp. 1319-1321, 1 September 1991.
19. R. K. DeFreez, Z. Bao, P. D. Carleson, C. Largent, C. Moeller, G. C. Dente, D. J. Gallant, J. Metz, M. L. Tilton, G. A. Evans, W. F. Reichert, C. A. Wang, and H. K. Choi, "A high power unstable resonator semiconductor laser," *Proceedings of the Conference on Lasers and Electro-Optics, paper CWN3*, pp. 340-342, Anaheim, California, May 10-15, 1992.
20. Z. Bao, R. K. DeFreez, P. D. Carleson, C. Largent, C. Moeller, and G. C. Dente, "Spatio-spectral characteristics of a high power, high brightness CW InGaAs/AlGaAs unstable resonator semiconductor laser," *Electron. Lett.*, vol. 29(18), pp. 1597-1599, 2nd September 1993.
21. Z. Bao, R. K. DeFreez, P. D. Carleson, M. K. Felisky, C. Largent, and H. B. Serreze, "Design considerations for high power GaInP/AlGaInP unstable resonator semiconductor lasers," *Appl. Opt.*, vol. 32(36), pp. 7402-7407, 20 December 1993.
22. S. T. Srinivasan, C. F. Schaus, S. Sun, E. A. Armour, A. H. Paxton, D. J. Gallant, and C. E. Moeller, "Semiconductor laser with unstable resonator consisting of negative cylindrical lenses," *Proc. SPIE, Laser Diode Technology and*

Applications IV, vol. 1634, pp. 413-419, 1992.

23. S. T. Srinivasan, C. F. Schaus, S.-Z. Sun, E. A. Armour, S. D. Hersee, J. G. McInerney, A. H. Paxton, and D. J. Gallant, "High-power spatially coherent operation of unstable resonator semiconductor lasers with regrown lens trains," *Appl. Phys. Lett.*, vol. 61(11), pp. 1272-1274, 14 September 1992.
24. A. H. Paxton, C. F. Schaus, and S. T. Srinivasan, "Semiconductor laser with regrown-lens-train unstable resonator: Theory and design," *IEEE J. Quantum Electron.*, vol. QE-29(11), pp. 2784-2792, November 1993.
25. Z. Bao and R. K. DeFreez, "Theoretical analysis of unstable resonator semiconductor lasers," *Proc. SPIE*, vol. 2146, to be published, 1994.
26. L. W. Casperson, "Power characteristics of high magnification semiconductor lasers," *Optical and Quantum Electronics*, vol. 18, pp. 155-167, 1986.
27. J. L. Merz and R. A. Logan, "GaAs double heterostructure lasers fabricated by wet chemical etching," *J. Appl. Phys.*, vol. 47(8), pp. 3503-3509, August 1976.
28. J. E. Whiteaway and G. H. B. Thompson, "Optimisation of power efficiency of (GaAl)As injection lasers operating at high power levels," *Solid-state and Electron Devices*, vol. 1(3), pp. 81-88, April 1977.
29. K. Petermann, *Laser Diode Modulation and Noise*, Chapter 2, Kluwer Academic Publishers, Netherlands, 1988.
30. H. Kressel and J. K. Butler, *Semiconductor Lasers and Heterojunction LEDs*, Academic Press, Inc, 1977.
31. C. H. Henry, "The origin of quantum wells and the quantum well laser," *Quantum Well Lasers*, pp. 1-16, P. S. Zory, Jr. ed., Academic Press, Inc., 1993.
32. C. Weisbuch, "Fundamental properties of III-V semiconductor two-dimensional quantized structures: The basis for optical and electronic device applications," *Semiconductors and Semimetals*, vol. 24, pp. 1-133, Raymond Dingle ed., Academic Press, Inc., 1987.
33. S. Itoh, H. Okuyama, S. Matsumoto, N. Nakayama, T. Ohata, T. Miyajima, A. Ishibashi, and K. Akimoto, "Room temperature pulsed operation of 498 nm laser with ZnMgSSe cladding layers," *Electron. Lett.*, vol. 29(9), pp. 766-767, 29 April 1993.
34. P. S. Zory, Editor, *Quantum Well Lasers*, Academic Press, 1993.
35. K. Y. Lau, "Dynamics of quantum well lasers," *Quantum Well Lasers*, pp. 217-

276, P. S. Zory, Jr. ed., Academic Press, Inc., 1993.

36. J. J. Coleman, "Strained layer quantum well heterostructure lasers," *Quantum Well Lasers*, pp. 367-414, P. S. Zory, Jr. ed., Academic Press, Inc., 1993.

37. G. H. B. Thompson, *Physics of Semiconductor Laser Devices*, John Wiley & Sons, Ltd, 1980.

38. G. P. Agrawal and N. K. Dutta, *Long-Wavelength Semiconductor Lasers*, Van Nostrand Reinhold, 1986.

39. J. Z. Wilcox, S. Ou, J. J. Yang, M. Jansen, and G. L. Peterson, "Dependence of external differential efficiency on laser length and reflectivities in multiple quantum well lasers," *Appl. Phys. Lett.*, vol. 55(9), pp. 825-827, 28 August 1989.

40. A. Sugimura, "Threshold currents for AlGaAs quantum well lasers," *IEEE J. Quantum Electron.*, vol. QE-20(4), pp. 336-343, April 1984.

41. A. R. Reisinger, P. S. Zory, and R. G. Waters, "Cavity length dependence of the threshold behavior in thin quantum well semiconductor Lasers," *IEEE J. Quantum Electron.*, vol. QE-23(6), pp. 993-999, June 1987.

42. R. Nagarajan, T. Kamiya, and A. Kurobe, "Band filling in GaAs/AlGaAs multiquantum well lasers and its effect on the threshold current," *IEEE J. Quantum Electron.*, vol. QE-25(6), pp. 1161-1170, June 1989.

43. H. C. Casey, Jr., "Room-temperature threshold current dependence of $GaAs-Al_xGa_{1-x}As$ double heterostructure lasers on x and active layer thickness," *J. Appl. Phys.*, vol. 49, pp. 3684-3692, July 1978.

44. R. W. H. Engelmann, C. L. Shieh, and C. Shu, "Multiquantum well lasers: Threshold considerations," *Quantum Well Lasers*, pp. 131-188, P. S. Zory, Jr. ed., Academic Press, Inc., 1993.

45. P. S. Zory, A. R. Reisinger, L. J. Mawst, G. Costrini, C. A. Zmudzinski, M. A. Emanuel, M. E. Givens, and J. J. Coleman, "Anomalous length dependence of threshold in thin quantum well AlGaAs diode lasers," *Electron. Lett.*, vol. 22(9), pp. 475-476, 24 April 1986.

46. S. S. Ou, J. J. Yang, R. J. Fu, and C. J. Hwang, "High-power 630-640 nm GaInP/GaAlInP laser diodes," *Appl. Phys. Lett.*, vol. 61(8), pp. 892-894, 24 August 1992.

47. C. B. Su and R. Olshansky, "Carrier lifetime measurement for determination

of recombination rates and doping levels of III-V semiconductor light sources," *Appl. Phys. Lett.*, vol. 41(9), pp. 833-835, 1 November 1982.

48. R. Olshansky, C. B. Su, J. Manning, and W. Powazinik, "Measurement of radiative and nonradiative recombination rates in InGaAsP and AlGaAs light sources," *IEEE J. Quantum Electron.*, vol. QE-20(8), pp. 838-854, August 1984.
49. N. K. Dutta, R. L. Hartman, and W. T. Tsang, "Gain and carrier lifetime measurements in AlGaAs single quantum well lasers," *IEEE J. Quantum Electron.*, vol. QE-19(8) , pp. 1243-1246, August 1983.
50. N. Yu, R. K. DeFreez, D. J. Bossert, G. A. Wilson, R. A. Elliott, S. S. Wang, and H. G. Winful, "Spatio-spectral and picosecond spatio-temporal properties of a broad area operating channeled-substrate-planar laser array," *Appl. Opt.*, vol. 30, pp. 2503-2513, 20 June 1991.
51. N. Yu, "Dynamic Characterization of Coherent Semiconductor Laser Arrays," *Ph.D. Dissertation*, Oregon Graduate Institute of Science & Technology, Beaverton, Oregon, 1990.
52. C. A. Wang and H. K. Choi, "Organometallic vapor phase epitaxy of high-performance strained-layer InGaAs-AlGaAs diode lasers," *IEEE J. Quantum Electron.*, vol. QE-27(3), pp. 681-686, March 1991.
53. D. K. Wagner, R. G. Waters, P. L. Tihanyi, D. S. Hill, A. J. Roza, Jr., H. J. Vollmer, and M. M. Leopold, "Operating characteristics of single-quantum-well AlGaAs/GaAs high-power lasers," *IEEE J. Quantum Electron.*, vol. QE-24(7), pp. 1258-1265, July 1988.
54. J. Z. Wilcox, G. L. Peterson, S. Ou, J. J. Yang, and M. Jansen, "Gain-and threshold-current dependence for multi-quantum-well lasers," *J. Appl. Phys.*, vol. 64(11), pp. 6564-6567, 1 December 1988.
55. T. A. DeTemple and C. M. Herzinger, "On the semiconductor laser logarithmic gain-current density relation," *IEEE J. Quantum Electron.*, vol. QE-29(5), pp. 1246-1252, May 1993.
56. J. Manning, R. Olshansky, and C. B. Su, "The carrier-induced index change in AlGaAs and 1.3 μm InGaAsP diode lasers," *IEEE J. Quantum Electron.*, vol. QE-19, pp. 1525-1530, 1983.
57. B. W. Hakki and T. L. Paoli, "Gain spectra in GaAs double heterostructure injection lasers," *J. Appl. Phys.*, vol. 46, pp. 1299-1306, March 1975.

58. A. Yariv, *Introduction to Optical Electronics*, Holt, Rinehart and Winston, 2nd Edition, 1976.

59. A. E. Siegman, "Defining the effective radius of curvature for a nonideal optical beam," *IEEE J. Quantum Electron.*, vol. QE-27(5), pp. 1146-1148, May 1991.

60. A. E. Siegman, "New developments in laser resonators," *Proc. SPIE, Laser Resonators*, vol. 1224, pp. 2-14, 1990.

61. J. A. Ruff and A. E. Siegman, "Single-pulse laser beam quality measurements using a CCD camera system," *Appl. Opt.*, vol. 31(24), pp. 4907-4909, 20 August 1992.

62. M. W. Sasnett and T. F. Johnston, "Beam characterization and measurement of propagation attributes," *Proc. SPIE., Laser Beam Diagnostics (1991)*, vol. 1414, pp. 21-32, 1991.

63. G. Hatakoshi, K. Itaya, M. Ishikawa, M. Okajima, and Y. Uematsu, "Short-wavelength InGaAlP visible laser diodes," *IEEE J. Quantum Electron.*, vol. QE-27(6), pp. 1476-1482, June 1991.

64. K. Kobayashi, I. Hino, A. Gomyo, S. Kawata, and T. Suzuki, "AlGaInP double heterostructure visible-light laser diodes with a GaInP active layer grown by metalorganic vapor phase epitaxy ," *IEEE J. Quantum Electron.*, vol. QE-23(6), pp. 704-711, June 1987.

65. D. P. Bour, "AlGaInP quantum well lasers," *Quantum Well Lasers*, pp. 415-460, P. S. Zory, Jr. ed., Academic Press, Inc., 1993.

66. H. Hamada, M. Shono, S. Honda, R. Hiroyama, K. Yodoshi, and T. Yamaguchi, "AlGaInP visible laser diodes grown on misoriented substrates," *IEEE J. Quantum Electron.*, vol. QE-27(6), pp. 1483-1490, June 1991.

67. M. Ikeda, Y. Mori, H. Sato, K. Kaneko, and N. Watanabe, "Room-temperature continuous-wave operation of an AlGaInP double heterostructure laser grown by atmospheric pressure metalorganic chemical vapor deposition," *Appl. Phys. Lett.*, vol. 47(10), pp. 1027-1028, 15 November 1985.

68. K. Kobayashi, S. Kawata, A. Gomyo, I. Hino, and T. Suzuki, "Room-temperature cw operation of AlGaInP double heterostructure visible lasers," *Electron. Lett.*, vol. 21, pp. 931-932, 1985.

69. H. Okuda, M. Ishikawa, H. Shiozawa, Y. Watanabe, K. Itaya, K. Nitta, G. Hatakoshi, Y. Kokobun, and Y. Uematsu, "Highly reliable InGaP/InGaAlP visible light emitting inner stripe lasers with 667 nm lasing wavelength," *IEEE*

J. Quantum Electron., vol. QE-25, p. 1477, 1989.

70. T. Katsuyama, I. Yoshida, J. Shinkai, J. Hashimoto, and H. Hayashi, "High temperature (> 150 °C) and low threshold current operation of AlGaInP/$Ga_xIn_{1-x}P$ strained multiple quantum well visible laser diodes," *Appl. Phys. Lett.*, vol. 59(26), pp. 3351-3353, 23 December 1991.

71. H. Tanaka, Y. Kawamura, and H. Asahi, "Room-temperature operation of MBE-grown InGaP/InGaAlP MQW visible laser diodes," *Electron. Lett.*, vol. 22, p. 707, 1986.

72. H. Hamada, K. Tominaga, M. Shono, S. Honda, K. Yodoshi, and T. Yamaguchi, "Room-temperature CW operation of 610 nm band AlGaInP strained multiquantum well laser diodes with multiquantum barrier," *Electron. Lett.*, vol. 28(19), pp. 1834-1835, 10 September 1992.

73. T. Katsuyama, I. Yoshida, J. Hashimoto, and H. Hayashi, "Strain effects on the performance of AlGaInP/$Ga_xIn_{1-x}P$ single quantum well visible laser diodes," *Tech. Digest, Conf. on Lasers and Electro-Optics (CLEO 1991)*, p. 96, 1991.

74. T. Katsuyama, I. Yoshida, J. Shinkai, J. Hashimoto, and H. Hayashi, "Very low threshold current AlGaInP/$Ga_xIn_{1-x}P$ strained single quantum well visible laser diode," *Electron. Lett.*, vol. 26(17), p. 1375, 16 August 1990.

75. J. Hashimoto, T. Katsuyama, I. Yoshida, and H. Hayashi, "Effects of strained-layer structures on the threshold current density of AlGaInP/GaInP visible lasers," *Appl. Phys. Lett.*, vol. 58(9), pp. 879-880, 4 March 1991.

76. H. B. Serreze, Y. C. Chen, and R. G. Waters, "High-power, very low-threshold, GaInP/AlGaInP visible diode lasers," *Appl. Phys. Lett.*, vol. 58, pp. 2464-2466, 3 June 1991.

77. H. B. Serreze, Y. C. Chen, R. G. Waters, and C. M. Harding, "Very low threshold, high power GaInP/AlGaInP visible laser diodes," *Tech. Digest, Conf. on Lasers and Electro-Optics (CLEO 1991)*, p. 571, postdeadline paper CPDP1-1, 1991.

78. D. P. Bour and J. R. Shealy, "Organometallic vapor phase epitaxial growth of $(Al_xGa_{1-x})_{0.5}In_{0.5}P$ and its heterostructures," *IEEE J. Quantum Electron.*, vol. QE-24(9), pp. 1856-1863, September 1988.

79. D. P. Bour and J. R. Shealy, "High power (1.4 W) AlGaInP graded-index separate confinement heterostructure visible ($\lambda \sim 658$ nm) laser," *Appl. Phys.*

Lett., vol. 51, p. 1658, 1987.

80. D. P. Bour, N. W. Carleson, and G. A. Evans, "Characteristic temperature of GaInP/AlGaInP single quantum well lasers," *Electron. Lett.*, vol. 25(18), pp. 1243-1245, 31 August 1989.

81. M. Ikeda, A. Toda, K. Nakano, Y. Mori, and N. Watanabe, "Room-temperature continuous-wave operation of a GaInP/AlGaInP multiquantum well laser grown by metalorganic chemical vapor deposition," *Appl. Phys. Lett.*, vol. 50(16), pp. 1033-1034, 20 April 1987.

82. H. B. Serreze, C. M. Harding, and R. G. Waters, "1 W CW, 672 nm visible laser diode," *Electron. Lett.*, vol. 27(24), pp. 2245-2246, 21 November 1991.

83. D. P. Bour, D. W. Treat, R. L. Thornton, T. L. Paoli, R. D. Bringans, B. S. Krusor, R. S. Geels, D. F. Welch, and T. Y. Wang, "Low threshold, 633 nm, single tensile-strained quantum well $Ga_{0.6}In_{0.4}P/(Al_xGa_{1-x})_{0.5}In_{0.5}P$ laser," *Appl. Phys. Lett.*, vol. 60(16), pp. 1927-1929, 20 April 1992.

84. H. B. Serreze and Y. C. Chen, "Low-threshold, strained-layer GaInP/AlGaInP GRINSCH visible diode lasers," *IEEE Photonics Technol. Lett.*, vol. 3, pp. 397-399, May 1991.

85. K. Itaya, M. Ishitkawa, Y. Watanabe, K. Nitta, G. Hatakoshi, and Y. Uematsu, "A new transverse-mode stabilized InGaAlP visible light laser diode using p-p isotype heterobarrier blocking," *Jpn. J. Appl. Phys.*, vol. 27(12), pp. L2414-2416, 1988.

86. H. Asai and K. Oe, "Energy band-gap shift with elastic strain in $Ga_xIn_{1-x}P$ epitaxial layers on (001) GaAs substrate," *J. Appl. Phys.*, vol. 54(4), pp. 2052-2056, 1983.

87. R. S. Geels, D. F. Welch, D. R. Scifres, D. P. Bour, D. W. Treat, and R. D. Bringans, "High power, low threshold single-mode 630 nm laser diodes," *Electron. Lett.*, vol. 28(19), pp. 1810-1811, 10 September 1992.

88. W. T. Tsang, "Extension of lasing wavelengths beyond 0.87 μm in $GaAs/Al_xGa_{1-x}As$ double heterostructure lasers by In incorporation in the GaAs active layers during molecular beam epitaxy," *Appl. Phys. Lett.*, vol. 38, pp. 661-663, 1981.

89. D. Feketa, K. T. Chan, J. M. Ballantyne, and L. F. Eastman, "Graded-index separate-confinement InGaAs/GaAs strained-layer quantum well laser grown by metalorganic chemical vapor deposition," *Appl. Phys. Lett.*, vol. 49, pp.

1659-1660, 1986.

90. J. N. Baillargeon, P. K. York, C. A. Zmudzinski, G. E. Fernandez, K. J. Beernink, and J. J. Coleman, "High-power phase-locked InGaAs strained-layer quantum well heterostructure periodic laser array," *Appl. Phys. Lett.*, vol. 53, pp. 457-459, 1988.

91. S. E. Fisher, R. G. Waters, D. Feketa, J. M. Ballantyne, Y. C. Chen, and B. A. Soltz, "Long-lived InGaAs quantum well lasers," *Appl. Phys. Lett.*, vol. 54, pp. 1861-1862, 1989.

92. H. K. Choi and C. A. Wang, "InGaAs/AlGaAs strained single quantum-well diode lasers with extremely low threshold current density and high efficiency," *Appl. Phys. Lett.*, vol. 57, pp. 321-323, 1990.

93. R. N. Hall, G. E. Fenner, J. D. Kingsley, T. J. Soltys, and R. O. Carlson, "Coherent light emission from GaAs p-n junctions," *Phys. Rev. Lett.*, vol. 9, p. 366, November 1962.

94. M. I. Nathan, W. P. Dumke, G. Burns, F. H. Dill, and G. J. Lasher, "Stimulated emission of radiation from GaAs p-n junctions," *Appl. Phys. Lett.*, vol. 1, p. 62, November 1962.

95. T. M. Quist, R. H. Rediker, R. J. Keyes, W. E. Krag, B. Lax, A. L. McWhorter, and H. J. Zeiger, "Semiconductor maser of GaAs," *Appl. Phys. Lett.*, vol. 1, p. 91, December 1962.

96. N. Holonyak, Jr. and S. F. Bevacqua, "Coherent (visible) light emission from $Ga(As_{1-x}P_{x})$ junctions," *Appl. Phys. Lett.*, vol. 1, p. 82, December 1962.

97. J. P. von der Ziel, R. Dingle, R. C. Miller, W. Wiegmann, and W. A. Nordland, Jr., "Laser oscillations from quantum states in very thin $GaAs-Al_{0.2}Ga_{0.8}As$ multilayer structures," *Appl. Phys. Lett.*, vol. 26, pp. 463-465, 1975.

98. W. T. Tsang, "Quantum confinement heterostructure semiconductor lasers," *Semiconductors and Semimetals*, vol. 24, pp. 397-458, Raymond Dingle ed., Academic Press, Inc., 1987.

99. W. F. Kosonocky, R. H. Corneley, and I. J. Hegyi, "Multilayer GaAs injection laser," *IEEE J. Quantum Electron.*, vol. QE-4(4), pp. 176-179, April 1968.

100. H. F. Lockwood, K. F. Etzold, T. E. Stockton, and D. P. Marinelli, "The GaAs P-N-P-N laser diode," *IEEE J. Quantum Electron.*, vol. QE-10(7), pp. 567-569, July 1974.

101. J. P. van der Ziel and W. T. Tsang, "Integrated multilayer GaAs lasers separated by tunnel junctions," *Appl. Phys. Lett.*, vol. 41(6), pp. 499-501, 15 September 1982.

102. C. P. Lee, A. Gover, S. Margalit, I. Samid, and A. Yariv, "Barrier-controlled low-threshold pnpn GaAs heterostructure laser," *Appl. Phys. Lett.*, vol. 30(10), pp. 535-538, 15 May 1977.

103. W. T. Tsang and N. A. Olsson, "New large optical cavity laser with distributed active layers," *Appl. Phys. Lett.*, vol. 42(10), pp. 850-852, 15 May 1983.

104. R. G. Waters, M. A. Emanuel, and R. J. Dalby, "Integrated quantum-well manifold laser," *J. Appl. Phys.*, vol. 66(2), pp. 961-963, 15 July 1989.

105. R. G. Waters, Y. C. Chen, and R. J. Dalby, "Monolithically Stacked quantum well lasers," *Proc. SPIE, Laser-Diode Technology and Applications II*, vol. 1219, pp. 69-78, 1990.

106. W. T. Tsang, "Extremely low threshold (AlGa)As graded-index waveguide separate-confinement heterostructure lasers grown by molecular beam epitaxy," *Appl. Phys. Lett.*, vol. 40(3), pp. 217-219, 1 Febuary 1982.

107. J. Puretz, R. K. DeFreez, R. A. Elliott, and J. Orloff, "Focused-ion-beam micromachined AlGaAs semiconductor laser mirrors," *Electron. Lett.*, vol. 22 , pp. 700-702, 19 June 1986.

108. R. K. DeFreez, J. Puretz, R. A. Elliott, J. Orloff, and L. W. Swanson, "CW operation of widely and continuously tunable micromachined-coupled-cavity diode lasers," *Electron. Lett.*, vol. 22, pp. 919-921, 14 August 1986.

109. J. Puretz, R. K. DeFreez, R. A. Elliott, J. Orloff, and T. L. Paoli, "300 mW operation of a surface-emitting phase-locked array of diode lasers," *Electron. Lett.*, vol. 23, pp. 130-131, 29 January 1987.

110. R. K. DeFreez, J. Puretz, R. A. Elliott, G. A. Crow, H. Ximen, D. J. Bossert, G. A. Wilson, and J. Orloff, "Focused-ion-beam micromachined diode laser mirrors," *Proc. SPIE, Laser Diode Technology and Applications*, vol. 1043, pp. 25-35, 1989.

111. L. W. Swanson, G. A. Schwind, A. E. Bell, and J. E. Brady, "Emission characteristics of gallium and bismuth liquid metal field ion sources," *J. Vac. Sci. Technol.*, vol. 16, pp. 1864-1867, November/December 1979.

112. J. Orloff and L. W. Swanson, "Optical column design with liquid metal ion sources," *J. Vac. Sci. Technol.*, vol. 19, pp. 1149-1152, November/December

1981.

113. J. Orloff, "Optical design approaches for use with liquid metal ion sources," *J. Vac. Sci. Technol. B*, vol. 5, pp. 175-177, 1987.

114. *Operation Manual for FEI FIB Workstation 610*, FEI Company, Beaverton, Oregon, 1993.

115. L. R. Harriott, R. E. Scotti, K. D. Cummings, and A. F. Ambrose, "Micromachining of integrated optical structures," *Appl. Phys. Lett.*, vol. 48(25), pp. 1704-1706, 23 June 1986.

116. A. Toda, T. Kobayashi, M. Dohsen, and Y. Mori, "Gain-guided laser diode having a curved-mirror-cavity with a low astigmatism," *Appl. Phys. Lett.*, vol. 63(6), pp. 726-728, 9 August 1993.

117. *Laser Interferometric Microscope Maxim 3D Model 5700, Zygo Catalog*, Zygo Corporation, 1990.

118. G. Crow, J. Puretz, J. Orloff, R. K. DeFreez, and R. A. Elliott, "The use of vector scanning for producing arbitrary surface contours with a focused ion beam," *J. Vac. Sci. Technol. B*, vol. 6, pp. 1605-1607, September/October 1988.

119. L. R. Harriott, R. E. Scotti, K. D. Cummings, and A. F. Ambrose, "Micromachining of optical structures with focused ion beams," *J. Vac. Sci. Technol. B*, vol. 5(1), pp. 207-210, Jan/Feb 1987.

120. L. R. Harriott, "A second generation of focused ion beam micromachining system," *Proc. SPIE, Electron-Beam, X-Ray, and Ion-Beam Lithographies VI*, vol. 773, pp. 190-194, 1987.

121. R. A. Elliott, R. K. DeFreez, J. Puretz, J. Orloff, and G. A. Crow, "Focused-ion-beam micromachining of diode laser mirrors," *Proc. SPIE., Symposium on Communications Networking in Dense Electromagnetic Environments*, vol. 876, pp. 114-120, January 1988.

122. H. Ximen, R. K. DeFreez, J. Orloff, R. A. Elliott, G. A. Evans, N. W. Carlson, M. Lurie, and D. P. Bour, "Focused ion beam micromachined three dimensional features by means of a digital scan," *J. Vac. Sci. Technol. B*, vol. 8 (6), pp. 1361-1365, Nov/Dec 1990.

123. J. Puretz, "A Theoretical and Experimental Study of Liquid Metal Ion Sources and Their Application to Focused Ion Beam Technology," *Ph.D. Dissertation*, Oregon Graduate Center (currently Oregon Graduate Institute of Science & Technology), Beaverton, Oregon, December 1988.

124. G. A. Crow, "Focused Ion Beam Micromachining of *Si* and *GaAs* Using *Ga* and *Au* Liquid Metal Ion Sources," *Ph.D. Dissertation*, Oregon Graduate Institute of Science & Technology, Beaverton, Oregon, October 1990.

125. H. Ximen, "A Study of Focused Ion Beam Micromachining by Development of a 3-D Computer Simulation and a 3-D Digital Scan Strategy," *Ph.D. Dissertation*, Oregon Graduate Institute of Science & Technology, Beaverton, Oregon, September 1990.

126. J. B. Cser, "Unstable Resonator Semiconductor Lasers Fabricated by Focused Ion Beam Micromachining," *M.S. Thesis*, Oregon Graduate Institute of Science & Technology, Beaverton, Oregon, October 1990.

127. M. H. F. Overwijk and J. A. de Poorter, "High-quality focused-ion-beam-made mirrors for InGaP/InGaAlp visible-laser diodes," *J. Appl. Phys.*, vol. 74(12), pp. 7048-7053, 15 December 1993.

128. J. Orloff, "High-resolution focused ion beams," *Rev. Sci. Instrum.*, vol. 64(5), pp. 1105-1130, May 1993.

129. The American Society of Mechanical Engineers, *Surface Texture (Surface Roughness, Waviness, and Lay)*, p. 30, ANSI/ASME, New York, 1985.

130. R. W. Herrick, L. G. Sabo, and J. L. Levy, "Novel method for measuring and analyzing surface roughness on semiconductor laser etched facets," *J. Vac. Sci. Technol. B*, vol. 9(6), pp. 2778-2783, Nov/Dec 1991.

131. M. Born and E. Wolf, *Principles of Optics*, Pergamon Press, New York, 1980 .

132. K. Iga, K. Wakao, and T. Kunikane, "Mode reflectivity of tilted mirrors in semiconductor lasers with etched facets," *Appl. Opt.*, vol. 20, pp. 2367-2371, 15 July 1981.

133. S. K. Ghandi, *VLSI Fabrication Principles*, Wiley, New York, 1985.

134. J. Melngailis, "Focused ion beam technology and applications," *J. Vac. Sci. Technol. B*, vol. 5(2), pp. 469-495, Mar/Apr 1987.

135. R. K. DeFreez, J. Puretz, J. Orloff, R. A. Elliott, H. Namba, E. Omura, and H. Namizaki, "Operating characteristics and elevated lifetests of focused-ion-beam micromachined transverse junction stripe lasers," *Appl. Phys. Lett.*, vol. 53 (13), pp. 1153-1155, 26 September 1988.

136. K. A. Hartnett, "Streak Camera Analysis of Dynamic Characteristics of Current Modulated Diode Laser Arrays," *M.S. Thesis*, Oregon Graduate

Center, Beaverton, Oregon, March 1988.

137. G. A. Wilson, "Picosecond Dynamics of Twin-Emitter Coherent Semiconductor Laser Arrays," *Ph.D. Dissertation*, Oregon Graduate Institute of Science & Technology, Beaverton, Oregon, April 1992.

138. G. C. Dente and M. L. Tilton, Private Communication, G. C. D. Associates and Rockwell Power Systems, Albuquerque, New Mexico, 1994.

139. M. E. Rogers and J. H. Erkkila, "Resonator mode analysis using linear prolate functions," *Appl. Opt.*, vol. 22(13), pp. 1992-1995, 1 July 1983.

140. R. J. Freiberg, P. P. Chenausky, and C. J. Buczek, "An experimental study of unstable confocal CO_2 resonators," *IEEE J. Quantum Electron.*, vol. QE-8(12), pp. 882-892, December 1972.

141. A. E. Siegman, "Unstable optical resonators," *Appl. Opt.*, vol. 13(2), pp. 353-367, February 1974.

142. G. C. Lim and W. M. Steen, "Instrument for instantaneous *in situ* analysis of the mode structure of a high-power laser beam," *J. Phys. E: Sci. Instrum.*, vol. 17, pp. 999-1007, 1984.

143. G. C. Lim and W. M. Steen, "Measurement of the temporal and spatial power distribution of a high-power CO_2 laser beam," *Optics and Laser Technology*, vol. 14, pp. 149-153, June 1982.

144. Yu. A. Anan'ev, "Establishment of oscillations in unstable resonators," *Sov. J. Quant. Electron.*, vol. 5, pp. 615-617, 1975.

145. H. C. Casey, Jr. and M. P. Panish, *Heterostructure Lasers, Part A*, p. 175, Academic, New York, 1978.

146. M. V. Klein, *Optics*, John Wiley & Sons, Inc., 1970.

147. *750 mW CW Single Mode MOPA Laser Diode*, SDL-5760 Series Catalog, SDL, Inc., San Jose, CA, 1994.

148. G. C. Dente, Private Communication, G. C. D. Associates, Albuquerque, New Mexico, 1992.

149. B. L. Frescura, C. J. Hwang, H. Luechinger, and J. E. Ripper, "Suppression of output nonlinearities in double-heterostructure lasers by use of misaligned mirrors," *Appl. Phys. Lett.*, vol. 31(11), pp. 770-773, 1 December 1977.

150. R. W. H. Engelmann and E. Bourkoff, "Proton-isolated stripe GaAs/GaAlAs lasers with tilted facet reflectors," *Inst. of Phys. Conf. Ser.*, vol. 56, pp. 309-318,

1981.

151. J. Salzman, R. Lang, S. Margalit, and A. Yariv, "Tilted-mirror semiconductor lasers," *Appl. Phys. Lett.*, vol. 47(1), pp. 9-11, 1 July 1985.

152. J. Salzman, R. Lang, A. Larson, and A. Yariv, "Confocal unstable-resonator semiconductor laser," *Opt. Lett.*, vol. 11(8), pp. 507-509, August 1986.

153. R. K. DeFreez, Private Communications, Linfield Research Institute, McMinnville, Oregon, 1994.

154. R. W. H. Engelmann, Private communication, Oregon Graduate Institute of Science & Technology, Portland, Oregon, 1994.

155. R. J. Lang, "Design of aberration-corrected curved-mirror and curved-grating unstable resonator diode lasers," *IEEE J. Quantum Electron.*, vol. QE-30(1), p. 31, January 1994.

156. D. Attwood, "New opportunities at soft-X-ray wavelengths," *Physics Today*, vol. 45(8), Part I, pp. 24-31, August 1992.

157. L. Goldberg and J. F. Weller, "Broad-area high-power semiconductor optical amplifier," *Appl. Phys. Lett.*, vol. 58(13), pp. 1357-1359, 1 April 1991.

158. S. O'Brien, D. Mehuys, D. F. Welch, R. Parke, and D. Scifres, "High power monolithically integrated diode laser, preamplifier, and coherent beam expander," *Appl. Phys. Lett.*, vol. 61(22), pp. 2638-2640, 30 November 1992.

159. J. N. Walpole, E. S. Kintzer, S. R. Chinn, C. A. Wang, and L. J. Missaggia, "High-power strained-layer InGaAs/AlGaAs tapered traveling wave amplifier," *Appl. Phys. Lett.*, vol. 61, pp. 740-742, 17 August 1992.

160. D. F. Welch, R. Parke, D. Mehuys, A. Hardy, R. Lang, S. O'Brien, and S. Scifres, "1.1 W CW, diffraction-limited operation of a monolithically integrated flared-amplifier master oscillator power amplifier," *Electron. Lett.*, vol. 28(21), pp. 2011-2013, 8 October 1992.

161. J. N. Walpole, E. S. Kintzer, S. R. Chinn, J. C. Livas, C. A. Wang, L. J. Missaggia, and J. D. Woodhouse, "High-power monolithic tapered semiconductor oscillators," *Tech. Digest, Conf. on Lasers and Electro-Optics (CLEO 1994)*, p. 1, 1994.

162. D. Mehuys, D. F. Welch, L. Goldberg, and J. Weller, "11.6 W peak power, diffraction-limited diode-to diode optical amplifier," *Appl. Phys. Lett.*, vol. 62(6), pp. 544-546, 8 February 1993.

163. L. Goldberg and D. Mehuys, "21 W broad area near-diffraction-limited semiconductor amplifier," *Appl. Phys. Lett.*, vol. 61(6), pp. 633-635, 10 August 1992.

164. E. S. Kintzer, J. N. Walpole, S. R. Chinn, C. A. Wang, and L. J. Missaggia, "High-power, strained-layer amplifiers and lasers with tapered gain regions," *IEEE Photon. Tech. Lett.*, vol. 5(6), pp. 605-608, June 1993.

165. R. J. Lang, A. Hardy, R. Parke, D. Mehuys, S. O'Brien, J. Major, and D. Welch, "Numerical analysis of flared semiconductor laser amplifiers," *IEEE J. Quantum Electron.*, vol. QE-29(6), pp. 2044-2051, June 1993.

166. R. J. Lang, D. Mehuys, A. Hardy, K. M. Dzurko, and D. F. Welch, "Spatial evolution of filaments in broad area diode laser amplifiers," *Appl. Phys. Lett.*, vol. 62(11), pp. 1209-1211, 15 March 1993.

167. S. A. Biellak, G. Fanning, Y. Sun, S. S. Wong, and A. E. Siegman, "High power diffraction-limited reactive-ion-etched unstable resonator diode lasers," *Tech. Digest, Conf. on Lasers and Electro-Optics (CLEO 1994)*, p. 4, 1994.

Appendix A. Calculation of Transverse Beam Size from Transverse Divergence Angle

For a semiconductor laser, the transverse divergence angle of its output beam can be measured by recording its far-field pattern[51]. Then the transverse beam size, full width at half maximum (or FWHM for short), can be calculated in the following way.

A gaussian beam[58] profile is usually assumed for the transverse direction. Expressions for the electric field and intensity distribution are

$$E(y,z) = E_0 exp\left(-\frac{y^2}{\omega^2(z)}\right), \tag{A1}$$

$$I(y,z) = |E_0|^2 exp\left(-\frac{2y^2}{\omega^2(z)}\right), \tag{A2}$$

with

$$\omega^2(z) = \omega_{0y}^2\left(1+\frac{z^2}{z_0^2}\right), \tag{A3}$$

$$z_0 = \pi\omega_{0y}^2/\lambda, \tag{A4}$$

where ω_{0y} is the gaussian beam spot size, λ is the wavelength, y is the coordinate along the transverse direction, and z is the coordinate along the longitudinal direction with z=0 at the plane of the output mirror.

1) Assuming $y = y_{hm}(z)$ as the transverse position for half maximum of intensity, then, we have:

$$exp\left(-\frac{2y^2{}_{hm}(z)}{\omega^2(z)}\right) = \frac{1}{2}, \tag{A5}$$

i.e.,

$$y_{hm}(z) = \sqrt{\frac{ln2}{2}}\omega(z). \tag{A6}$$

At the beam waist, we have z=0, and $\omega(z)\big|_{z=0} = \omega_{0y}$, so the beam size at FWHM can be written as

$$h_{\perp} = 2y_{hm}(z)\Big|_{z=0} = \sqrt{2ln2}\,\omega_{0y}. \tag{A7}$$

2) The transverse divergence angle (FWHM) $\theta_{\perp}$ can be expressed as:

$$\tan\left(\frac{\theta_{\perp}}{2}\right) = \lim_{z\to\infty}\frac{y_{hm}(z)}{z} = \sqrt{\frac{ln2}{2}}\lim_{z\to\infty}\frac{\omega(z)}{z}, \tag{A8}$$

Substituting equations (A3) and (A4) into (A8), we have

$$\tan\left(\frac{\theta_{\perp}}{2}\right) = \sqrt{\frac{ln2}{2}}\frac{\omega_{0y}}{z_0} = \left(\frac{\lambda}{\pi\omega_{0y}}\right)\sqrt{\frac{ln2}{2}}. \tag{A9}$$

From equations (A7) and (A9), the beam size at FWHM can be related to the divergence angle as

$$h_{\perp} = \frac{\lambda ln2}{\pi\tan(\theta_{\perp}/2)}. \tag{A10}$$

Appendix B. Total Internal Reflection Considerations

For high magnification URSLs, the lateral divergence angle of the output beams can be so large that total internal reflection (TIR) could occur at the two side regions of the output mirrors. The formula for calculating the TIR conditions will be derived here. For an half-symmetric URSL with stripe width 2a, cavity length L, and resonator magnification M, as shown in Figure B1, relevant URSL parameters[13] are the radius curvature of the curved mirror, as derived from equations (2.5) and (2.6) with $R_1 \to \infty$, $R_2 = -R$,

$$R = \frac{4ML}{(M-1)^2} \quad , \tag{B1}$$

the Siegman center depth for the curved mirror

$$R_{sc} = \frac{2ML}{M-1} \quad , \tag{B2}$$

and Siegman center depth for the flat mirror side

$$R_{sf} = \frac{(M+1)L}{M-1} . \tag{B3}$$

First, let's consider the refraction process at the curved mirror. For a out-going ray striking the mirror at a lateral position x, its incident angle θ_3 and refraction angle θ_4 can be calculated using the following expressions:

$$\theta_1 = \tan^{-1} \frac{x}{R_{sc} + R - \sqrt{R^2 - x^2}} \tag{B4}$$

$$\theta_2 = \sin^{-1}(x/R) \tag{B5}$$

$$\theta_3 = \theta_1 + \theta_2, \tag{B6}$$

and

$$\sin\theta_4 = \mu_e \sin\theta_3, \tag{B7}$$

where μ_e is the modal effective refractive index. Then, the TIR condition is

$$\sin\theta_4\Big|_{x_{tir}} = \mu_e \sin\theta_3\Big|_{x_{tir}} = 1.0. \tag{B8}$$

Similarly, as shown in Figure B2, the refraction angle from the flat mirror can be related to the lateral position x and Siegman center depth R_{sf} in the following way:

$$\sin\theta = \mu_e x / \sqrt{R_{sf}^2 + x^2}. \tag{B9}$$

The corresponding TIR limit is

$$x_{tir} = R_{sf} / \sqrt{\mu_e^2 - 1} \tag{B10}$$

For an URSL with 750 μm long cavity and 6.0 magnification, the TIR limited stripe width $2x_{tir}$ is about 311 μm at the curved mirror side, and 657 μm at the flat mirror side. The effective index was assumed to be 3.35 in the calculations.

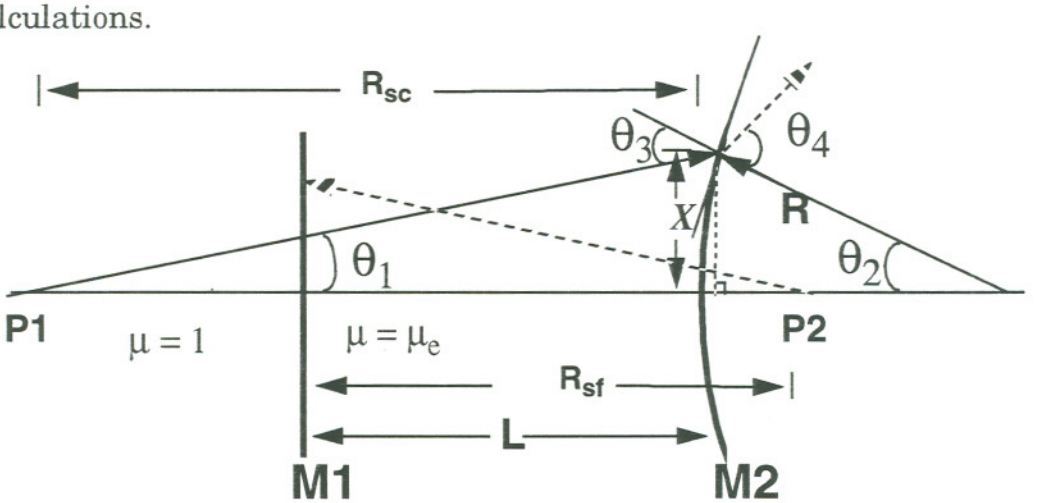

Figure B1. Schematic illustration of the refraction at the curved mirror of an URSL.

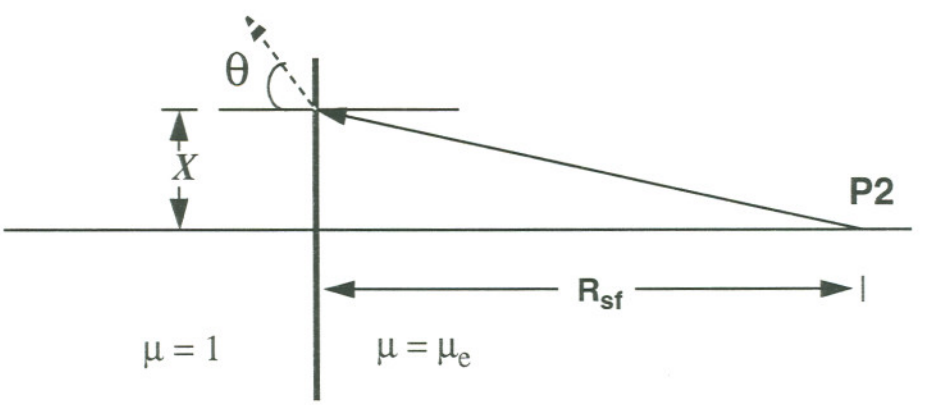

Figure B2. Schematic illustration of the refraction at the flat mirror.

Appendix C. Mirror Reflectivity Considerations

Due to the strong curvatures of both the wave fronts and the curved mirrors, the mirror reflectivities have nonnegligible spatial dependence for URSLs having high resonator magnifications and/or broad apertures. Accurate analysis could be achieved by decomposing reflected optical waves into eigen mode functions.[132] As a first order approximation, the reflection and refraction processes at the end mirrors can be described by the geometrical ray tracing method. The reflection angles are dependent on the specific positions on the mirror surfaces, so are the reflectivities and power transmission coefficients. Furthermore, the characteristics of the lateral variation of reflectivity are expected to be different for the two types of polarization of optical fields.

For the reflection at a perfect (no scattering loss) cylindrical mirror, as schematically shown in Figure C(a), the incidence angle θ_3 and refraction angle θ_4 can be calculated from the lateral coordinate x and effective index μ_e of the laser medium in the following way (neglecting sag)

$$\theta_1 = \tan^{-1}\left(x/\left((r_1+1)L\right)\right), \tag{C1}$$

$$\theta_2 = \tan^{-1}\left(x/(r_2 L)\right), \tag{C2}$$

$$\theta_3 = \theta_1 + \theta_2, \tag{C3}$$

$$\theta_4 = \sin^{-1}\left(\mu_e \sin\theta_3\right), \tag{C4}$$

where the effective index of air is taken as unity. Then the optical power reflectivity $\rho_c^{TE}(x)$ for TE modes can be expressed as

$$\rho_c^{TE}(x) = \left|\left(\cos\theta_3 - \mu_e\cos\theta_4\right)/\left(\cos\theta_3 + \mu_e\cos\theta_4\right)\right|^2. \tag{C5}$$

And the power transmission coefficient $T_c^{TE}(x)$ is

$$T_c^{TE}(x) = 1 - \rho_c^{TE}(x), \tag{C6}$$

where the scattering and absorption effects are ignored.

Similar expressions can be derived for TM UR modes as

$$\rho_c^{TM}(x) = \left|(\mu_e \cos\theta_3 - \cos\theta_4) / (\mu_e \cos\theta_3 + \cos\theta_4)\right|^2, \tag{C7}$$

and

$$T_c^{TM}(x) = 1 - \rho_c^{TM}(x). \tag{C8}$$

For the reflection at the planar mirror of a half-symmetric URSL, as shown in Figure C(b), the incidence angle θ_1 and refraction angle θ_2 can be derived as

$$\theta_1 = \tan^{-1}(x/(r_2 + 1)L), \tag{C9}$$

$$\theta_2 = \sin^{-1}(\mu_e \sin\theta_1), \tag{C10}$$

respectively. The reflectances are

$$\rho_f^{TE}(x) = \left|(\cos\theta_1 - \mu_e \cos\theta_2) / (\cos\theta_1 + \mu_e \cos\theta_2)\right|^2, \tag{C11}$$

and

$$\rho_f^{TM}(x) = \left|(\mu_e \cos\theta_1 - \cos\theta_2) / (\mu_e \cos\theta_1 + \cos\theta_2)\right|^2, \tag{C12}$$

for TE and TM UR modes respectively. The optical power transmission coefficients can be calculated in the similar way as in equations (C6) and (C8).

In reality, the surface roughness of non-perfect mirrors will cause scattering losses, and decrease the mirror reflectivities and transmission coefficients. Relevant quantitative analysis were given in Chapter 4, and will not be repeated here. Eventually, the scattered light will be absorbed by the unpumped regions, or randomly escape away from the resonator.

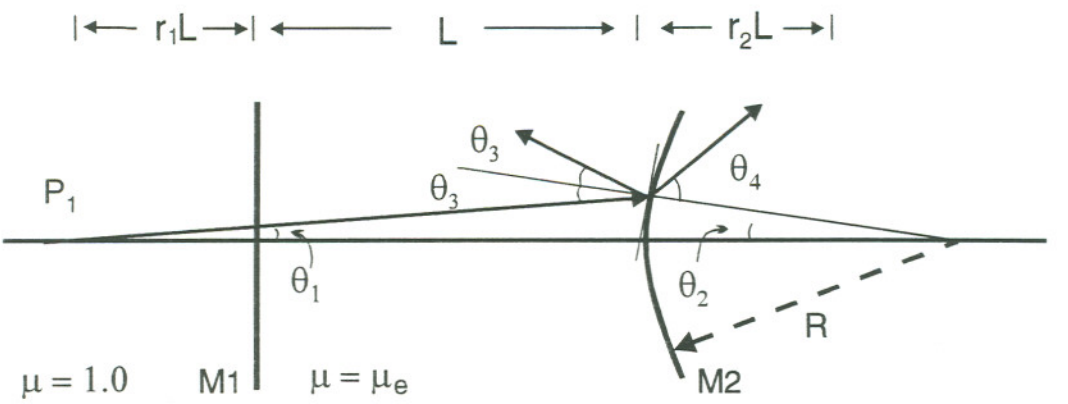

a)

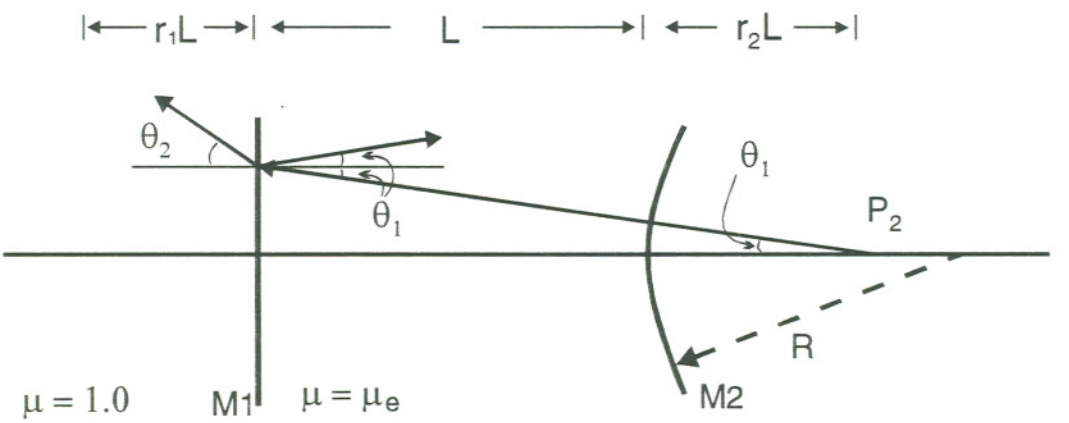

b)

Figure C Reflection at end mirrors -- reflectivity considerations; **a)** at the curved mirror, **b)** at the flat mirror.

Appendix D. Virtual Source Size Considerations

I. "Diffraction-limited" Apparent Virtual Source Size

Considering the diagram shown in Figure D1, the apparent virtual source from the curved mirror side is assumed to be a perfect point source. By collimating, or imaging with a large optical magnification, the spot source through a microscope objective, the smallest resolvable source size will be determined by the limiting aperture of the collimated beam. Assuming the limiting aperture width is D, and the focal length of the objective is f, then, the smallest resolvable source size (FWHM) is

$$d_0 = \left(\frac{1}{2}\right)\left(\frac{2f\lambda}{D}\right), \tag{D1}$$

where λ is the vacuum wavelength. Usually, the limiting aperture is determined by the divergence angle θ of the URSL output beam, which gives

$$D = 2f\tan\theta \approx 2fa/R_{v2}, \tag{D2}$$

where a is half of the stripe width, R_{v2} is the apparent virtual source depth measured from the cylindrical mirror surface. Substituting equation (D2) into (D1), we have

$$d_0 = R_{v2}\lambda/(2a)\,. \tag{D3}$$

This same expression can also be used to calculate the virtual source size from the flat mirror side, except that R_{v2} needs to be replaced by R_{v1}.

However, the objective aperture has to be used as the beam limiting aperture in equation (D1) when it is smaller than the calculated D in equation (D2).

For example, with a dimension of 200 μm × 500 μm and magnification of 2.5, "diffraction-limited" apparent virtual source sizes of URSLs fabricated from the following three types of materials are calculated as:

GaInP/AlGaInP (660 nm): 1.1 μm,
InGaAs/AlGaAs (970 nm): 1.6 μm,
GaAs/AlGaAs Triplet (840 nm): 1.4 μm.

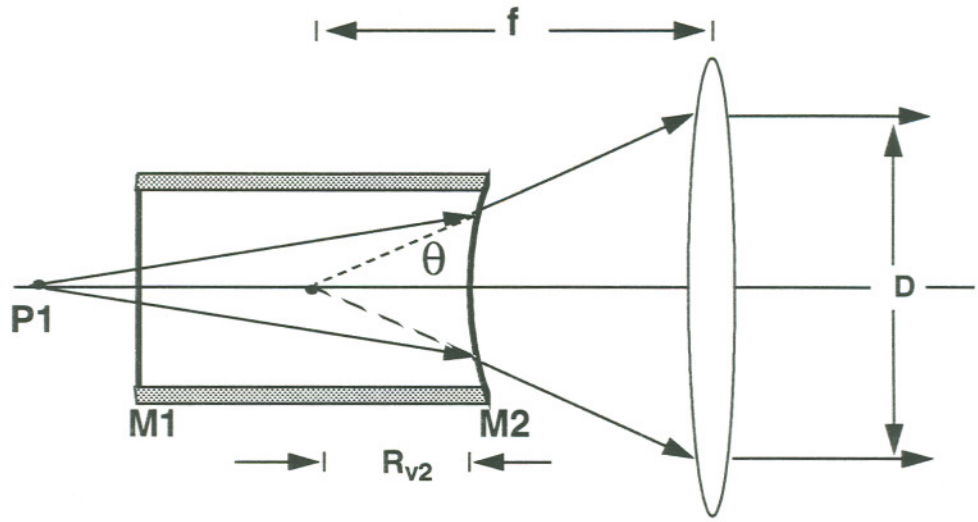

Figure D1. Diffraction-limited virtual source size.

II. Refractive Aberration Effect

Due to refractive circular aberration effects, as illustrated in Figure D2, circularly diverging waves from an ideal point "Siegman center" P1 will not form an ideal virtual spot source after refraction at the output mirror. From the point view of geometrical optics, rays that have different divergence angles will have different virtual source depths. The consequence is blurring of the virtual source away from an ideal point. In principle, this blurring effect will lead to measured virtual source sizes larger than the pure "diffraction-limited" source sizes described in the last section. Here, formulae are derived for the analysis of the aberration effects.

Considering a ray starting from the left Siegman center and striking the circular mirror at a lateral position x it forms an angle θ_s to the optical axis. After refraction at the curved mirror, the ray can be traced backward to a crossing point Vx on the optical axis. This crossing point is the local apparent virtual source. The distance between Vx and the apex of the circular mirror is denoted as the apparent virtual source depth $R_{v2}(x)$, which can be derived through the following procedures (neglecting sag).

$$\theta_s = \tan^{-1}(x/R_{sc}), \tag{D4}$$

$$\theta_m = \sin^{-1}(x/R), \tag{D5}$$

$$\theta_i = \theta_s + \theta_m, \tag{D6}$$

$$\theta_o = \sin^{-1}(\mu_e \sin\theta_i), \tag{D7}$$

$$\phi = \theta_o - \theta_m, \tag{D8}$$

$$R_{v2}(x) = x/\tan\phi. \tag{D9}$$

The notations in Figure D2 are: R for the radius curvature of the circular mirror, R_{sc} is the Siegman center depth from the circular mirror, R_{v2} is the nominal apparent virtual source depth, and μ_e is the effective refractive index.

For rays that are very close to the optical axis, i.e., $x \ll R$, we have

$$\theta_o \approx \mu_e(\theta_s + \theta_m) \approx \mu_e\left(\frac{x}{R} + \frac{x}{R_{sc}}\right), \tag{D10}$$

$$R_{v2} \approx x/\phi \approx x/(\theta_o - \theta_m) \approx \left[\mu_e\left(\frac{1}{R} + \frac{1}{R_{sc}}\right) - \frac{1}{R}\right]^{-1}, \tag{D11}$$

where R is taken as positive for convex mirrors here (as in Appendix B), which is opposite to the standard used in chapter 2 of this dissertation. R_{v2} is usually taken as the nominal apparent virtual source depth for the circular mirror side. The position of this nominal apparent virtual source is denoted in Figure D2 as Vo.

For broad-area URSLs, the approximation of $x \ll R$ is not valid any more. The position Vx of local apparent virtual source for a ray at the stripe edge can be far away from Vo, and shall be calculated using equations (D4) - (D9). The splitting effect of local apparent virtual sources will blur the virtual source profile. If the virtual source profile is taken from the nominal apparent virtual source plane, as shown in Figure D2, a ray off the optical axis with x on the mirror will cross the plane with a lateral shift of δ away from the nominal source.

Example: Considering a 200 μm $\times$ 500 μm URSL with 2.5 magnification, the marginal ray (x = 100μm) will correspond to a lateral shift δ of

5.84 μm, which is substantially more than the diffraction limited values calculated from equation (D3). The calculated lateral shift δ values are plotted versus lateral position x in Figure D3.

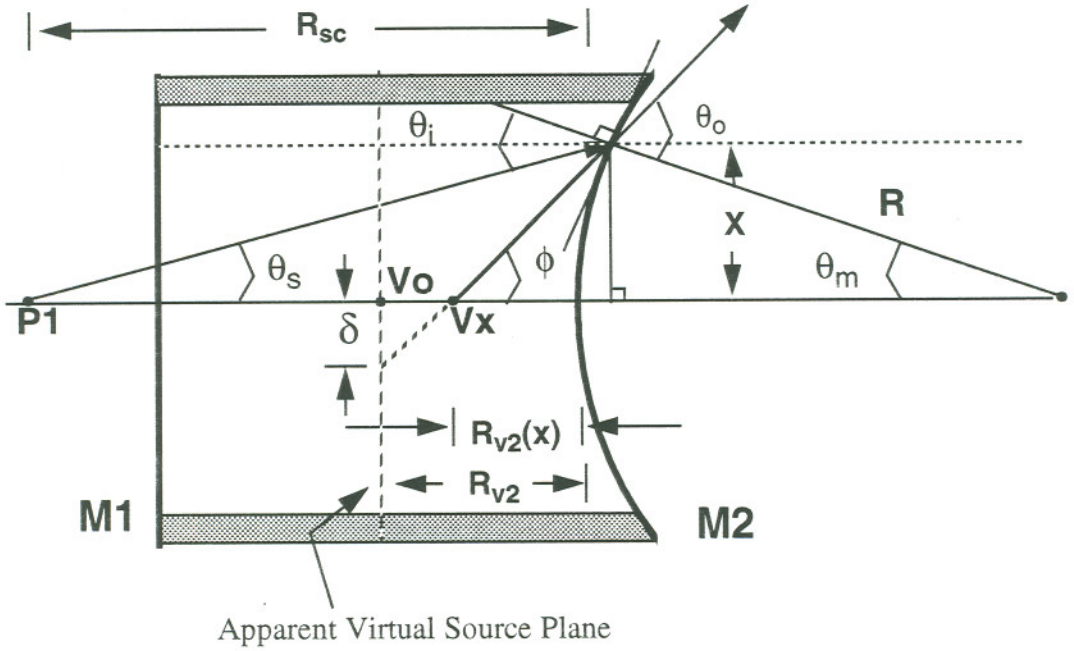

Figure D2. Refractive aberration effects on the virtual source size.

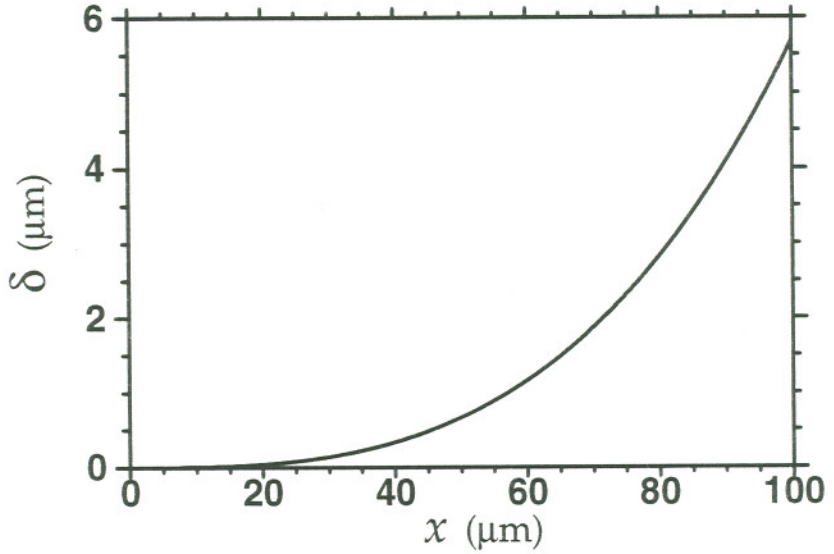

Figure D3. Aberration induced lateral shift of apparent virtual source positions.

III. Computer programs for aberration calculations

PROGRAM DIFFRACTION.F

```
**********************************************************************************
**
C  This will propagate the initial complex field data file through the sag region and then back some
C  distance to the position of apparent virtual source.
C**********************************************************************************
***
      integer npts, m3
      real Er(20000), Ei(20000), X(20000), work(20000)
      real distance, k, phase, rlam, vrs,vrv,iratio, alpha,vmag, pi, xk, delx, rin, rr, ax,az
      common /int/ npts
      common /working/ Er, Ei, X, rlam, work,pi

c Get the input value for the variables
c input wavelength
      rlam=1.0d-04
c cavity length
      az=5.0d-02
c input the number of lateral steps
      npts=2048
c refractive index
      rin=3.35
c resonator magnification
      vmag=2.5
c lateral step size
      delx=5.d-06
c lateral domain width
      ax=(npts-1)*delx
c mirror aperture size
      sw=2.0d-02
      pi=3.1415926535898d0
      m3=(1.-sw/ax)*npts/2
c calculate the mirror radius of curvature and virtual source depth
      rr=az*(((vmag+1.d0)/(vmag-1.d0))**2 -1.d0)
      vrs=(vmag-1.d0)*rr/2.d0
      vrv=1.d0/(rin/vrs + (rin-1.d0)/rr)
      print*,"Apparent Virtual Source Depth=", vrv

c set propagation distance
      distance=(-1.02d0)*vrv
c     wave vector
      k= 2*3.14159265d0/rlam
c Setting up a field with circular phase front centered at the apparent virtual source of the curved mirror
side.
      do 21 l=(m3)+1,(npts-m3+1)
      X(l)=(l-1)*delx
```

```
      xk=(l-1)*delx-ax/2.d0
      phase= k* (dsqrt(vrv*vrv + xk*xk) - vrv)
      Er(l)=dcos(phase)
      Ei(l)=dsin(phase)
21    continue
      do 22 l=1,m3
      X(l)=(l-1)*delx
      Ei(l)=0.d0
      Er(l)=0.d0
22    continue
      do 23 l=(npts-m3)+2,npts
      X(l)=(l-1)*delx
      Er(l)=0.d0
      Ei(l)=0.d0
23    continue

      call OUTPUT(distance, delx, k)

      stop
      end


    subroutine OUTPUT(distance, xstep, k)
C_____________________________________________________________________
___
C     This subroutine propagates a complex field a given distance by the FFT technique.
C          distance- physical distance
C          k- Wavenumber in material
C          xstep - physical separation of points
C   And then output the optical intensity distribution.
C_____________________________________________________________________
___
      integer npts
      double precision distance, xstep, k,pi
      double precision Er(20000), Ei(20000), X(20000), work(20000)
      double precision Er2(20000), Ei2(20000), fint(20000)
      double precision term, term2, cst, snt, twopi, rlam
      common /int/ npts
      common /working/ Er, Ei, X,rlam, work,pi

c     write(6,*) "Distance = ",distance
c     write(6,*) "xstep = ",xstep
c     write(6,*) "k = ",k
C-------------First transform
      IFAIL=0
c     write(6,*) "Making first transform..."
      call C06FCF( Er, Ei, npts, work, IFAIL)

C-------------Multiply by progation factor and make complex
C  conjugate(CC), ready for inverse transform
      twopi=2*pi
```

```
        term= (twopi/(npts*xstep))**2 * distance/2.d0/k
        do 55 i=1, npts/2
        term2=dfloat(i-1)**2
        cst=dcos(dmod( term2*term, twopi ))
        snt=dsin(dmod( term2*term, twopi ))
        Er2(i)= Er(i)*cst + Ei(i)*snt
        Ei2(i)= -( Ei(i)*cst - Er(i)*snt )
55      continue
        do 56 i=npts/2+1, npts
        term2=dfloat(i-npts-1)**2
        cst=dcos(dmod( term2*term, twopi ))
        snt=dsin(dmod( term2*term, twopi ))
        Er2(i)= Er(i)*cst + Ei(i)*snt
        Ei2(i)= -( Ei(i)*cst - Er(i)*snt )
56      continue

C---------------Transform back (but answer is still CC)
        IFAIL=0
c       write(6,*) "Making inverse transform..."
        call C06FCF( Er2, Ei2, npts, work, IFAIL)

C------------Reset initial arrays, making CC adjustment
        do 57 i=1, npts
        Er(i)=Er2(i)
        Ei(i)=-Ei2(i)
57      continue

c  open data file to record the optical intensity distribution
        open (11, file='vs.dat', status='new')
        do 60 j=npts/4, (npts*3/4)
        fint(j)= Er(j)*Er(j)+Ei(j)*Ei(j)
        write(11,1000) X(j), fint(j)
60      continue
1000    format(1x,2e16.8)
        close(11)
        return
        end
```

PROGRAM CONVOLUTION.F

```
**********************************************************************************
**
C  This code has the following two functions:
C  (1) First, it models the density of number of geometrical rays at the position of virtual source, the
C        output  data  is the lateral distribution of that density--or the optical intensity. Uniform angular
C        distribution is assumed.
C  (2) Then, it reads in the optical intensity distribution calculated in last code "diffraction.f", and does
the
C        convolution with the aberration based intensity distribution.
**********************************************************************************
**
        integer n,ll,mm,cy
        real dy,ddy,l,rm,rin,naobj,w,m,mag,rs,s, pi,dnalim,lambda,dw,h,hm
        real thss,ths,thm,tho,x,out,phimax,nalas,nalim
        real phi(10000),rv(10000), fi(10000)
        real y(20000),ym(20000),xv(10000),ccy(20000)

        open(2,file="con.dat")
        open(3,file="vs.dat",status="old")

        read (3,*) n
         if (n.le.1) stop
         do 10 j=1,n
         read (3,*) xv(j), fi(j)
 10     continue
        xstep=xv(2) - xv(1)
        lambda=0.66
        pi=3.141592654
c Cavity length (all lengths in microns)
        l=500.
c Curved mirror radius
        rm=2222
c Laser effective refractive index
        rin=3.35
c Numerical aperture of objective lens
        naobj=0.40
c Full width of laser stripe
        w=200
c Calculate little m
        m=1+2*l/rm
c Calculate resonator magnification
        mag=m+sqrt(m*m-1)
c Calculate Siegman source distance (R sub s or L sub v)
        rs=rm*(mag-1)/2.
c Calculate mirror sag
        s=rm-sqrt(rm*rm-w*w/4.0)
c Initialize height, h, on the curved output mirror
        h=w/2.
        ths=atan(h/(rs+s))
        thm=asin(h/rm)
```

```
            tho=asin(rin*sin(ths+thm))
            phimax=tho-thm
            nalas=sin(phimax)
            nalim=amin1(naobj,nalas)
c Calculate FWHM diameter of minimum resolvable spot due to system numerical aperture
            dnalim=0.52*lambda/nalim
c Calculate FWHM diameter of minimum spot due to stripe width
            dw=2*1.4/pi/w*rs
c For each height h on the mirror:
            do 100 i=1,4000
c Calculate half angle subtended at the Siegman source
            thss=i*ths/4000.
c Calculate half angle subtended at the mirror center of curvature
            hm=(rs+s)*tan(thss)
            thm=asin(hm/rm)
c Calculate angle of external ray relative to mirror radius
            tho=asin(rin*sin(thss+thm))
c Calculate the virtual source internal radiation angle
            phi(i)=tho-thm
c Calculate the virtual source position behind mirror on axis
            rv(i)=hm/tan(phi(i))-s
c           print*, i, rv(i)
 100        continue
            x=rv(1)
            do 200 j=1,4000
            y(j)=(x-rv(j))*tan(phi(j))
            ym(j)=(-1.)*y(j)
 200        continue

c calculate the ray density distribution at the apparent virtual source plane
            jj=1
            do 400 dy=xv(1),xv(n),xstep
            ddy=dy+xstep
            cy=0
            do 300 j=1, 4000
            if (y(j).gt.dy.and.y(j).le.(ddy)) then
            cy=cy+1
            else if (ym(j).gt.dy.and.ym(j).le.(ddy)) then
            cy=cy+1
            end if
 300        continue
            ccy(jj)=1.0*cy
c           print*, jj, ccy(jj)
            jj=jj+1
 400        continue

c  calculate the convolution of the pure diffraction-limited source profile and the aberration-induced ray
c  density distribution
            do 800 ll=1,2*n
            x=(ll-n)*xstep
            out=0.0
```

```
      do 450 mm=1,ll
      out=out + fi(mm)*ccy(ll-mm+1)*xstep
450   continue
      write (2,480) x, out
800   continue
      print*, xstep, out, x, ll, n
      close(2)
      close(3)
480   format(1x,f12.6,2x,f12.6)
      end
```

Appendix E. Simple Algorithm for Calculations of URSL Sub-threshold Spatio-spectral Patterns

Emission frequencies of lasing modes from a Fabry-Perot type resonator are expressed as (mode number m)

$$\gamma_m = mc/(2L\mu_e), \tag{E1}$$

where c is the vacuum velocity of light, μ_e is the effective refractive index of the resonator medium. The group index of the medium can be written as

$$\mu_g = \mu_e + \gamma_m\left(\frac{d\mu_e}{d\gamma}\right). \tag{E2}$$

Assuming the center of the *mth* longitudinal mode corresponds to

$$\gamma_0 = \gamma_m\Big|_{x=0} = \gamma(L_0, \mu_e) = \frac{mc}{2L_0\mu_e}, \tag{E3}$$

where L_0 is the cavity length for the center region, and μ_e is the corresponding refractive index. Then the frequencies of the same longitudinal mode at different lateral positions with cavity length L_x is

$$\gamma_m(x) = \frac{mc}{2L(x)}\left(\mu_e + \Delta\gamma\frac{d\mu_e}{d\gamma}\right)^{-1}. \tag{E4}$$

And the frequency variation can be written as

$$\Delta\gamma = \gamma_m(x) - \gamma_0 = \left(\frac{mc}{2L(x)} - \gamma_0\mu_e\right)\Big/\left(\mu_e + \gamma_0\frac{d\mu_e}{d\gamma}\right), \tag{E5}$$

where only the first order approximation is considered. Furthermore, let's assume a constant μ_g for a narrow spectral region as shown in Figure 5.10, and introduce (E1) into (E5), then we have

$$\Delta\gamma = \frac{mc}{2\mu_g}\left[\frac{1}{L(x)} - \frac{1}{L_0}\right] \approx -\gamma_0\frac{\mu_e}{\mu_g}\frac{\Delta L(x)}{L_0}, \tag{E6}$$

where the spatial variation of effective refractive index was ignored. The

equivalent expression in wavelength is

$$\Delta\lambda = \lambda_0 \frac{\mu_e}{\mu_g} \frac{\Delta L(x)}{L_0}. \tag{E7}$$

For URSLs with cylindrical mirrors, the cavity length variations versus the lateral positions $\Delta L(x)$ can be calculated accordingly, so are the mode wavelength variations. Figure 5.11 was obtained by mapping the data calculated using Equation (E7).

Stating with the expression of mode spacing in wavelength

$$\delta\lambda = \frac{\lambda^2}{2L\mu_g}, \tag{E8}$$

the variation of mode spacing with lateral positions can be straightforwardly derived as

$$\Delta(\delta\lambda) \propto \delta\lambda \frac{\Delta L(x)}{L_0}. \tag{E9}$$

For URSLs, the ratio $\Delta L(x)/L_0$ is usually very small, so this lateral variation of mode spacing $\Delta(\delta\lambda)$ is negligible since $\delta\lambda$ is far less than λ_0.

VITA

The author was born on February 8, 1966 in Anhui province, China. He attended the Anqing Teacher's College in September 1981, and graduated in July 1985 with a B.S. degree in physics. After the summer, he spent one year in The Graduate School of The Chinese Academy of Science to complete a graduate course study, and two years in Wuhan Institute of Physics to conduct research in the areas of laser spectroscopy, nonlinear optics, and atomic/molecular physics. He received a M.S. degree in Quantum Electronics in July 1988. In the following two years, he remained in the same institute to complete the research projects in which he had been involved. In 1990, he decided to switch his interest to applied research, and came to the Oregon Graduate Institute to pursue a Ph.D. degree in applied physics. After working on semiconductor lasers and focused-ion-beam micromachining for four years, he completed all the requirements towards his degree in 1994.

He married the former Mei Hong in January 1993.

During his stay at Oregon Graduate Institute, he contributed to the following list of publications in journals and conference proceedings:

(1) R. K. DeFreez, Z. Bao, G. A. Evans, B. W. Baird, and R. S. Harris, "Focused-ion-beam micromachined unstable resonator semiconductor lasers," *Proceedings of the Annual Meeting of the Optical Society of America,* Dallas, October 2-7, 1994.

(2) Z. Bao, and R. K. DeFreez, "Theoretical analysis of unstable resonator semiconductor lasers," To be published in *Proc. SPIE, Physics and Simulation of Optoelectronic Devices II,* Vol. 2146, 1994.

(3) Z. Bao, R. K. DeFreez, P. D. Carleson, M. K. Felisky, C. Largent, and H. B. Serreze,

"Design considerations for high power GaInP/AlGaInP unstable resonator semiconductor lasers," *Applied Optics*, Vol. 32(36), pp. 7402-7407, 20th December 1993.

(4) Z. Bao, R. K. DeFreez, P. D. Carleson, C. Largent, C. Moeller, and G. C. Dente, "Spatio-spectral characteristics of a high power, high brightness CW InGaAs/AlGaAs unstable resonator semiconductor laser," *Electronics Letters*, Vol. 29(18), pp. 1597-1599, 2nd September 1993.

(5) R. K. DeFreez, Z. Bao, P. D. Carleson, M. K. Felisky, and C. Largent, "High-brightness unstable resonator semiconductor lasers," *Proc. SPIE, Laser Diode Technology and Applications V*, Vol. 1850, pp. 75-83, 1993.

(6) R. K. DeFreez, Z. Bao, P. D. Carleson, C. Largent, C. Moeller, G. C. Dente, D. J. Gallant, J. Metz, M. L. Tilton, G. A. Evans, W. F. Reichert, C. A. Wang, and H. K. Choi, "A high power unstable resonator semiconductor laser," in *Conference on Lasers and Electro-Optics*, Vol. 12 of OSA Proceedings (Optical Society of America, Washington, D. C., 1992), pp. 340, 342.